Encapsulation of Selected Metallated Phthalocyanines in Aluminium Aminoterephthalate Framework, NH_2-MIL-101(Al), with Heterogeneous Catalytic and Hydrogen Storage Applications

Submitted in fulfilment of the requirements in respect of the Doctoral degree qualification

Philosophiae Doctor

in the Department of

Department of Chemistry

in the Faculty of

Natural and Agricultural Sciences

at the

University of the Free State

by

Frederick Hermanus Peens

Date

31 January 2017

Supervisor

Dr. E.H.G. Langner

Dedication

I dedicate this thesis to my first-born daughter, Carolien Alexa Peens who I love ever so much.

Proverbs 1:7

The fear of the Lord is the beginning of knowledge, but fools despise wisdom and instruction.

Table of Contents

TABLE OF CONTENTS

Acknowledgements

It is my utmost pleasure to firstly thank God Almighty for the strength, wisdom, perseverance and the unrelenting passion for chemistry He bestows on me every day.

I would like to thank my supervisor, Dr. E.H.G. Langner, for his excellent guidance during this research project. His patients, love for chemistry and helpfulness inspired me every day. Thank you for your exceptional leadership, support as well as your catching enthusiasm towards science.

To all my family, friends and colleagues: thank you very much for your support during my studies and the joys we shared together.

I want to thank my wife, Roné Peens, for her everlasting inspiration, love, joy and support. You are the reason that I see life's problems only as stepping stones. I love you my dear.

Lastly, I want to thank the National Research Foundation (NRF) for financial support and thus making it possible for me to live out my passion. I also want to thank iThemba LABS for the analysis of my products with low-angle PXRD.

Declaration

I, Frederick Hermanus Peens, declare that the Doctoral Degree research thesis or interrelated, publishable manuscripts / published articles, or coursework Doctoral Degree mini-thesis that I herewith submit for the Doctoral Degree qualification Ph.D. Chemistry at the University of the Free State is my independent work, and that I have not previously submitted it for a qualification at another institution of higher education.

I, Frederick Hermanus Peens, hereby declare that I am aware that the copyright is vested in the University of the Free State.

I, Frederick Hermanus Peens, hereby declare that all royalties as regards intellectual property that was developed during the course of and/or in connection with the study at the University of the Free State, will accrue to the University.

Signed: 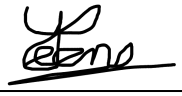 Date: 2017/04/06

List of Abbreviations

-act	-	activated
-as	-	as-synthesised
-C=O	-	carbonyl
-COO	-	carbonyl-carbonyl
$-NH_2$	-	amine
-sol	-	solution phase infiltration
-sox	-	soxhlet extracted
-temp	-	templating
^{1}H-NMR	-	proton nuclear magnetic resonance
2Θ	-	2-theta
δ	-	chemical shift
°C	-	degrees Celsius
ΔE_p	-	separation of anodic peak and cathodic peak potentials
ε	-	molar extinction coefficient
λ	-	wavelength
μ -	-	micro
$[NBu_4][PF_6]$	-	tetrabutylammonium hexafluorophosphate
Å	-	Ångström
A	-	Ampere
ASAP	-	accelerated surface area and porosity
BET	-	Brunauer, Emmett and Teller
B_x	-	soret band
cm^{-1}	-	wave number
cm^3	-	cubic centimetres
CV	-	cyclic voltammetry
DBU	-	1,8-diazabicyclo[5.4.0]undec-7-ene
DCM	-	dichloromethane
DMF	-	dimethylformamide
DMSO	-	dimethyl sulfoxide
DRS	-	diffuse reflectance spectroscopy
E°′	-	formal reduction potential
E_{pa}	-	anodic peak potential
E_{pc}	-	cathodic peak potential
eq.	-	equivalents
etc.	-	et cetera
Fc	-	ferrocenyl
FcH	-	ferrocene
FcH*	-	decamethyl ferrocene
FTIR	-	Fourier transform infrared
H_2	-	hydrogen
ICP-AES	-	inductively coupled plasma atomic emission spectroscopy
ICP-OES	-	inductively coupled plasma optical emission spectroscopy

LIST OF ABBREVIATIONS

i_{pa}	-	anodic peak current
i_{pc}	-	cathodic peak current
IR	-	infrared
K	-	Kelvin
KOH	-	potassium hydroxide
M	-	molar
Maldi-TOF	-	matrix-assisted laser desorption ionization-time of flight
MeOH	-	methanol
mbar	-	millibar
mmol	-	millimole
MIL	-	Matériaux de l'Institut Lavoisier
MOF	-	metal organic framework
m.p.	-	melting point
MPc	-	metallated phthalocyanine
$MPc(COOH)_4$	-	tetra-substituted carboxymetallophthalocyanine
MPc^tBu_4	-	tetra-substituted tert-butylmetallophthalocyanine
mV	-	millivolts
mV/s	-	millivolts per second
MX	-	metal salt
N_2	-	nitrogen
NaOH	-	sodium hydroxide
nm	-	nanometres
Pc	-	phthalocyanine
POM	-	polyoxometalate
p/p^o	-	relative pressure
ppm	-	parts per million
PSM	-	post-synthetic modification
PTA	-	*para*-phthalic acid
PXRD	-	powder X-ray diffraction / diffractogram
$Q_{x/y}$	-	Q-band
SAXS	-	small-angle X-ray scattering
SEM-EDX	-	scanning electron microscopy-energy dispersive X-ray spectroscopy
TGA	-	thermogravimetric analysis
THF	-	tetrahydrofuran
TON	-	turnover number
UV-vis	-	ultraviolet–visible
V	-	Volts
vs.	-	versus
WAXS	-	wide-angle X-ray scattering
wt%	-	weight percentage
XPS	-	X-ray photoelectron spectroscopy

List of Products

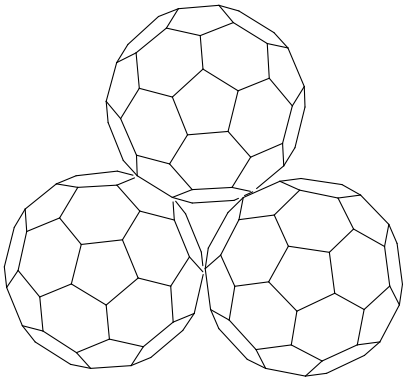

1 ≡
Representation of
NH_2-MIL-101(Al)

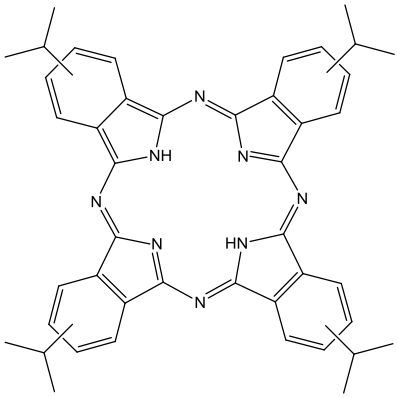

2 ≡ $2HPc^tBu_4$

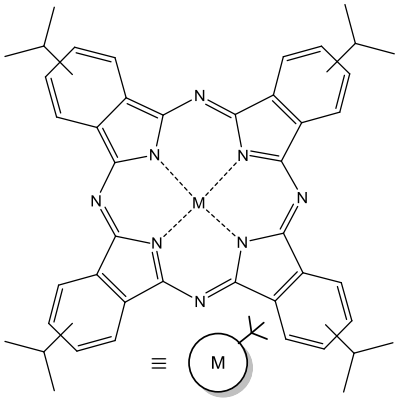

3 ≡ $ZnPc^tBu_4$ (M = Zn)
4 ≡ $NiPc^tBu_4$ (M = Ni)

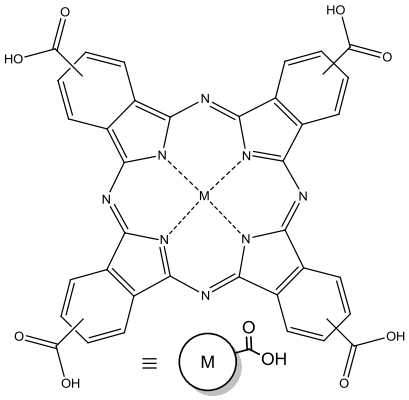

5 ≡ $ZnPc(COOH)_4$ (M = Zn)
6 ≡ $FeClPc(COOH)_4$ (M = FeCl)
7 ≡ $CoPc(COOH)_4$ (M = Co)
8 ≡ $NiPc(COOH)_4$ (M = Ni)

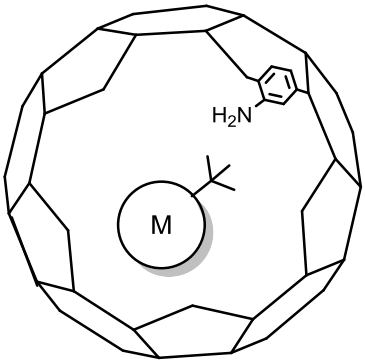

9 ≡ $ZnPc^tBu_4$@NH_2-MIL-101(Al)
(M = Zn)
10 ≡ $NiPc^tBu_4$@NH_2-MIL-101(Al)
(M = Ni)

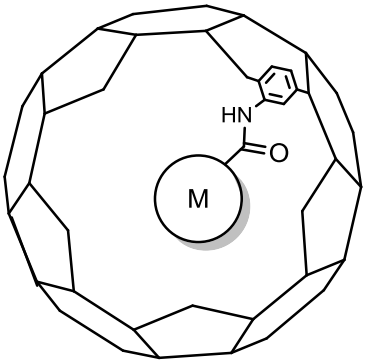

11 ≡ $ZnPc(COOH)_3$-CONH-MIL-101(Al)
(M = Zn)
12 ≡ $FeClPc(COOH)_3$-CONH-MIL-101(Al)
(M = FeCl)
13 ≡ $CoPc(COOH)_3$-CONH-MIL-101(Al)
(M = Co)
14 ≡ $NiPc(COOH)_3$-CONH-MIL-101(Al)
(M = Ni)

Abstract

The amine-functionalised metal organic framework (MOF), NH_2-MIL-101(Al) was successfully synthesised and optimised with a benchtop method. A newly developed activation method to evacuate the pores of the MOF, achieved a larger BET surface area (3192 ± 57 m^2g^{-1}) than those currently reported in literature.

2(3),9(10),16(17),23(24)-Tetra-*tert*-butylphthalocyanine ($2HPc^tBu_4$) was successfully synthesised by either the lithium method or the hydroquinone method. The latter was superior since it is a solvent-free synthesis, with a 60% higher yield than the lithium method. Successful metallation of $2HPc^tBu_4$ with the acetate salts of Zn^{2+} and Ni^{2+}, gave single Q-bands at ~670 nm during UV-Vis absorbance measurements, while double Q-band maxima were observed at 660 nm and 690 nm for the metal-free $2HPc^tBu_4$.

Four tetracarboxymetallophthalocyanines ($MPc(COOH)_4$) with Zn^{2+}; Fe^{3+}; Co^{2+} or Ni^{2+} as central metal cations were synthesised in a two-step cyclotetramerisation method. Their aggregation behaviour was determined by UV-Vis spectroscopy. For concentrations up to 180 μM, only $NiPc(COOH)_4$ showed aggregation from 5 μM, whereas $ZnPc(COOH)_4$, $FeClPc(COOH)_4$ and $CoPc(COOH)_4$ showed little to no aggregation.

Two different methods were used to encapsulate the MPcs in the pores of NH_2-MIL-101(Al): templating, as well as customised solution phase infiltration. In both procedures MPc^tBu_4 was encapsulated by the MOF via physical interaction, while all $MPc(COOH)_4$ derivatives could covalently bind to the NH_2-MIL-101(Al) structure via amide bonds. Encapsulation in the pores of the MOF would eliminate aggregation of the MPc molecules. DRS-UV-Vis showed that solution phase infiltration led to a higher loading of MPc in the MOF than when templating was used. This correlated with ASAP and PXRD results showing that all solution phase infiltration products, except for $NiPc(COOH)_3$-CONH-MIL-101(Al), had smaller BET surface areas (between 244 cm^3g^{-1} and 89 cm^3g^{-1}) due to their high loadings of MPcs.

Hydrogen storage capacities of $CoPc(COOH)_3$-CONH-MIL-101(Al) and $NiPc(COOH)_3$-CONH MIL-101(Al) were measured as 0.47 wt% (at 16 bar) and 1.5 wt% (at 128 bar) respectively.

A trial test showed that $CoPc(COOH)_3$-CONH-MIL-101(Al) catalysed the photo-oxidation of cis-cyclooctene to cis-cyclooct-2-enol with a 5% conversion.

ABSTRACT

For both $MPc^{t}Bu_4$ derivatives, liquid state cyclic voltammetry showed four Pc ring-based redox processes in DCM. With $MPc(COOH)_4$ derivatives in DMSO , three redox couples were observed. For the Co^{2+}-containing MPc, two metal-based redox processes ($E°' = -738$ mV and -289 mV vs. ferrocene) and for the Fe^{3+}-containing MPc, only one metal-based couple ($E°' = -88$ mV vs. ferrocene) was observed.

With solid state cyclic voltammetry of all MOF-encapsulated MPcs only one redox couple (near 200 mV vs. ferrocene) was detected, with the exception of $ZnPc(COOH)_3$-CONH-MIL-101(Al) which gave an additional redox couple ($E°' = 1158$ mV vs. ferrocene) and with $NiPc(COOH)_3$-CONH-MIL-101(Al) two additional couples ($E°' = 1146$ mV and 1383 mV vs. ferrocene) were present. These processes were mostly electrochemically and chemically irreversible, but showed that the MOF's matrix had a conductive effect on the flow of electrons during oxidation and reduction of the encapsulated MPcs.

Keywords: amine-functionalised, metal organic framework, benchtop method, aggregation, amide bonds, hydrogen storage, photo-oxidation, solid state, cyclic voltammetry.

Opsomming

Die amien-gefunksionaliseerde metaal organiese netwerk (MOF), NH_2-MIL-101(Al) is suksesvol gesintetiseer en geoptimiseer met die gebruik van ‘n werksbankmetode. ‘n Nuutontwerpte aktiveringsmetode om die porieë van die MOF te evakueer, het ‘n groter BET oppervlakarea (3192 ± 57 m^2g^{-1}) gegee as dié wat tans in die literatuur gerapporteer word.

2(3),9(10),16(17),23(24)-Tetra-*tert*-butielftalosianien ($2HPc^tBu_4$) is suksesvol gesintetiseer deur die litiummetode of die hidrokinoon metode. Die laaste is ‘n beter metode omdat dit ‘n oplosmiddelvrye sintese is, en ‘n 60% hoër opbrengs as die litiummetode gegee het. Suksesvolle metallering van $2HPc^tBu_4$ met die asetaatsoute van Zn^{2+} en Ni^{2+} het enkel Q-bande gegee by ~670 nm gedurende UV-Sigbare (UV-Vis) absorpsiemetings, terwyl dubbel Q-band maksima by 660 nm en 690 nm vir die metaalvrye $2HPc^tBu_4$ waargeneem is.

Vier tetrakarboksiemetalloftalosianiene ($MPc(COOH)_4$) met Zn^{2+}; Fe^{3+}; Co^{2+} of Ni^{2+} as metaalsenters is gesintetiseer in ‘n twee-stap siklotetramerisasiemetode. Hulle aggregasiegedrag is met UV-Vis spektroskopie bepaal. Vir konsentrasies tot en met 180 μM het slegs $NiPc(COOH)_4$ aggregasie getoon vanaf 5 μM, terwyl $ZnPc(COOH)_4$, $FeClPc(COOH)_4$ en $CoPc(COOH)_4$ min tot geen aggregasie getoon het nie.

Twee verskillende metodes is gebruik om die MPcs in die porieë van NH_2-MIL-101(Al) vas te vang: templatering, sowel as ‘n aangepasde vloeistoffase infiltrasiemetode. In beide prosedures is MPc^tBu_4 deur die MOF omsluit via fisiese interaksie, terwyl alle $MPc(COOH)_4$ derivate kovalent aan die NH_2-MIL-101(Al) struktuur gebind kon word via amiedbindings. Omsluiting deur die porieë van die MOF kan aggregasie van die MPc molekule uitskakel. DRS-UV-Vis het getoon dat die vloeistof-fase infiltrasiemetode tot ‘n hoër lading van MPc in die MOF gelei het, in vergelyking met templatering. Dit stem ooreen met ASAP en PXRD resultate wat gewys het dat alle vloeistof-fase infiltrasieprodukte, behalwe $NiPc(COOH)_3$-CONH-MIL-101(Al), kleiner BET oppervlaktes (tussen 244 cm^3g^{-1} and 89 cm^3g^{-1}) het, weens hulle hoë MPc ladings.

Waterstofbergingskapasiteite van $CoPc(COOH)_3$-CONH-MIL-101(Al) en $NiPc(COOH)_3$-CONH-MIL-101(Al) is gemeet as 0.47 m% (by 16 bar) en 1.5 m% (by 128 bar) onderskeidelik.

OPSOMMING

‘n Proefeksperiment het getoon dat $CoPc(COOH)_3$-CONH-MIL-101(Al) die foto-oksidasie van cis-sikloökteen na cis-sikloökt-2-enol met ‘n 5% omskakeling gekataliseer het.

Vir beide MPc^tBu_4 derivate het vloeistoffase sikliese voltammetrie in DCM vier Pc-ringgebaseerde redoksprosesse getoon. Vir die $MPc(COOH)_4$ derivate is drie redokskoppels in DMSO waargeneem. Vir die Co^{2+}-bevattende MPc is twee metaalgebaseerde redoksprosesse ($E°' = -738$ mV en -289 mV vs. ferroseen) en vir die Fe^{3+}-bevattende MPc slegs een metaalgebaseerde koppel ($E°' = -88$ mV vs. ferroseen) waargeneem.

Met vastetoestand sikliese voltammetrie van alle MPc-bevattende MOFs is slegs een redokskoppel (naby 200 mV vs. ferroseen) waargeneem, met die uitsondering van $ZnPc(COOH)_3$-CONH-MIL-101(Al) wat nog ‘n redokskoppeling getoon het ($E°' = 1158$ mV vs. ferroseen), asook $NiPc(COOH)_3$-CONH-MIL-101(Al) wat twee bykomende redokskoppelings ($E°' = 1146$ mV en 1383 mV vs. ferroseen) getoon het. Hierdie prosesse was meestal elektrochemies asook chemies onomkeerbaar, maar het getoon dat die MOF se matriks ‘n geleidende effek het op die vloei van elektrone tydens oksidasie en reduksie van die vasgevangde MPcs.

Kernwoorde: amien-gefunksionaliseerde, metaal organiese netwerk, werksbankmetode, aggregasie, amiedbindings, waterstofberging, foto-oksidasie, vaste toestand, sikliese voltammetrie.

1 Introduction and Aims

1.1 Introduction

In the last decade, the focus of Metal Organic Framework (MOF) research shifted from synthesis and discovery to derivatisation and the search for applications. MOFs, with their regular pore sizes,[1] chemical versatility[2] and large surface areas[3] are being investigated as gas storage and separation materials,[4] as well as catalysts, catalyst supports[5] and even as drug carriers.[6] The scope for specialisation in the field of MOFs is still wide open, especially with regard to the post-synthetic modification (PSM) of known MOF structures. With PSM, a large number of possible derivatives for each MOF structure can be synthesised. When the physical and chemical properties of the original MOF and the introduced substituents are combined, it may result in new materials with interesting and useful properties.[2]

Phthalocyanines (Pcs) are synthetic macrocyclic compounds, known as intense blue-green dyes. These compounds can be coordinated with almost any metal and functionalised on the peripheral, nonperipheral and axial positions, to tailor their chemical and physical properties towards specific applications. This would allow Pcs to be used in oxidation catalysis,[7] gas sensors,[8] solar cells,[9] photodynamic therapy[10] and as corrosion inhibitors.[11] Lithium phthalocyanines[12] as well as the combination of phthalocyanines and metal organic frameworks were recently investigated for hydrogen storage.[13]

For this study, the chosen MOF is MIL-101 (**M**atériaux de l'**I**nstitut **L**avoisier). The focus will be particularly on the aluminium-centred, amino-functionalised NH_2-MIL-101(Al) derivative, with its mesoporous cages, large enough to encapsulate macrocyclic molecules such as metallophthalocyanines (MPcs). For NH_2-MIL-101(Al) to accommodate these large molecules, its pores have to be fully evacuated, since this MOF has a tendency to be highly hygroscopic and any molecules still adsorbed (chemically or physically) to the MOF will decrease its surface area and lower its adsorptive capacity. In order to encapsulate MPcs in NH_2-MIL-101(Al), a proper procedure has to be developed. MPcs are diverse in applicability, but their low solubility and tendency to aggregate are major drawbacks which decrease their activity. By incorporating MPcs into MOFs as a support material, aggregation is

alleviated, since only single molecules will be encapsulated in each pore of the MOF. In addition, by covalently binding the MPc to the MOF structure, all unreacted molecules can be removed, leaving only the attached moieties. This would enhance the use of these MPc-MOF conjugates in applications such as heterogeneous catalysis (e.g. CoPc as oxidation catalyst) and drug delivery (e.g. ZnPc in photodynamic therapy). In this study, two types of MPcs will be employed: tetra-*tert*-butyl- ($^tBu_4$) MPcs (M = Zn^{2+} and Ni^{2+}) as well as tetracarboxy-substituted ($(COOH)_4$) MPcs (M = Zn^{2+}; Fe^{3+}; Co^{2+} and Ni^{2+}). MPc$^tBu_4$ has no functional group to covalently bind with the amine groups of the MOF, while MPc$(COOH)_4$ can possibly form an amide bond with the amine groups. Both types of MPcs were chosen for their small molecular diameter, in order to pass through the MOF's pore windows. Carboxylic acid functional groups (on MPc$(COOH)_4$ MPcs) were chosen, since they will not react with the amine groups during infiltration of the MOF's pores at room temperature, but only after infiltration with reaction conditions will be applied. This will allow maximum loading of MPc without blocking the pore windows. MPc$^tBu_4$ derivatives are much more soluble than MPc$(COOH)_4$ derivatives, an important factor to keep in mind throughout the study.

1.2 Aims

1) Improvement of the benchtop method for NH_2-MIL-101(Al), as well as the workup and activation procedure to fully evacuate the pores of the MOF. Characterisation of the final products will be done by Fourier Transform Infrared (FTIR) spectroscopy, Accelerated Surface Area and Porosity (ASAP) analyses, Thermal Gravimetric Analyses (TGA) and low angle Powder X-ray Diffraction (PXRD).

2) Synthesis of MPc$^tBu_4$'s (M = Zn^{2+} and Ni^{2+}) and MPc$(COOH)_4$'s (M = Zn^{2+}, Fe^{3+}, Co^{2+} and Ni^{2+}) by adapting the best current methods, followed by characterisation with Proton Nuclear Magnetic Resonance spectroscopy (^{1}H NMR), FTIR, TGA and Mass Spectroscopy (MS). The aggregation behaviour of the MPcs will be investigated by UV-Vis spectroscopy down to nano-concentrations.

3) Comparison of two different methods to encapsulate macrocyclic MPcs in the pores of NH_2-MIL-101(Al): a) templating (temp), where the particular MPc is already present in the reaction mixture during MOF synthesis and b) customised novel solution phase infiltration (sol), where a solution of the particular MPc is added to the already, fully evacuated MOF and allowed to infiltrate the pores. Success of these methods will be evaluated by FTIR, TGA, Diffuse-Reflectance UV-Vis Spectroscopy (DRS-UV-Vis), N_2 and H_2 ASAP analysis and PXRD.

The MPc loading will also be analysed with quantitative techniques like XPS, SEM-EDX and ICP-AES.

4) A trial test, to investigate the possible photo-oxidative oxidation of cis-cyclooctene with an MOF-encapsulated MPc will be performed.

5) Comparison of the electrochemical characteristics of the free MPcs (liquid state Cyclic Voltammetry, CV), with those of the MOF-encapsulated MPc (measured with solid state CV). For all solid state CVs, a standard technique will be adapted to fixate the MOF particles to the surface of the electrode so that the encapsulated MPcs may be detected even at low loading percentages. With CV, the influence of the MOF matrix on the flow of electrons, when the encapsulated MPcs are oxidised and reduced, may be observed.

1.3 References

[1] T. Lescouet, E. Kockrick, G. Bergeret, M. Pera-Titus, S. Aguado and D. Farrusseng, *J. Mater. Chem*. 2012, **22**, 10287-10293.

[2] S.J. Garibay, Z. Wang, K.K. Tanabe and S.M. Cohen, *Inorg. Chem.* 2009, **48**, 7341-7349.

[3] M. Latroche, S. Surblé, C. Serre, C. Mellot-Draznieks, P.L. Llewellyn, J. Lee, J. Chang, S.H. Jhung and G. Férey, *Angew. Chem.* 2006, **118**, 8407-8411.

[4] J. Kim, W.Y. Kim, W. Ahn, *Fuel* 2012, **102**, 574-579.

[5] Y. Huang, Z. Zheng, T. Liu, J. Lü, Z. Lin, H. Li, R. Cao, *Catal. Commun.* 2011, **14**, 27-31.

[6] P. Horcajada, C. Serre, G. Maurin, N.A. Ramsahye, F. Balas, M. Vallet-Regí, M. Sebban, F. Taulelle, and G. Férey, J. *Am. Chem. Soc.* 2008, **130**, 6774-6780.

[7] L. Li and E.W. Diau, *Chem. Soc. Rev.* 2013, **42**, 291-304.

[8] N. Padma, A. Joshi, A. Singh, S.K. Deshpande, D.K. Aswal, S.K. Gupta and J.V. Yakhmia, *Sensor. Actuator. B* 2009, **143**, 246-252.

[9] D. Wöhrle, D. Meissner, *Adv. Mater*. 1991, **3**, 129-138.

[10] E.A. Lukyanets, *J. Porphyrins Phthalocyanines* 1999, **3**, 424-432.

[11] H.I. Beltrán, R. Esquive, A. Sosa-Sánchez, J.L. Sosa-Sánchez, L.S. Zamudio-Rivera, *Inorg. Chem.* 2004, **43**, 3555-3557.

[12] J. Guo, H. Zhang, Z. Liu and X. Cheng, *J. Phys. Chem.* C 2012, **116**,15908-15917.

[13] H.W. Langmia, J. Rena, B. Northa, M. Mathea, D. Bessarabov, *Electrochimica Acta*, 2014, **128**, 368-392.

2 Literature Survey

2.1 Introduction

This chapter starts off with the description of fundamentals, background and analysis of the metal organic framework type, MIL-101 and related porous materials. The background will include synthetic routes and will move on to post-synthetic modification and catalytic applications. The fundamentals and background study of phthalocyanines and their relevance to this study will be discussed next. Lastly, characterisation techniques such as UV-visible spectroscopy, electrochemistry, thermal gravimetric analysis, Fourier transform infrared spectroscopy as well as surface area and porosity analysis etc. will be discussed.

2.2 Metal Organic Frameworks

2.2.1 General History and Outlook

Metal organic frameworks (MOF) are a class of porous materials which surfaced in the early 1990's. Scientists dabbled with these materials merely out of curiosity until about 1996 when it was realised how incredibly diverse and application-rich MOFs can be. The rate at which papers appeared about porous materials and particularly MOFs increased rapidly.[1] Today many applications have already been tested with an array of MOFs with each MOF bringing its own uniqueness to the field. One branch of MOFs is the MIL series (MIL = *Matériaux de l'Institut Lavoisier*) which originated from Férey and co-workers at the Institute Lavoisier in France. One of the most prominent MILs still actively being researched are the MIL-101 derivatives.[2] MIL-101(Cr) was first synthesised in 2005 by Férey *et al*.[3] and its amine functionalised analogue, NH_2-MIL-101(Al) only six years later.[4] Instead of using chromium, aluminium was used as the coordinating metal to further explore the applications and structural characteristics when a different tri-dentate metal is used. Recently, the demand for porous catalysts and catalyst support materials increased, due to a need for porous hybrid materials with large, readily available and structurally intact tunnels and cages. The micro- and mesoporosity of materials such as MOFs can be used in applications such as the sensing,[5] storage and separation of gasses[6] and

catalysis.[7] MOFs bring unique attributes to the field of heterogeneous catalysis, since their porous cavities/cages/tunnels are uniform in size, flexible and can act as nano-reactors. This may enable new types of reactions which otherwise may not be possible in a bulk reaction. The tuneability of the MOFs cages and pore sizes can enhance the reaction in two ways:[3]

1) The larger the cage size of the MOF, the more reagents can be stored inside each cage before the reaction commences.

2) The particular size of the pores and pore windows will only allow certain molecules to enter the cage or it will only select certain products/side-products to exit.

2.2.2 Amino Terephthalate NH_2-MIL-101

The structure of NH_2-MIL-101(Al) is built from supertetrahedral (ST) blocks forming two types of quasi-spherical, mesoporous cages **(Figure 2. 1, p 7)**. The smaller sphere has only pentagonal windows with a pore size of 12 Å while the larger sphere has both hexagonal (14.5 Å x 16 Å) and pentagonal windows.[4] These entrances are larger than the tunnels of NH_2-MIL-53(Al), which ranges from 7.85 Å to 13.04 Å.[8] NH_2-MIL-53(Al) is a MOF with the same chemical composition, but a different topology due to different reaction conditions.

When compared to similarly produced MOFs like MIL-53, it becomes apparent that reaction conditions play a very particular role in the formation of these materials. This is because MIL-101 and MIL-53 (amine functionalised or not) are made from the same reagents: a tridentate metal salt and benzenedicarboxylic acid (bdc). Initial studies done on NH_2-MIL-101(Fe) and NH_2-MIL-53(Fe) concluded that NH_2-MIL-101(Fe) can be regarded as the kinetically favoured product, formed in the starting nucleation phases, while NH_2-MIL-53(Fe) is the thermodynamically stable product, formed afterwards.[9] After the discovery of NH_2-MIL-101(Al), another in-depth study was performed to understand the *in-situ* formation of MIL-101 and MIL-53 during synthesis. Kapteijn *et al.*[10] found that using water or N,N-dimethylformamide (DMF) or a combination of the two, results in a third metastable precursor called NH_2-MOF-235. In this system, solvents were varied and reactants kept constant (NH_2-bdc and Al^{3+}). With the use of SAXS/WAXS analyses, characteristics such as kinetic data and crystal growth was extracted from the experiments. Three systems were deduced **(Figure 2. 1, p 7)**:

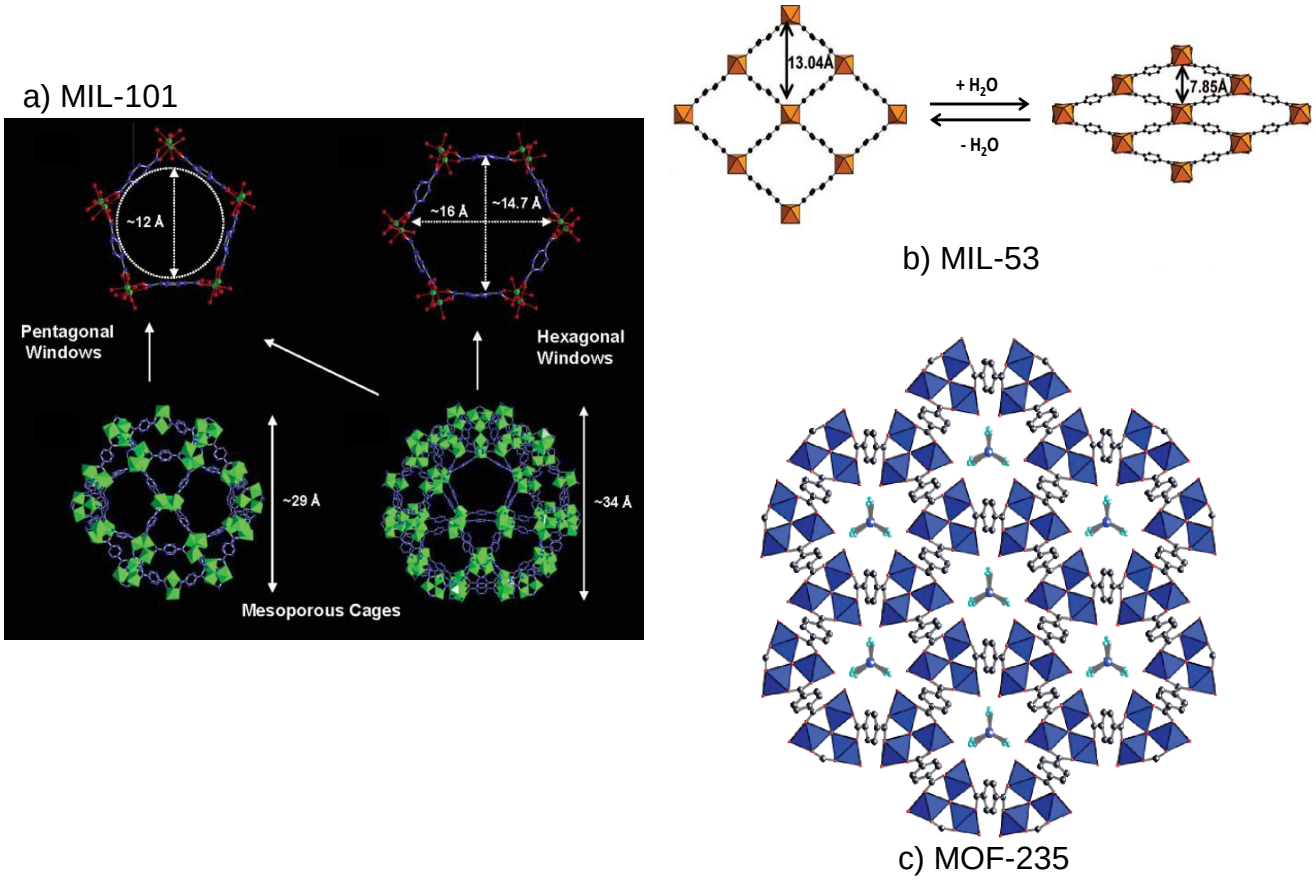

Figure 2. 1: Structural representation of a) MIL-101, b) MIL-53 and c) MOF-235 which can all be synthesised during similar conditions using a metal salt, terephthalic acid and DMF and/or water as solvent. Adapted with permission from a) G. Férey, C. Mellot-Draznieks, C. Serre, F. Millange, J. Dutour, S. Surble and I. Margiolaki, *Science* 2005, **309**, 2040-2042. Copyright 2016 The American Association for the Advancement of Science. b) P. Horcajada, C. Serre, G. Maurin, N. A. Ramsahye, F. Balas, M. Vallet-Regí, M. Sebban, F. Taulelle and G. Férey, J. Am. Chem. Soc. 2008, **130**, 6774-6790. Copyright 2016 American Chemical Society. c) A.C. Sudik , A.P. Côté and O.M. Yaghi, J. Am. Chem. Soc. 2005, **44**, 2998-3000. Copyright 2016 American Chemical Society.

1) In low reactant concentrations, with the use of only DMF, it was found that NH_2-MOF-235(Al) exists in the lower temperature range during synthesis, while at the higher temperature range NH_2-MIL-101(Al) formed. NH_2-MOF-235(Al) was regarded as the kinetically stable product which leaded up to NH_2-MIL-101(Al) as the thermodynamically stable product.

2) In higher concentrations, while using H_2O/DMF as the solvent system, it was found that NH_2-MOF-235(Al) was present as well. In this case, the presence of water played a vital role in that it hydrolysed NH_2-MOF-235(Al) to become NH_2-MIL-53(Al) at higher reaction temperatures.

3) In high reactant concentrations using H_2O as solvent the formation of only NH_2-MIL-53(Al) is seen at higher temperatures. Pure H_2O is unfavourable for NH_2-MOF-235(Al) formation.

The reason for observing NH_2-MOF-235(Al) in the early stages of the reaction can be attributed to fast nucleation which is aided by the fast dissolution of the NH_2-bdc building blocks. The fast nucleation and stabilisation of NH_2-MOF-235(Al) proved vital for the proper crystal growth of NH_2-MIL-101(Al) **(Scheme 2. 1, p 8)**.

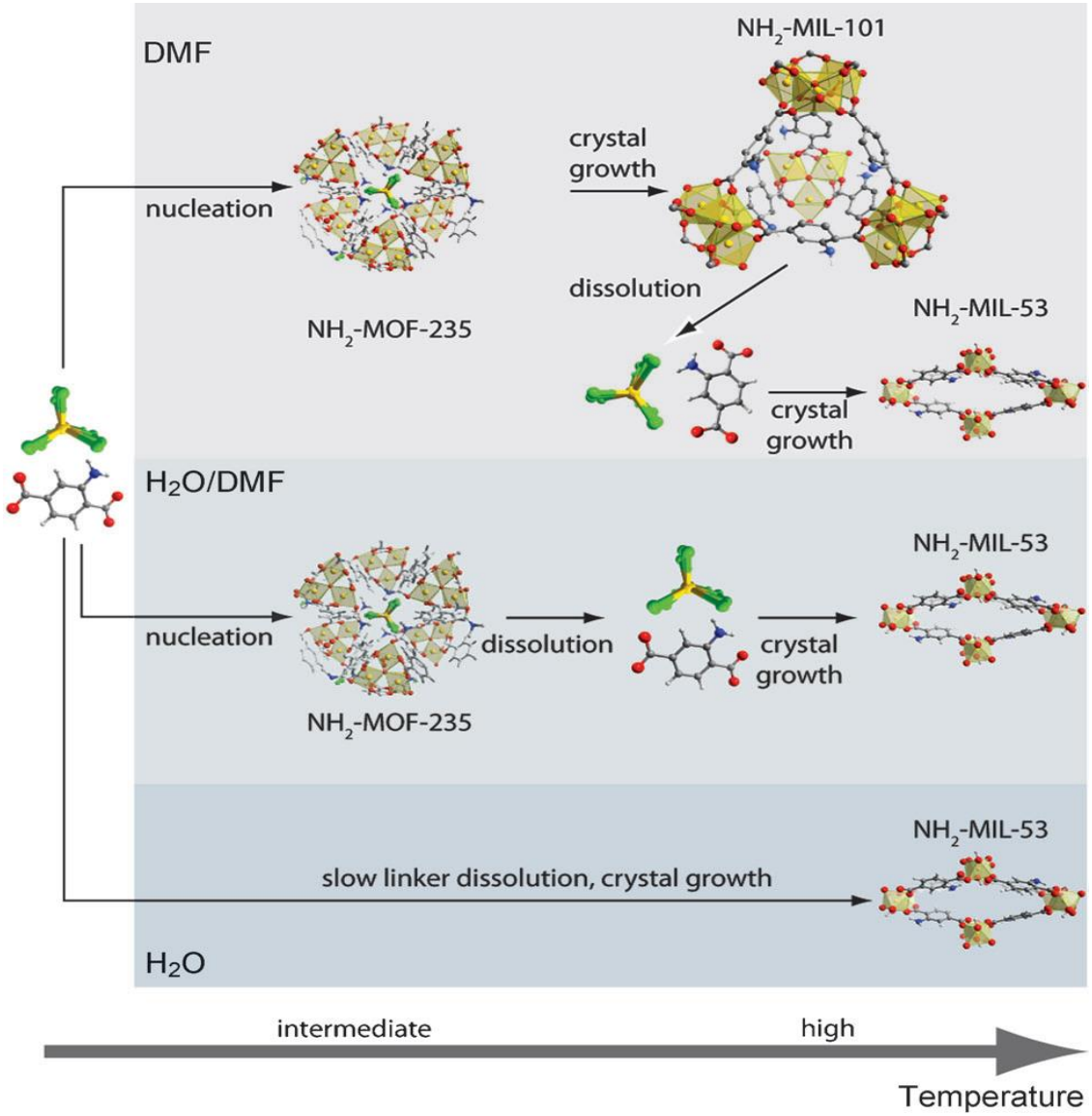

Scheme 2. 1: Representation of the different MOF formations when using certain solvents and reactant concentrations all starting with the same terephthalate linker and metal salt. Low reactant concentrations were used for a) DMF and high reactant concentrations for b) H_2O/DMF and c) H_2O. Atom description: C (grey), H (white), N (blue), O (red), Al (yellow), Cl (green). Reprinted with permission from E. Stavitski, M. Goesten, J. Juan-Alcañiz, A. Martinez-Joaristi, P. Serra-Crespo, A.V. Petukhov, J. Gascon and F. Kapteijn, *Angew. Chem. Int. Ed.* 2011, **50**, 9624-9628. Copyright 2016 John Wiley and Sons.

MIL-101 MOFs are usually synthesised during a hydrothermal or solvothermal approach.[3,4,12,15] During a typical solvothermal (any solvent combination except pure H_2O) or hydrothermal (H_2O as solvent) synthesis, the reactants are placed in an autoclave and allowed to react without stirring at pressures above one atmosphere, to allow proper nucleation and crystal growth of each specific MOF structure **(Figure 2. 2, p 9)**. Hydro-/solvothermal syntheses are standard methods of creating MOF structures with tested and reproducible results. Reactant concentration and volume are often big limitations on the mass production of MOFs. To be able to synthesise MIL-101 under benchtop conditions, similarly to those of zeolitic imidazole frameworks,[11] would be an improvement. Not long after the first solvothermal synthesis of NH_2-MIL-101(Al),[4] Hartmann and Fischer developed a simple

benchtop method for synthesising NH_2-MIL-101(Al).[12] They achieved a BET surface area of 3099 m^2g^{-1} and was considerably higher than what Serra-Crespo *et al.* reported (2100 m^2g^{-1}) for the solvothermal NH_2-MIL-101(Al) product. To achieve this high surface area the average reaction concentration was almost half of what Serra-Crespo *et al.* used and the reactant stoichiometry of $AlCl_3 \cdot 6H_2O$ to 2-aminoterephthalic acid was 2:1 and not 1:1. The reaction time was less than a third (21 hours) of the time Serra-Crespo *et al.* used (72 hours) and the reaction temperature was also 20°C lower: 110°C as opposed to 130°C for the solvothermal process.

To achieve full MOF activation and get rid of excess reactants and side-products, the as-synthesised product is cleaned during one or two steps. Serra-Crespo *et. al.* used acetone to wash the as-synthesised MOF and then boiled it in methanol for 16 hours after which it was stored at 100°C. Hartmann and Fischer used a thorough cleaning procedure by first washing the as-synthesised MOF with DMF and then ethanol. Soxhlet extraction with ethanol was done for 24 hours after which it was activated for another 24 hours at 90°C and stored in a desiccator. The reason for these rigorous evacuation steps is that the DMF is used to remove the left-over 2-aminoterephthalic acid inside the pores of the MOF. The lighter boiling solvents, methanol and ethanol are then used to replace the high boiling DMF, allowing for lower activation temperatures.

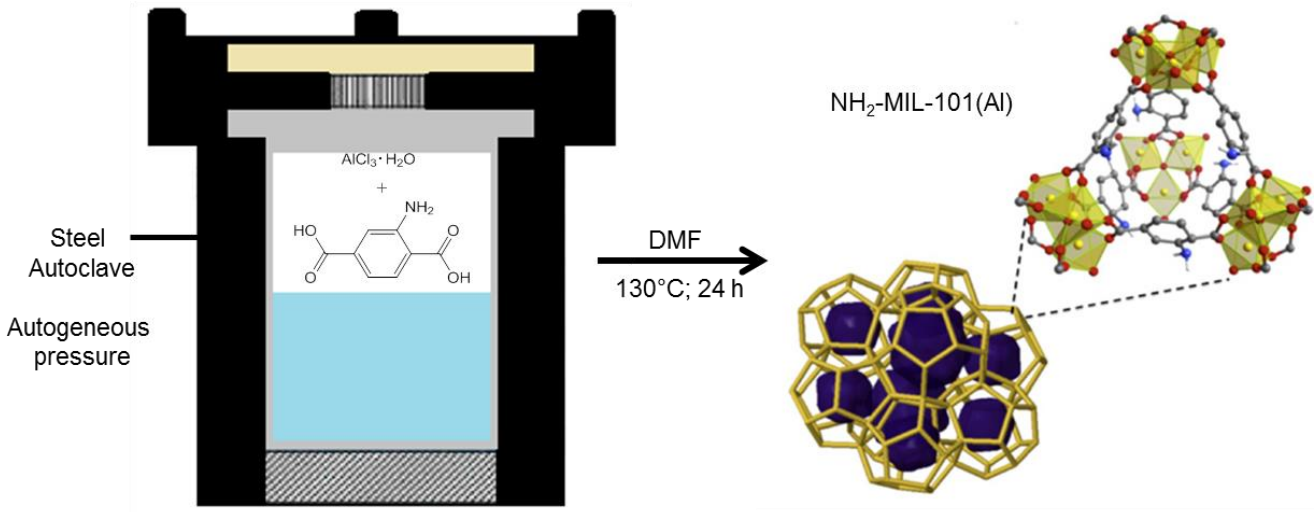

Figure 2. 2: The solvothermal synthesis of NH_2-MIL-101(Al) with the use of an autoclave. The precursors are allowed to form the product under static, autogeneous pressure. Adapted with permission from P. Serra-Crespo, E.V. Ramos-Fernandez, J. Gascon and F. Kapteijn, *Chem. Mater*. 2011, **23**, 2565-2572. Copyright 2016 American Chemical Society.

2.2.3 Characterisation of NH_2-MIL-101

2.2.3.1 Fourier Transform Infrared Spectroscopy (FTIR)

Fourier transform infrared spectroscopy is in most cases used to track certain vibrational frequencies coming from groups such as carbonyls, amines, hydroxides, amides and contained water. FTIR is used as one of the most efficient and cheap ways to quickly obtain fingerprints from compounds since sample preparation is minimal. In MOF chemistry, FTIR can be used as a tool to follow the different steps during evacuation of the MOF's internal channels or pores. In the case of NH_2-MIL-101, the carbonyl peak (~1600 cm^{-1}) of free amino-terephthalic acid is easily distinguished from the bound amino-terephthalic acid in the MOF structure (double peak: ~1570 cm^{-1} and ~1430 cm^{-1}). The carbonyl peaks of DMF are also easily detectable during purification. Their absence after DMF removal indicates clean cavities.[13] Other characteristics which can be extracted from FTIR results are possible interactions which may arise when functional groups such as amine groups are incorporated into the MOF structure. Hydrophilicity of a MOF can be influenced by functionalisation of its linkers. This behaviour can be followed by the –OH signal between 3000 cm^{-1} and 4000 cm^{-1}.[4]

In the case of NH_2-MIL-101(Al) the FTIR spectra can be viewed in terms of a high and a low wavenumber region. The high wavenumber region contains vibrational frequencies from metal-hydroxyl stretching frequencies (~3700 cm^{-1}) which are contained in the supertetrahedral spaces of the MOF. The classical amine symmetrical and asymmetrical stretching frequencies can be seen at ~3400 cm^{-1} and 3500 cm^{-1} respectively **(Figure 2. 3, Ax & Ay, p 11)**. Symmetrical stretching frequencies take up lower energy and in return, yields lower wavenumbers. In the low wavenumber region the fingerprint area of the specific MOF is found between 1800 cm^{-1} and 500 cm^{-1} due to the usual complexity of vibrational bands. From all the vibrational frequencies that appear in this region the most relevant frequencies are that of carbonyl stretching frequencies (C=O) based at ~1600 cm^{-1}. The amino groups have two important absorptions based at ~1620 cm^{-1} (N-H bending vibration) and at ~1350 cm^{-1} (C-N stretching frequency). The above frequencies are illustrated by **Figure 2. 3, A (p 11)**.[4,12] The FTIR spectrum of NH_2-MIL-101(Fe), synthesised by Hartmann and Fischer compare well with that of NH_2-MIL-101(Al) **(Figure 2. 3, p 11)**.

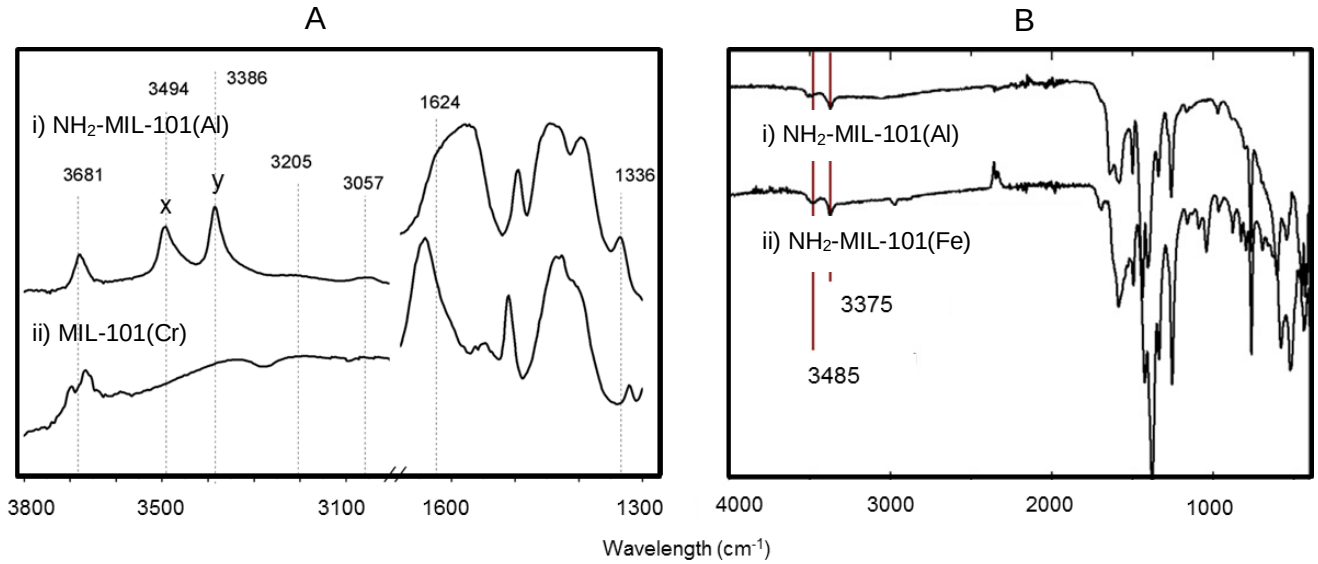

Figure 2. 3: FTIR spectrum of Ai) NH_2-MIL-101(Al) where the amine symmetrical and asymmetrical stretching frequencies can be seen at ~3400 cm^{-1} and 3500 cm^{-1} which are not present with Aii) MIL-101(Cr). To the right the FTIR spectrum of Bi) NH_2-MIL-101(Al) is compared to that of B ii) NH_2-MIL-101(Fe). Adapted with permission from a) P. Serra-Crespo, E.V. Ramos-Fernandez, J. Gascon and F. Kapteijn, *Chem. Mater*. 2011, **23**, 2565-2572. Copyright 2016 American Chemical Society. b) M. Hartmann and M. Fischer. *Micropor. Mesopor. Mat.* 2012, **164**, 38-43. Copyright 2016 Elsevier.

2.2.3.2 Thermal Gravimetric Analysis (TGA)

Thermal gravimetric analysis is used to analyse the structural integrity and thermal stability of MOFs. TGA results can be used to quantify certain content such as the amount of adsorbed water inside the cavities of the MOF as well as the amount of metal oxide which is usually left. In the as-synthesised MOF, excess reactants in the pores can also be quantified by TGA after identification by FTIR.

TGA results of NH_2-MIL-101(Al) done by Serra-Crespo *et al.*[4] showed remarkable structural integrity **(Figure 2. 4, a, p 12)**. A 5 wt% was lost due to adsorbed water, followed by the release of DMF from 127°C. The MOF only started to decompose above 377°C, comparing well with MIL-101(Cr) (decomposed at ~400°C). This decomposition temperature is higher than that of other NH_2-MIL-101 MOFs containing metals such as vanadium[14] and iron[12] (decomposed at ~250°C) **(Figure 2. 4, b, p 12)**.

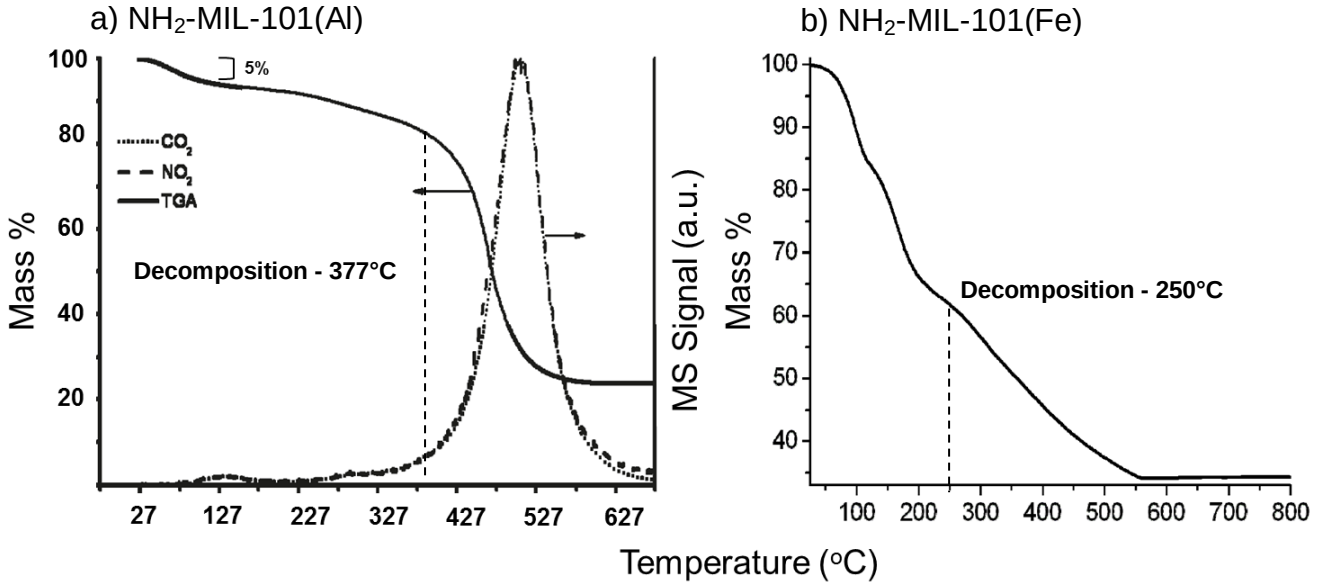

Figure 2. 4: TGA curves of a) NH_2-MIL-101(Al) (accompanied by MS analyses of CO_2 and NO_2) and b) NH_2-MIL-101(Fe). Adapted with permission from a) P. Serra-Crespo, E.V. Ramos-Fernandez, J. Gascon and F. Kapteijn, *Chem. Mater*. 2011, **23**, 2565-2572. Copyright 2016 American Chemical Society. b) S. Bauer, C. Serre, T. Devic, P. Horcajada, J. Marrot, G. Férey and N. Stock, *Inorg. Chem.* 2008, **47**, 7568-7576. Copyright 2016 American Chemical Society.

2.2.3.3 Surface Area and Porosity Analysis

In the race for the best microporous storage material, MOF structures with large pore sizes, very high surface areas and respectable pore volumes are desirable. These characteristics of a MOF can be determined from very low pressures up to 1 atm during surface area and porosity analyses. The nitrogen, low pressure analysis of NH_2-MIL-101(Al) at 77 K shows a typical type I isotherm **(Figure 2. 5, b, p 13)**, with a very steep uptake of gas in a three-step adsorption process at $P/P_o < 0.3$ as shown in **Figure 2. 5, c (p 13)**. This is due to the three different sized cavities. The supertetrahedral spaces are filled up first at $P/P_o < 0.5$ where after the medium cavities are filled giving rise to the first step on the isotherm at $\sim P/P_o = 0.15$. Lastly, the larger cavities are filled which leads to the second and third step. Isorecticular MOFs such as MIL-53 will not show this trend since all their cavities or channels are of similar size throughout the structure. Serra-Crespo *et al.* found the Brunauer-Emmett-Teller (BET) surface area of NH_2-MIL-101(Al) to be 2100 m^2g^{-1}, much lower than that of MIL-101(Cr) (4100 m^2g^{-1}). Hartmann and Fischer achieved a BET surface area for NH_2-MIL-101(Al) of 3099 m^2g^{-1} by using a novel benchtop synthesis method, completely different from the conventional solvothermal method used by Serra-Crespo *et al.*[4]

Using normal solvothermal synthesis for NH_2-MIL-101(Fe), a BET surface area of 3438 m^2g^{-1} was obtained. BET surface area is equated from the theory of multi-layered gas molecules adsorbed onto the surface of the cavities and can be related to the pore volumes of the MOF. When looking at the different ranges of BET surface areas obtained from MIL-101(Cr), NH_2-MIL-101(Fe) and

NH_2-MIL-101(Al), it can be seen that the pore volume of the specific MOF decreases as the BET surface area decreases, as shown in **Table 2. 1 (p 14)**.

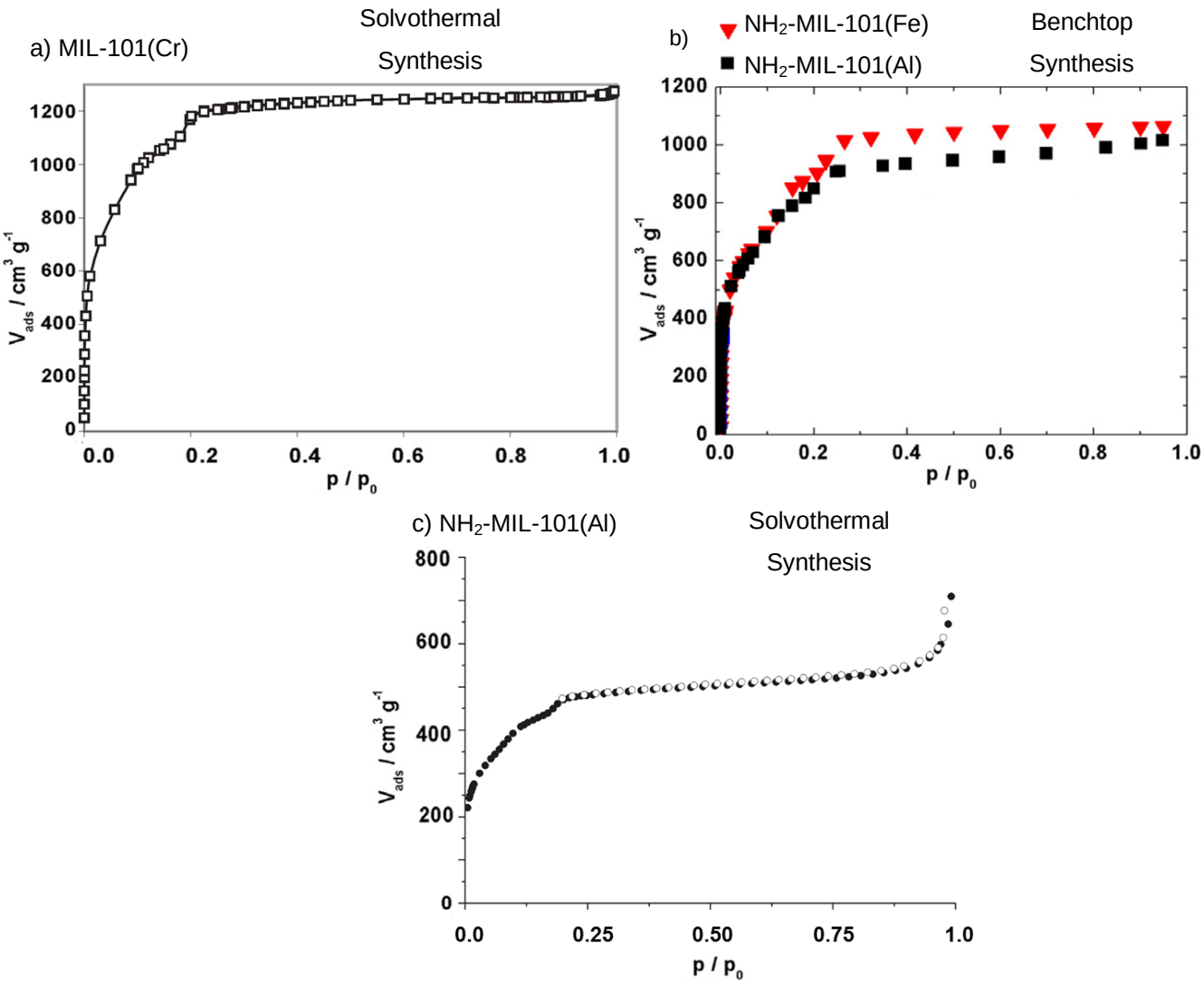

Figure 2. 5: Surface area uptake of nitrogen at 77 K between a) MIL-101(Cr) synthesised solvothermally, b) NH_2-MIL-101(Fe) **(red triangles)** synthesised solvothermally as well as NH_2-MIL-101(Al) **(black squares)** and c) NH_2-MIL-101(Al) synthesised solvothermally. Adapted with permission from a) G. Férey, C. Mellot-Draznieks, C. Serre, F. Millange, J. Dutour, S. Surble and I. Margiolaki, *Science* 2005, **309**, 2040-2042. Copyright 2016 The American Association for the Advancement of Science. b) M. Hartmann and M. Fischer. *Micropor. Mesopor. Mat.* 2012, **164**, 38-43. Copyright 2016 Elsevier. c) P. Serra-Crespo, E.V. Ramos-Fernandez, J. Gascon and F. Kapteijn, *Chem. Mater*. 2011, **23**, 2565-2572. Copyright 2016 American Chemical Society.

Table 2. 1: Summary of the surface area characteristics of the MIL-101 framework.

Metal organic framework	Molecular composition	BET surface area (m^2g^{-1})	Pore volume (cm^3g^{-1})	Reference
MIL-101(Cr)	$Cr_3OF(H_2O)_2(bdc)_3 \cdot nH_2O$	4100	1.90	**3**
NH_2-MIL-101(Cr)	$Cr_3OF(H_2O)_2(NH_2\text{-}bdc)_3 \cdot nH_2O$	2070	2.26	**15**
MIL-101(Fe)	$Fe_3OCl(H_2O)_2(NH_2\text{-}bdc)_3$	3739	1.75	**12**
NH_2-MIL-101(Fe)	$Fe_3OCl(H_2O)_2(bdc)_3$	3438	1.64	**12**
NH_2-MIL-101(Al) (solvothermal synthesis)	$Al_3O(DMF)(NH_2\text{-}bdc)_3 \cdot nH_2O$	2100	0.77	**4**
NH_2-MIL-101(Al) (benchtop synthesis)	$Al_3OCl(H_2O)_2(NH_2\text{-}bdc)_3$	3099	1.53	**12**

The structural integrity of the MOF's framework can be determined by surface area analyses with multiple intervals. NH_2-MIL-101(Al) was tested for its decomposition in air by exposing the material for 96 hours and performing four runs in between. The MOF showed very good stability as shown in **Figure 2. 6 (p 14)**.

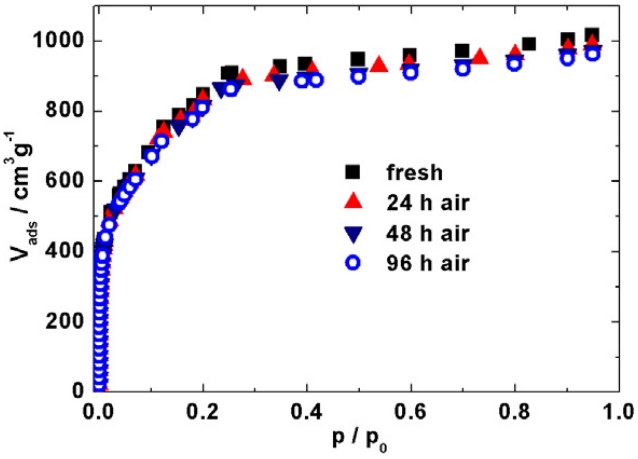

Figure 2. 6: Structural integrity analysis of NH_2-MIL-101(Al) through four consequent N_2 isotherms. Little degradation is observed throughout 96 hours of exposure to air. Reprinted with permission from M. Hartmann and M. Fischer. *Micropor. Mesopor. Mat.* 2012, **164**, 38-43. Copyright 2016 Elsevier.

2.2.3.4 Powder X-ray Diffraction (PXRD) and Small Angle X-ray Scattering (SAXS)

Since most MOFs are powders, PXRD is generally used characterise them. For NH_2-MIL-101, almost all of its PXRD patterns lie in the low angle region $2\theta < 10°$ **(Figure 2. 7, p 15)** and most PXRD instruments can only give reliable PXRD patterns from $2\theta > 5°$ without special attachments. This

excludes part of the fingerprint area of NH_2-MIL-101. SAXS is the detection of X-rays reflected in the smallest possible angles $0° < 2\theta < 5°$ and is used to obtain structural info on the meso- to nano-length range. SAXS can be measured separately, but is mostly part of the bulk PXRD scan of a synchrotron instrument, to give a complete diffraction pattern of the sample. In this study, low-angle PXRD analysis will only be used for the verification of the MOF structures.

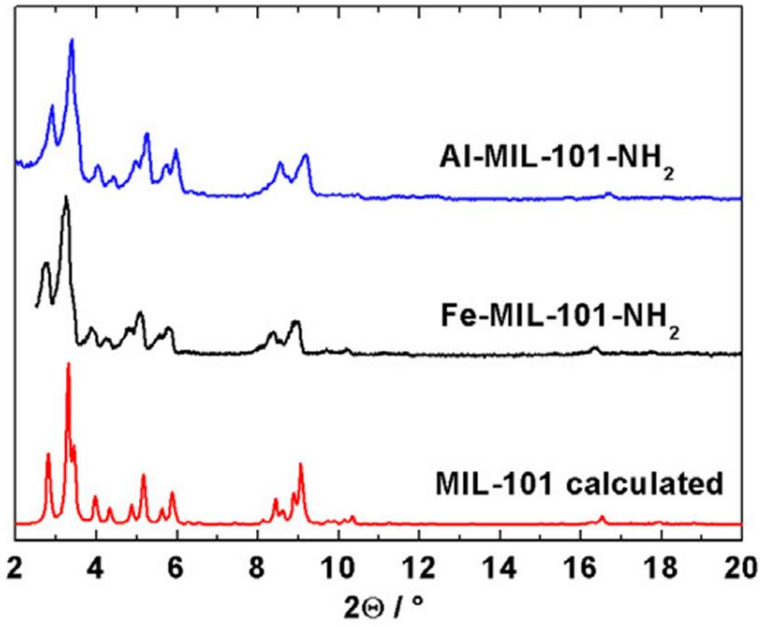

Figure 2. 7: PXRD analysis of NH_2-MIL-101(Al) (**blue line**), NH_2-MIL-101(Fe) (**black line**) and compared to the calculated pattern of MIL-101(Cr) (**red line**).[12] Reprinted with permission from M. Hartmann and M. Fischer. *Micropor. Mesopor. Mat.* 2012, **164**, 38-43. Copyright 2016 Elsevier.

2.3 Phthalocyanines

2.3.1 Introduction

Phthalocyanines (Pcs) are macrocyclic compounds with an 18-π electron system closely related to the natural occurring porphyrin complexes which are widely used in catalysis and sensitised solar cells.[16] Structurally, Pcs are between tetrabenzoporphyrins and tetraazoporphyrins as shown in **Figure 2. 8 (p 16)**. This configuration gives rise to rich-coloured (blue or green) compounds making them one of the main products used in dyeing. The structure of Pcs allows for an abundance of functionalities and applications of which some are catalysts[17], sensors[18], anti-viral agents[19], non-linear optics[20], liquid crystal technology[21], photodynamic therapy[22] and photovoltaic solar cells.[23]

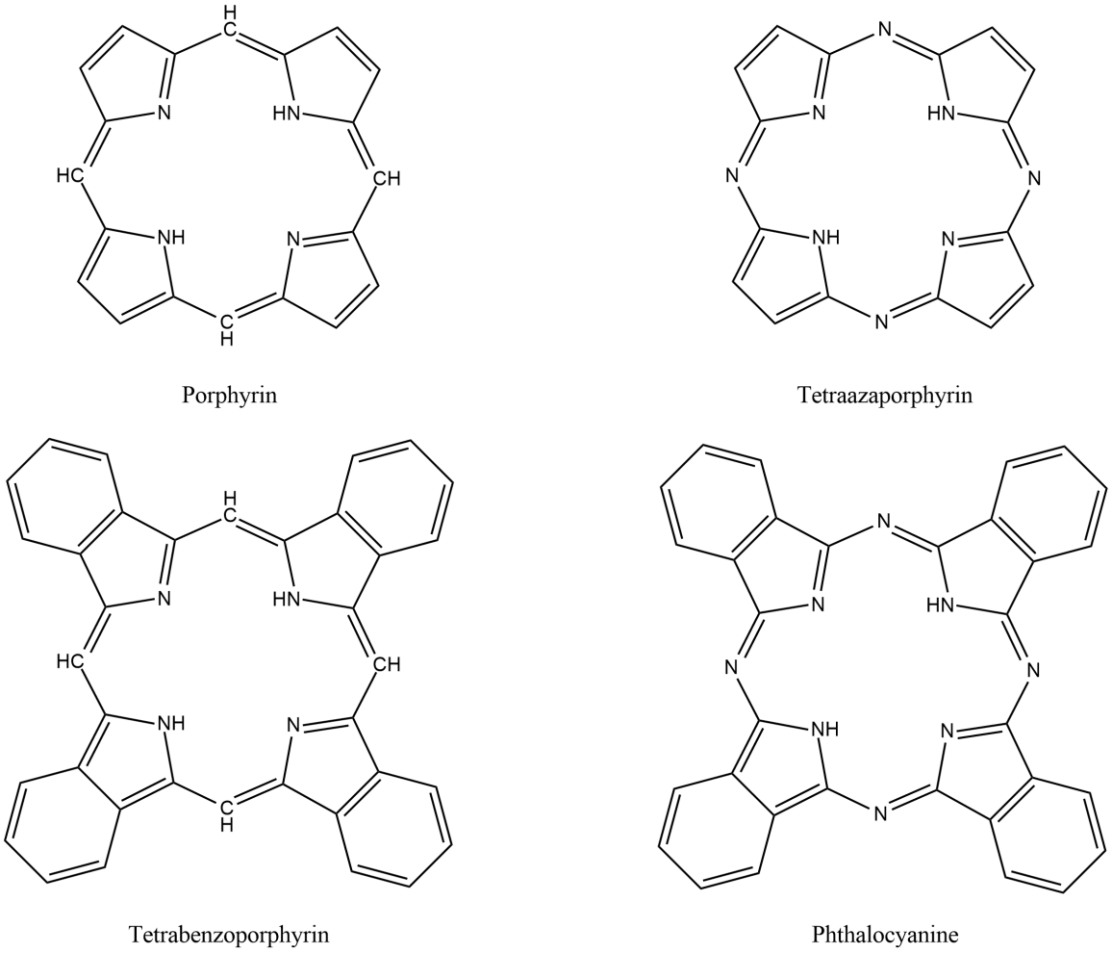

Figure 2. 8: Different members of the porphyrin family.

2.3.2 Synthesis of Phthalocyanines

Phthalocyanines can be synthesised by the cyclotetramerization of reactants such as phthalic acid or anhydride derivatives, phthaloamides, phthaloimides, phthalonitriles, *ortho*-disubstituted benzene derivatives as well as diiminoisoindolines. Phthalonitrile derivatives are the most common and preferred precursors **(Figure 2. 9 and 2. 10, p 17)**, because they can be functionalised with ease on both positions 3 and 4 of the benzene ring, before cyclotetramerization to the corresponding phthalocyanine. Post-synthetic functionalisation of phthalocyanines is troublesome due to their lower solubility as well as aggregated species which can prevent full functionalisation.

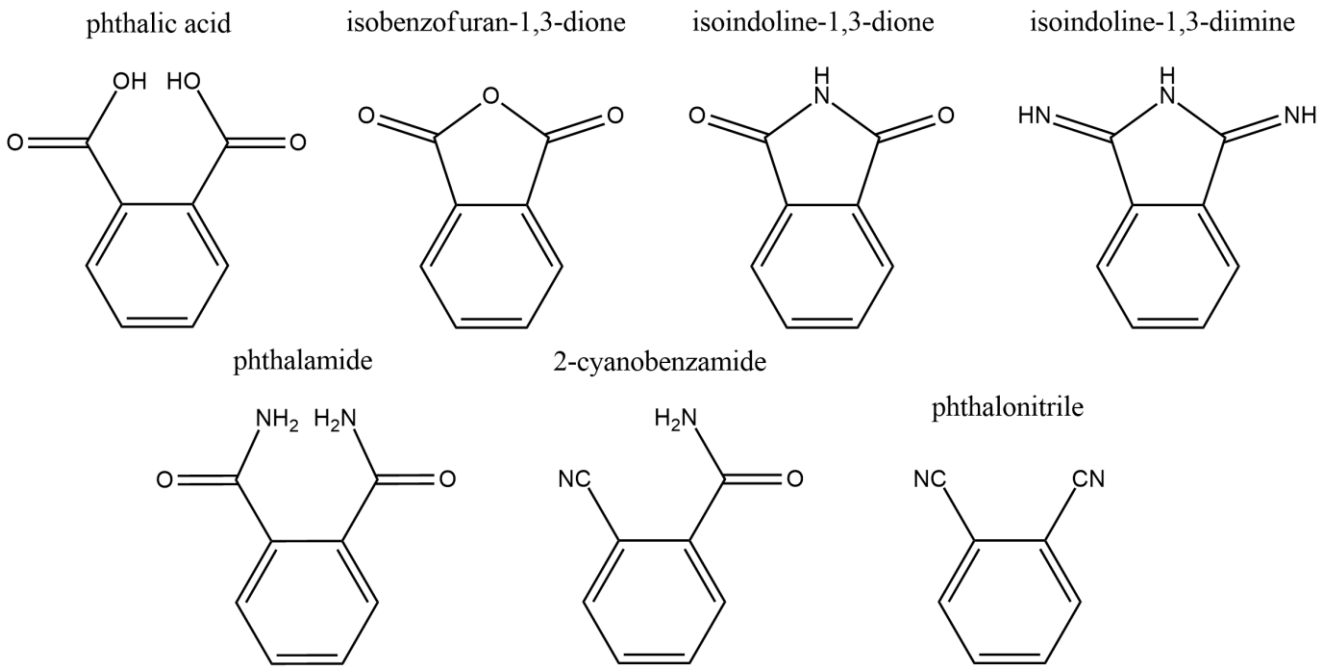

Figure 2. 9: The most important reactants for the formation of phthalocyanines.

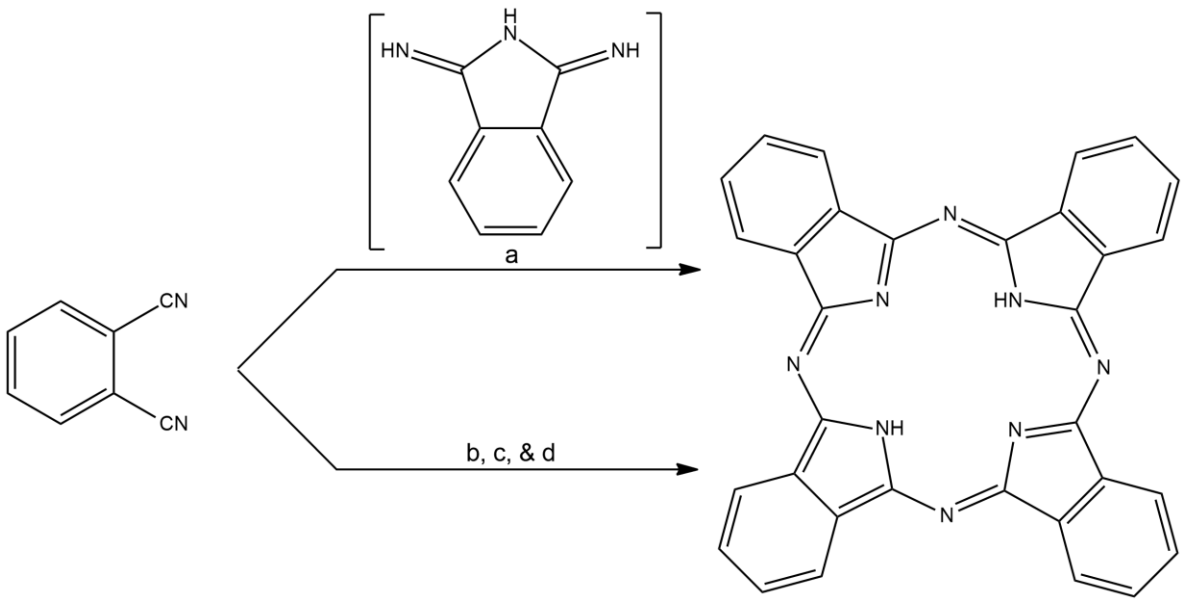

Figure 2. 10: Different synthetic pathways towards phthalocyanines:

a) By reacting a phthalonitrile with ammonia, it first forms a diiminoisoindoline which then condenses under mild conditions to form the 2HPc.

b) Hydroquinone can be used as a reducing agent to allow full formation of the 2HPc and excludes the need for other solvents and metal complexes.

c) 1,8-diazabicyclo[4.3.0]non-5-ene (DBN) or 1,8-diazabicyclo[5.4.0]undec-7-ene (DBU) are amidine, non-nucleophilic bases which can be used to produce 2HPc with or without a solvent such as pentanol.

d) By reacting a phthalonitrile with lithium under refluxing conditions using pentanol as solvent. The formed 2LiPc can then be easily demetallated with a dilute acid.

2.3.3 Metallophthalocyanines

Phthalocyanines (MPcs) prefer to be synthesised in the presence of metal salts (usually in the form of chlorides, sulfates or acetates). When a metal salt is used, the metal is inserted in the centre of the Pc structure and replaces two hydrogen atoms connected to the indoline groups **(Figure 2. 11, p 18)**. Covalent metal-nitrogen bonds are formed in order to obtain the MPc complex.

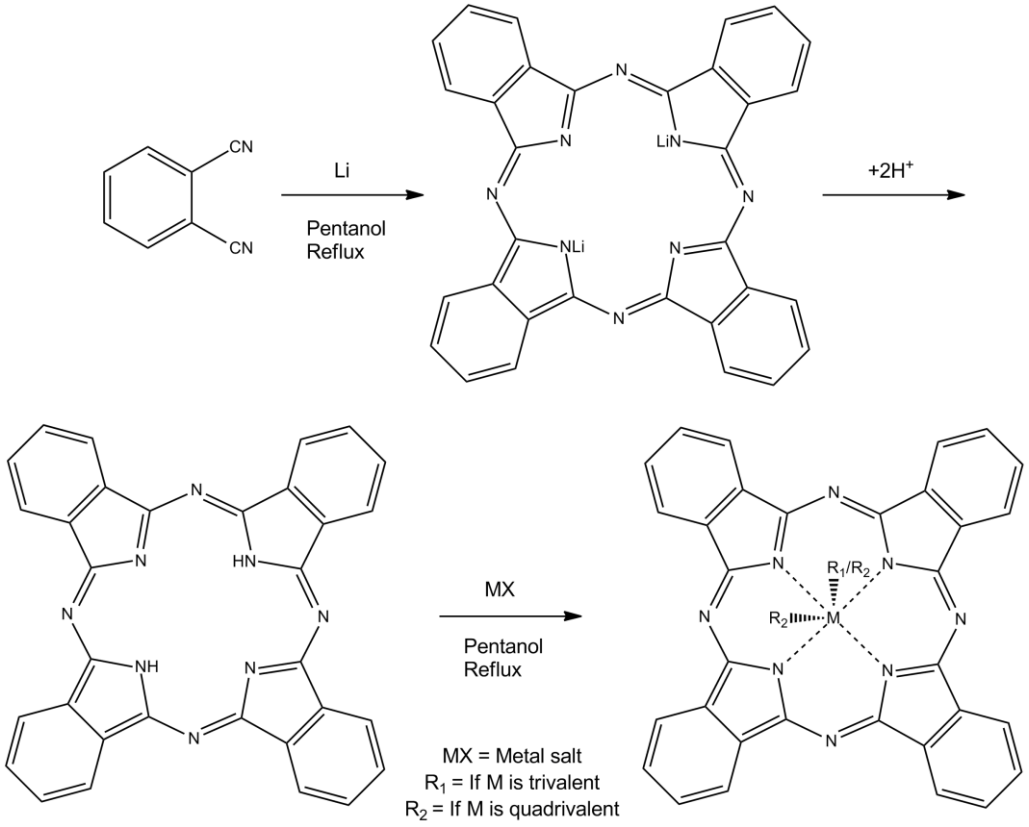

Figure 2. 11: The general cyclotetramerisation of phthalonitrile and lithium, followed by the Pc's demetallation with a weak acid and another metallation of choice.

2.3.4 Carboxylic Acid Substituted Metallophthalocyanines

Tetracarboxy-substituted MPcs (substituted on the periphery) are usually synthesised in two steps: simultaneous cyclotetramerisation and metallation to give a tetra-amidemetallophthalocyanine. The metal precursor can act as a templating point for the Pc ring. Afterwards the amide groups are hydrolysed with an aqueous base or acid to give the desired carboxylic acids.

Trimellitic anhydride/acid, in the presence of urea and the metal precursor (usually a chloride or acetate) is fused together in a high temperature reaction (~185°C). Without a solvent, the urea reacts in a melt (boiling point = 133°C) to allow the reaction to proceed.

Sakamoto and Ohno[24] reported some of the first syntheses of octacarboxyphthalocyanine complexes in 1997. Cyclotetramerisation of pyromellitic dianhydride was used in the presence of

1,8-diazabicycloundec-7-ene (DBU) as catalyst and cobalt(II)chloride. The reagents were fused together at 250°C to give a yield of 30% . The duration of the reaction was not given.

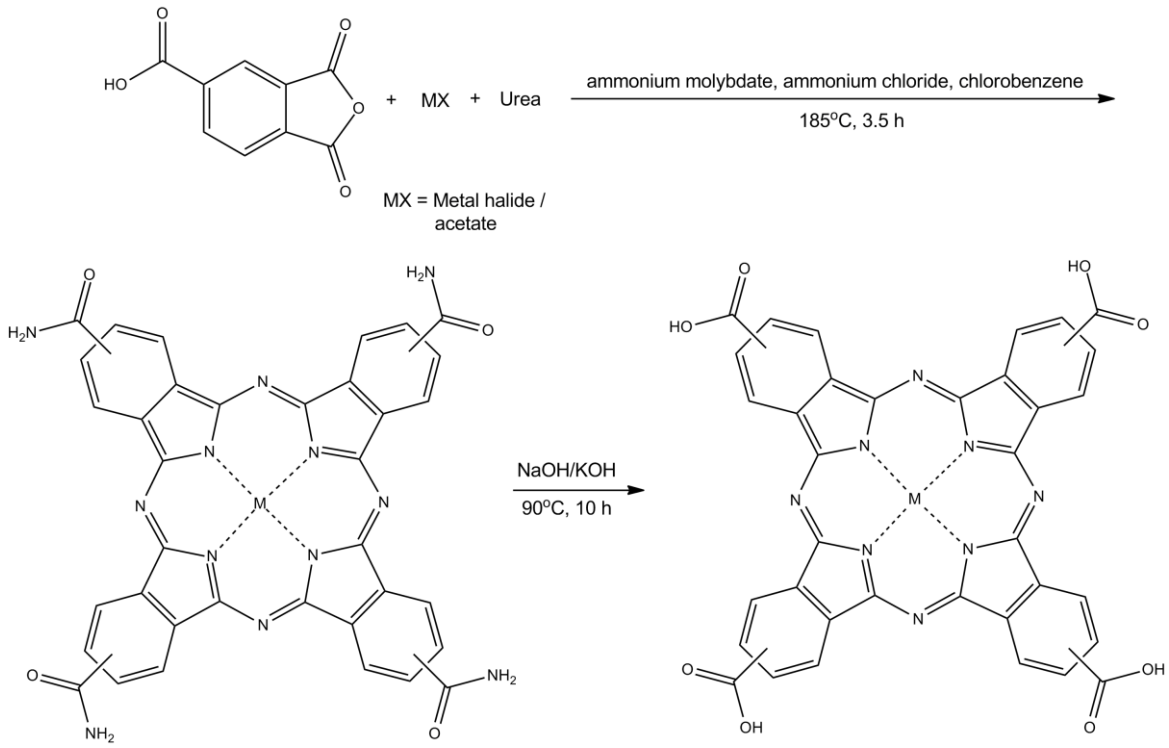

Figure 2. 12: General synthesis of tetracarboxymetallophthalocyanine.

In 2005 Zhang and co-workers[25] introduced tetracarboxyphthalocyanines with the metals cobalt, copper, iron(II) and zinc to investigate the aerobic catalytic activities of the these MPcs on *p*-nitrotoluene to synthesise *p*-nitrobenzoic acid. Instead of using DBU as the catalyst for the cyclotetramerisation of the Pc ring, ammonium molybdic acid was used together with chlorobenzene and ammonium chloride. The reaction at 185°C and running for 3.5 hours gave tetra-analidometallophthalocyanine. Base hydrolysis then gave the final tetracarboxylic acid phthalocyanine **(Figure 2. 12, p 19)**.

Milder conditions employed for a slightly longer time was used for the synthesis of the octacarboxylic acid phthalocyanines. The reported yields varied from 3% (Zn) to 35% (Co).[24] In 2015 Szuneritz and co-workers[26] introduced microwave-aided synthesis of the same tetracarboxylic acid cobalt phthalocyanine for the electrocatalytic detection of peroxynitrite and hydrogen peroxide. The reagents used were similar to those of the former reported procedure, but without chlorobenzene. After grinding the reagents to a pulp, it was transferred to a ceramic crucible and radiated for 15 minutes at 350 W to give a yield of 65%.

2.3.5 Characterisation of Phthalocyanines

2.3.5.1 UV-Vis Spectroscopy

The unique colour-intensive characteristic of Pcs, make for easy and reliable analyses through UV-Vis absorption studies in the liquid-phase. Pcs generally show a highly detectable adsorption Soret or B band in the ultraviolet region (350 nm), as well as a Q-band in the near-infrared region (650-700 nm). The B band is usually less intense than the Q-band. Both the B-band and Q-band results from π-π* transitions. Unmetallated Pcs are usually in the square-planar form (D_{2h}-symmetry) and give a recognisable split in the Q-band.[27,32] If a metal is inserted into the cavity of the Pc and the new MPc stays planar, the symmetry will increase to D_{4h}.[28] The Q-band of the MPc will be slightly blue-shifted since the coordinated metal will decrease electron density around the π-π bond ring structure **(Figure 2. 13, p 20)**. The shift in the Q band is dependent on more than just the metal. Almost any change in the Pc structure e.g. axial ligation, substitution on the periphery or non-periphery, solvent and aggregation may affect Q band behaviour.[29] Splitting of the Q band is also possible which can be due to interaction between axial ligands and the Pc.[30] When the symmetry of the Pc is changed, splitting of the Q band is also possible.[31] The use of different solvents also influences the position of the Q band **(Figure 2. 14, p 21)**.[32]

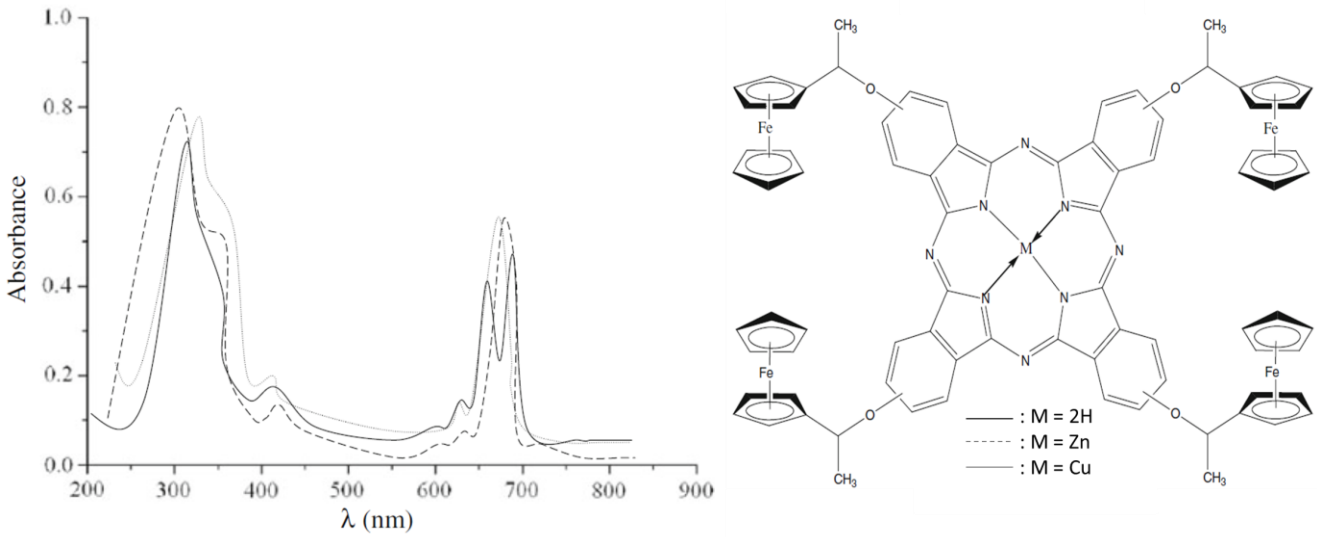

Figure 2. 13: UV Vis Spectra **(left)** of 2(3),9(10),16(17),23(24)-tetra-4-(α-methylferrocenyl-mehoxy)phthalocyanine derivatives **(right)** containing no metal **(black or solid line)**, zinc **(dashed line)** or copper **(grey line)** in the central cavity.[27] Adapted with permission from A. Bilgin¸ Ç. Yağcı, A, Mendi and U. Yıldız, *J. Incl. Phenom. Macrocycl. Chem.* 2010, **67**, 377-383. Copyright 2016 Springer.

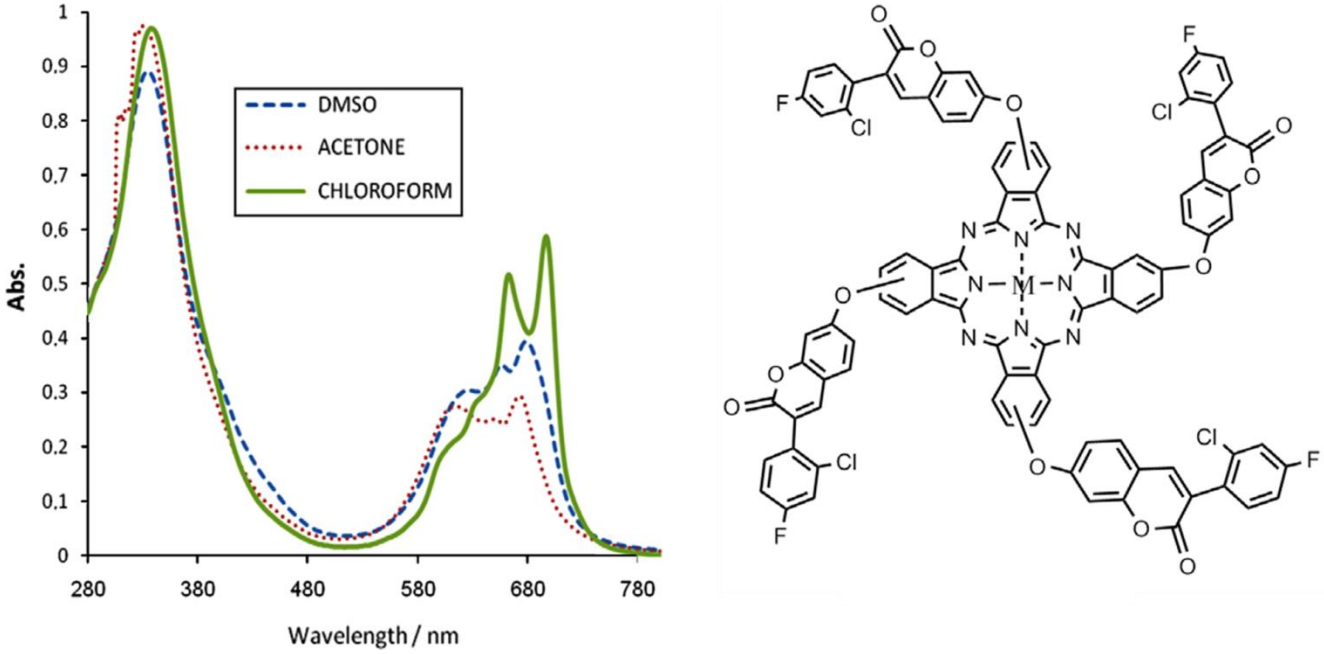

Figure 2. 14: UV Vis spectra (**left**) of 2(3),9(10),16(17),23(24)-tetra-α-[7-oxo-3-(2-chloro-4-fluorophenyl)coumarin metal-free phthalocyanine in different solvents.[32] Adapted with permission from A. Alemdar, A.R. Özkaya and M. Bulut, Polyhedron 2009, **28**, 3788-3796. Copyright 2016 Elsevier.

2.4 Post-synthetic Modification of Metal Organic Frameworks

Post-synthetic modification (PSM) of MOFs is one of the reasons why they have made such a considerable contribution towards material sciences. PSM is a powerful method to add novel functionalities after synthesis due to limitations usually experienced during hydro- or solvothermal syntheses. The harsh conditions (mostly highly acidic or basic)[8] present during these syntheses may be unsuitable for certain functionalised ligands. On the other hand, when functionalised ligands are synthesised before MOF formation occurs, it may also alter the conditions of the reaction, causing the MOF not to have the intended characteristics and obtain the correct structure. Although MOFs have desirable properties such as high porosity, stability, flexibility, crystalline pores and ordered frameworks, they still have unavoidable negative traits. MOFs are, most of the time, chemically stable in certain pH ranges with high porosity often leading to less stability.[33] The combination of MOFs with functional materials allows for the mitigation of those shortcomings as well as the gain of new characteristics. These characteristics are then combined in one, whole composite material, which would otherwise, be impossible with the MOF and functional material separately.[34] PSM allows for the functionalisation of the MOF structure, whether it is on coordinative metal sites, bridging metal sites or the organic linker. This usually occurs in a heterogeneous fashion due to the MOFs structural integrity and insolubility towards most organic solvents. This insolubility of MOFs can also be a stumbling block on its own and/or be a way to perform the reaction workup quicker and more effective. With PSM, it is possible to attach a wide variety of functional groups to the MOF's structure on the internal surface and/or the external surface area, depending on the method of insertion, the

structural size and the pore sizes of the MOF including its internal cavities. By using very specific conditions during reactions, the porosity, crystallinity and structural integrity of the MOF can be kept intact.[35]

There are mainly four ways to introduce functionalised moieties to MOF materials:

a) gas phase infiltration,

b) solution phase infiltration,

c) template synthesis and

d) solid grinding formation.

2.4.1 Gas Phase Infiltration

Gas phase infiltration is often used to incorporate volatile guest molecules into MOFs. Infiltration occurs by enclosing the evacuated MOF and the inclusion molecules together inside a schlenk tube. The inclusion molecules are then vaporised and introduced into the pores of the MOF under static vacuum and elevated temperature conditions (depending on the vapour pressure of the inclusion molecules). Fisher and co-workers designed this solvent-free method and was able to successfully incorporate functional molecules such as palladium, gold and copper nanoparticles into MOFs like MOF-5 and MOF-177.[36,37,38,39] One study that was performed, focussed on the selective intrusion of the palladium complex, $[(\eta^5\text{-}C_5H_5)Pd(\eta^3\text{-}C_3H_5)]$ into MIL-101(Cr).[40] The palladium complex was hydrogenised to form Pd@MIL-101(Cr). It was tested for catalytic activity on the reduction of aryl alkyl ketones to their respective alcohols and/or aryl alkanes. It was found that Pd@MIL-101(Cr) were size-selective during catalysis and that the MOF was stable, but decomposed only after very long periods of being active. Atomic layer deposition is another method to insert metal complexes into MOFs by adsorbing monolayers of two different precursors on the MOF's surface.[41] With this method, monolayer stacking of the precursors can be individually controlled. With normal chemical vapour deposition controlled stacking is impossible to achieve. Chemical vapour deposition is ideally suited for loading only one precursor into the MOF's pores.

2.4.2 Solution Phase Infiltration

Solution phase infiltration or the *ship-in-a-bottle* method incorporates the inclusion of a molecule from its solution, illustrated in **Figure 2. 15 (p 24)**. Organometallic molecules included in the MOF structure can later be reduced to metal nanoparticles. This method can also be used to insert any functional molecule into a MOF's framework that is smaller than the pore windows of the MOF. This method works by first evacuating the MOF's internal cavities and then submerging it into a solution of the inclusion molecule. These molecules are then forced into the channels of the MOF by capillary

action. In the case of metal nanoparticles, the intruded species are hydrolysed to obtain the active metal nanoparticles. The downside of this method is that it often yields fewer molecules per unit cell of MOF as per other methods such as gas phase infiltration. To overcome this issue the amount of solution can be tweaked to match the total pore volume of the MOF in a method called incipient wetness impregnation. In this way the inclusion molecules cannot extrude out of the cavities of the MOF which decreases loading after time. The concentration of the inclusion molecules also influences the loading into the MOF's cavities. With solution phase and gas phase infiltration a typical problem is the deposition of the intruded materials onto the external surface area of the MOF. When a MOF has large cavities, it is preferred to contain the inclusion molecules inside since the cavities can control aggregation by means of compartmentalisation. Zhu *et al.* designed a method to overcome external build-up by a dual-solvent intrusion method. A hydrophilic solution such as water was used to intrude an alloy of AlNi nanoparticles into MIL-101. To minimise the nanoparticles from settling on the external surface area and to help facilitate intrusion greatly, a hydrophobic solution such as hexane was used to suspend the MOF. The nanoparticles will then prefer to intrude into the MOF since the MOF is also hydrophilic.

2.4.3 Template Synthesis

During template synthesis or otherwise known as the *bottle-around-the-ship* approach, pre-synthesised, functional molecules are added to the reaction solution containing the building materials for MOF formation, illustrated in **Figure 2. 15 (p 24)**. This method is preferred in cases where the inclusion molecules are larger than the window size of the MOF's pores. In the case of MIL-101 the pore windows range in size between 12 Å and 16 Å, but the internal cavities are considerably larger between 29 Å and 34 Å. Kapteijn and co-workers have applied this method to MIL-101(Cr) with the aim to directly encapsulate Keggin polyoxometalates (POMs).[42] By introducing phosphotungstic acid (PTA) into the solution when MIL-101(Cr) is synthesised, it was found that this specific POM was successfully encapsulated. Since the POM is larger than the pentagonal windows of the MIL-101(Cr), no leaching of the POM was found which is a beneficial quality for heterogeneous catalysis. In 2011 Kapteijn and co-workers studied the encapsulation of PTA by NH_2-MIL-101(Al) using *in-situ* X-ray scattering.[43] By analysing specific Bragg peaks, they found that the presence of the POM stabilised the formation of NH_2-MOF-235(Al), which is the essential precursor for NH_2-MIL-101(Al) formation.

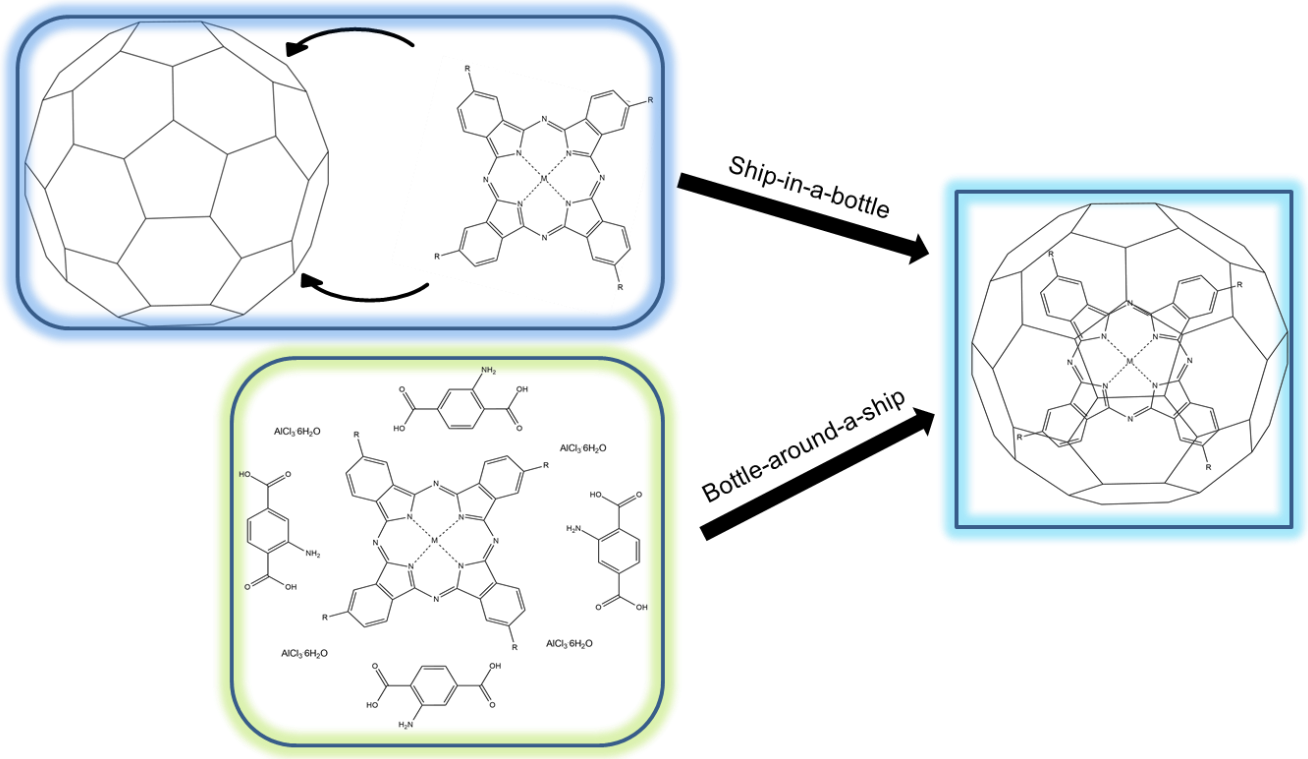

Figure 2. 15: Two different PSM methods: a) ship-in-a-bottle where an MPc is intruded inside the already formed MOF and b) bottle-around-a-ship where an MPc is used as a templating agent for MOF formation.

2.4.4 Solid Grinding Formation

The least known method for the formation of functional molecules @MOFs is solid grinding. This method is similar to gas phase infiltration by grinding MOFs onto volatile molecules which have a specific vapour pressure at room temperature. This allows for the sublimation of those molecules and to move into the evacuated pores of the MOF. Although this method is limited to volatile molecules, it has been effective to deposit nanoparticles, e.g. gold nanoparticles which have been extensively studied with one dimensional MOFs such as MIL-53(Al) and HKUST-1.[34]

2.5 Macrocyclic Complexes Encapsulated in MOFs and Their Catalytic Properties

Metal organic frameworks have shown for the past 15 years to be promising heterogeneous catalysts and support systems.[1,44,45,46] MIL-101, a rigid and thermally stable compound, has important attributes towards heterogeneous catalysis.[47] Although MIL-101 has already been extensively studied and applied in heterogeneous catalysis, mostly small catalysts and metal nanoparticles were employed as inclusion compounds.[34,48,49] The relatively large size and aggregation of macrocyclic complexes often lead to catalyst inactivity. When combining structured, porous frameworks with these macrocycles, powerful catalysts could be synthesised. It was shown that hydrocarbons are selectively oxidised by

MOFs containing metallic clusters.[50,51,52] Zeolites have been used extensively as a matrix support system to host catalysts inside their cages.[53] Zeolites, mesoporous silica and activated carbon do not have large cavities needed for the hosting of large catalytic systems. The 3D structure of MIL-101 shows potential as a catalytic support system due to its large cavity size. Eddaoudi and co-workers[54] encapsulated a functionalised, free-base porphyrin into a zeolitic-like MOF and metallated the porphyrin post-synthetically with various metals like Mn, Cu, Co and Zn **(Figure 2. 16, p25)**. Catalytic tests on the Mn complex to oxidise cyclohexane into cyclohexanol and cyclohexanone gave much higher yields and TONs than previous studies on other supported Fe(III) porphyrin complexes. The higher yields are due to the limited formation of bridged μ-oxide dimers resulting in oxidative self-degradation. This could be the result of less aggregation of the macrocycles.[55] Another advantage of encasing the catalyst inside a support such as a MOF is that leaching does not occur. By separating the heterogeneous catalyst by filtration from the reaction, it was able to be recycled eleven times before activity was lost.

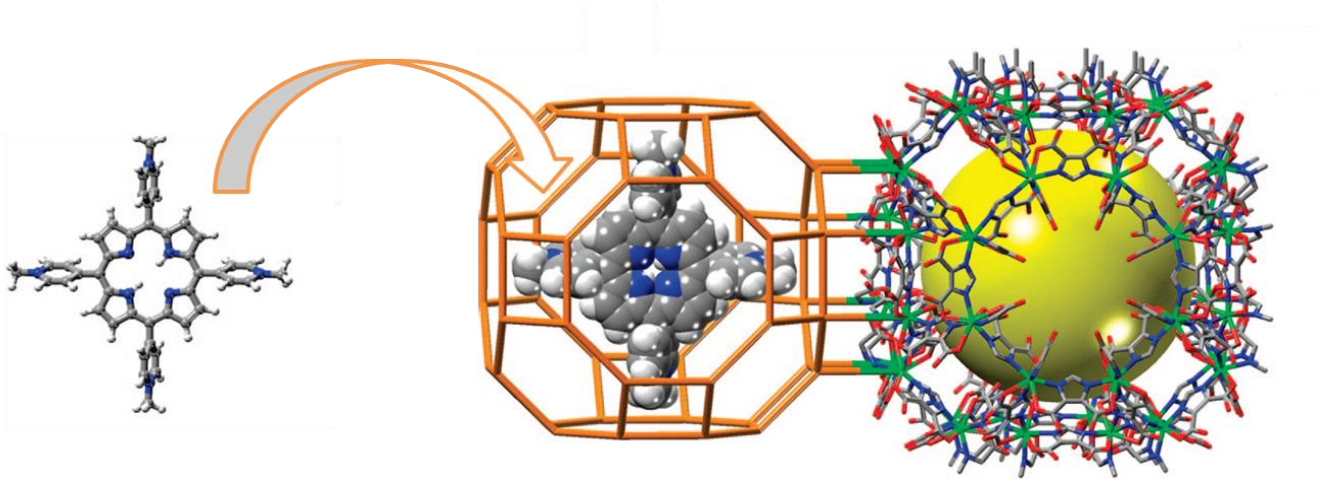

Figure 2. 16: Illustration of 5,10,15,20- tetrakis(1-methyl-4-pyridinio)porphyrin (**left)** encaged inside the structure of a imidazoledicarboxylate-based MOF (**right**).[54] Adapted with permission from M.H. Alkordi, Y.L. Liu, R.W. Larsen, J.F. Eubank and M. Eddaoudi, *J. Am. Chem. Soc.* 2008, **130**, 12639-12641. Copyright 2016 American Chemical Society.

Metal phthalocyanines (MPcs), just like MOFs, are excellent liquid-phase oxidative catalysts and have already been used with several organic compounds.[56] Extensive research was done on the oxidative abilities of the N-bridged diiron phthalocyanine complex, $(FePcR_4)_2N$, on molecules such as alkyl aromatics, benzene and methane.[57,58,59] MPcs' catalytic activity is easily hindered by agglomeration through π-π stacking leaving the internal MPcs completely inactive. MOFs can provide a solution to this problem by compartmentalisation. Farruseng and co-workers[60] encapsulated three types of MPcs namely $FePcF_{16}$, $RuPcF_{16}$ and $(FePc^tBu_4)_2N$ into the cages of MIL-101(Cr) to selectively oxidise tetralin to 1-tetralone. Solution phase infiltration was used to incorporate the MPcs into the MOF. Though a theoretical loading of 9 wt% was predicted, the total loadings, as confirmed by IPC-OES were: $FePcF_{16}$@MIL-101(Cr) = 2.1 wt%, $RuPcF_{16}$@MIL-101(Cr) = 3.6 wt% and $(FePc^tBu_4)_2N$@

MIL-101(Cr) = 5.2 wt%. Surface area studies were done to investigate whether the MPcs were allocated inside the cavities of the MOF. The smaller MPcs, $FePcF_{16}$ and $RuPcF_{16}$ resulted in a higher loss of pore volume compared to their loading percentage. For $FePcF_{16}$, a pore volume decrease of 16% is almost five times more than its loading percentage (3.6%), a clear indication that most of the MPcs are incorporated inside the cavities of the MOF. In contrast, $(FePc^tBu_4)_2N$ resulted in a pore volume decrease of 5% from a loading of 5.2 wt% an indication that the bulky $(FePc^tBu_4)_2N$ is not contained inside the MOF's cavities. Thorough removal of all excess MPcs showed that $(FePc^tBu_4)_2N$ has a very strong affinity towards MIL-101(Cr). This indicates that $(FePc^tBu_4)_2N$ is allocated on the outside surface area of the MOF and may be trapped by macroporous cavities formed by MOF agglomeration during the infiltration procedure.

The turnover numbers (TONs) for the formation of 1-tetralone after 6 hours were 30 900 and 24 200 for $RuPcF_{16}$@MIL-101(Cr) and $FePcF_{16}$@MIL-101(Cr) respectively, much higher than that of $(FePc^tBu_4)_2N$@MIL-101(Cr) (TON = 5100). The two encapsulated MPcs also showed better selectivity and TONs compared to the homogenous catalysts, $FePcF_{16}$ and $RuPcF_{16}$. This proves the synergistic effect of reduced agglomeration of the active catalytic sites when confined inside a porous MOF.

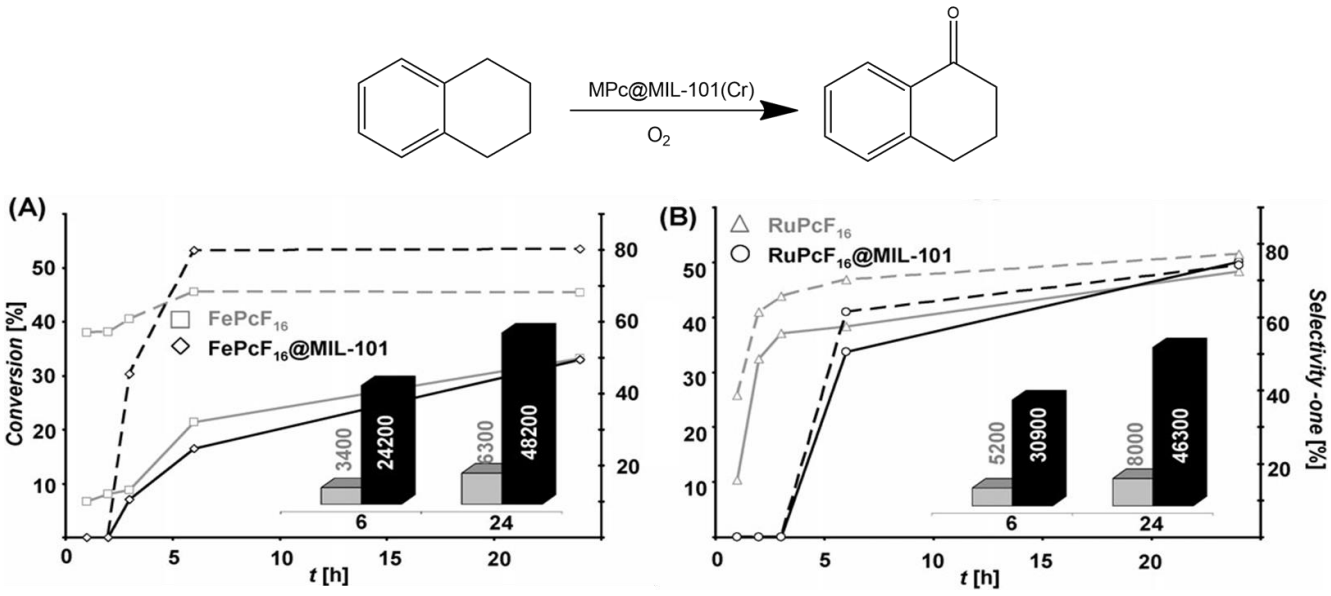

Figure 2. 17: The conversion % (**solid line**) and selectivity (**dashed line**) of tetralin to 1-tetralone (**top reaction**). The turnover numbers of the homogeneous catalysts $FePcF_{16}$ and $RuPcF_{16}$ (**grey**) with respect to $FePcF_{16}$@MIL-101 (**A**) and $RuPcF_{16}$@MIL-101 (**B**) are given at 6 hours (**grey bars**) and 24 hours (**black bars**). Adapted with permission from E. Kockrick, T. Lescouet, E.V. Kudrik, A.B. Sorokin and D. Farrusseng, *Chem. Commun.* 2011, **47**, 1562-1564. Copyright 2016 Royal Society of Chemistry.

In a similar study on MIL-101(Cr) in 2010, Fedin and co-workers[61] investigated the oxidative capabilities of iron tetrasulfophthalocyanine (FePcS), well-known for selectively oxidising aromatic

compounds in the liquid-phase with ^{t}BuOOH.[62] To improve on the catalytic activity of FePcS, it was immobilised inside MIL-101(Cr) through solution phase infiltration from a known concentration of the FePcS. The infiltration process was tracked by the decrease in FePcS concentration using UV-Vis analysis (λ = 645 nm) and took only 15 minutes. A 22 wt% loading was obtained and was found to be irreversible by means of an extraction test with $NaClO_4$. This meant that the Pc did not just interact with the MOF's structure through electrostatic forces, but possibly also π-π interaction. The immobility and high loading % of the FePcS was probed by X-ray photoelectron spectroscopy (XPS) before and after argon ion spattering, giving an $Fe2p_{3/2}$ binding energy of 710.1 eV, similar to that of the bulk FePcS (710 eV). The ratio Fe/Cr found on the surface of the MOF was close to that of ICP-AES results, confirming that FePcS infiltrated the pores of MIL-101(Cr) even though the molecular size of FePcS (1.7 x 1.7 nm) is slightly larger than that of MIL-10(Cr)'s biggest pore size (1.6 x 1.5 nm). This phenomenon is possible when the host pore size and guest size are very close to each other.[63,64] The hybrid FePcS@MIL-101(Cr)'s catalytic ability was tested on benzyl alcohol, 2,3,6-trimethylphenol and 8-hydroxyquinoline which were oxidised to benzaldehyde, 2,3,5-trimethylcyclohexa-2,5-diene-1,4-dione and quinolone-5,8-dione respectively. Compared to the homogeneous $FePcS(Bu_4N)_4$, similar conversion rates were found for benzyl alcohol. In the case of 2,3,6-trimethylphenol and 8-hydroxyquinoline the conversion rates for FePcS@MIL-101(Cr) were almost double that of the homogeneous catalyst.

2.6 Characterisation of Macrocyclic Complexes @MOFs

Although all techniques which were discussed in **2.2.3** (**p 10**) for the characterisation of macrocyclic complexes @MOFs, only new and/or relevant methods will be discussed as follows.

2.6.1 Diffuse Reflectance Solid State UV-Vis Spectroscopy (DRS UV-Vis)

Liquid phase UV-Vis spectroscopy is used for the analysis of homogeneous solutions or transparent solid materials. The results obtained are from the absorbance or transmittance of electromagnetic radiation passing through the sample. DRS UV-Vis Spectroscopy is used for insoluble materials usually pressed into a thin film on a quartz plate, and radiated with electromagnetic radiation, giving reflected or scattered energy. Reflected light can be specular or diffuse reflected light. Diffuse reflected light will be used in this study, assuming that the reflected light is scattered in all directions.

DRS-UV-Vis is readily used to detect inclusion molecules inside or on the external surface of MOFs. Eddaoudi and co-workers[54] used DRS UV-Vis as partial confirmation that the porphyrin they encapsulated and post-synthetically metallated was present in the structure. Although the porphyrin

was soluble, its solid-state UV-Vis data was needed for comparison. Five noticeable adsorption bands (434, 522, 556, 593 and 648 nm) were detected in the porphyrin @MOF products which were comparable to those of the MOF-free phorphyrin. Just as with phthalocyanines, a clear red-shift is noticeable when the porphyrin is complexed with the different metals, Mn, Co, Cu and Zn as shown in **Figure 2. 18** (**p 28)**.

This method was applied similarly by Farruseng and co-workers[60] when they incorporated the different MPcs, $(FePc^{t}Bu_4)_2N$, $FePcF_{16}$ and $RuPcF_{16}$ into MIL-101(Cr). As shown in **Figure 2. 19** (**p 29)**, a well-defined red-shift is noticeable when comparing the MPcs@MIL-101(Cr) with pure MIL-101(Cr). The absorption maximum of the MIL-101(Cr) (~600 nm) is closely related to that of the MPcs due to the chromium metal inside the MOF, which also has a green colour. This differs greatly in comparison to MIL-101(Fe) which reflects a brown-reddish colour and MIL-101(Al) reflecting yellow.

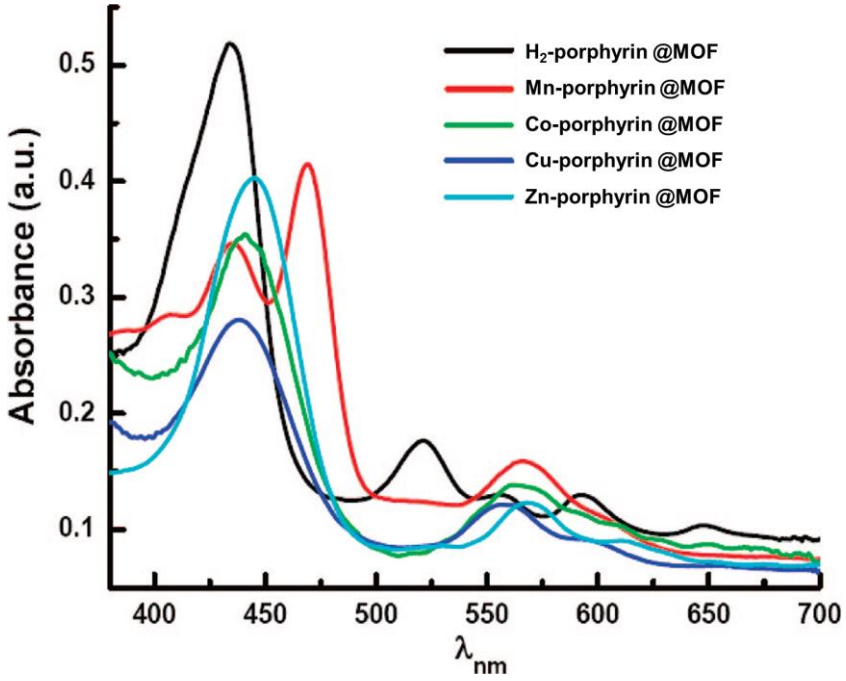

Figure 2. 18: DRS UV-Vis analyses of the metal-free 5,10,15,20- tetrakis(1-methyl-4-pyridinio)porphyrin @MOF (**black line**) and the post-synthetically metallated porphyrin complexes @MOF (**coloured lines**). [54] Adapted with permission from M.H. Alkordi, Y.L. Liu, R.W. Larsen, J.F. Eubank and M. Eddaoudi, *J. Am. Chem. Soc.* 2008, **130**, 12639-12641. Copyright 2016 American Chemical Society.

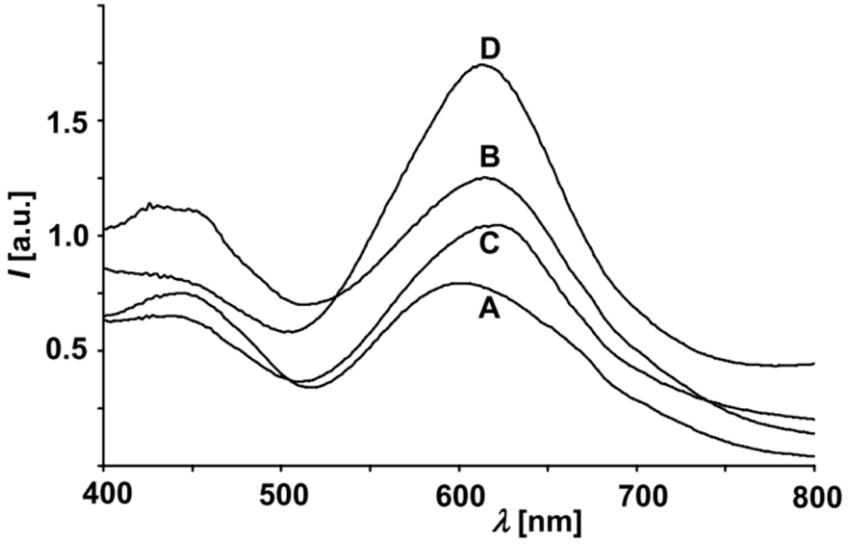

Figure 2. 19: DRS UV-Vis of pure MIL-101(Cr) (**A**), $(FePc^{t}Bu_4)_2N$@MIL-101(Cr) (**B**), $FePcF_{16}$@MIL-101(Cr) (**C**) and $RuPcF_{16}$@MIL-101(Cr) (**D**).[60] Adapted with permission from E. Kockrick, T. Lescouet, E.V. Kudrik, A.B. Sorokin and D. Farrusseng, *Chem. Commun.* 2011, **47**, 1562-1564. Copyright 2016 Royal Society of Chemistry.

It is possible to analyse the adsorption process of a complex into a MOF substrate, but with the use of liquid state UV-Vis spectroscopy. Fedin and co-workers,[61] showed a simple method where the decrease in concentration of the MPc at timed intervals is measured during its intrusion into the MOF.

2.6.2 Surface Area and Porosity Analysis

Although this topic has been discussed thoroughly in **2.5 (p 24)**, these analyses may help to detemine whether a particular inclusion molecule has been successfully encapsulated and/or if it is adhered to the external surface of the MOF. Surface area studies were used to confirm the whereabouts of the bulky $(FePc^{t}Bu_4)_2N$ which is theoretically much larger than the pore windows of MIL-101(Cr). Even though it gave a high loading wt%, it was found that $(FePc^{t}Bu_4)_2N$ decreased the internal surface area the least in comparison to other compounds as shown in **Figure 2. 20 (p 30)**. Other properties such as pore size distribution was constant showing that the loading of a particular complex did not fracture the MOF's framework.

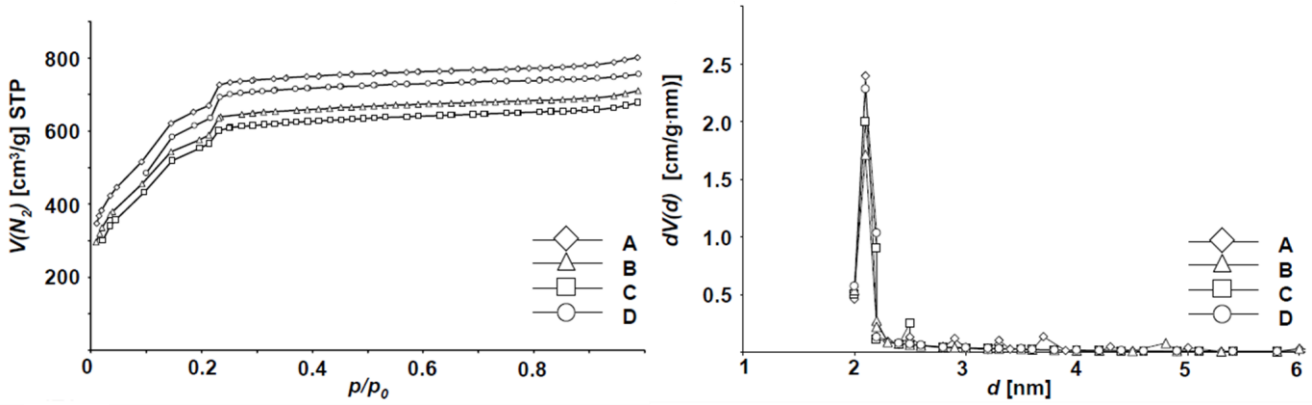

Figure 2. 20: N_2 adsorption isotherms @ 77 K (**left**) of pure MIL-101 (**A**), $(FePc^tBu_4)_2N$@MIL-101(Cr) (**B**), $FePcF_{16}$@MIL-101(Cr) (**C**) and $RuPcF_{16}$@MIL-101(Cr) (**D**). The pore volume distribution is also given to show static pore sizes (**right**). Adapted with permission from E. Kockrick, T. Lescouet, E.V. Kudrik, A.B. Sorokin and D. Farrusseng, *Chem. Commun.* 2011, **47**, 1562-1564. Copyright 2016 Royal Society of Chemistry.

Surface area studies can be used to correlate the loading percentage of a particular inclusion molecule by confirming that the internal surface area decreases as the wt% of the inclusion molecules increases. If the internal surface area does not decrease with a confirmed increase in loading percentage, then the inclusion molecules are most likely to be adhered to the outside surface area of the MOF **(Figure 2. 21, p 30)**.[61]

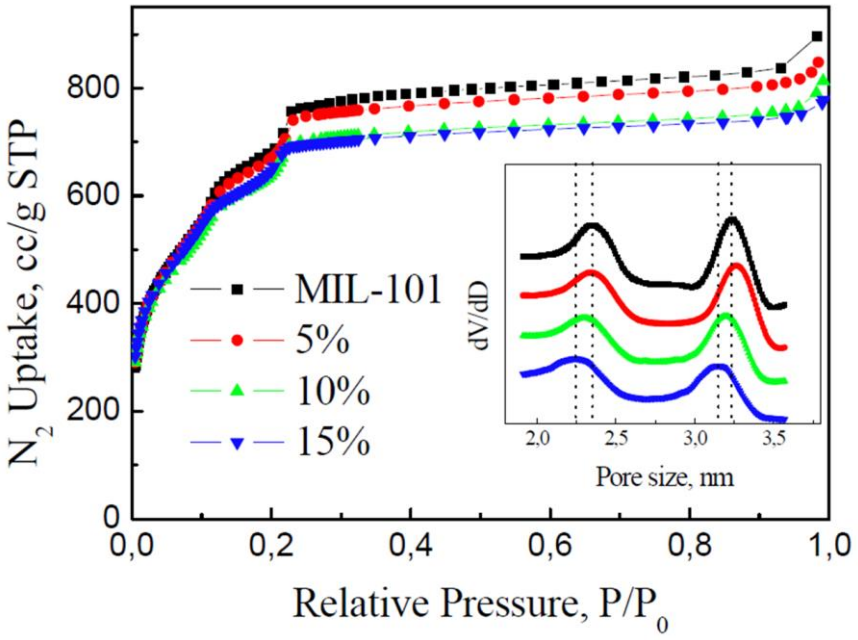

Figure 2. 21: N_2 adsorption isotherms @ 77 K of pure MIL-101(Cr) (**black cubes**), FePcS@MIL-101(Cr) (5% loading) (**red circles**), FePcS@MIL-101(Cr) (10% loading) (**green triangles**) and FePcS@MIL-101(Cr) (15% loading) (**blue inverted triangles**). The pore volume distribution is also given (**right insert**) to show static pore sizes. Reprinted with permission from O.V. Zalomaeva, K.A. Kovalenko, Y.A. Chesalov, M.S. Melgunov, V.I. Zaikovskii, V.V. Kaichev, A.B. Sorokin, O.A. Kholdeeva and V.P. Fedin, *Dalton Trans.* 2011, **40**, 1441-1444. Copyright 2016 Royal Society of Chemistry.

2.7 Electrochemistry

2.7.1 Introduction

Electrochemistry is the study of the flow of electrons and the derived chemical reactions from redox active species. A classical method to analyse redox active species is cyclic voltammetry (CV) where the change in current is monitored over a potential range, which is usually scanned in a short, timed interval. In a static, homogeneous solution, the change in current is observed while the potential is cycled between a working electrode and an auxiliary electrode. The potential of the working electrode is then held relative to a reference electrode. This setup is typically called a three phase electrochemical cell. Instead of using a reference electrode, an internal reference such as ferrocene can be employed due to its reversible electrochemistry. The detail that can be extracted from the cyclic voltammograms can range from simple, one electron processes, to very complex. In general, the following detail is always present: in **Figure 2. 22 (p 32),** a general redox process of a metal $M^{II/III}$ occurs in the ideal form. **Point A** is regarded as the resting position. This is where no electrolysis occurs. As the potential increases in the forward scan up to **point B**, the electrode becomes a sufficiently strong oxidant to oxidise the M^{II} to $[M^{III}]^{+}$. The anodic current increases, but at the same time the concentration of M^{II} decreases at the electrode surface. At **point C** a peak oxidation current is reach due to the concentration of M^{II} which has been extensively diminished at the electrode surface. At **point D** the anodic current is decreasing due to the concentration of $[M^{III}]^{+}$ overshadowing the concentration of M^{II} at the double layer of the working electrode. At **point E** a turning point occurs and the potential starts to decrease. As the potential decreases further, **point F** is reached where the electrode becomes a sufficient reductant enabling it to reduce the $[M^{III}]^{+}$ again back to M^{II}. The concentration of M^{II} increases as the cathodic current increases and at **point G** the concentration of $[M^{III}]^{+}$ has been extensively diminished and a peak reduction current is reached. During **point H** the concentration of M^{II} starts to overshadow the concentration of $[M^{III}]^{+}$ and the cathodic current decreases up to **point I** where a full redox process occurred.

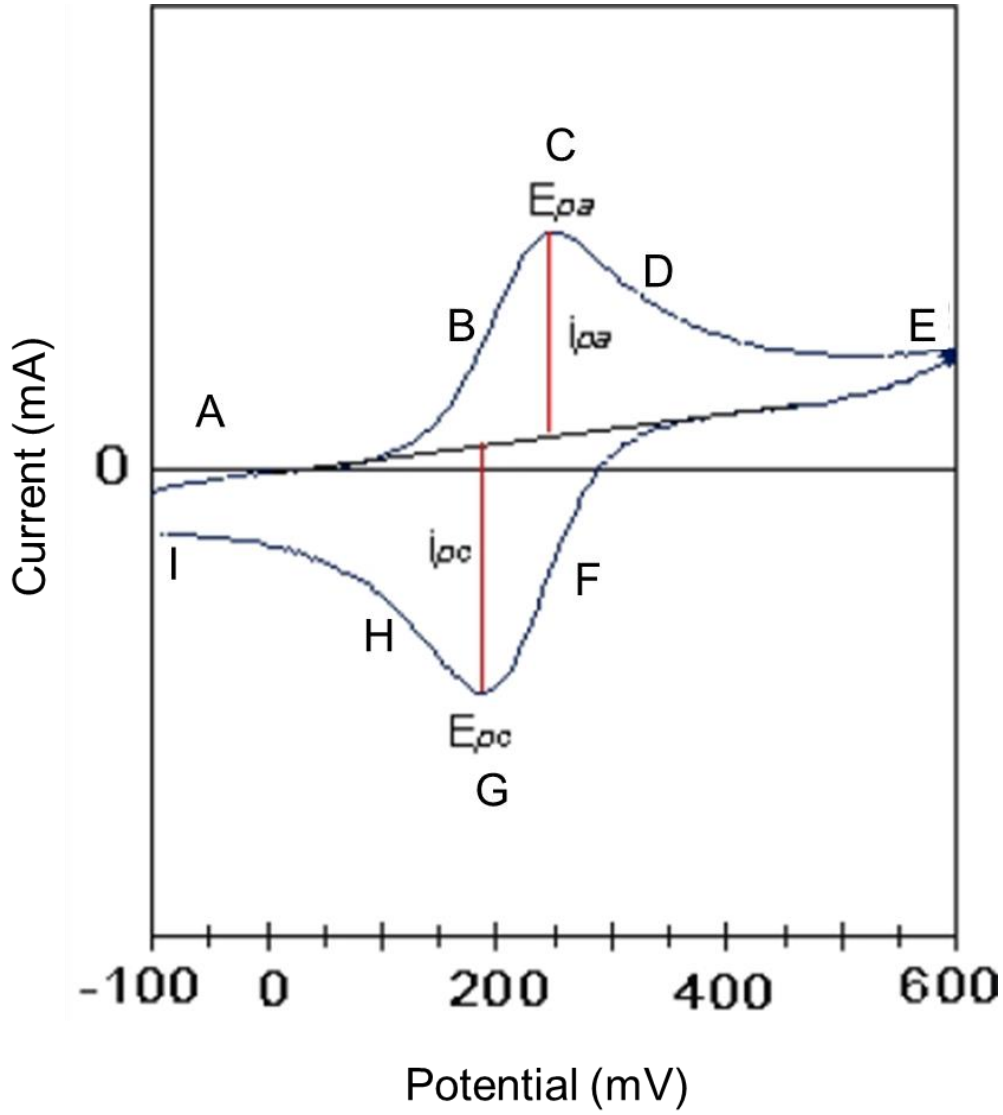

Figure 2. 22: A general cyclic voltammogram of a metal $M^{II/III}$ undergoing an ideal, one electron redox process (ΔE = 59 mV and i_{pc}/i_{pa} = 1).[65] Adapted with permission from R.N. Vyas and B. Wang, *Int. J. Mol. Sci.* 2010, **11**, 1956-1972. Open access 2010 International Journal of Molecular Sciences.

The essential values that can be obtained from the cyclic voltammogram: peak anodic potential (E_{pa}), peak cathodic potential (E_{pc}), peak anodic current (i_{pa}) and peak cathodic current (i_{pc}). The peak potentials are used to calculate the formal reduction potential ($E°'$) where $E°' = (E_{pa} + E_{pc})/2$. The difference in peak potentials are displayed as ΔE_p where ΔE_p = 59 mV in ideal conditions. The ratio i_{pc}/i_{pa} can be used to determine chemical reversibility whereas ΔE_p is used to determine electrochemical reversibility. For full chemical reversibility i_{pc}/i_{pa} should equal 1. In everyday conditions full chemical and electrochemical reversibility is considered for $i_{pc}/i_{pa} \sim 1$ and $\Delta E_p < 90$ mV. Electrochemical quasi-reversibility is considered for 90 mV $< \Delta E_p <$ 150 mV and for electrochemical irreversibility $\Delta E_p >$ 150 mV **(Figure 2. 23, p 33)**.

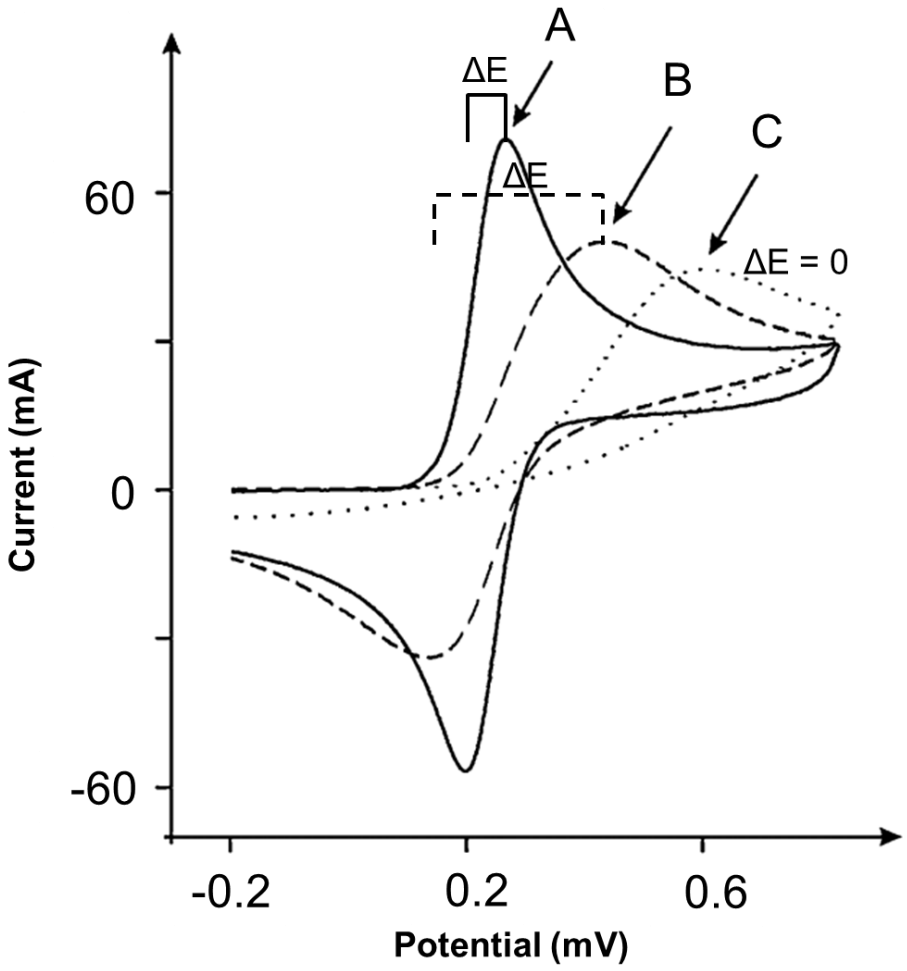

Figure 2. 23: Three different redox processes displaying a full electrochemical and chemical reversible process (**A**), chemical reversible, but electrochemical irreversible process (**B**) and a full electrochemical and chemical irreversible process (**C**). Adapted with permission from D.A.C. Brownson, The electrochemistry of graphene, Springer, 2014.

2.7.2 Electrochemistry of Phthalocyanines

The electrochemistry of MPcs can be very rich due to the redox processes which can occur on both the macrocylic ring and the central metal. Electrochemically active transition metals such as Co and Fe give rise to additional redox couples, because of the way they alter the electron environment on the MPc ring.[66] If the central metal is not electrochemically active, it is possible to determine the electrochemical properties of the Pc's ring-based processes. Under the correct conditions it is possible for a MPc to be oxidised into two anionic states, $[MPc^{-2/-1}]^{0/+1}/[MPc^{-1/0}]^{+1/+2}$, and four cationic states, $[MPc^{-2/-3/-4/-5}]^{0/-1/-2/-3}/[MPc^{-3/-4/-5/-6}]^{-1/-2/-3/-4}$. These anionic and cationic states are easily altered by substituents and the type of interaction the metal center has on the electrochemical environment of the ring. This can cause some redox couples to be absent and other to be irreversible.[67] Szunerits and co-workers[26] studied the electrochemistry of tetracarboxylic acid cobalt phthalocyanine and was able to detect two redox processes for Co: an irreversible oxidation band at E = 0.65 V for $Co^{III/II}$ and a reversible redox couple at $E^{\circ\prime}$= -0.22 V for $Co^{II/I}$ **(Figure 2. 24, p 34)**. Only one irreversible oxidation

band belonging to the MPc ring was observed at E = 0.8V. The catalytic oxidation of O_2 to $O_2^{\cdot-}$ increased dramatically in the absence of an argon atmosphere **(Figure 2. 24, p 34)**. This process occurs commonly in aprotic solvents stressing the importance of inertness.

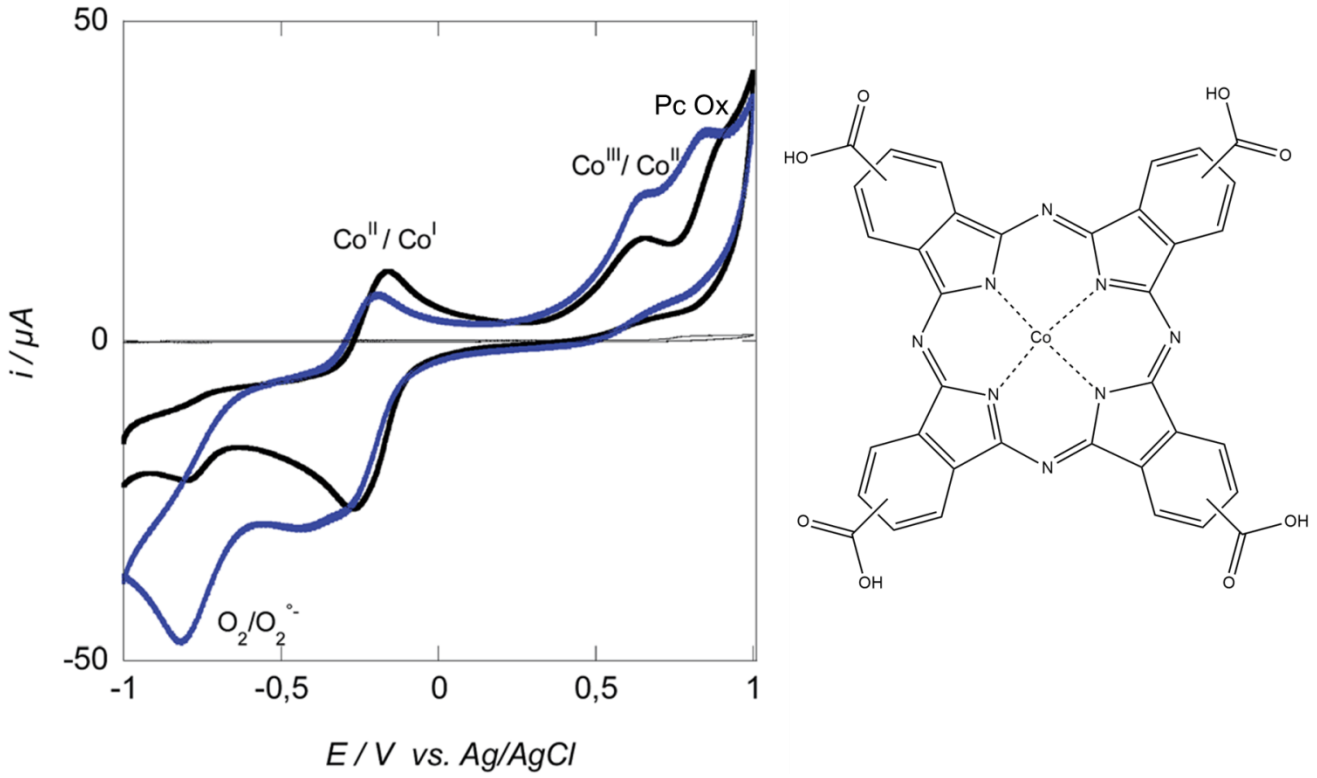

Figure 2. 24: Cyclic voltammograms of tetracarboxylic acid cobalt phthalocyanine in inert (black) and air (blue) conditions. Adapted with permission from I.S. Hosu, Q. Wang, A. Vasilescu, S.F. Peteu, V. Raditoiu, S. Railian, V. Zaitsev, K. Turcheniuk, Q. Wang, M. Li, R. Boukherrouba and Sabine Szunerits, *RSC Adv*. 2015, **5**,1474-1487. Copyright 2016 Royal Society of Chemistry.

2.7.3 Metal Organic Framework Electrochemistry in the Solid State

Solid state electrochemistry of MOFs is complex[68] and thus far attracted little attention in comparison to pure homogeneous electrochemistry. The MOF is fixated to the surface of a working electrode either by means of grafting[69] or by using an electro-conductive sealant, depending on the type of solvent used during the experiment. If an aqueous medium is used, the analyte can be fixated with Nafion®, a polymer with very high proton conductivity and good chemical resistance, making a very good electrode modifier.[70] If an organic medium is required, KCl can be used to fixate the analyte. Marken and co-workers[69] investigated the electrochemical activity of various amide-modified MOFs which included NH_2-IRMOF-3 and the analogous NH_2-MIL-53. The MOFs were post-synthetically modified with ferrocene (Fc) which was then electrochemically analysed in both organic and aqueous mediums. Rapid decay of the Fc signals was observed, due to oxidation in an aqueous medium whilst

good chemical reversibility was obtained in organic electrolyte. HO^- groups present in the aqueous media break down the framework when oxidised.

To the best of our knowledge, the electrochemical activity of MOF-incorporated phthalocyanines has not yet been extensively investigated and will be attempted in this study.

2.8 References

[1] G. Férey, *Chem. Soc. Rev*. 2008, **37**, 191-214.

[2] N.V. Maksimchuk, O.V. Zalomaeva, I.Y. Skobelev, K.A. Kovalenko, V.P. Fedin and O.A. Kholdeeva, *Proc. R. Soc. A.* 2012, **468**, 2017–2034.

[3] G. Férey, C. Mellot-Draznieks, C. Serre, F. Millange, J. Dutour, S. Surble and I. Margiolaki, *Science* 2005, **309**, 2040-2042.

[4] P. Serra-Crespo, E.V. Ramos-Fernandez, J. Gascon and F. Kapteijn, *Chem. Mater*. 2011, **23**, 2565-2572.

[5] S. Achmann, G. Hagen, J. Kita, I.M. Malkowsky, C. Kiener and R. Moos, *Sensors* 2009, **9**, 1574-1589.

[6] S. Lee, J. Yoon, Y. Seo, M. Kim, S. Lee, U. Lee, Y.K. Hwang, Y. Bae and J. Chang, *Micro. Meso. Mat*. 2014, **193**, 160-165.

[7] J.S. Seo, D. Whang, H. Lee, S.I. Jun, J. Oh, Y.J. Jeon and K. Kim, *Nature* 2000, **404**, 982-986.

[8] C. Serre, F. Millange, C. Thouvenot, M. Noguès, G. Marsolier, D. Louër and G. Férey, *J. Am. Chem. Soc.* 2002, **124**, 13519-13526.

[9] S. Bauer, C. Serre, T. Devic, P. Horcajada, J. Marrot, G. Férey and N. Stock, *Inorg. Chem.* 2008, **47**, 7568-7576.

[10] E. Stavitski, M. Goesten, J. Juan-Alcañiz, A. Martinez-Joaristi, P. Serra-Crespo, A.V. Petukhov, J. Gascon and F. Kapteijn, *Angew. Chem. Int. Ed.* 2011, **50**, 9624-9628.

[11] W. Zhou, H. Wu, M.R. Hartman, and T. Yildirim, *J. Phys. Chem. C* 2007, *Angew. Chem. Int. Ed*. 2011, **50**, 16131-16137.

[12] M. Hartmann and M. Fischer. *Micropor. Mesopor. Mat.* 2012, **164**, 38-43.

[13] T. Ahnfeldt, D. Gunzelmann, T. Loiseau, D. Hirsemann, J. Senker, G. Férey, and N. Stock, *Inorg. Chem.* 2009, **48**, 3057-3064.

[14] S. Biswas, S. Couck, M. Grzywa, J.F.M. Denayer, D. Volkmer, and P. Van Der Voort, *Eur. J. Inorg. Chem.* 2012, 2481-2486.

[15] D. Jiang, L.L. Keenan, A.D. Burrows and K.J. Edler, *Chem. Commun.* 2012, **48**, 12053–12055.

[16] L. Li and E.W. Diau, *Chem. Soc. Rev.* 2013, **42**, 291-304.

[17] J. Haber, R. Iwanejko, J. Połtowicz, P. Battioni and D. Mansuy, *J. Mol. Cat. A: Chem.* 2000, **152**, 111-115.

[18] N. Padma, A. Joshi, A. Singh, S.K. Deshpande, D.K. Aswal, S.K. Gupta and J.V. Yakhmia, *Sensor. Actuator. B* 2009, **143**, 246-252.

[19] A.N. Vzorov, L.G. Marzilli, R.W. Compans and D.W. Dixon, *Antiviral Research* 2003, **59**, 99-109.

[20] H.A. Abdeldayem, D.O. Frazier, B.G. Penn, D.D. Smith and C.E. Banks, *Thin Solid Films* 1999, **350**, 245-248.

[21] F. Yilmaz, D. Atilla and V. Ahsen, *Polyhedron* 2004, **23**, 1931-1937.

[22] Y. Zorlu, F. Dumoulin, D. Bouchu, V. Ahsen and D. Lafont, *Tetrahedron Lett.* 2010, **51**, 6615-6618.

[23] Y. Yoshida, M. Nakamura, S. Tanaka, I. Hiromitsu, Y. Fujita and K. Yoshino, *Synth. Met.* 2006, **156**, 1213-1217.

[24] K. Sakamoto and E. Ohno, *Prog. Org. Coat.* 1997, **31**, 139-145.

[25] X. Song, Y. She, H. Ji, and Y. Zhang, *Org. Process Res. Dev.* 2005, **9**, 2228-2232.

[26] I.S. Hosu, Q. Wang, A. Vasilescu, S.F. Peteu, V. Raditoiu, S. Railian, V. Zaitsev, K. Turcheniuk, Q. Wang, M. Li, R. Boukherrouba and S. Szunerits, *RSC Adv*. 2015, **5**,1474-1487.

[27] A. Bilgin¸ Ç. Yağcı, A, Mendi and U. Yıldız, *J. Incl. Phenom. Macrocycl. Chem.* 2010, **67**, 377-383.

[28] J. Mack and M.J. Stillman, *Coord. Chem. Rev.* 2001, **219-221**, 993-1023

[29] A. Muranaka, M. Okuda, N. Kobayashi, K. Somers, and A. Ceulemans, *J. Am. Chem. Soc.* 2004, **126**, 4596-4604.

[30] N. Kobayashi, A. Muranaka, and K. Ishii, *Inorg. Chem.* 2000, **39,** 2256-2257.

[31] S.G. Makarov, O.N. Suvorova, C. Litwinski, E.A. Ermilov, B. Röder, O. Tsaryova, T. Dülcks and D. Wöhrle, *Eur. J. Inorg. Chem.* 2007, 546-552.

[32] A. Alemdar, A.R. Özkaya and M. Bulut, Polyhedron 2009, **28**, 3788-3796.

[33] H. Deng, S. Grunder, K.E. Cordova, C. Valente, H. Furukawa, M. Hmadeh, F. Gándara, A.C. Whalley, Z. Liu, S. Asahina, H. Kazumori, M. O'Keeffe, O. Terasaki, J.F. Stoddart and O.M. Yaghi, *Science* 2012, **336**, 1018-1023.

[34] Q. Zhu and Q. Xu, *Chem. Soc. Rev.*, 2014, **43**, 5468-5512.

[35]S.J. Garibay, Z. Wang, K.K. Tanabe and S.M. Cohen, *Inorg. Chem.* 2009, **48**, 7341-7349.

[36] D. Esken, X. Zhang, O.I. Lebedev, F. Schröder and R.A. Fischer, *J. Mater. Chem.*, 2009, **19**, 1314-1319.

[37] M. Müller, O.I. Lebedev and R.A. Fischer, *J. Mater. Chem.*, 2008, **18**, 5274-5281.

[38] F. Schröder, D. Esken, M. Cokoja, M.W.E. Van Den Berg, O.I. Lebedev, G. Van Tendeloo, B. Walaszek, G. Buntkowsky, H. Limbach, B. Chaudret, and R.A. Fischer, *J. Am. Chem. Soc.* 2008, **130**, 6119-6130.

[39] D. Esken, S. Turner, O.I. Lebedev, G. Van Tendeloo, and R.A. Fischer, *Chem. Mater.* 2010, **22**, 6393-6401.

[40] J. Hermannsdçrfer and R. Kempe, *Chem. Eur. J.* 2011, **17**, 8071-8077.

[41] R.W. Johnson, A. Hultqvist and S.F. Bent, *Mater. Today* 2014,**17**, 236-246.

[42] J. Juan-Alcañiz, E.V. Ramos-Fernandez, U. Lafont, J. Gascon and F. Kapteijn, *J. Catal.* 2010, **269**, 229-241.

[43] J. Juan-Alcañiz, M. Goesten, A. Martinez-Joaristi, E. Stavitski, A.V. Petukhov, J. Gascon and F. Kapteijn, *Chem. Commun*. 2011, **47**, 8578-8580.

[44] U. Mueller, M. Schubert, F. Teich, H. Puetter, K. Schierle-Arndt and J. Pastre, *J. Mater. Chem.* 2006, **16**, 626-636.

[45] J.Y. Lee, O.K. Farha, J. Roberts, K.A. Scheidt, S.B.T. Nguyen and J.T. Hupp, *Chem. Soc. Rev.* 2009, **38**, 1450-1459.

[46] L.Q. Ma, C. Abney and W.B. Lin, *Chem. Soc. Rev.* 2009, **38**, 1248-1256.

[47] J. Kim, S. Bhattacharjee, K. Jeong, S. Jeong and W. Ahn, *Chem. Commun.* 2009, 3904-3906.

[48] A. Corma, H. García and F.X. Llabrés i Xamena, *Chem. Rev.*, 2010, **110**, 4606-4655.

[49] D. Farrusseng, S. Aguado and C. Pinel, *Angew. Chem. Int. Ed*. 2009, **48**, 7502-7513.

[50] K. Schlichte, T. Kratzke and S. Kaskel, *Microporous Mesoporous Mater.* 2004, **73**, 81-88.

[51] L. Alaerts, J. Wahlen, P.A. Jacobs and D.E. De Vos, *Chem. Commun.* 2008, 1727-1737.

[52] M. Tonigold, Y. Lu, B. Bredenkotter, B. Rieger, S. Bahnmuller, J. Hitzbleck, G. Langstein and D. Volkmer, *Angew. Chem., Int. Ed.* 2009, **48**, 7546-7550.

[53] M. Sabo, A. Henschel, H. Froede, E. Klemm and S. Kaskel, *J. Mater. Chem.* 2007, **17**, 3827-3832.

[54] M.H. Alkordi, Y.L. Liu, R.W. Larsen, J.F. Eubank and M. Eddaoudi, *J. Am. Chem. Soc.* 2008, **130**, 12639-12641.

[55] C. Guo, J. Song, X. Chen and G.J. Jiang, *Mol. Catal. A.* 2000, **157**, 31-40.

[56] A. B. Sorokin, J.L. Seris and B. Meunier, *Science*, 1995, **268**, 1163-1166; (b) N. Grootboom and T. Nyokong, *J. Mol. Catal. A: Chem.* 2002, **179**, 113-123; (c) N. d'Alessandro, L. Liberatore, L. Tonucci, A. Morvillo and M. Bressan, *New J.Chem.* 2001, **25**, 1319-1324; (d) S.L. Kachkarova-Sorokina, P. Gallezot and A.B. Sorokin, *Chem. Commun.* 2004, 2844-2845; (e) V.B. Sharma, S.L. Jain and B. Sain, *Catal. Commun.* 2006, 7, 454-456; (f) A.B. Sorokin and B. Meunier, *Eur. J. Inorg. Chem.* 1998, 1269-1281.

[57] A.B. Sorokin, E.V. Kudrik and D. Bouchu, *Chem. Commun.* 2008, 2562-2564.

[58] E.V. Kudrik and A.B. Sorokin, *Chem. Eur. J.* 2008, **14**, 7123-7126.

[59] U. Işci, P. Afanasiev, J.M.M. Millet, E.V. Kudrik, V. Ahsen and A.B. Sorokin, *Dalton Trans.* 2009, 7410-7420.

[60] E. Kockrick, T. Lescouet, E.V. Kudrik, A.B. Sorokin and D. Farrusseng, *Chem. Commun.* 2011, **47**, 1562-1564.

[61] O.V. Zalomaeva, K.A. Kovalenko, Y.A. Chesalov, M.S. Melgunov, V.I. Zaikovskii, V.V. Kaichev, A.B. Sorokin, O.A. Kholdeeva and V.P. Fedin, *Dalton Trans.* 2011, **40**, 1441-1444.

[62] O.V. Zalomaeva, I.D. Ivanchikova, O.A. Kholdeeva and A.B. Sorokin, *New J. Chem.* 2009, **33**, 1031-1037; (b) O.V. Zalomaeva, A.B. Sorokin and O.A. Kholdeeva, *Green Chem.* 2010, **12**, 1076-1082; (c) C. Pérollier, C. Pergrale-Mejean and A.B. Sorokin, *New J. Chem.* 2005, **29**, 1400-1403; (d) S.V. Sirotin, A.Y. Tolbin, I.F. Moskovskaya, S.S. Abramchuk, L.G. Tomilova and B.V. Romanovsky, *J. Mol. Catal. A: Chem.* 2010, **319**, 39-45.

[63] H. Jobic, B.J. Borah and S. Yashonath, *J. Phys. Chem. B* 2009, **113**, 12635.

[64] B.J. Borah, H. Jobic and S. Yashonath, *J. Chem. Phys.*, 2010, **132**, 144507.

[65] R.N. Vyas and B. Wang, *Int. J. Mol. Sci.* 2010, **11**, 1956-1972.

[66] T. Nyokong, *Polyhedron*, 1993, **12**, 375-381.

[67] G.K. Karaoğlan, G. Gümrükçüa, A. Koca, A. Gülm, *Dyes and Pigments* 2011, **88**, 247-256.

[68] A. Doménech, H. García, M.T. Doménech-Carbó and F. Llabrés i Xamena, *J. Phys. Chem. C*, 2007, **111**, 13701-13711.

[69] J.E. Halls, A. Hernan-Gomez, A.D. Burrows and F. Marken, *Dalton Trans.* 2012, **41**, 1475-1480.

[70] J. Wang, M. Musameh, and Y. Lin, *J. Am. Chem. Soc.* 2003, **125**, 2408-2409.

3 Results and Discussions

3.1 Introduction

In this chapter the synthesis, purification and characterisation of NH_2-MIL-101(Al) **(1)** are described, followed by the synthesis and characterisation of peripherally, tetra-substituted *tert*-butylmetallophthalocyanines (MPc^tBu_4) (M = Zn and Ni) and peripherally, tetra-substituted carboxymetallophthalocyanines ($MPc(COOH)_4$) (M = Zn, Fe^{III}, Co and Ni). The next topic is the incorporation and/or amidation of NH_2-MIL-101(Al) with these various MPcs through two post-synthetic-modification (PSM) methods namely solution phase infiltration and template synthesis. The unique properties of these newly formed products were investigated with FTIR, DRS-UV-Vis, TGA, low-angle PXRD, solid-state electrochemistry as well as surface area and porosity studies. $CoPc(COOH)_3$-CONH-MIL-101(Al) **(9)** and $NiPc(COOH)_3$-CONH-MIL-101(Al) **(10)** were also investigated for hydrogen storage capability. The photocatalytic oxidative activity of $CoPc(COOH)_3$-CONH-MIL-101(Al) **(9)** was then determined for the oxidation of *cis*-cyclooctene.

3.2 NH_2-MIL-101(Al)

3.2.1 Synthesis and Yield Optimisation

Until recently, NH_2-MIL-101(Al) was only synthesised by a solvothermal process (see Chapter 2). The reagents react under static autogeneous pressure in an autoclave to form the desired MOF. One major limitation of this method is low yield due to small reactor volume. The alternative benchtop synthesis, applied during this study, was developed by Hartmann *et al.*[1] Although unconventional for the MIL-101 series of MOFs, this method was proven to produce a higher surface area for NH_2-MIL-101(Al) when compared to solvothermal synthesis. This could be due to the formation of amorphous material during the solvothermal process, which may be absent during the benchtop synthesis.

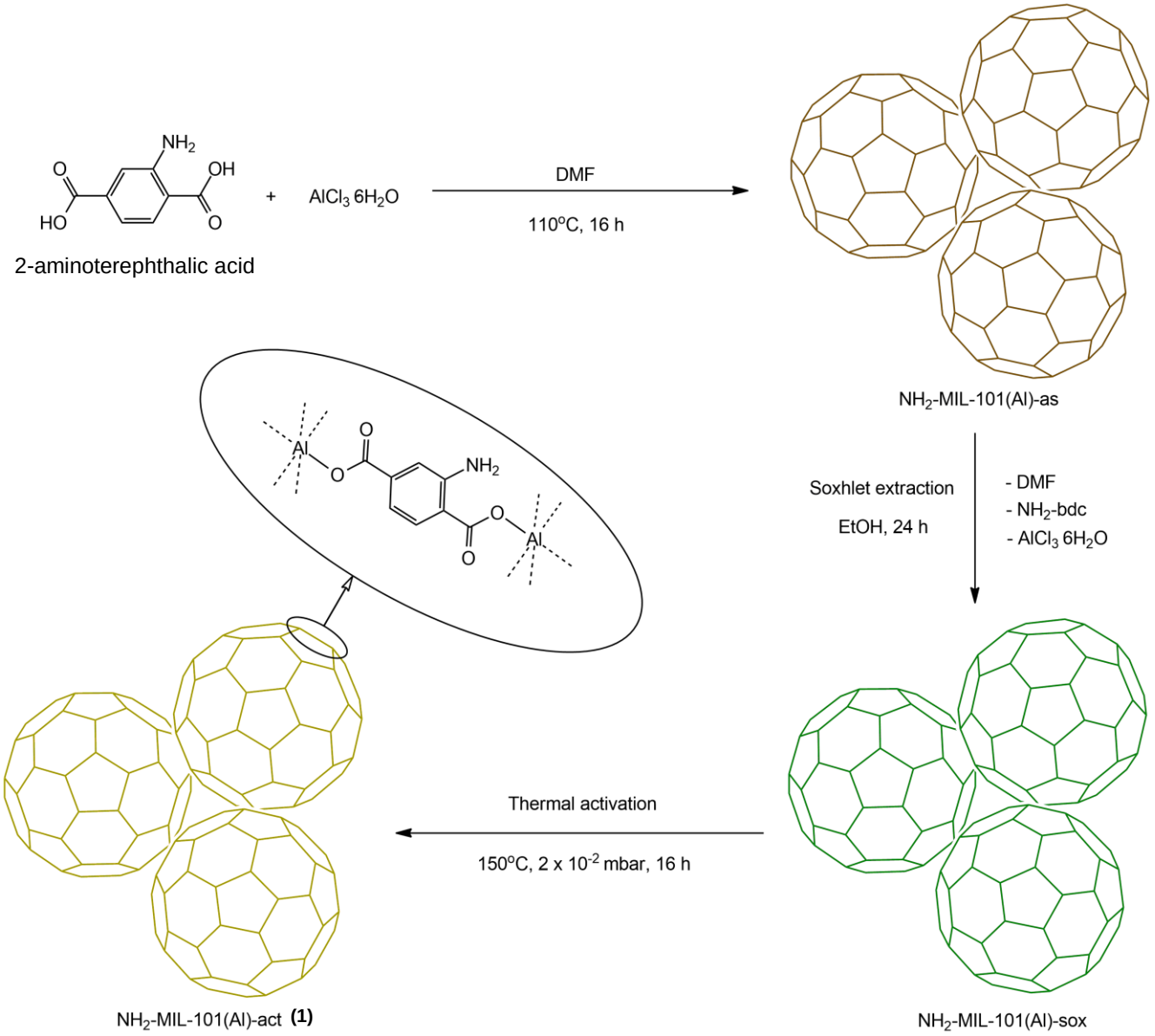

Figure 3. 1: Synthesis of NH_2-MIL-101(Al).*

In a typical NH_2-MIL-101(Al) synthesis, the organic linker, 2-aminoterephthalic acid, was first fully dissolved in anhydrous DMF and heated to ~100°C before adding $AlCl_3 \cdot 6H_2O$ **(Figure 3. 1, p 40)**. A yellow suspension formed shortly after the first addition of $AlCl_3 \cdot 6H_2O$, due to the *in-situ* formation of NH_2-MOF-235(Al), a critical step for proper crystal growth of NH_2-MIL-101(Al). $AlCl_3 \cdot 6H_2O$ was added in delayed portions to avoid excessive heat build-up, and the mixture rapidly stirred for another three hours to promote proper nucleation before crystal growth of NH_2-MIL-101(Al) commenced. The reaction was left under static conditions for ideal crystal growth and in the absence of light for 16 hours at 110°C. In order to avoid the formation of NH_2-MIL-53(Al) during the synthesis of NH_2-MIL-101(Al), strict anhydrous conditions were applied. Water in the mixture can cause the formed NH_2-MIL-235(Al) molecules to dissolute and grow into NH_2-MIL-53(Al).[2] Even a normal reflux setup was avoided, because DMF is hygroscopic and can attract water vapour.

* Product structure resembles a simplified structure of NH_2-MIL-101(Al)

During work-up, the MOF's pores are evacuated in a two-step process. The crude NH_2-MIL-101(Al) has large enough particles to be vacuum-filtered. To rinse the excess, unreacted $AlCl_3 \cdot 6H_2O$ and 2-aminoterephthalic acid, the MOF was filtered with wet DMF, before replacing the DMF with lower boiling ethanol. After drying in air, the as-synthesised MOF, NH_2-MIL-101(Al)-as, was soxhlet extracted with ethanol for 24 hours and dried at 70°C in air. Lastly, the MOF was activated under vacuum at 150°C overnight to give NH_2-MIL-101(Al)-act. It is critical for the temperature to be increased very slowly during this activation step to avoid rupture of the MOF's framework. To obtain best results, a stable vacuum should first be established before heating from room temperature to 150°C.

3.2.2 Characterisation

3.2.2.1 Fourier Transform Infrared Spectroscopy (FTIR)

The FTIR spectra in **(Figure 3. 2, p 42**) represent the products of all three synthesis steps: NH_2-MIL-101(Al) (as-synthesised [-as] **(Figure 3. 2, a, p 42)**, soxhlet-washed [-sox] **(Figure 3. 2, b, p 42)** and activated [-act] **(Figure 3. 2, c, p 42)**). N-H asymmetric and symmetric stretching frequencies of the amine groups are noticeable at 3440 cm^{-1} and 3357 cm^{-1} respectively **(Figure 3. 2, a-c, i, p 42)**. For NH_2-MIL-101(Al)-as, the free NH_2-bdc and DMF still present in the pores have overlapping C=O stretching frequencies at 1640 cm^{-1} **(Figure 3. 2, a, ii, p 42)**. The absence of this peak after the product was soxhlet extracted, shows that ethanol is a good solvent for the extraction of both NH_2-bdc and DMF. In previous studies the free NH_2-bdc was first extracted with DMF and then exchanged with methanol as the low-boiling solvent before activation.[3] NH_2-MIL-101(Al)-sox and NH_2-MIL-101(Al)-act have similar FTIR spectra, except for the barely visible alkane stretching frequencies of ethanol at 2893 cm^{-1} and 2823 cm^{-1} **(Figure 3. 2, b, iii, p 42)**. The hydrophilicity of NH_2-MIL-101(Al) is shown by the broad O-H stretching band between 2700 cm^{-1} and 3700 cm^{-1} from adsorbed water vapour. The bending frequency of water shows as a shoulder at 1600 cm^{-1} next to the carbonyl peaks **(Figure 3. 2, c, iv, p 42)**. The bidentate coordinated carbonyl bonds in the supertetrahedron cages gave the most prominent FTIR peaks due to the -COO asymmetric (1571 cm^{-1} and 1496 cm^{-1}) and –COO symmetric (1434 cm^{-1} and 1388 cm^{-1}) stretching frequencies from the bound NH_2-bdc linkers **(Figure 3. 2, c, v&vi, p 42)**.

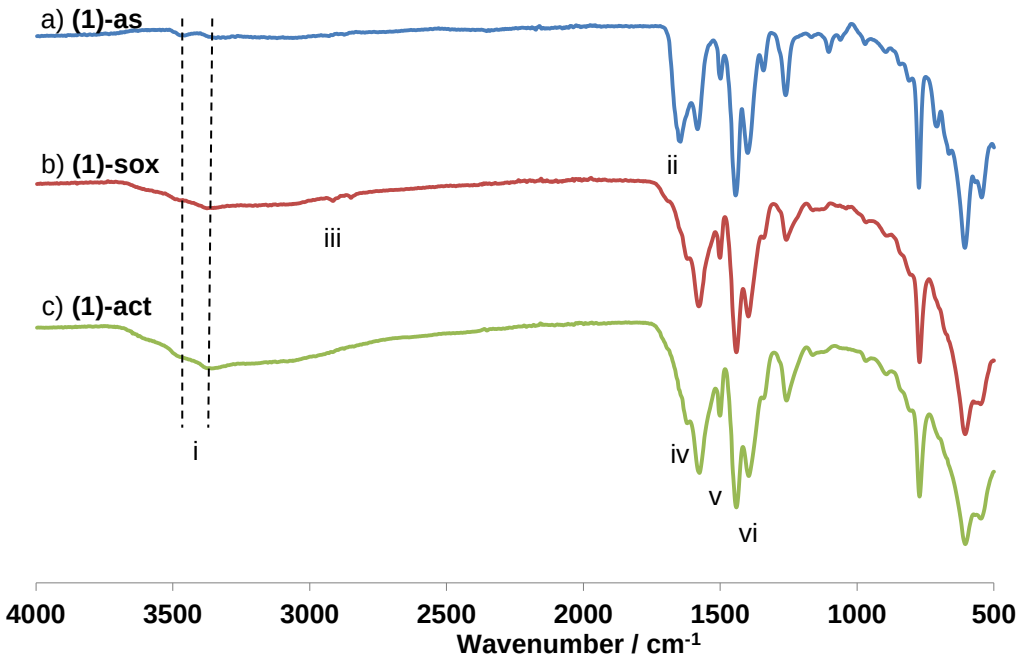

Figure 3. 2: FTIR spectra of NH_2-MIL-101(Al) **(1)**: a) the as-synthesised product through benchtop synthesis **(1-as)**; b) after soxhlet extraction **(1-sox)** and c) after final thermal activation under vacuum (2 x 10^{-2} mbar) **(1-act)**.

3.2.2.2 Thermal Gravimetric Analysis (TGA)

To complement the FTIR analyses of NH_2-MIL-101(Al), TGA was performed on the products of each phase during the synthesis of NH_2-MIL-101(Al). In **Figure 3. 3, a (p 43)**, the as-synthesised form of NH_2-MIL-101(Al) lost water between 50°C - 115°C (step 1a, 2.8% mass loss). Between 116°C and 372°C (step 2a), unreacted NH_2-bdc is removed from the framework together with DMF: 22% mass loss. The framework's collapse starts at 457°C (step 3a), with the NH_2-bdc linkers' decomposition leaving Al_2O_3 as residue. For both NH_2-MIL-101(Al)-sox **(Figure 3. 3, b, p 43)** and NH_2-MIL-101(Al)-act **(Figure 3. 3, c, p 43)** a mass loss of about 5% between 54°C and 130°C was observed (steps 1b and 1c). The water uptake was the highest after the final activation (step 1c) indicating that the cages of the MOF was fully cleansed. Step 2b is due to a small amount of DMF still present in the framework. For all three phases of synthesis, the main framework of NH_2-MIL-101(Al) started to decompose at 457°C (steps 3a, 3b and 2c).

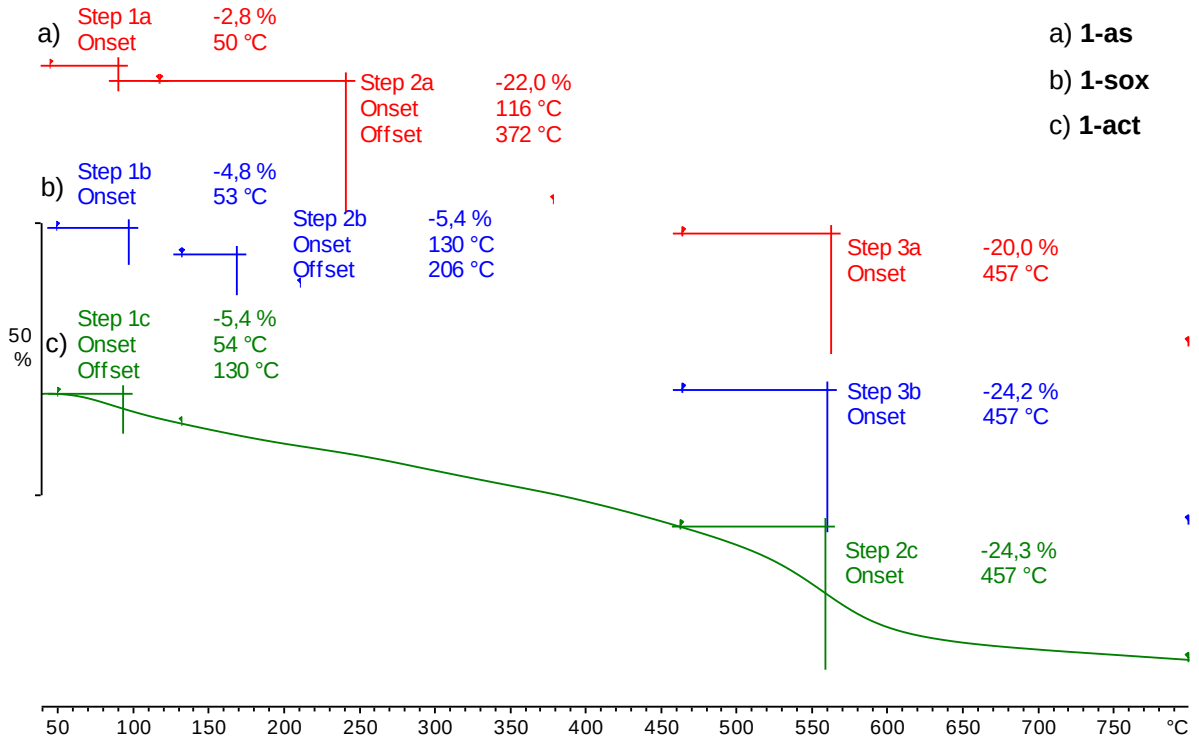

Figure 3. 3: TGA thermograms under N_2 of NH_2-MIL-101(Al) **(1)**: **a)** the as-synthesised product through benchtop synthesis **(1-as)**, **b)** after soxhlet extraction **(1-sox)** and **c)** after thermal activation under vacuum (2×10^{-2} mbar) **(1-act)**.

3.2.2.3 Surface Area and Porosity Analysis

The BET surface area analysis of NH_2-MIL-101(Al)-act, determined from its Type I N_2 isotherm at 77 K **(Figure 3. 4, p 44)**, was determined between a relative pressure (p/p^o) of 0.04 and 0.23 as 3192 ± 57 m^2g^{-1} as well as a maximum cumulative pore volume of 1.52 cm^3g^{-1} (at $p/p^o = 0.9$). These values are in good correlation with the BET surface area of 3099 m^2g^{-1} and a pore volume of 1.53 cm^3g^{-1}, found by Hartmann and Fischer.[1] The adsorption and desorption isotherms in **Figure 3. 4 (p 44)** display a step between 0.1 and 0.23 p/p^o, typical to MIL-101. This step indicates the start of N_2 filling of the larger cages of the MOF after the smaller cages. No hysteresis during desorption is an indication that the pores are free from other molecules and fully evacuated. The BET surface area obtained is larger than literature values[1] with a slightly smaller pore volume, proving that the evacuation method used in this study is superior to past practices. The measurement of the MOF's pore sizes and window sizes gave unreliable results due to insufficient theoretical models for data evaluation.

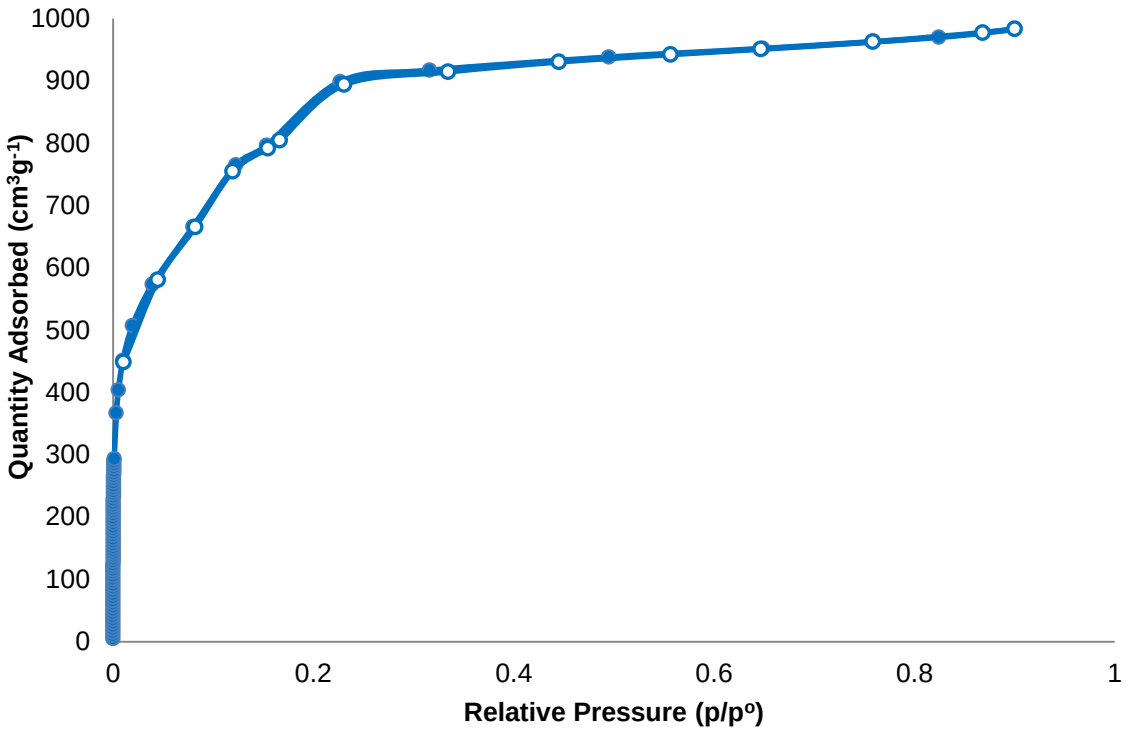

Figure 3. 4: N_2 adsorption (full dots) and desorption (empty circles) isotherms @ 77 K of NH_2-MIL-101(Al) **(1-act)**.

3.2.2.4 Powder X-ray Diffraction (PXRD)

For this study, low-angle PXRD analyses were only used for the identification of NH_2-MIL-101(Al) and its post-synthetically modified products. Most of the NH_2-MIL-101(Al) fingerprint is found below $2\theta = 10$ degrees **(Figure 3. 5, p 44,** compare to **Figure 2. 7, p 15)**. An instrumental air scattering slit is needed to obtain high resolution scans between $0.5 \leq 2\theta \leq 10$ without the use of SAXS.

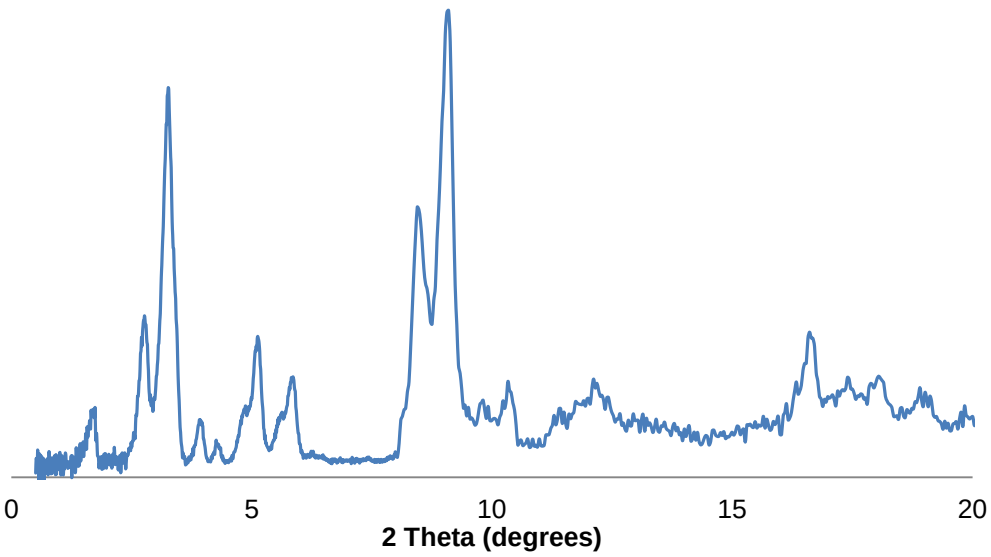

Figure 3. 5: PXRD spectrum of NH_2-MIL-101(Al) **(1-act)**.

3.3 Synthesis and Characterisation of Tetra-substituted Phthalocyanines

3.3.1 2(3),9(10),16(17),23(24)-Tetra-*tert*-butylphthalocyanine (2HPc^{t}Bu$_4$)

2HPc^{t}Bu$_4$ **(2)** was synthesised by two different cyclotetramerisation methods of the phthalonitrile: in a solvent (a) and in a melt (b). In the first method (a) the Pc was synthesised from 4-*tert*-butylphthalonitrile and lithium in 1-pentanol. After 20 hours at 115°C, the crude 2LiPc^{t}Bu$_4$ was demetallated with a weak acid (CH_3COOH). 2HPc^{t}Bu$_4$ was obtained in 17.6% yield, after work-up and purification. To improve on the yield, 2HPc^{t}Bu$_4$ was synthesised with the use of molten hydroquinone (b), which acts as a reducing agent and internal solvent so that the phthalocyanine can be formed without a metal precursor. The yield for this reaction was 29.3%, 60% more than with the lithium route **(Scheme 3. 1, a, p 45)**.

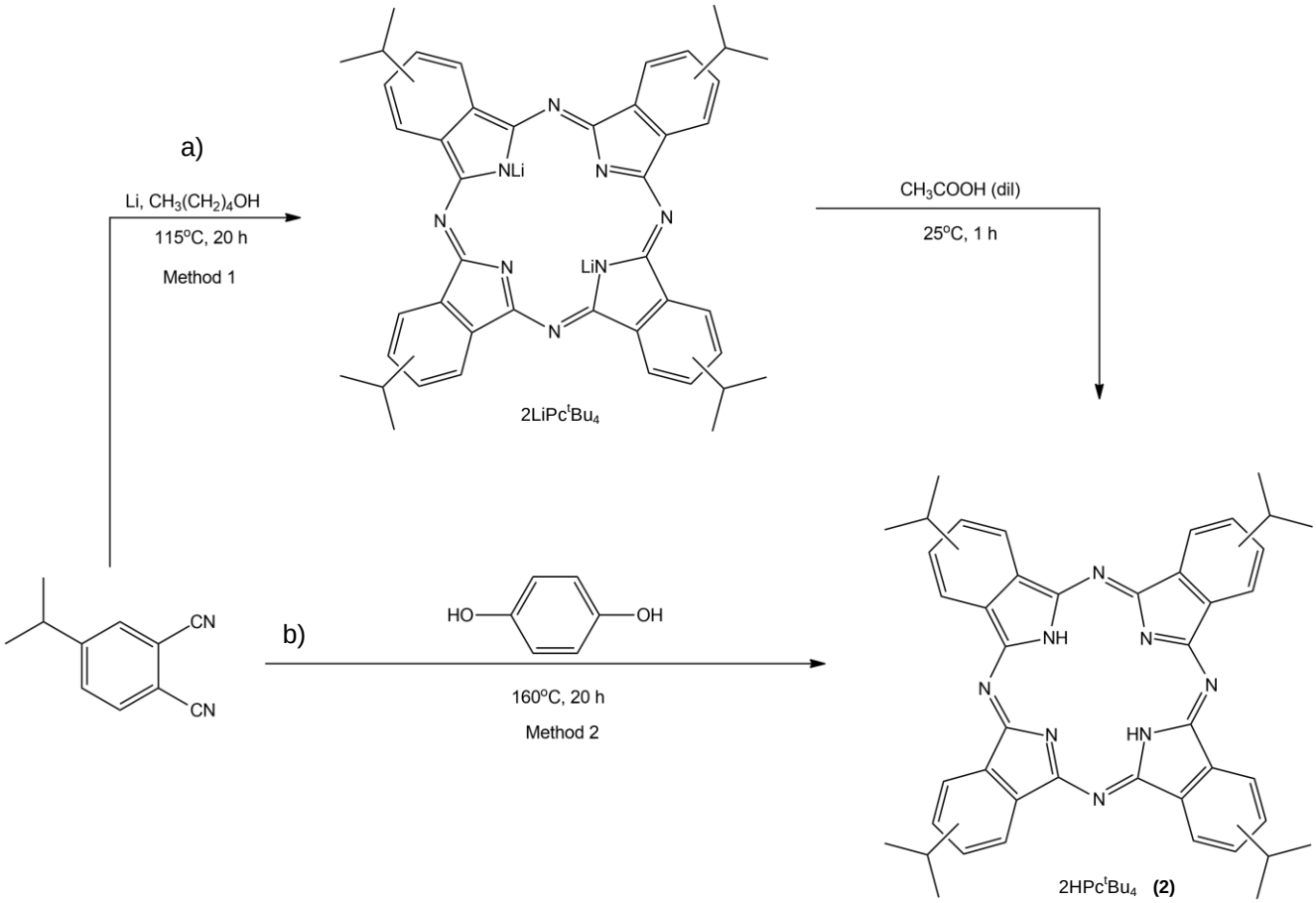

Scheme 3. 1: Synthesis of 2HPc^{t}Bu$_4$ **(2)** via a) Lithiation in 1-pentanol followed by demetallation with acetic acid or b) cyclotetramerisation in molten hydroquinone.

2HPc^{t}Bu$_4$ was characterised with ^{1}H NMR, UV-Vis-spectroscopy, FTIR and MALDI-TOF mass spectrometry.

3.3.1.1 Proton Nuclear Magnetic Resonance Spectroscopy (^{1}H NMR)

The ^{1}H NMR spectrum of $H_2Pc^tBu_4$ synthesised via the hydroquinone route **(Scheme 3. 1, b, p 45)** was identical to the spectrum in **Figure 3. 6 (p 46)** and can be found in Appendix A-3. Since phthalocyanines tend to aggregate in solution, leading to poor solubility, the sample was diluted and the analysis extended to 1.5 hours. In **Figure 3. 6 (p 46)** it is shown that both synthesis pathways produced similar products. The eight protons, **H_a,** on the non-peripheral positions of the phthalocyanine, are strongly shielded by the 18-π conjugation of the phthalocyanine and are therefore shifted furthest downfield. The four protons, **H_b**, on the peripheral positions of the phthalocyanine, are deshielded by the tetra-*tert*-butyl groups and are found upfield at 8.2 ppm. The four peripheral *tert*-butyl substituents give a strong singlet at 1.85 ppm. The four singlets at ~ -1 ppm, **H_d**, represent the four different positions in which the imino protons in the cavity of the Pc's π-π ring system can resonate. These two protons experience the least amount of shielding from the electron density in the phthalocyanine ring system.

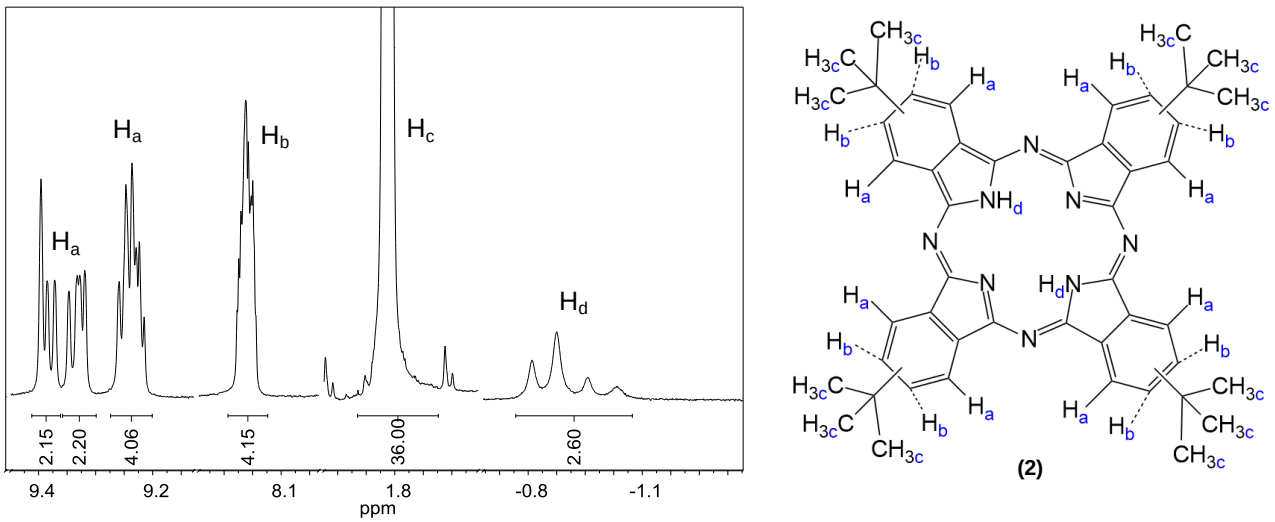

Figure 3. 6: ^{1}H NMR spectrum of $2HPc^tBu_4$ **(2)** synthesised via the lithium method.

3.3.1.2 UV-Vis Spectroscopy

$2HPc^tBu_4$ is soluble in most common solvents and shows a dark blue colour in solution, since its lowest absorbance is in the blue-light region between 450 nm – 495 nm **(Figure 3. 7, p 47)**. The UV-Vis spectrum of $2HPc^tBu_4$ has a split Q-band (Q_x = 660 nm and Q_y = 690 nm), typical for a metal-free Pc. The Soret band (B-band) is found at 410 nm.

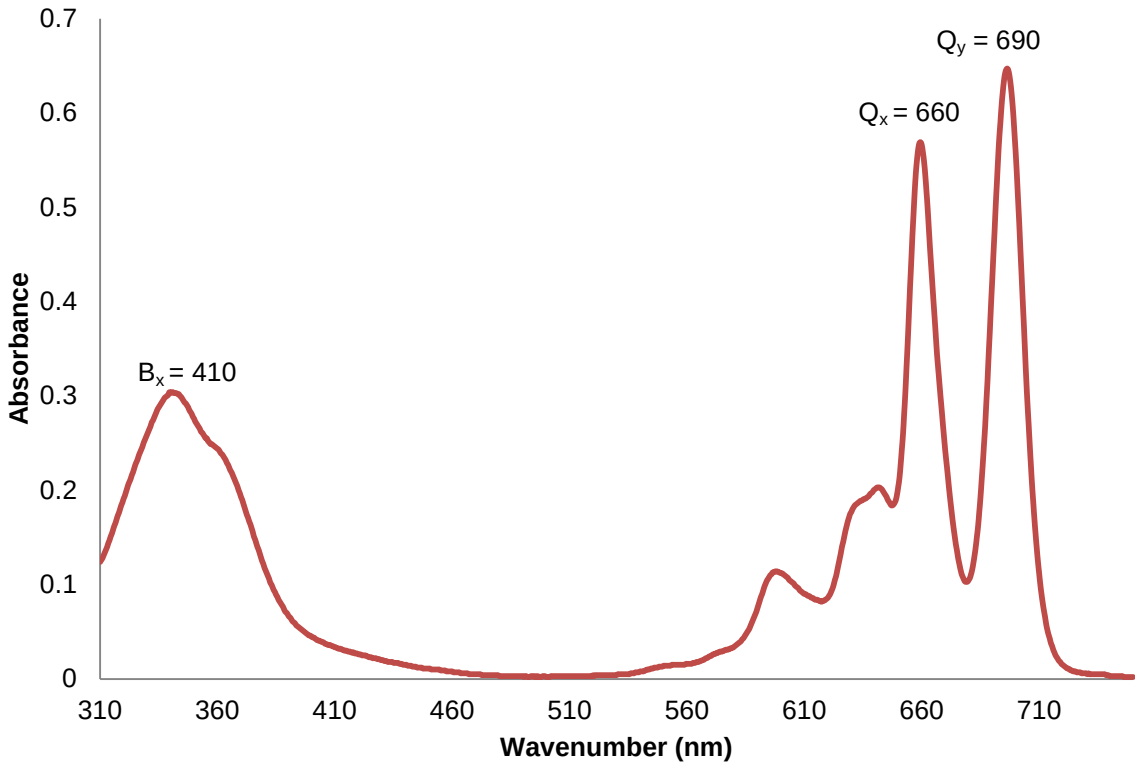

Figure 3. 7: UV-Vis spectrum of 2HPc^{t}Bu$_4$ **(2)**.

3.3.1.3 FTIR

The FTIR spectrum of 2HPc^{t}Bu$_4$ **(Figure 3. 8, p 47)** clearly shows the C-H$_3$ stretching frequency of the peripherally bound, *tert*-butyl groups at 2900 cm^{-1}. In the fingerprint area, strong C-N vibration frequencies from the aromatic ring structure of the phthalocynanine are observed **(Figure 3. 8, ii and iii, p 47)**.

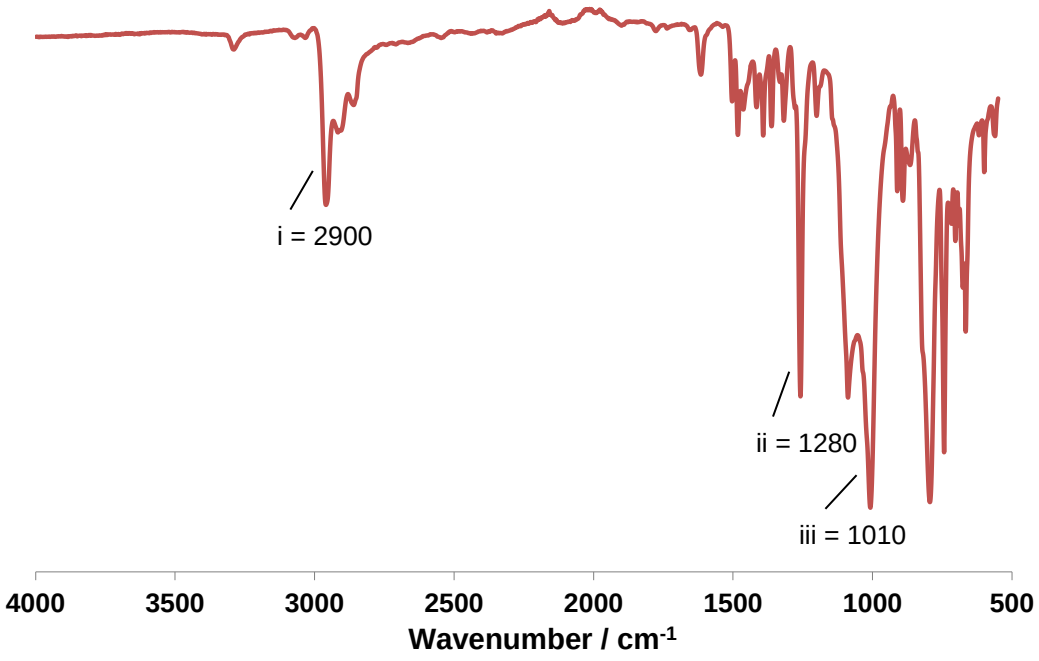

Figure 3. 8: FTIR spectra of 2HPc^{t}Bu$_4$ **(2)**

3.3.2 Metalation of 2(3),9(10),16(17),23(24)-Tetra-*tert*-butylphthalocyanine with Zn^{2+} and Ni^{2+}

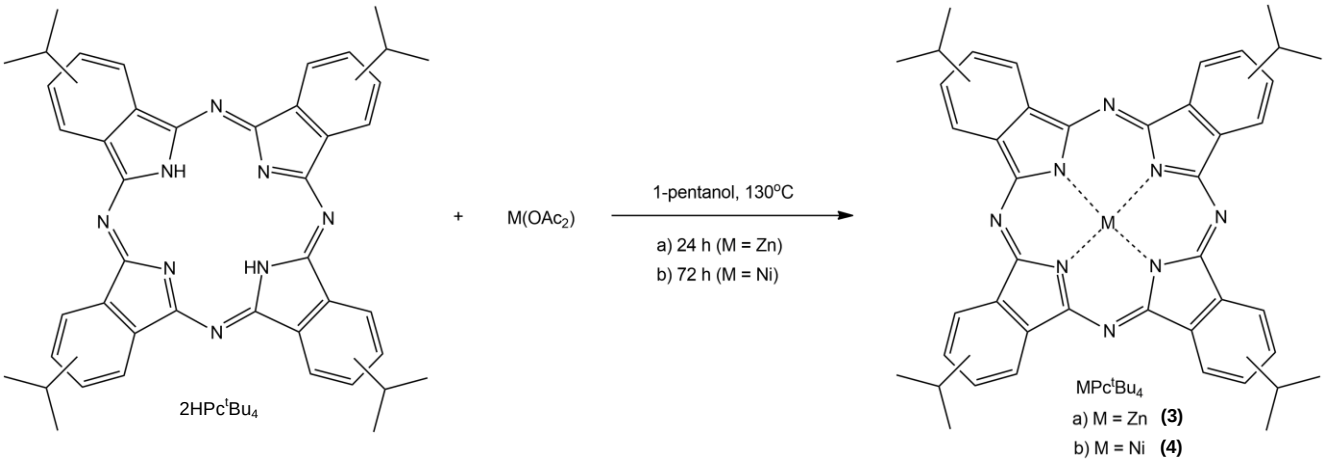

Scheme 3. 2: Synthesis of a) ZnPc^{t}Bu$_4$ **(3)** and b) NiPc^{t}Bu$_4$ **(4)** from 2HPc^{t}Bu$_4$ **(2)**.

ZnPc^{t}Bu$_4$ **(3)** and NiPc^{t}Bu$_4$ **(4)** were synthesised through the complexation of metal-free 2HPc^{t}Bu$_4$ with zinc acetate and nickel acetate respectively **Scheme 3. 2 (p 48)**. The metal-free Pc was refluxed with the respective metal salt in 1-pentanol. The work-up started by adding methanol to precipitate the crude products before it was filtered, washed with methanol and recrystallised with a THF/MeOH mixture. Purification by column chromatography was avoided due to the danger of decomposition. Full complexation was achieved after 24 hours for ZnPc^{t}Bu$_4$ and after 72 hours for NiPc^{t}Bu$_4$.

3.3.2.1 ^{1}H-NMR

A clear ^{1}H-NMR spectrum was obtained for ZnPc^{t}Bu$_4$, with the non-peripheral protons resonating at 8.8 ppm and the peripheral protons at 8.0 ppm **(Figure 3. 9, a, p 49)**. The *tert*-butyl protons' signal is shifted upfield to 1.7 ppm (from 1.8 ppm in 2HPc^{t}Bu$_4$), but resonates too close to water at 1.6 ppm to be integrated properly. NiPc^{t}Bu$_4$ was less soluble, resulting in a poorly resolved ^{1}H-NMR spectrum **(Figure 3. 9, b, p 49)**. The peaks of the non-peripheral protons (H_a) were shifted downfield by 0.3 ppm and the peripheral protons (H_b) with 0.1 ppm, in comparison with those of ZnPc^{t}Bu$_4$. A clear influence by the electronegativities of the central metals inside the cavity of the MPcs are illustrated by these shifts. When comparing the signals of the non-peripheral protons (H_a) of both MPc^{t}Bu$_4$ (M = Zn/Ni) with those of 2HPc^{t}Bu$_4$ **(Figure 3. 6, p 46)**, a slight upfield shift is found, relating to the electronegativity (2H > Ni > Zn ≡ 2.1 > 1.9 > 1.6) with Zn resulting in the greatest shift.

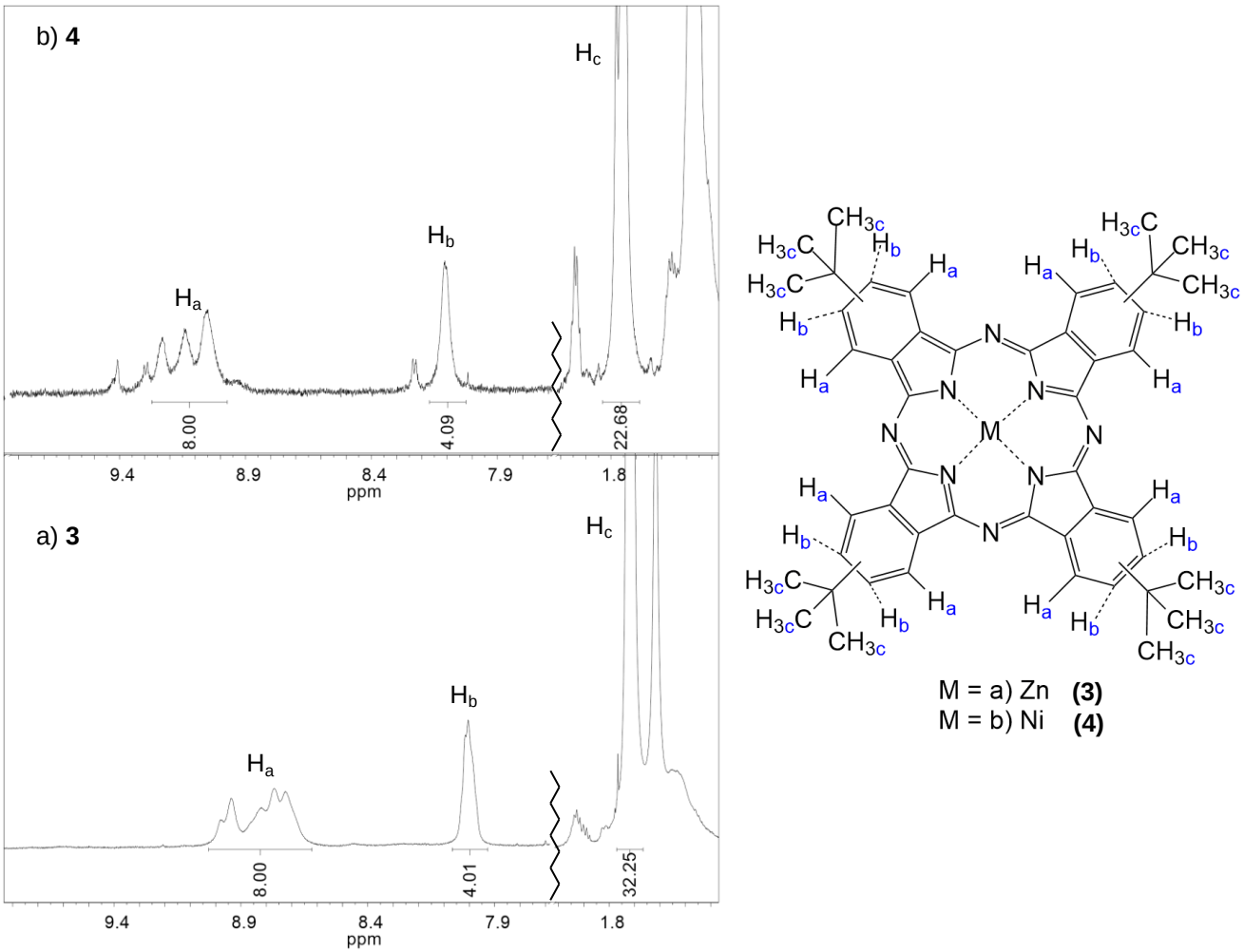

Figure 3. 9: ^{1}H NMR spectra of a) ZnPc^{t}Bu$_4$ **(3)** and b) NiPc^{t}Bu$_4$ **(4)**

3.3.2.2 FTIR

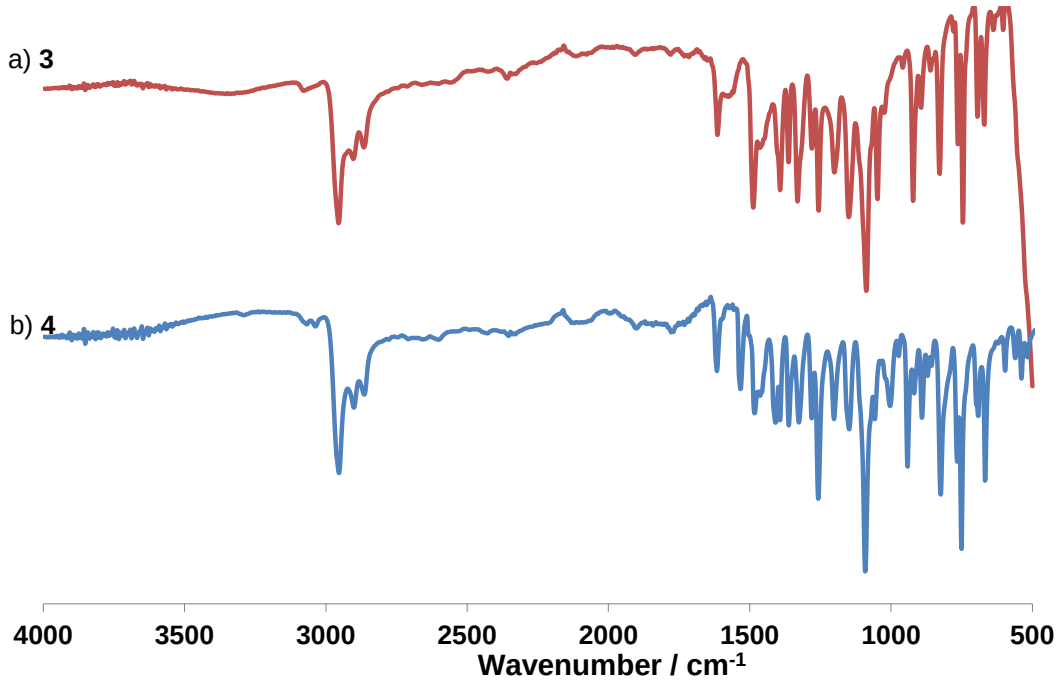

Figure 3. 10: FTIR spectra a) ZnPc^{t}Bu$_4$ (red) **(3)** and b) NiPc^{t}Bu$_4$ (blue) **(4)**.

The FTIR spectra of $ZnPc^tBu_4$ **(Figure 3. 10, a, p 49)** and $NiPc^tBu_4$ **(Figure 3. 10, b, p 49)** are both similar to that of $2HPc^tBu_4$ **(Figure 3. 8, p 47)** with a prominent C-H_3 *tert*-butyl stretching frequency at 2900 cm^{-1}.

3.3.2.3 TGA

Both $ZnPc^tBu_4$ and $NiPc^tBu_4$ have melting points above 250°C, thus thermal gravimetric analyses were used to establish that both $ZnPc^tBu_4$ and $NiPc^tBu_4$ start to decompose after 400°C (step 2a and 1b respectively) **(Figure 3. 11, p 50)**. $ZnPc^tBu_4$ has a small mass loss of 1.4% after 104°C (step 1a) due to water being trapped in the aggregated MPc **(Figure 3. 11, a, p 50)**. This was not observed for $NiPc^tBu_4$ even though both products were activated at 70°C under vacuum.

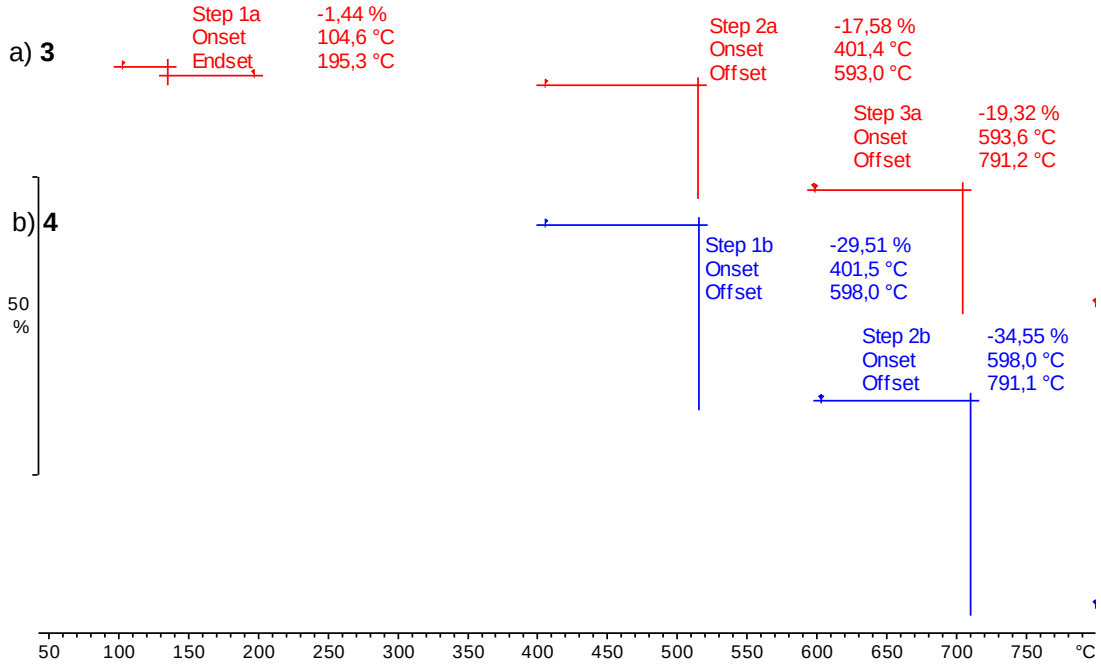

Figure 3. 11: TGA thermograms under N_2 of a) $ZnPc^tBu_4$ (red) **(3)** and b) $NiPc^tBu_4$ (blue) **(4)**.

3.3.2.4 UV-Vis

Both $ZnPc^tBu_4$ and $NiPc^tBu_4$ have intense blue solutions even when minute quantities were dissolved in HPLC grade THF. In this section, the effect of aggregation in these MPc solutions was investigated in seven solutions each with concentrations ranging from 250 nM to 19 µM. Samples were prepared and immediately analysed to eliminate photo-degradation. UV-Vis spectra of both $ZnPc^tBu_4$ **(Figure 3. 12, p 51)** and $NiPc^tBu_4$ **(Figure 3. 13, p 51)** show an intense Q-band at Q_x = 671 nm and Q_x = 667 nm respectively giving an indication that metallation of the empty Pc cavity was successful. The spectra are accompanied by an insert of absorbance versus concentration to show the concentration ranges where these compounds still adhere to the Beer-Lambert Law: $\varepsilon = AC\ell$, where ε is the extinction coefficient ($dm^3mol^{-1}cm^{-1}$), A the absorbance, C the concentration and ℓ the path length. A linear relation with a good trendline fit were found for both $ZnPc^tBu_4$ (C < 16265 nM) and $NiPc^tBu_4$

(C < 19229 nM), meaning that aggregation does not occur at these concentrations. This high aggregation threshold is caused by the bulky *tert*-butyl groups, preventing the formation of stacked structures. Aggregation limits the activity of MPcs in applications such as catalysis.

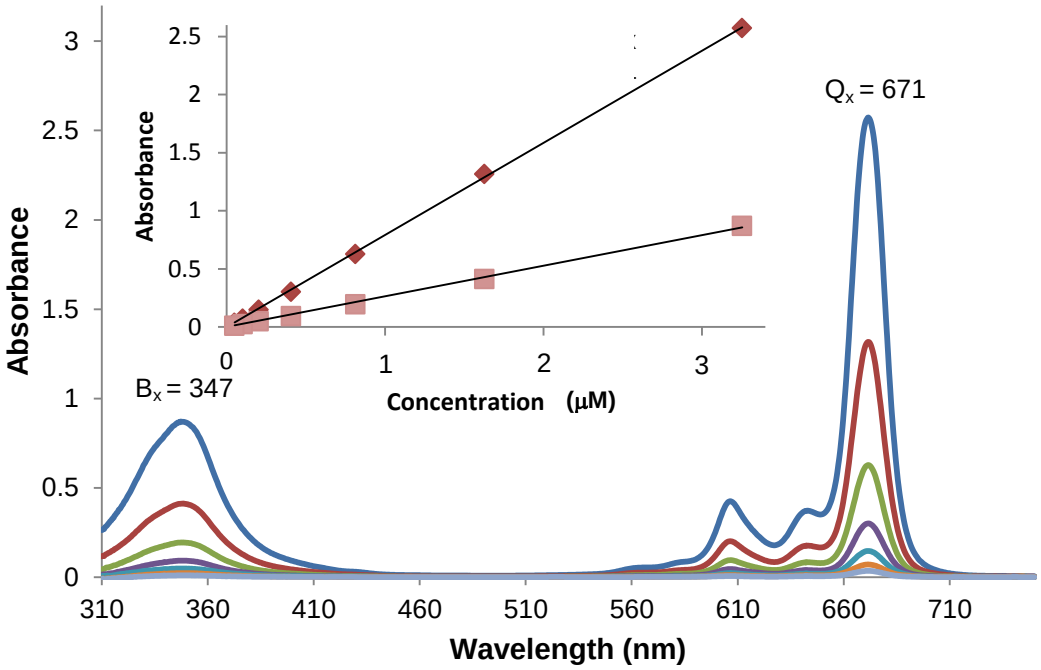

Figure 3. 12: UV-Vis spectrum of ZnPc^{t}Bu$_4$ **(3)**. Insert: Absorbance vs. Concentration for both the Q-band and the B-band.

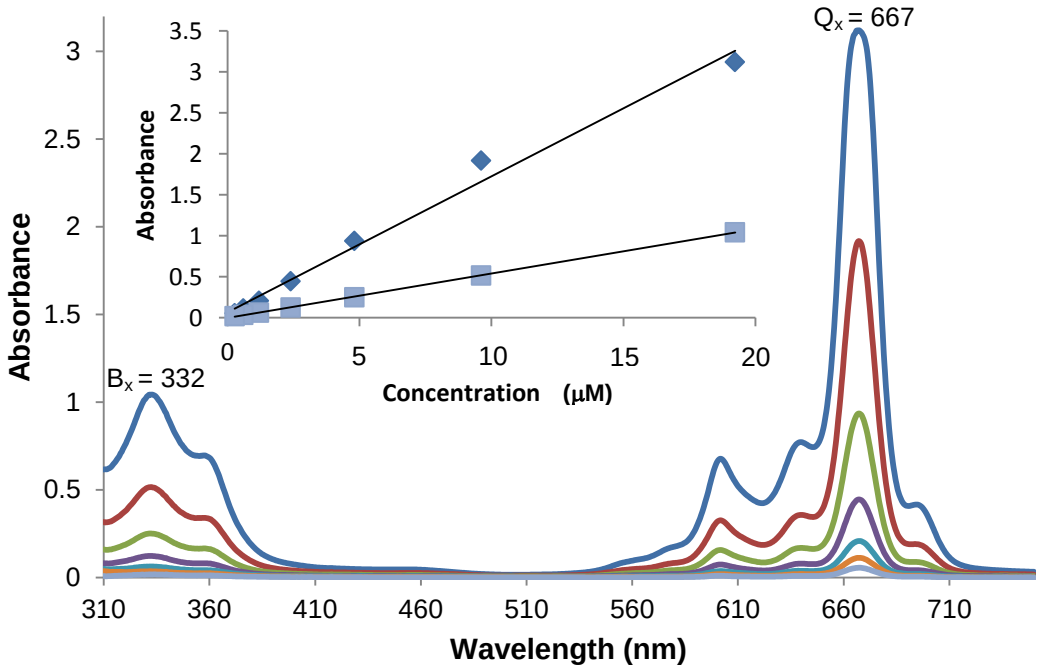

Figure 3. 13: UV-Vis spectrum of NiPc^{t}Bu$_4$ **(4)**. Insert: Absorbance vs. Concentration for both the Q-band and the B-band.

Both the B-band and the Q-band of $NiPc^tBu_4$ are blue-shifted with respect to the same peaks of $ZnPc^tBu_4$. The molar extinction coefficients for both $ZnPc^tBu_4$ and $NiPc^tBu_4$ were similar (ε = 158540 $M^{-1}cm^{-1}$ at 671 nm for $ZnPc^tBu_4$ and ε = 171070 $M^{-1}cm^{-1}$ at 667 nm for $NiPc^tBu_4$). All relevant extinction coefficients are found in **Table 3. 1 (p 60)**.

3.3.3 2(3),9(10),16(17),23(24)-tetracarboxyphthalocyanatozinc/ iron(III)-chloride/ cobalt/ nickel [$ZnPc(COOH)_4$, $FeClPc(COOH)_4$, $CoPc(COOH)_4$ and $NiPc(COOH)_4$]

Tetracarboxy MPcs were synthesised by combining the methods of Szuneritse *et al.* and Zhang *et al.*,[4,5] in a two-step reaction of which the first was cyclotetramerisation of the specific metal and trimellitic anhydride with ammonium chloride and ammonium molybdate in molten urea **(Scheme 3. 3, p 53)**. After removal of the unreacted material, the crude tetra-analido-metallophthalocyanine was directly hydrolysed with aqueous potassium hydroxide to obtain the tetracarboxymetallophthalocyanines. Since the cyclotetramerisation of the MPcs occur in a rather viscious molten urea and form a solid rock-hard product mixture, continuous stirring was done manually and not magnetically. Acetate metal salts **(as in Section 3.3.1, p 45)**, are preferred over chlorides, since chlorides are hygroscopic and failed to give the desired product. When acetates were used, the reaction mixture stayed dry. The second step (hydrolysis) is key to optimise yield. The intermediate MPcs are unstable when treated with a base such as potassium or sodium hydroxide. Although Zhang and co-workers,[5] suggested that the MPc's ring formation occurs quite fast (3.5 hours) and that a lengthy hydrolysis should occur afterwards (10 hours), the reaction time in this study had to be extended to achieve ring formation. MPcs in solution are prone to photo-degradation. Thus, the hydrolysis of the tetra-analidometallophthalocyanine intermediate was shortened to five hours. Mass spectrometry of $ZnPc(COOH)_4$ gave the theoretical m/z value, 752.4, while m/z for $FeClPc(COOH)_4$ was 783.3 (M^{+4}), due to its very low solubility and resulted in signals near the detection limit of the instrument. The m/z values of $CoPc(COOH)_4$ (745.2, theoretical m/z = 747.2) and $NiPc(COOH)_4$ (743.2, theoretical m/z = 746.2) indicate that only 50% and 25% of the analido groups were respectively hydrolysed to carboxyl groups after five hours. When the hydrolysis of the tetra-analido-metallophthalocyanine intermediates were prolonged for longer than five hours, the MPcs decomposed almost fully resulting in a yellow reaction solution.

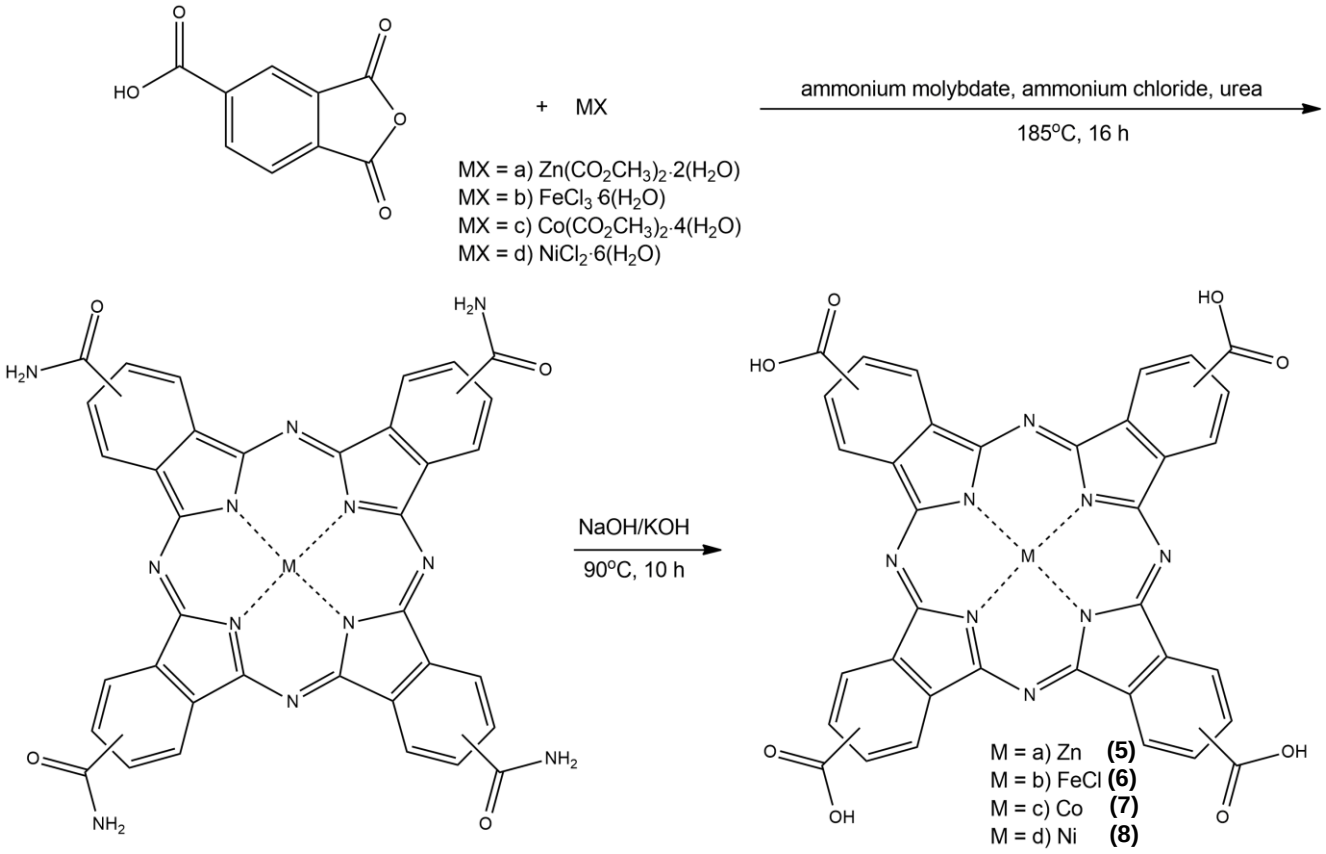

Scheme 3. 3: Synthesis of a) $ZnPc(COOH)_4$ **(5)**, b) $FeClPc(COOH)_4$ **(6)**, c) $CoPc(COOH)_4$ **(7)** and $NiPc(COOH)_4$ **(8)**.

3.3.3.1 FTIR

The FTIR spectra of $ZnPc(COOH)_4$, $FeClPc(COOH)_4$, $CoPc(COOH)_4$ and $NiPc(COOH)_4$ **(Figure 3. 14, p 54)** all show a clear band between 2300 cm^{-1} and 3600 cm^{-1} **(i)** attributed to the O-H stretching frequency of the carboxylic acid groups, with the C=O stretching frequencies of these groups at 1705 cm^{-1} **(ii)**.

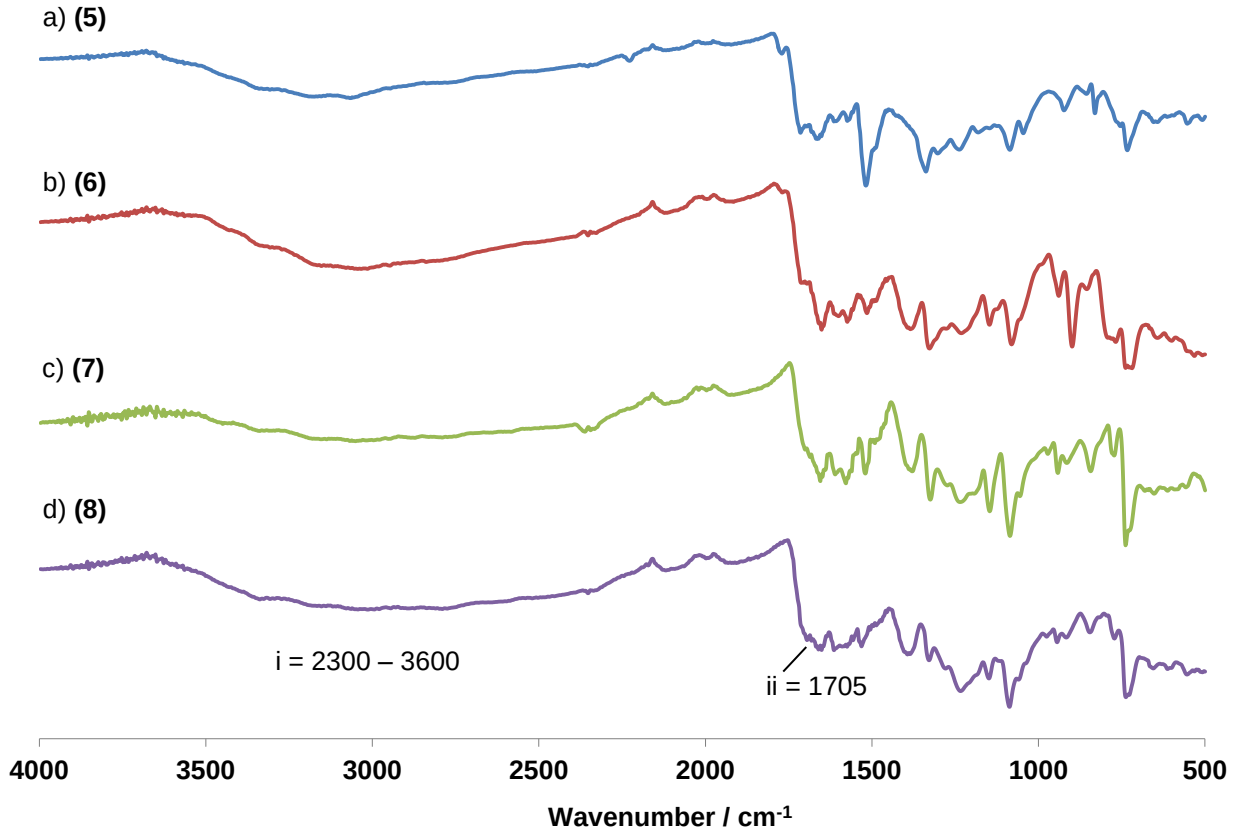

Figure 3. 14: FTIR spectra of a) $ZnPc(COOH)_4$ (blue) **(5)**, b) $FeClPc(COOH)_4$ (red) **(6)**, c) $CoPc(COOH)_4$ (green) **(7)** and d) $NiPc(COOH)_4$ (purple) **(8)**.

3.3.3.2 TGA

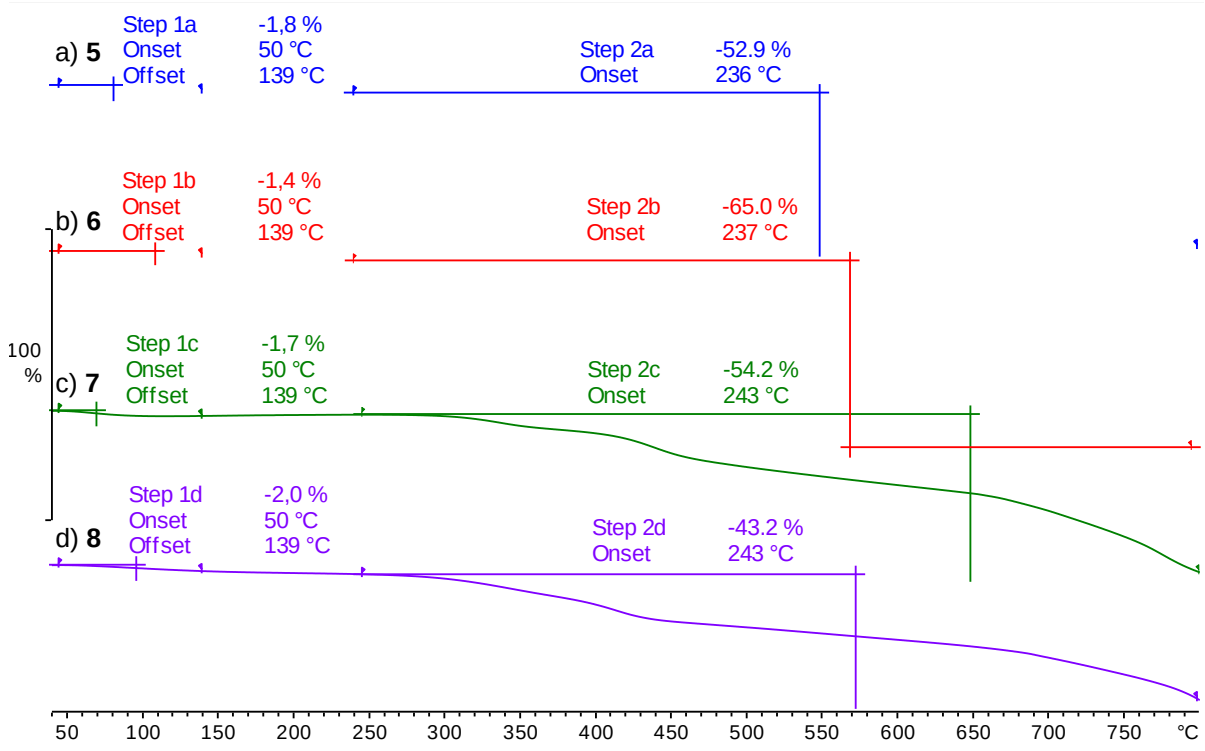

Figure 3. 15: TGA thermograms under N_2 of a) $ZnPc(COOH)_4$ (blue) **(5)**, b) $FeClPc(COOH)_4$ (red) **(6)**, c) $CoPc(COOH)_4$ (green) **(7)** and d) $NiPc(COOH)_4$ (purple) **(8)**.

The TGA thermograms of $ZnPc(COOH)_4$, $FeClPc(COOH)_4$, $CoPc(COOH)_4$ and $NiPc(COOH)_4$ **(Figure 3. 15, p 54)** have similar mass loss steps: steps 1a-d (50°C - 139°C) represent the mass loss of water trapped during aggregation of the MPc molecules. The mass losses of steps 2a-d are due to the decomposition of the main MPc ring structures.

3.3.3.3 UV-Vis

All four carboxylated MPcs were only soluble in limited amounts in the polar aprotic solvents, DMSO and DMF. The cobalt Pc was the easiest to dissolve, but for the Zn, Fe and Ni Pcs, solutions had to be sonicated for at least five minutes depending on the concentration. To investigate the aggregation behaviour of these MPcs, concentrations from as low as 39 nM up to 180 μM in DMSO were analysed (See Appendix A-7 for photos of all MPcs in equimolar solutions).

The UV-Vis spectrum of $ZnPc(COOH)_4$ **(Figure 3. 16, a, p 56)** shows a Q-band maximum at 687 nm and B-band maximum at 349 nm. The Absorbance vs. Concentration graphs **(Figure 3. 16, c&d, p 56)** for $ZnPc(COOH)_4$ are linear in the concentration range between 142 nM and 75 μM, proof that the compound does not aggregate, since it adheres to the Beer-Lambert Law at these concentrations. Only a slight tendency for aggregation was found at the highest concentration (75 μM).

The UV-Vis spectrum of $FeClPc(COOH)_4$ **(Figure 3. 17, a, p 57)** has a Q-band maximum at 664 nm and the B-band maximum at 340 nm. In the concentration range studied, between 151 nM and 60 μM, no clear indication for aggregation was found.

The UV-Vis spectrum of $CoPc(COOH)_4$ **(Figure 3. 18, a, p 58)** shows similar absorption wavelengths compared to $FeClPc(COOH)_4$ with a Q-band maximum at 667 nm and a B-band maximum at 334 nm. In the concentration range between 39 nM and 18 μM, no clear indication for aggregation was found.

The UV-Vis spectrum of $NiPc(COOH)_4$ **(Figure 3. 19, p 59)** displays a unique double Q-band with maxima at 681 nm which dominates the low concentrations and 616 nm dominating at high concentrations. $NiPc(COOH)_4$ have the highest tendency for aggregation starting between 5 μM and 10 μM **(Figure 3. 19, c, p 59)** as seen by the difference in the slopes between low (main graph) and high concentrations (inserted graph).

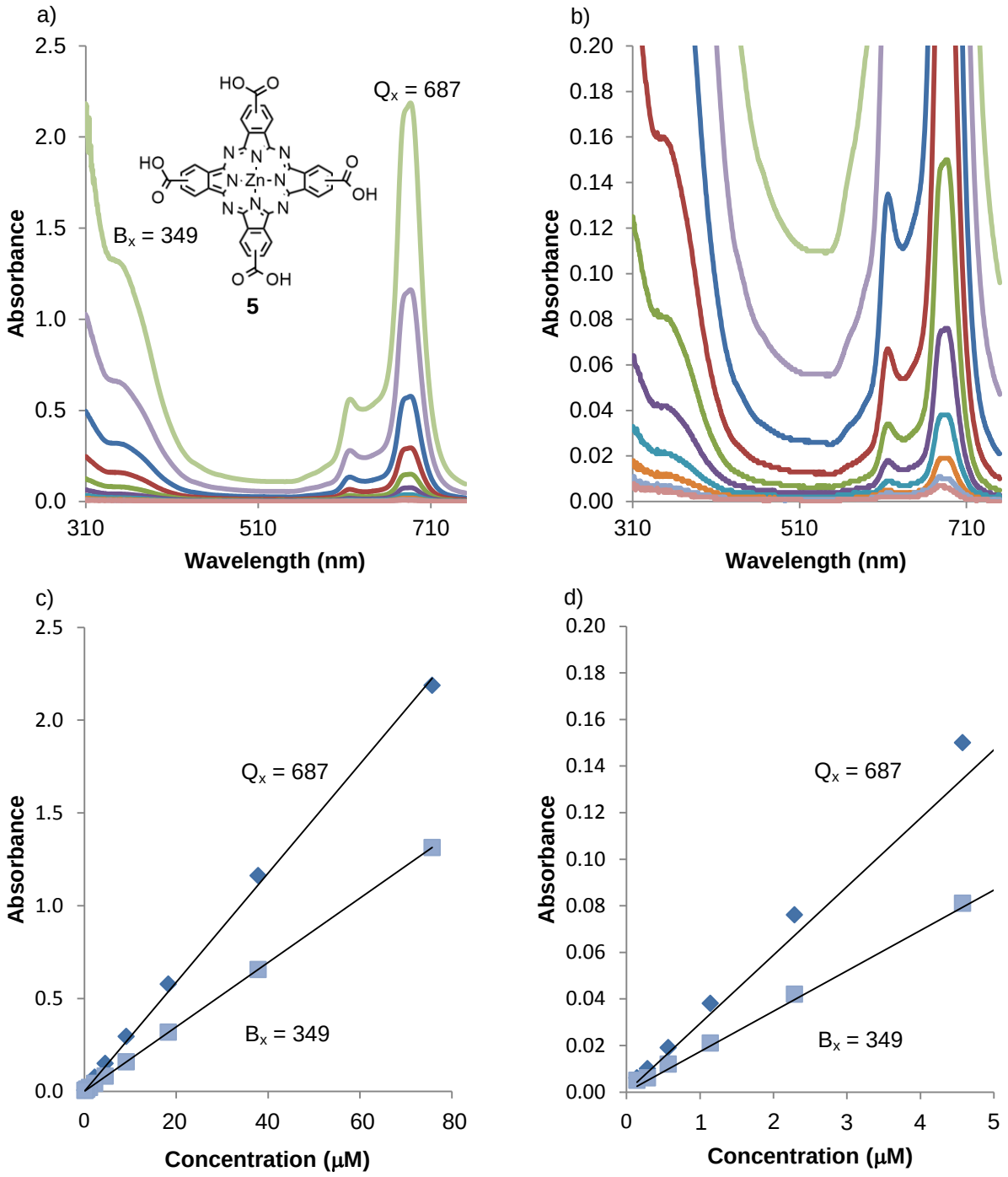

Figure 3. 16: UV-Vis spectrum of a) $ZnPc(COOH)_4$ **(5)** and b) at an absorbance < 0.2 together with c) the Absorbance vs. Concentration plot for $ZnPc(COOH)_4$ **(5)** of both the Q-band and the B-band and d) its enlarged portion at absorbance < 0.2.

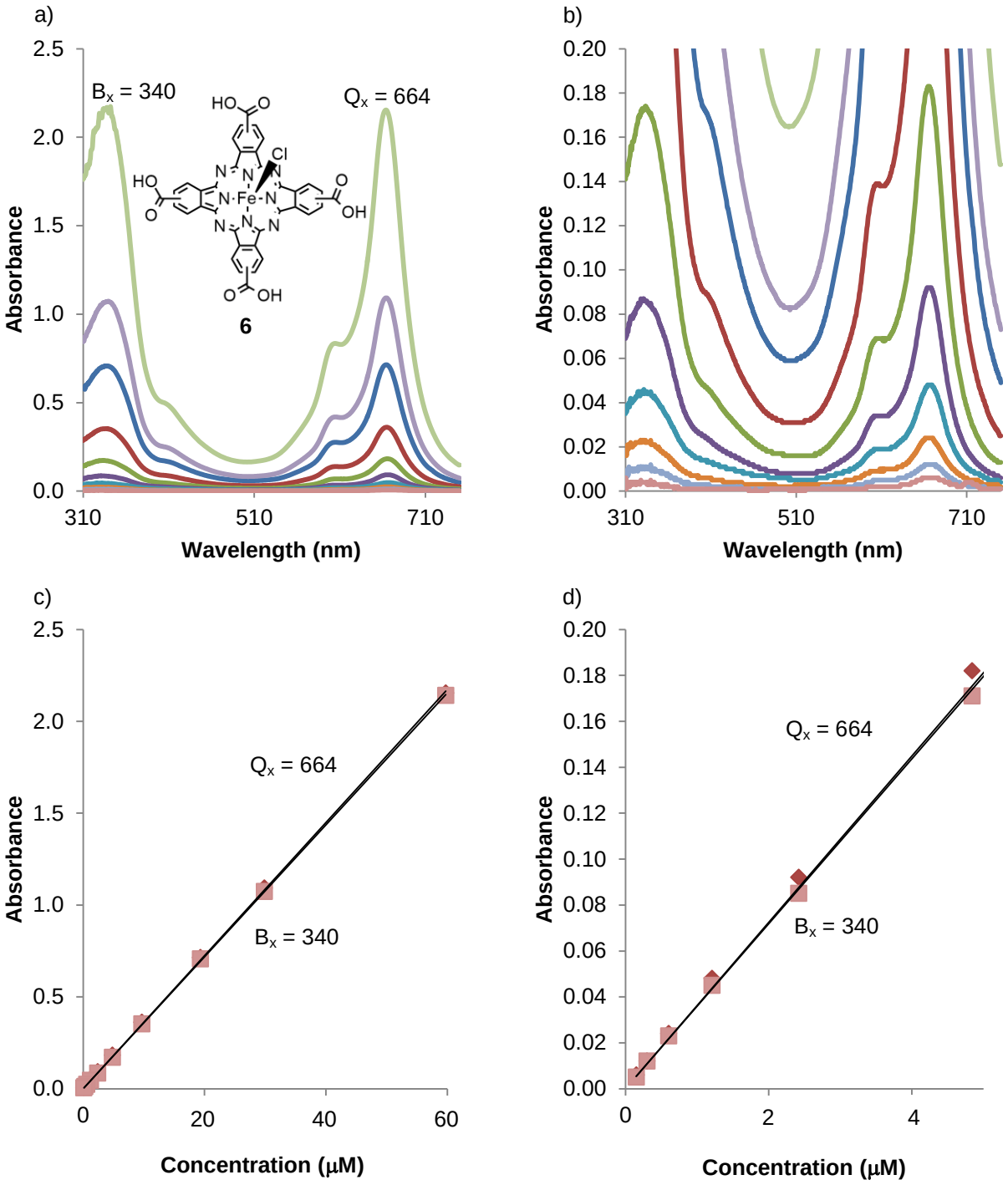

Figure 3. 17: UV-Vis spectrum of a) $FeClPc(COOH)_4$ **(6)** and b) at an absorbance < 0.2 together with c) the Absorbance vs. Concentration plot for $FeClPc(COOH)_4$ **(6)** of both the Q-band and the B-band and d) its enlarged portion at absorbance < 0.2.

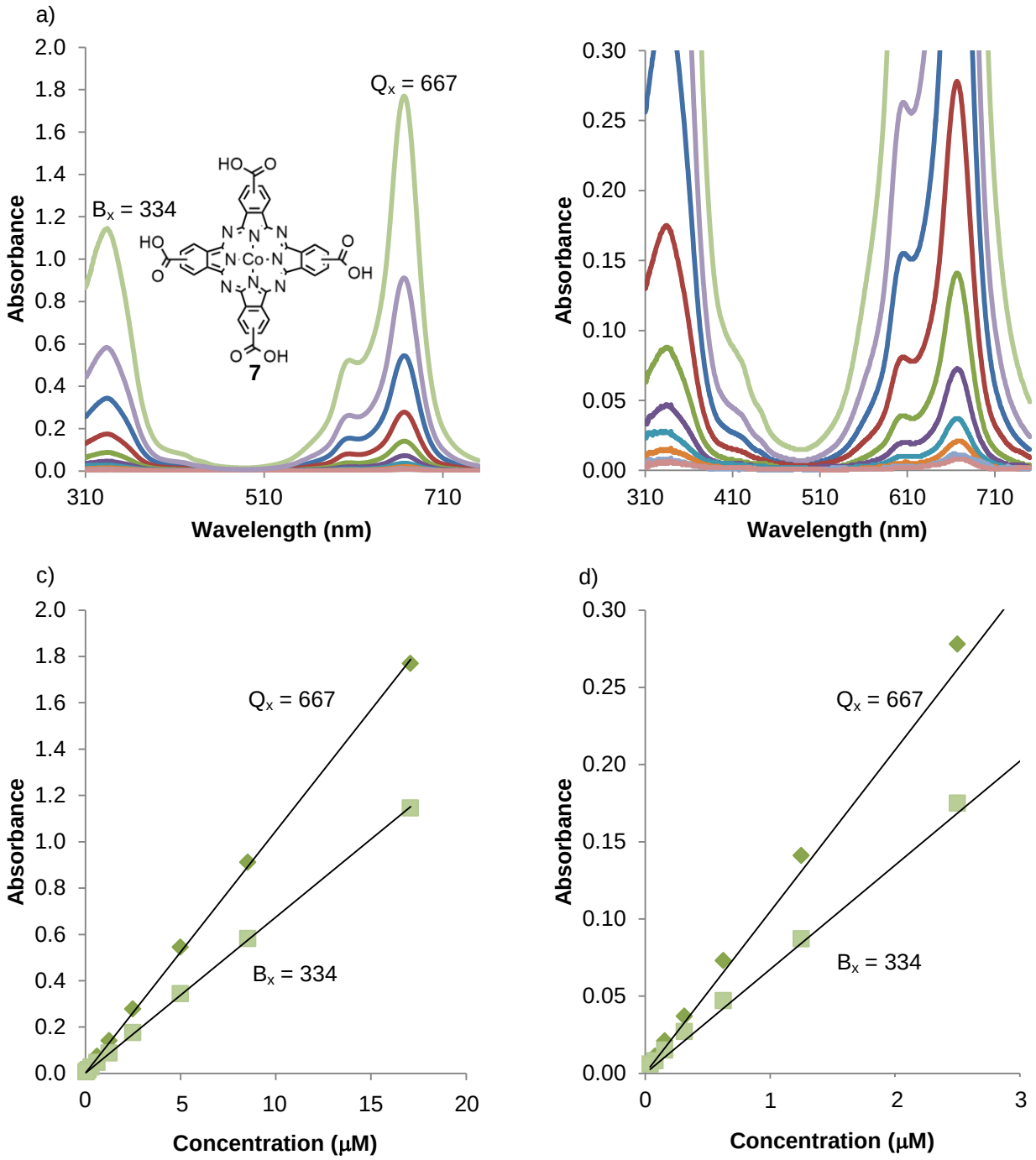

Figure 3. 18: UV-Vis spectra of a) $CoPc(COOH)_4$ **(7)** and b) at an absorbance < 0.2 together with c) the Absorbance vs. Concentration plot for $CoPc(COOH)_4$ **(7)** of both the Q-band and the B-band and d) its enlarged portion at absorbance < 0.3.

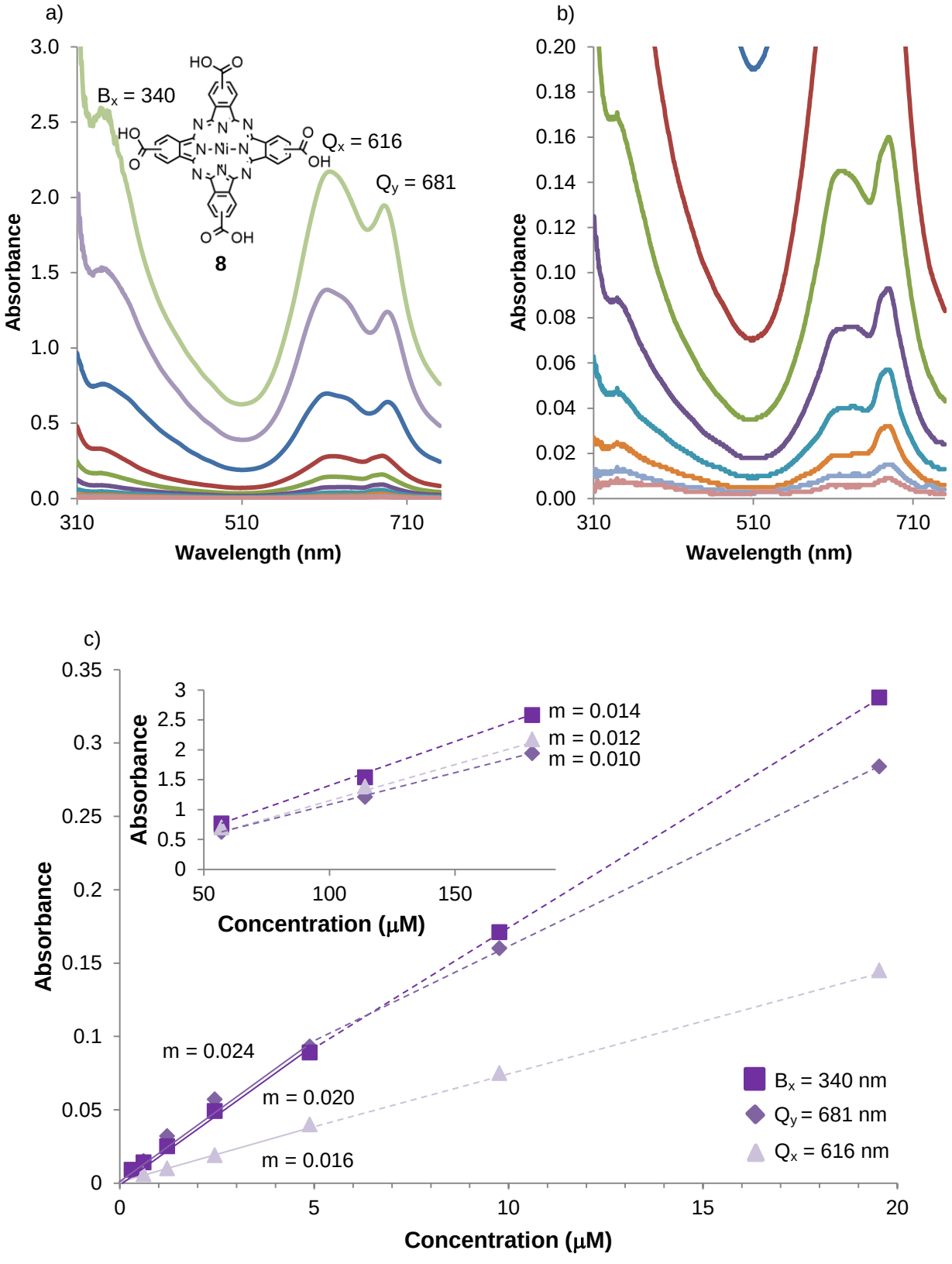

Figure 3. 19: UV-Vis spectra of $NiPc(COOH)_4$ **(8)**: a) at A < 3.0 a), b) at A < 0.2 and c) the Absorbance vs. Concentration plot for $NiPc(COOH)_4$ **(8)** of both the Q-bands as well as the B-band. The insert represent the high concentration range (50-200 μM).

Table 3. 1: Molar extinction coefficients of the various MPcs

Product (MPc)	Extinction coefficient B_x (M^{-1} cm^{-1})	Wavelength B_x (nm)	Extinction coefficient Q_x (M^{-1} cm^{-1})	Wavelength Q_x (nm)	Extinction coefficient Q_y (M^{-1} cm^{-1})	Wavelength Q_y (nm)
$ZnPc^tBu_4$	52631	347	158540	671	-	-
$NiPc^tBu_4$	54001	332	171070	667	-	-
$ZnPc(COOH)_4$	17348	349	29388	687	-	-
$FeClPc(COOH)_4$	35912	340	36235	664	-	-
$CoPc(COOH)_4$	67421	334	104640	667	-	-
$NiPc(COOH)_4$	14015	340	12080	616	10747	681

From **Table 3. 1 (p 60)** it can clearly be seen that $ZnPc^tBu_4$ and $NiPc^tBu_4$ have the highest extinction coefficients due to their high solubility in most organic solvents. $CoPc(COOH)_4$ (ε = 104640 $M^{-1}cm^{-1}$ at 667 nm) has the highest extinction coefficient and $NiPc(COOH)_4$ the lowest (ε = 12080 $M^{-1}cm^{-1}$ at 616 nm) of the tetracarboxy MPcs. The molar absorptivity of the tetracarboxy MPcs is in the following order: $CoPc(COOH)_4$ > $FeClPc(COOH)_4$ > $ZnPc(COOH)_4$ > $NiPc(COOH)_4$.

3.4 Post-Synthetic Modification of NH_2-MIL-101(Al)

Post-synthetic modification of NH_2-MIL-101(Al) with all the synthesised MPcs **(Section 3.3, p 45)** was performed with two methods: template synthesis where the specific MPc was added to the reaction mixture prior to the synthesis of NH_2-MIL-101(Al) **(Scheme 3. 4, p 61)**; method two was solution phase infiltration where the specific MPc, dissolved in anhydrous DMF, was allowed to infiltrate the pores of the evacuated NH_2-MIL-101(Al), after the vacuum was relieved **(Scheme 3. 5, p 62)**. These two different methods were investigated to determine which method would load the pores of the MOF best with the MPcs, in spite of their bulkiness and tendency for aggregation at high concentrations. The molar amounts for every product of both methods were kept similar, but the concentrations used for solution phase infiltration were six times more concentrated than for templating in order to achieve a near saturated solution for the highest possible loading. For $ZnPc^tBu_4$ and $NiPc^tBu_4$ the concentrations were ~0.96 M and 0.16 M for solution phase infiltration and template synthesis respectively. For $ZnPc(COOH)_4$, $FeClPc(COOH)_4$, $CoPc(COOH)_4$ and $NiPc(COOH)_4$, the concentrations were ~0.84 mM and 0.14 mM for solution phase infiltration and template synthesis respectively.

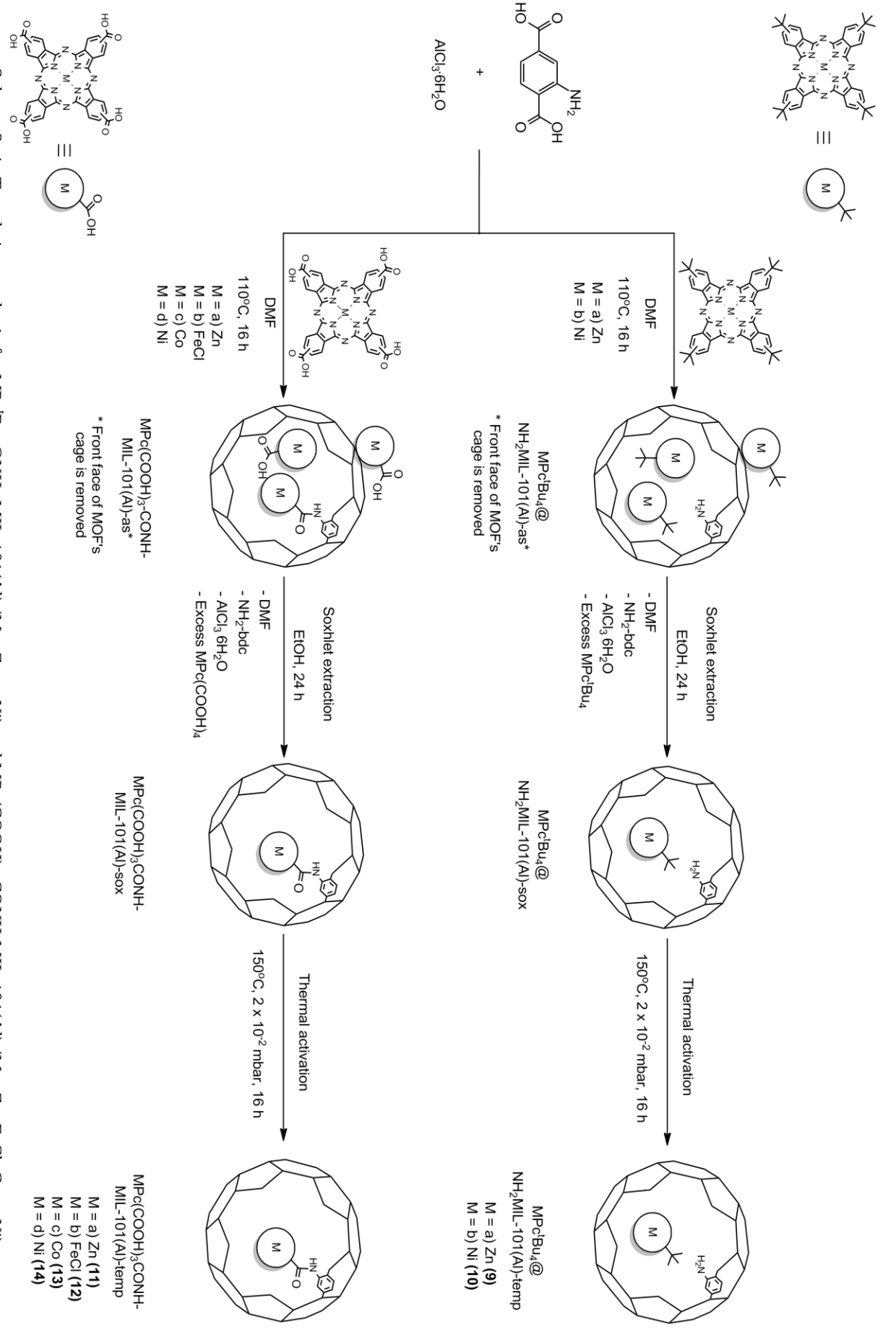

Scheme 3. 4: Templating synthesis for MPc^{t}Bu$_4$@NH$_2$-MIL-101(Al) (M = Zn or Ni) and MPc(COOH)$_3$-CONH-MIL-101(Al) (M = Zn, FeCl, Co or Ni).

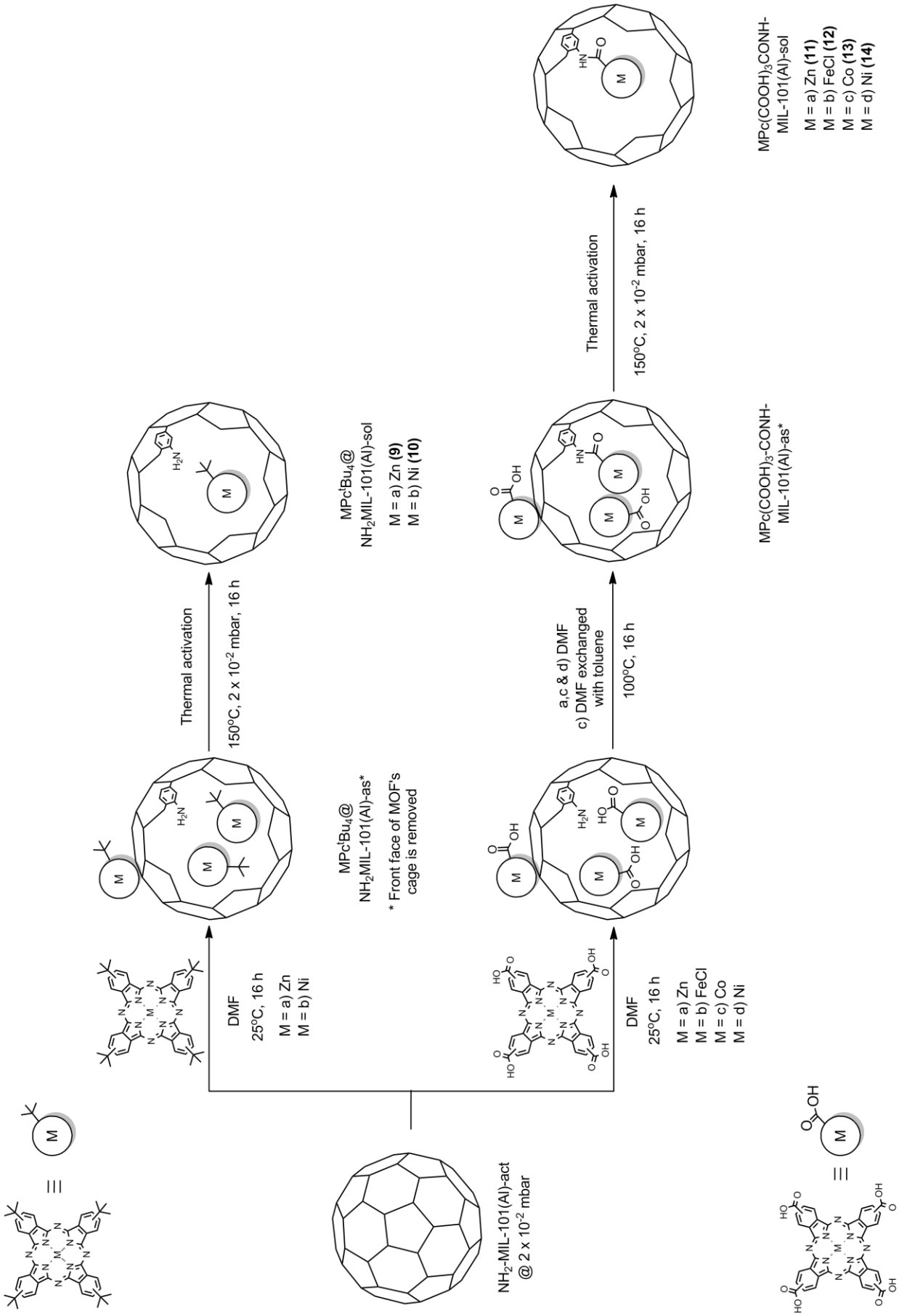

Scheme 3. 5: Solution phase infiltration for MPc^{t}Bu$_4$@NH$_2$-MIL-101(Al) (M = Zn or Ni) and MPc(COOH)$_3$-CONH-MIL-101(Al) (M = Zn, FeCl, Co or Ni).

3.4.1 Characterisation – ZnPc^{t}Bu$_4$@NH$_2$-MIL-101(Al) (9) and NiPc^{t}Bu$_4$@NH$_2$-MIL-101(Al) (10)

3.4.1.1 FTIR

The FTIR spectra of ZnPc^{t}Bu$_4$@NH$_2$-MIL-101(Al) and NiPc^{t}Bu$_4$@NH$_2$-MIL-101(Al), synthesised through templating and solution phase infiltration are compared in **Figure 3. 20 (p 63)**, and show that the presence of the MPcs did not influence the formation of the MOF during templating, since their spectra are identical to that of pure NH$_2$-MIL-101(Al). For NiPc^{t}Bu$_4$@NH$_2$-MIL-101(Al) **(10) (Figure 3. 20, c&d, p 63)** a distinct peak at 1640 cm^{-1} could indicate that a small amount of DMF was trapped inside the pores of the MOF. NiPc^{t}Bu$_4$ is less soluble than ZnPc^{t}Bu$_4$. ZnPc^{t}Bu$_4$@NH$_2$-MIL-101(Al) from the templating method remained yellow since most of the MPc was washed out after synthesis. It is also possible that the high concentration of the ZnPc^{t}Bu$_4$ caused aggregation, preventing the MOF from encapsulating it during the templating synthesis.

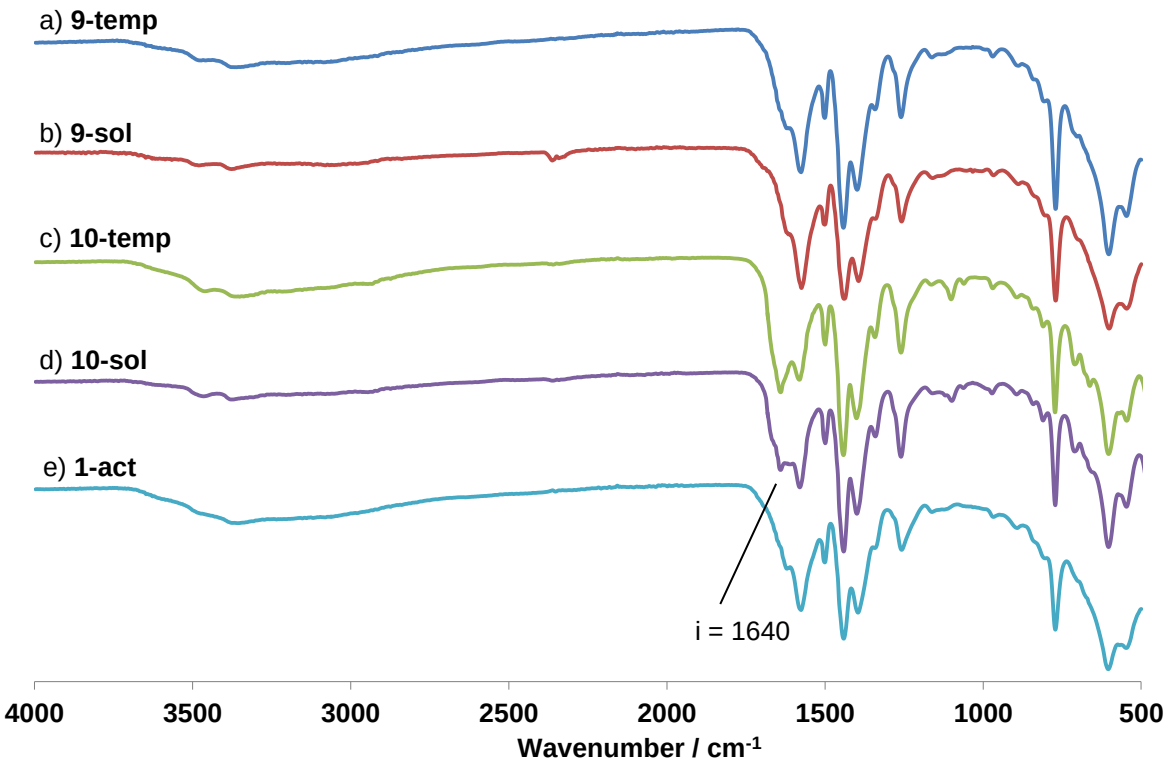

Figure 3. 20: FTIR spectra of a) ZnPc^{t}Bu$_4$@NH$_2$-MIL-101(Al) **(9-temp)** synthesised through templating (blue), b) ZnPc^{t}Bu$_4$@NH$_2$-MIL-101(Al) **(9-sol)** synthesised through solution phase infiltration (red), c) NiPc^{t}Bu$_4$@NH$_2$-MIL-101(Al) **(10-temp)** synthesised through templating (green), d) NiPc^{t}Bu$_4$@NH$_2$-MIL-101(Al) **(10-sol)** synthesised through solution phase infiltration (purple) and e) pure NH$_2$-MIL-101(Al) **(1)** (light-blue).

A definite colour change towards green was observed with solution phase infiltration of ZnPc^{t}Bu$_4$ into the MOF. Successful encapsulation is easily detected when the final solid product has a distinct green

colour. The intensity of the colour gives an indication of the concentration of the MPc inside the MOF.

3.4.1.2 TGA

The TGAs of ZnPc^{t}Bu$_4$@NH$_2$-MIL-101(Al) and NiPc^{t}Bu$_4$@NH$_2$-MIL-101(Al), synthesised through templating and solution phase infiltration are compared in **Figure 3. 21, (p 64)**. Steps 1a-d represent the mass loss of solvent molecules as well as adsorbed water vapour trapped inside the pores of the MOF. For ZnPc^{t}Bu$_4$@NH$_2$-MIL-101(Al) this mass loss **(Figure 3. 21, steps 1a-b, p 64)** is extended to about 179°C compared to NiPc^{t}Bu$_4$@NH$_2$-MIL-101(Al) **(Figure 3. 21, steps 1c-d, p 64)** where it stops earlier (~131°C). During steps 2a and 2c (templating method) the mass loss is possibly due to unreacted NH$_2$-bdc molecules trapped inside the pores of the MOF as well as partially decomposed MPc molecules for both ZnPc^{t}Bu$_4$@NH$_2$-MIL-101(Al) and NiPc^{t}Bu$_4$@NH$_2$-MIL-101(Al). The mass losses during steps 2b and 2d (solution phase infiltration) can only be from partially decomposed MPc molecules, since no unreacted NH$_2$-bdc molecules could be present in the pre-activated MOFs. The mass losses of step 2 for NiPc^{t}Bu$_4$@NH$_2$-MIL-101(Al) (2c & 2d) are almost three times more than the corresponding mass loss for ZnPc^{t}Bu$_4$@NH$_2$-MIL-101(Al) (2a & 2b) due to the presence of a larger amount of partially decomposed NiPc^{t}Bu$_4$ molecules. Steps 3a-d represent mass loss due to decomposition of the MOF (~370°C), as well as the encapsulated MPc.

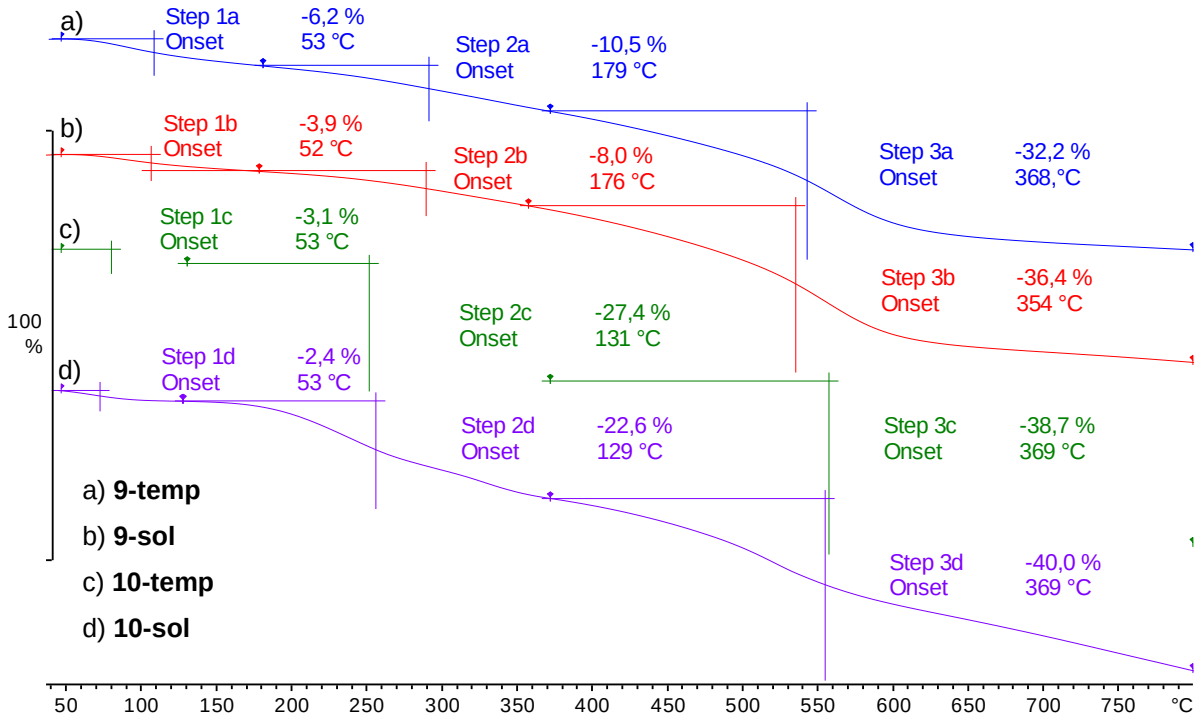

Figure 3. 21: TGA thermograms under N$_2$ of a) ZnPc^{t}Bu$_4$@NH$_2$-MIL-101(Al) **(9-temp)** (blue), b) ZnPc^{t}Bu$_4$@NH$_2$-MIL-101(Al) **(9-sol)** (red), c) NiPc^{t}Bu$_4$@NH$_2$-MIL-101(Al) **(10-temp)** (green) and d) NiPc^{t}Bu$_4$@NH$_2$-MIL-101(Al) **(10-sol)**. **Temp** = synthesised through templating and **sol =** synthesised through solution phase infiltration.

3.4.1.3 DRS-UV-Vis

Most of the MPc^{t}Bu$_4$-containing NH_2-MIL-101(Al) products are green with various intensities. NH_2-MIL-101(Al) is yellow, because it absorbs strongly in the blue region (400-450 nm), with no absorption in the red region (600-750 nm). It will thus be easy to detect the additional absorption bands in the red region from the particular encapsulated MPcs inside the MOF.

Diffuse-Reflectance Spectroscopy (DRS) was used to obtain the UV-Vis absorption spectra of ZnPc^{t}Bu$_4$@NH_2-MIL-101(Al) and NiPc^{t}Bu$_4$@NH_2-MIL-101(Al) **(Figure 3. 22, p 65)** in the solid state since these MOFs were all insoluble. For ZnPc^{t}Bu$_4$@NH_2-MIL-101(Al) **(9-temp) (Figure 3. 22, a, p 65)** (synthesised through templating), no adsorption bands were detected since the MPc was washed out of the MOF's pores during work-up. In contrast, the solution phase infiltrated product **(9-sol)** shows a strong absorption band in the red region. For both NiPc^{t}Bu$_4$@NH_2-MIL-101(Al) (synthesised through templating) **(10-temp)** and NiPc^{t}Bu$_4$@NH_2-MIL-101(Al) (synthesised through solution infiltration) **(10-sol),** weak absorption was detected in the red region with a blue-shift similar to that observed during pure liquid state UV-Vis studies of MPc^{t}Bu$_4$ **(Figure 3. 12, p 51 & Figure 3. 13, p 51)**. For both ZnPc^{t}Bu$_4$@NH_2-MIL-101(Al) and NiPc^{t}Bu$_4$@NH_2-MIL-101(Al) a double Q-band was detected, different from the solution phase spectra of the specific MPcs.

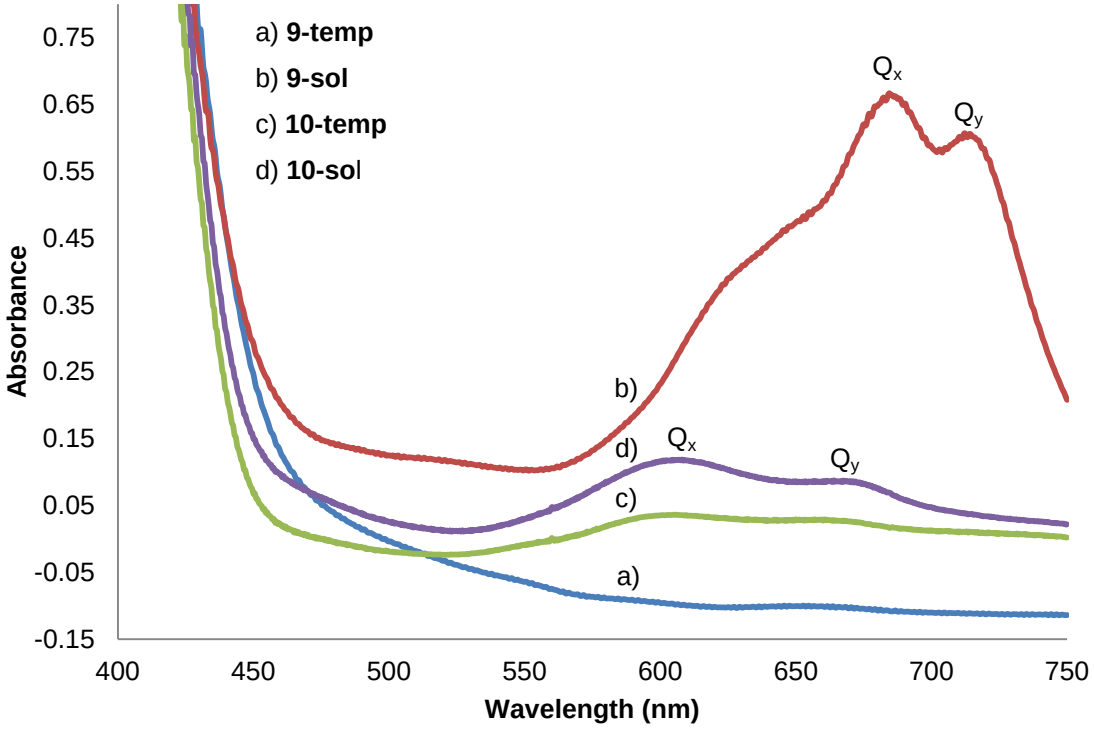

Figure 3. 22: DRS-UV-Vis of a) ZnPc^{t}Bu$_4$@NH_2-MIL-101(Al) **(9-temp)** (blue), b) ZnPc^{t}Bu$_4$@NH_2-MIL-101(Al) **(9-sol)** (red), c) NiPc^{t}Bu$_4$@NH_2-MIL-101(Al) **(10-temp)** (green) and d) NiPc^{t}Bu$_4$@NH_2-MIL-101(Al) **(10-sol)** (purple). **Temp** = synthesised through templating and **sol =** synthesised through solution phase infiltration.

3.4.1.4 ASAP

The N_2 isotherms of $ZnPc^tBu_4@NH_2$-MIL-101(Al) **(9-temp** and **9-sol)** and $NiPc^tBu_4@NH_2$-MIL-101(Al) **(10-temp** and **10-sol)** are all type I isotherms **(Figure 3. 23, p 67)**, similar to that of pure NH_2-MIL-101(Al) **(Figure 3. 4, p 44)**. The BET surface area of **9-temp** is 760.7 m^2g^{-1}, less than a third of the BET surface area of pure NH_2-MIL-101(Al), an indication that partially decomposed $ZnPc^tBu_4$ remnants are still trapped inside the MOF's pores after synthesis by templating. The pore sizes of **9-temp** from the BJH model (11 Å and 15 Å) as well as DFT (21 Å and 27 Å) are smaller compared to those of pure NH_2-MIL-101(Al) (27 Å and 34 Å). The BET surface area of $ZnPc^tBu_4@NH_2$-MIL-101(Al) (synthesised through solution infiltration) **(Figure 3. 23, b, p 67)**, is only 100.2 m^2g^{-1}, an indication of the higher loading of $ZnPc^tBu_4$ in the MOF's structure, supported by DRS-UV-Vis **(Figure 3. 22, b, p 65)** observations. Small pore widths of 14 Å and 17 Å (BJH adsorption) as well as 30 Å and 100 Å from the DFT model show that the normal porosity is disrupted by the load of $ZnPc^tBu_4$, as already suggested by the low BET surface area and a low pore volume (0.13 cm^3g^{-1}). For both **9-temp** and **9-sol**, the hysteresis during desorption between 0.3 p/p^o and 0.9 p/p^o indicates the presence of molecules which retard the desorption of N_2. It occurs due to a bottle-neck effect at the pore windows where movement is the slowest. The presence of guest molecules, such as the particular MPc can contribute to this effect.

The ASAP isotherms of $NiPc^tBu_4@NH_2$-MIL-101(Al) **(10-temp** and **10-sol)** in **Figure 3. 23, c & d (p 67)** show that both methods gave similar pore widths: DFT pore sizes of 21 Å and 28 Å and BJH pores sizes of 12 Å and 16 Å. These are identical to the pore width distribution of pure NH_2-MIL-101(Al). The presence of $NiPc^tBu_4$ during templating did not influence the formation of the MOF's structure. A difference is seen in the surface area indicating a high loading through the use of solution infiltration **(Figure 3. 23, c & d, p 67)**. The BET surface area for **10-temp** (1973 m^2g^{-1}) is ~500 m^2g^{-1} larger than that of **10-sol** (1458 m^2g^{-1}), an indication that **10-sol** has a higher loading of $NiPc^tBu_4$. This was also confirmed by the ~0.2 cm^3g^{-1} difference in pore volumes: 0.84 cm^3g^{-1} **(10-temp)** and 0.63 cm^3g^{-1} **(10-sol)**. No hysteresis upon desorption was found for both products, meaning that there was no obstruction near the pores of the MOF.

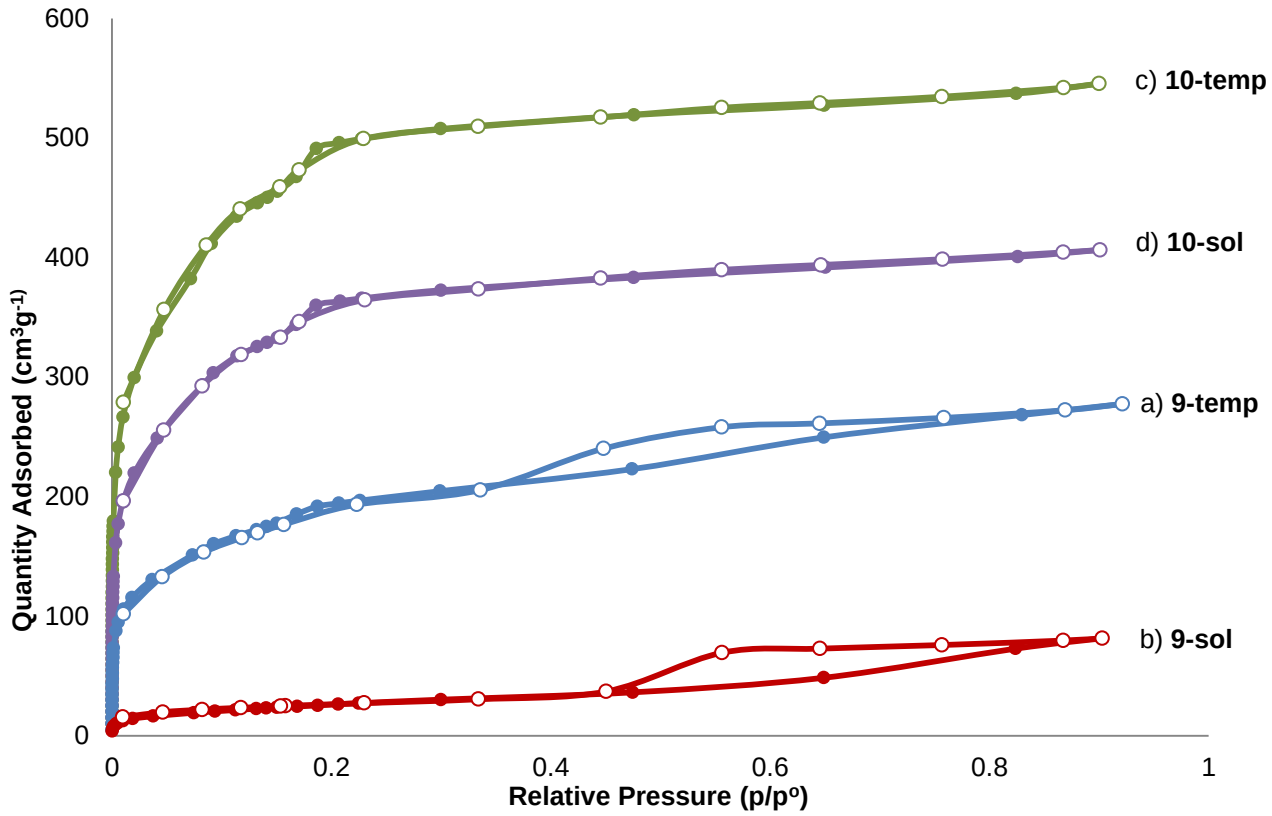

Figure 3. 23: N_2 adsorption (full dots) and desorption (empty circles) isotherms @ 77 K of a) ZnPc^{t}Bu$_4$@NH$_2$-MIL-101(Al) **(9-temp)** (blue), b) ZnPc^{t}Bu$_4$@NH$_2$-MIL-101(Al) **(9-sol)** (red), c) NiPc^{t}Bu$_4$@NH$_2$-MIL-101(Al) **(10-temp)** (green) and d) NiPc^{t}Bu$_4$@NH$_2$-MIL-101(Al) **(10-sol)** (purple). **Temp** = synthesised through templating and **sol** = synthesised through solution phase infiltration.

3.4.1.5 PXRD

The PXRD spectra of both ZnPc^{t}Bu$_4$@NH$_2$-MIL-101(Al) **(9)** and NiPc^{t}Bu$_4$@NH$_2$-MIL-101(Al) **(10)** after each synthesis method **(Figure 3. 24, p 68)** show that for a) **9-temp**, c) **10-temp** and d) **10-sol**, the fingerprint area of NH$_2$-MIL-101(Al) (compared to **Figure 3. 5, p 44**) is still detectable below 2θ = 10 degrees. This confirms that the crystalline structures of these three compounds are still identical to that of NH$_2$-MIL-101(Al). For **9-sol** in **Figure 3. 24b**, **(p 68)**, very little diffraction peaks are visible indicating that the high percentage of ZnPc^{t}Bu$_4$ present inside the MOF has disrupted the crystalline phase of the product.

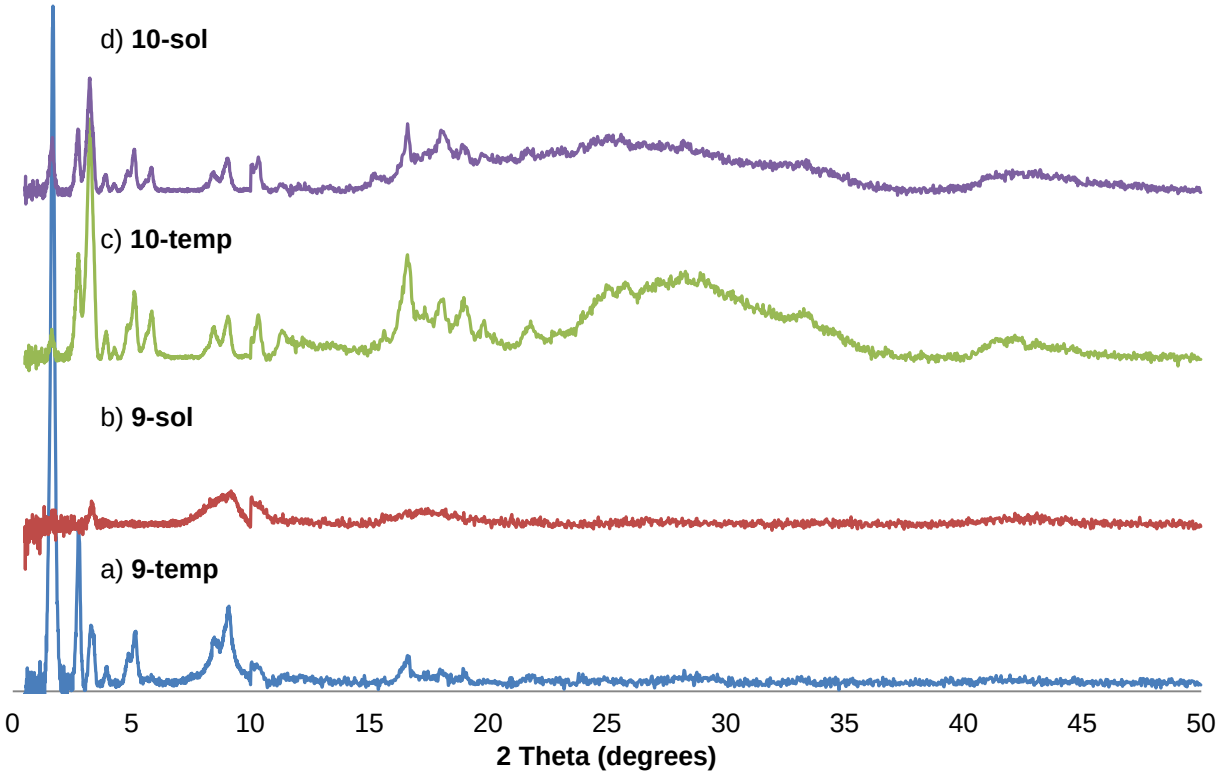

Figure 3. 24: PXRD patterns of a) ZnPc^{t}Bu$_4$@NH$_2$-MIL-101(Al) **(9-temp)** (blue), b) ZnPc^{t}Bu$_4$@NH$_2$-MIL-101(Al) **(9-sol)** (red), c) NiPc^{t}Bu$_4$@NH$_2$-MIL-101(Al) **(10-temp)** (green) and d) NiPc^{t}Bu$_4$@NH$_2$-MIL-101(Al) **(10-sol)** (purple). **Temp** = synthesised through templating and **sol =** synthesised through solution phase infiltration.

3.4.2 Characterisation - ZnPc(COOH)$_3$-CONH-MIL-101(Al) (11), FeClPc(COOH)$_3$-CONH-MIL-101(Al) (12), CoPc(COOH)$_3$-CONH-MIL-101(Al) (13) and NiPc(COOH)$_3$-CONH-MIL-101(Al) (14)

3.4.2.1 FTIR

The FTIR of ZnPc(COOH)$_3$-CONH-MIL-101(Al) **(11)**, FeClPc(COOH)$_3$-CONH-MIL-101(Al) **(12)**, CoPc(COOH)$_3$-CONH-MIL-101(Al) **(13)** and NiPc(COOH)$_3$-CONH-MIL-101(Al) **(14)** synthesised through templating and solution phase infiltration **(Figure 3. 25, p 69)** show that for **11-temp, 11-sol, 12-sol, 13-sol** and **14-temp** no additional FTIR frequencies were detected and are similar to the FTIR spectrum of pure NH$_2$-MIL-101(Al). For **12-temp** and **13-temp** an additional C=O frequency was detected at ~1645 cm^{-1} and a similar C=O stretching frequencies depicted as a doublet, is picked up in the same region at 1643 cm^{-1} for **14-sol**. These stretching frequencies indicate the presence of the MPc and/or DMF molecules trapped between the MPc rings as previously explained.

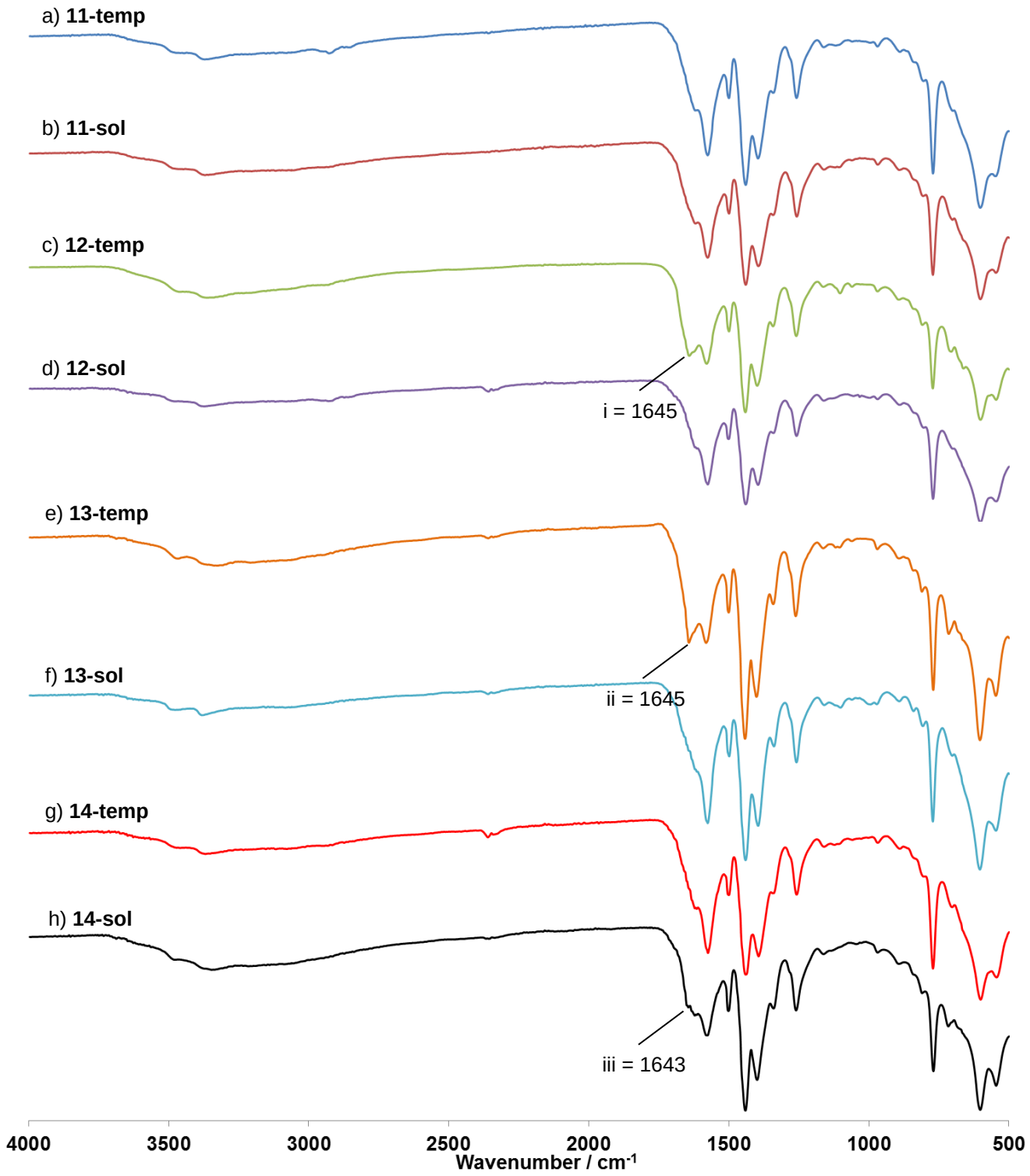

Figure 3. 25: FTIR spectra of a) ZnPc(COOH)$_3$-CONH-MIL-101(Al) **(11-temp)** (blue), b) ZnPc(COOH)$_3$-CONH-MIL-101(Al) **(11-sol)** (red), c) FeClPc(COOH)$_3$-CONH-MIL-101(Al) **(12-temp)** (green), d) FeClPc(COOH)$_3$-CONH-MIL-101(Al) **(12-sol)** (purple), e) CoPc(COOH)$_3$-CONH-MIL-101(Al) **(13-temp)** (orange), f) CoPc(COOH)$_3$-CONH-MIL-101(Al) **(13-sol)** (light-blue), g) NiPc(COOH)$_3$-CONH-MIL-101(Al) **(14-temp)** (light-red) and h) NiPc(COOH)$_3$-CONH-MIL-101(Al) **(14-sol)** (black). **Temp** = synthesised through templating and **sol** = synthesised through solution phase infiltration.

$FeClPc(COOH)_4$ decomposed after heating the reaction mixture during the templating reaction. The bulk reaction changed from dark blue-black to yellow, due to the collapse of the MPc ring structure, thus destroying its 18-π conjugation responsible for the intense light absorption. Due to the MPc's decomposition in hot DMF, a different procedure was used for the solution infiltration process: DMF was still used to infiltrate the MPc inside the MOF's structure for 16 hours at room temperature, but was then exchanged with anhydrous toluene, before the reaction mixture was heated to 100°C for the 24 hours amidation reaction. No decomposition was observed meaning that DMF under high temperature caused $FeClPc(COOH)_4$ to decompose.

3.4.2.2 TGA

The TGA thermograms of $ZnPc(COOH)_3$-CONH-MIL-101(Al) **(11)**, $FeClPc(COOH)_3$-CONH-MIL-101(Al) **(12)**, $CoPc(COOH)_3$-CONH-MIL-101(Al) **(13)** and $NiPc(COOH)_3$-CONH-MIL-101(Al) **(14)** synthesised through templating and solution phase infiltration **(Figure 3. 26, p 71)**, all show the loss of solvent and adsorbed water vapour from the pores of the MOFs: steps 1a-h ranging between 48°C and 169°C with mass losses of 2.4 wt% - 6.0 wt%. Steps 2a-h between 128°C and 392°C, represent the mass loss of higher boiling DMF, unreacted NH_2-bdc (only for templating) and partially decomposed MPc fragments with mass losses between 9 and 18.3 wt%. The second step overlaps with the start of the MPc's decomposition ~240°C **(Figure 3. 15, p 54)**. The MPc's decomposition also overlaps with steps 3a-h which mainly represent the breakdown of the MOF's structure starting at ~370°C with mass losses between 28.3 and 40.8 wt %.

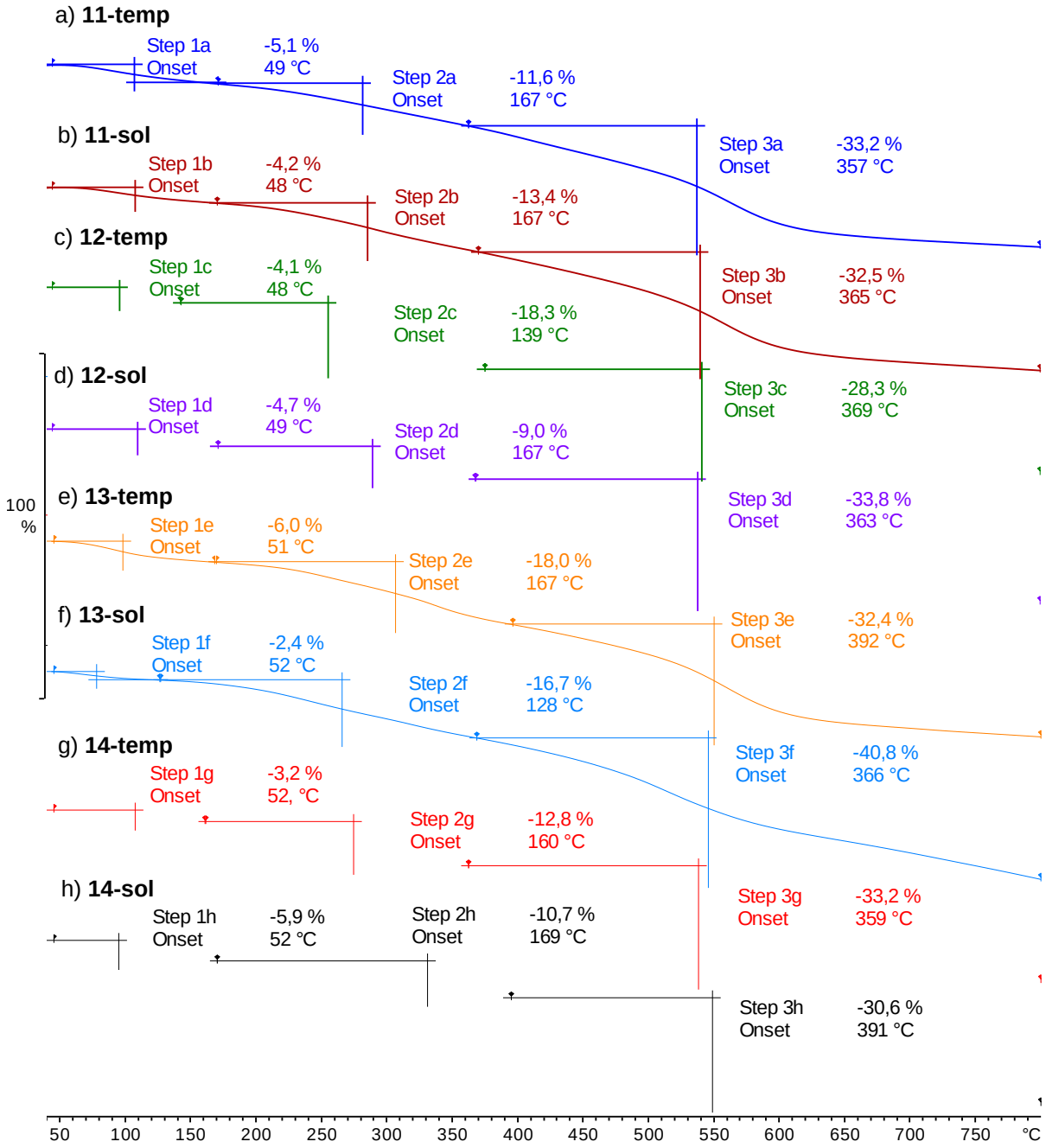

Figure 3. 26: TGA thermograms under N_2 of a) $ZnPc(COOH)_3$-CONH-MIL-101(Al) **(11-temp)** (blue), b) $ZnPc(COOH)_3$-CONH-MIL-101(Al) **(11-sol)** (red), c) $FeClPc(COOH)_3$-CONH-MIL-101(Al) **(12-temp)** (green), d) $FeClPc(COOH)_3$-CONH-MIL-101(Al) **(12-sol)** (purple), e) $CoPc(COOH)_3$-CONH-MIL-101(Al) **(13-temp)** (orange), f) $CoPc(COOH)_3$-CONH-MIL-101(Al) **(13-sol)** (light-blue), g) $NiPc(COOH)_3$-CONH-MIL-101(Al) **(14-temp)** (light-red) and h) $NiPc(COOH)_3$-CONH-MIL-101(Al) **(14-sol)** (black). **Temp** = synthesised through templating and **sol** = synthesised through solution phase infiltration.

3.4.2.3 DRS-UV-Vis

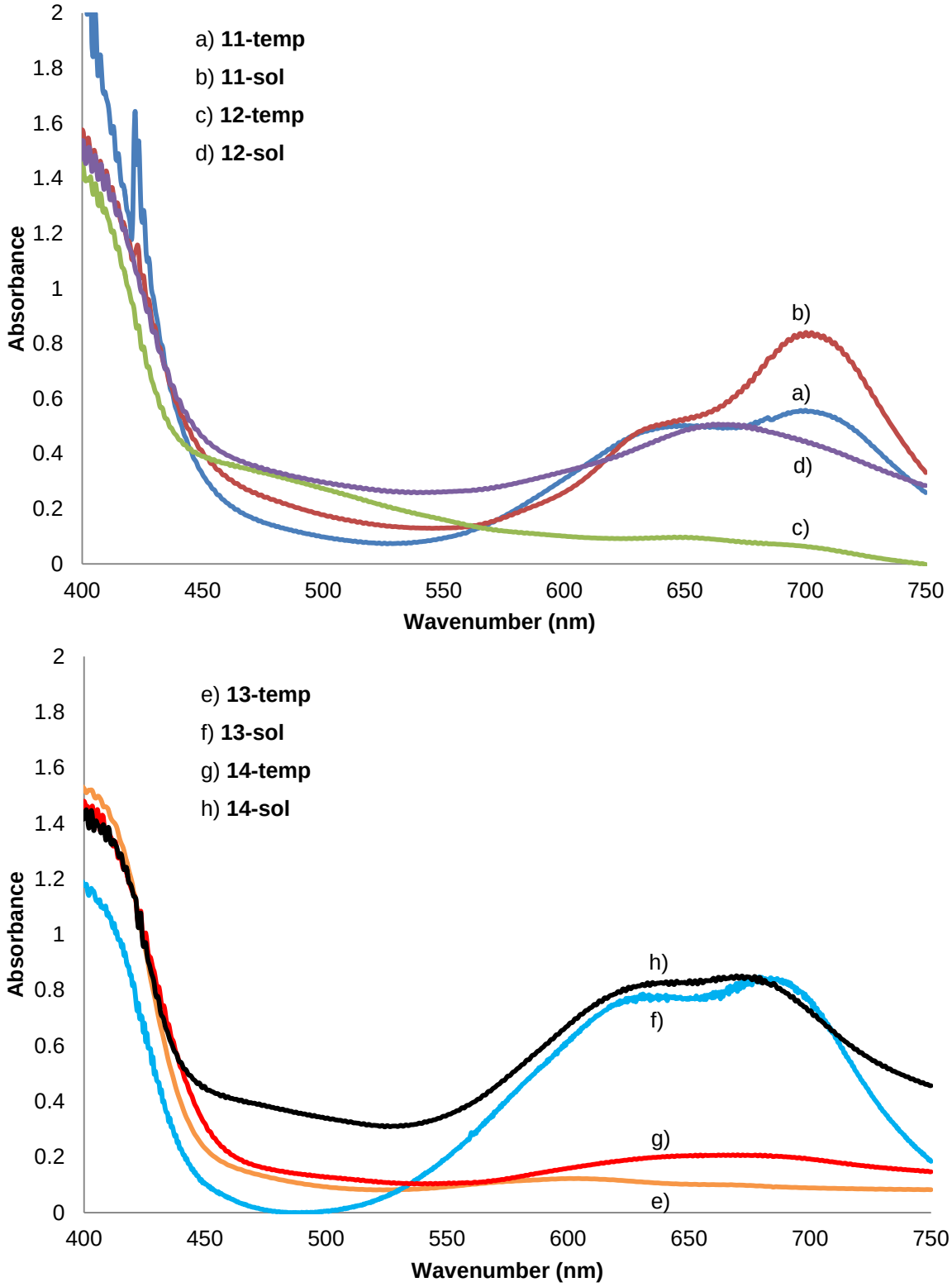

Figure 3. 27: DRS-UV-Vis spectra of a) $ZnPc(COOH)_3$-CONH-MIL-101(Al) **(11-temp)** (blue), b) $ZnPc(COOH)_3$-CONH-MIL-101(Al) **(11-sol)** (red), c) $FeClPc(COOH)_3$-CONH-MIL-101(Al) **(12-temp)** (green), d) $FeClPc(COOH)_3$-CONH-MIL-101(Al) **(12-sol)** (purple), e) $CoPc(COOH)_3$-CONH-MIL-101(Al) **(13-temp)** (orange), f) $CoPc(COOH)_3$-CONH-MIL-101(Al) **(13-sol)** (light-blue), g) $NiPc(COOH)_3$-CONH-MIL-101(Al) **(14-temp)** (light-red) and h) $NiPc(COOH)_3$-CONH-MIL-101(Al) **(14-sol)** (black). **Temp** = synthesised through templating and **sol** = synthesised through solution phase infiltration.

Except for FeClPc(COOH)$_3$-CONH-MIL-101(Al) (c), CoPc(COOH)$_3$-CONH-MIL-101(Al) (e) and NiPc(COOH)$_3$-CONH-MIL-101(Al) (g) (all synthesised through templating), where the MPc almost completely decomposed during synthesis, the DRS-UV-Vis spectra of ZnPc(COOH)$_3$-CONH-MIL-101(Al) (a & b), FeClPc(COOH)$_3$-CONH-MIL-101(Al) (d), CoPc(COOH)$_3$-CONH-MIL-101(Al) (f) and NiPc(COOH)$_3$-CONH-MIL-101(Al) (h) showed absorption bands between 550 nm and 750 nm. The only tetracarboxylated MPc that remained intact throughout templating was ZnPc(COOH)$_4$, as seen from significant absorbance peaks of ZnPc(COOH)$_3$-CONH-MIL-101(Al) **(Figure 3. 27, a, p 72).** These double Q-band peaks at 643 nm and 703 nm are just slightly lower in intensity, compared to those of solution phase infiltration, ZnPc(COOH)$_3$-CONH-MIL-101(Al) (b). Similar double Q-bands were observed for ZnPc^{t}Bu$_4$@NH$_2$-MIL-101(Al) **(Figure 3. 22, p 65)**. Only FeClPc(COOH)$_3$-CONH-MIL-101(Al) **(Figure 3. 27, d, p 72)** showed a single Q-band at 668 nm. The cobalt and nickel-containing compounds also displayed double Q-bands.

3.4.2.4 ASAP

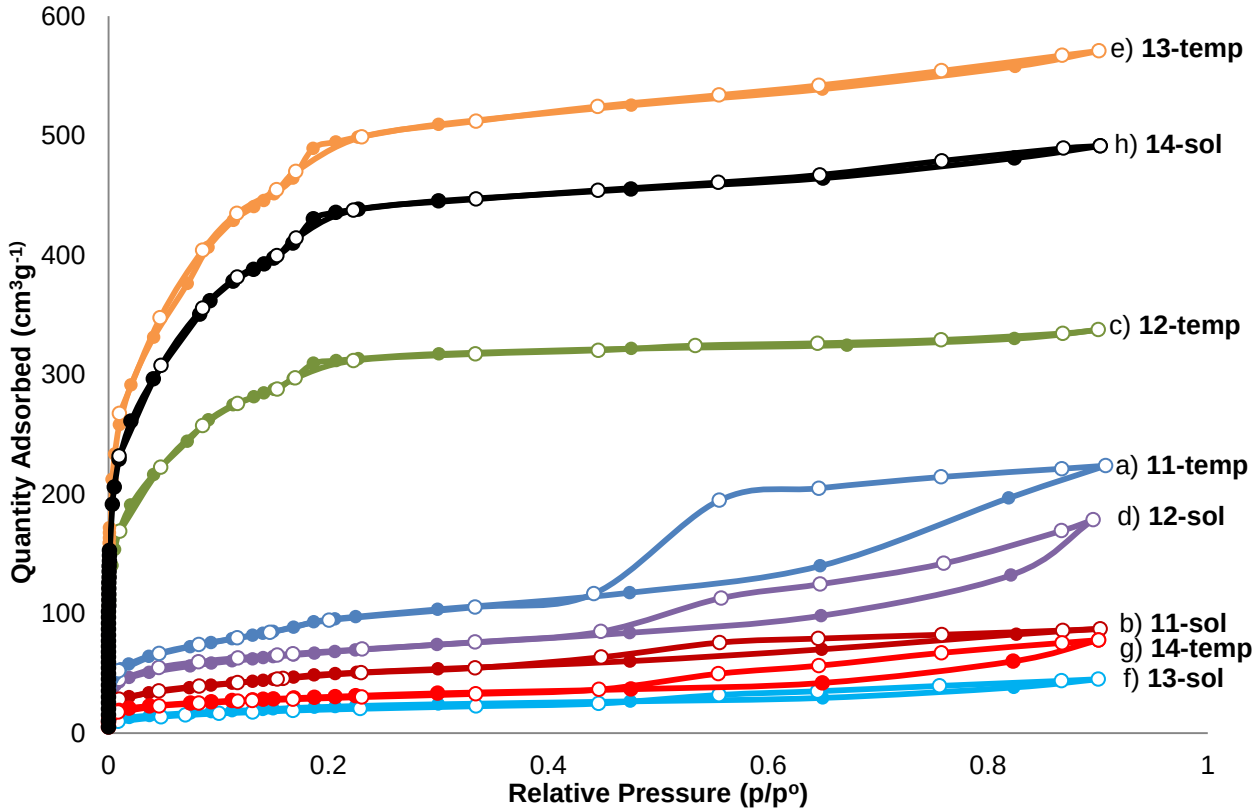

Figure 3. 28: N_2 adsorption (full dots) and desorption (empty circles) isotherms at 77 K of a) ZnPc(COOH)$_3$-CONH-MIL-101(Al) **(11-temp)** (blue), b) ZnPc(COOH)$_3$-CONH-MIL-101(Al) **(11-sol)** (red), c) FeClPc(COOH)$_3$-CONH-MIL-101(Al) **(12-temp)** (green), d) FeClPc(COOH)$_3$-CONH-MIL-101(Al) **(12-sol)** (purple), e) CoPc(COOH)$_3$-CONH-MIL-101(Al) **(13-temp)** (orange), f) CoPc(COOH)$_3$-CONH-MIL-101(Al) **(13-sol)** (light-blue), g) NiPc(COOH)$_3$-CONH-MIL-101(Al) **(14-temp)** (light-red) and h) NiPc(COOH)$_3$-CONH-MIL-101(Al) **(14-sol)** (black). **Temp** = synthesised through templating and **sol** = synthesised through solution phase infiltration.

The N_2 isotherms of ZnPc(COOH)$_3$-CONH-MIL-101(Al) **(11)**, FeClPc(COOH)$_3$-CONH-MIL-101(Al) **(12)**, CoPc(COOH)$_3$-CONH-MIL-101(Al) **(13)** and NiPc(COOH)$_3$-CONH-MIL-101(Al) **(14)** (synthesised through templating and solution phase infiltration) **(Figure 3. 28, p 73)**, show that the highest N_2 uptake for each compound was achieved after templating, with only NiPc(COOH)$_3$-CONH-MIL-101(Al) **(14-sol)** as the exception. For **13-temp**, **14-sol** and **12-temp**, a type I isotherm with no hysteresis was found, typical of NH_2-MIL-101(Al), indicating that these compounds have a low loading of MPc(COOH)$_4$. A sharp decrease in N_2 uptake was observed for **11-temp**, **12-sol**, **11-sol**, **14-temp** and **13-sol** due to their high MPc loading. All five of these isotherms display a desorption hysteresis, as expected for materials with a higher loading of guest molecules. The highest and lowest BET surface areas were found for the cobalt-containing materials with templating **(13-temp)** giving the highest (BET = 2010 m^2g^{-1} and pore volume = 0.88 cm^3g^{-1}) and solution phase infiltration **(13-sol)** the lowest (BET = 88.8 m^2g^{-1} and pore volume = 0.07 cm^3g^{-1}) values **(Table 3. 2, p 74)**. In this table all the porosity analyses values of the above mentioned MPc-modified MOFs are compared with the values of pure NH_2-MIL-101(Al).

Table 3. 2: Porosity parameters (Volume N_2 adsorbed, BET surface area and total pore volume) obtained by the ASAP analyses at 77 K of all MPc^{t}Bu$_4$@NH_2-MIL-101(Al) and MPc(COOH)$_3$-CONH-MIL-101(Al). **Temp** = synthesised through templating and **sol =** synthesised through solution phase infiltration.

Product	Volume N_2 Adsorped (cm^3g^{-1})	BET Surface Area (m^2g^{-1})	Total Pore Volume (cm^3g^{-1})
NH_2-MIL-101(Al) **(1-act)**	983	3192	1.52
ZnPc^{t}Bu$_4$@NH_2-MIL-101(Al) **(9-temp)**	278	761	0.43
ZnPc^{t}Bu$_4$@NH_2-MIL-101(Al) **(9-sol)**	82	100	0.13
NiPc^{t}Bu$_4$@NH_2-MIL-101(Al) **(10-temp)**	545	1973	0.84
NiPc^{t}Bu$_4$@NH_2-MIL-101(Al) **(10-sol)**	406	1459	0.63
ZnPc(COOH)$_3$-CONH-MIL-101(Al) **(11-temp)**	224	393	0.35
ZnPc(COOH)$_3$-CONH-MIL-101(Al) **(11-sol)**	87	197	0.14
FeClPc(COOH)$_3$-CONH-MIL-101(Al) **(12-temp)**	338	1221	0.52
FeClPc(COOH)$_3$-CONH-MIL-101(Al) **(12-sol)**	179	244	0.28
CoPc(COOH)$_3$-CONH-MIL-101(Al) **(13-temp)**	571	2010	0.88
CoPc(COOH)$_3$-CONH-MIL-101(Al) **(13-sol)**	45	89	0.07
NiPc(COOH)$_3$-CONH-MIL-101(Al) **(14-temp)**	78	110	0.12
NiPc(COOH)$_3$-CONH-MIL-101(Al) **(14-sol)**	491	1749	0.76

3.4.2.5 PXRD

The PXRD spectra of ZnPc(COOH)$_3$-CONH-MIL-101(Al) **(11)**, FeClPc(COOH)$_3$-CONH-MIL-101(Al) **(12)**, CoPc(COOH)$_3$-CONH-MIL-101(Al) **(13)** and NiPc(COOH)$_3$-CONH-MIL-101(Al) **(14)**, (synthesised through templating and solution phase infiltration) **(Figure 3. 29, p 75)** show that products with high surface areas **(Table 3. 2, p 74)**, also have well-defined crystalline spectra: **11-temp**, **12-temp**, **13-temp** and **14-sol**. Products with a particularly high loading of MPc in the pores gave weakly defined PXRD patterns: **11-sol**, **12-sol**, **13-sol** and **14-temp**. These compounds' low crystallinity correlates well with their low volumes of N_2 adsorbed during porosity analyses **(Figure 3. 28, p 73 & Table 3. 2, p 74)**.

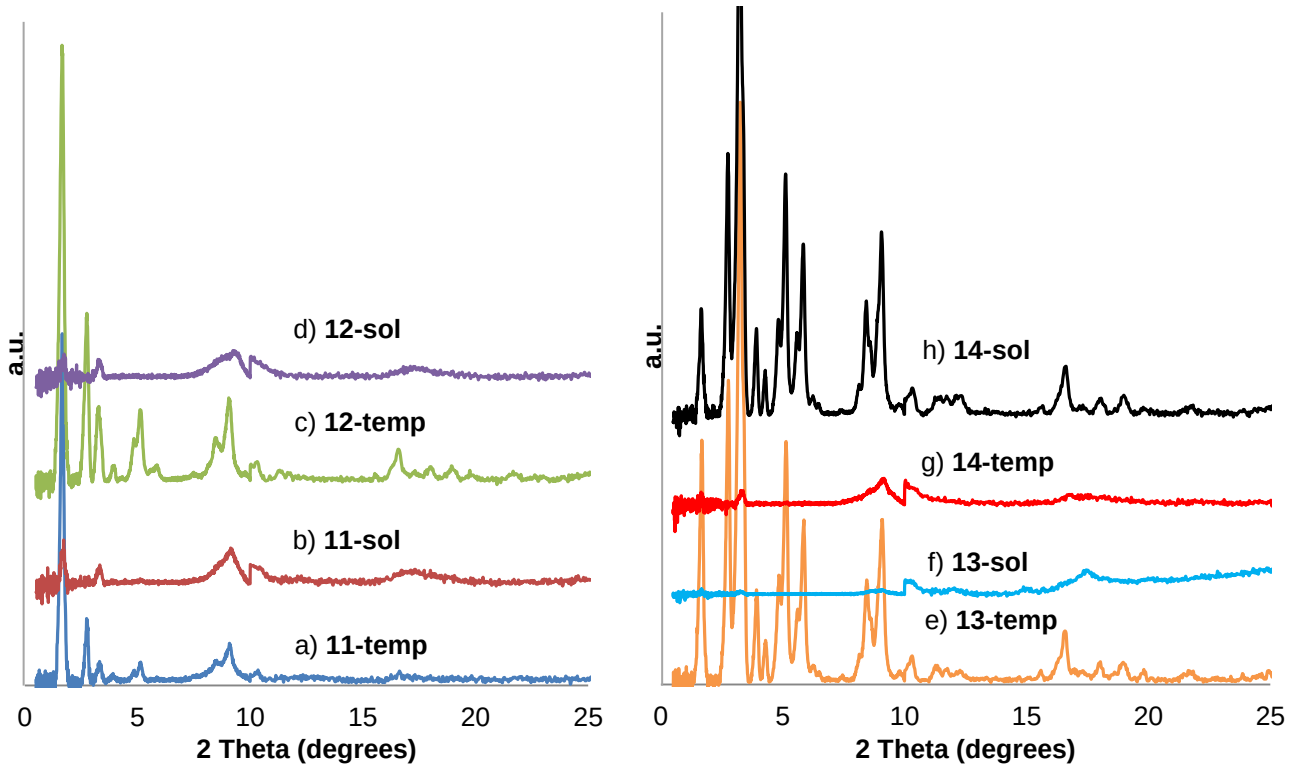

Figure 3. 29: PXRD patterns of a) ZnPc(COOH)$_3$-CONH-MIL-101(Al) **(11-temp)** (blue), b) ZnPc(COOH)$_3$-CONH-MIL-101(Al) **(11-sol)** (red), c) FeClPc(COOH)$_3$-CONH-MIL-101(Al) **(12-temp)** (green), d) FeClPc(COOH)$_3$-CONH-MIL-101(Al) **(12-sol)** (purple), e) CoPc(COOH)$_3$-CONH-MIL-101(Al) **(13-temp)** (orange), f) CoPc(COOH)$_3$-CONH-MIL-101(Al) **(13-sol)** (light-blue), g) NiPc(COOH)$_3$-CONH-MIL-101(Al) **(14-temp)** (light-red) and h) NiPc(COOH)$_3$-CONH-MIL-101(Al) **(14-sol)** (black). **Temp** = synthesised through templating and **sol** = synthesised through solution phase infiltration.

3.4.2.6 Hydrogen Adsorption ($CoPc(COOH)_3$-CONH-MIL-101(Al) and $NiPc(COOH)_3$-CONH MIL-101(Al))

MIL-101 derivatives are amongst the porous materials being investigated for hydrogen adsorption, a challenging field with a lot of room for improvement.[6,7,8] By encapsulating MPcs in the MOF's structure, its hydrogen adsorption may be affected negatively or positively depending on whether the MPc can contribute towards hydrogen spillover or not. During spillover the hydrogen molecules are split into hydrogen atoms on a metal and then transported to the MOF's structure. For this study only $CoPc(COOH)_3$-CONH-MIL-101(Al) **(13-sol)** (BET surface area = 88 m^2g^{-1}) and $NiPc(COOH)_3$-CONH MIL-101(Al) **(14-sol)** (BET surface area = 1749 m^2g^{-1}), both produced by the solution phase infiltration method, were investigated for high pressure H_2-adsorption and desorption **(Figure 3. 30, p 76)**. This clearly shows the direct relation between BET surface area and the amount of excess hydrogen adsorbed.

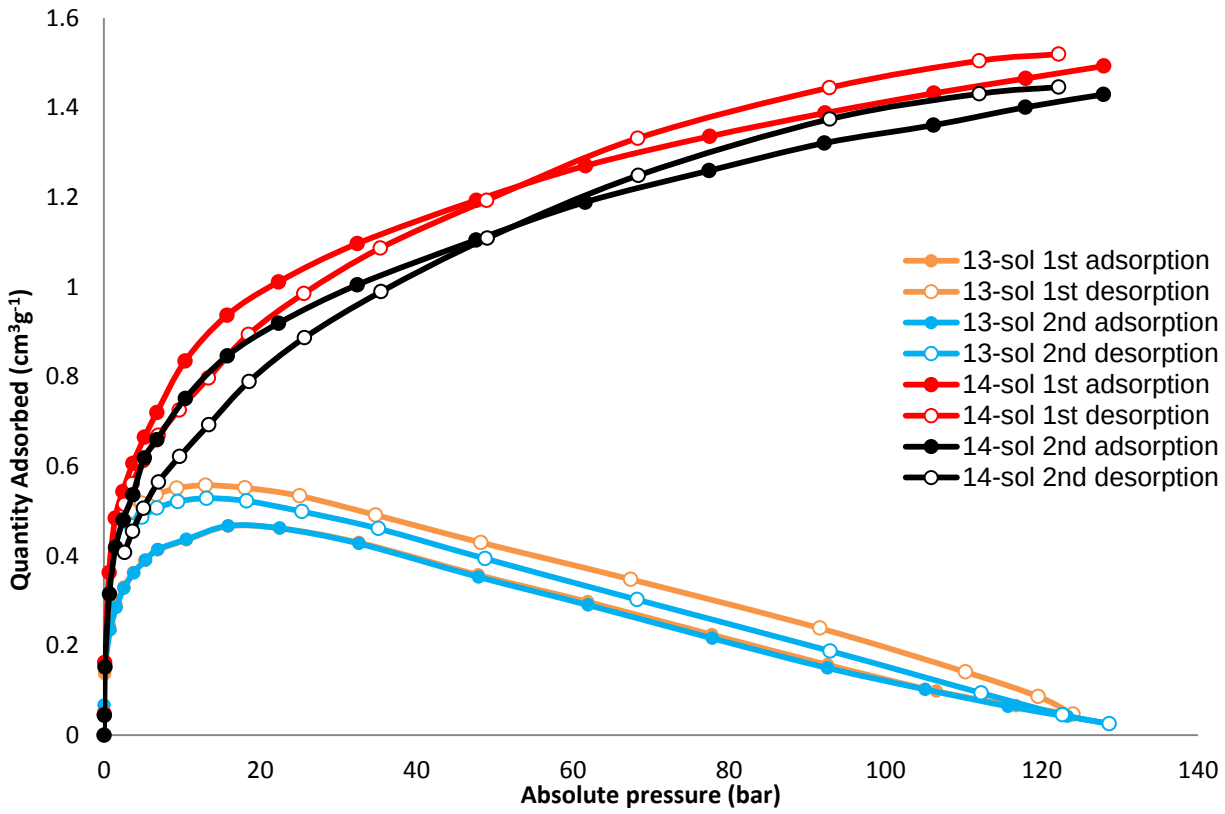

Figure 3. 30: Excess H_2 adsorption and desorption isotherms at 77 K of $CoPc(COOH)_3$-CONH-MIL-101(Al) **(13-sol)** (bottom) and $NiPc(COOH)_3$-CONH-MIL-101(Al) **(14-sol)** (top), performed in duplicate.

$CoPc(COOH)_3$-CONH-MIL-101(Al) **(13-sol)** reached a maximum excess hydrogen uptake of 0.47 wt% at 16 bar, considerably lower than that of pure NH_2-MIL-101(Al) (3.82 wt% at 41 bar).[9] For both desorption isotherms of $CoPc(COOH)_3$-CONH-MIL-101(Al) **(13-sol)** a hysteresis was found, due to the presence of MPc, which would retard the migration of the hydrogen molecules as they desorb from the Al or Co metal clusters. The low maximum excess adsorption of hydrogen could be due to the

high loading of the MPc inside the MOF. The presence of the MPc can also block the entrances to the inner part of the bulk MOF and thereby blocking open metal sites of adsorption.

For NiPc(COOH)$_3$-CONH MIL-101(Al) **(14-sol) (Figure 3. 30, p 76)**, the highest excess H_2 uptake measured was 1.5 wt% at 128 bar, but the uptake was still rising and only limited by the capabilities of the instrument. The presence of the Ni in the MOF altered the shape of the isotherm so that the MOF now requires a lot more pressure to adsorb H_2. The higher excess hydrogen uptake of **14-sol**, when compared to **13-sol**, can be attributed to its higher surface area of 1749 m^2g^{-1}, with the surface area of **13-sol** being only 88 m^2g^{-1}. Very little hysteresis upon desorption was observed for **14-sol**, due to a lower loading of the MPc in the MOF.

3.4.3 Metal Content Analysis

To obtain the loading percentage of each MPc inside NH_2-MIL-101(Al), quantitative techniques like XPS, SEM-EDX and ICP-AES was used to analyse the MPc-containing products. All of these attempts gave results that were below each of the particular instruments' detection limit meaning that the results could not be verified. In spite of the above methods failing to detect each MPc, a definte qualitative confirmation of the presence of these MPcs was obtained using DRS-UV-Vis, PXRD, ASAP and electrochemistry **(Section 3.5.2, p 86)**. Results from DRS-UV-Vis displayed a definite Q-band maximum for each compound made through solution phase infiltration with weaker Q-band maxima for the compounds that were made using templating. The exception of ZnPc^{t}Bu$_4$@NH_2-MIL-101(Al) **(9-temp) (Figure 3. 22, p 65)** and FeClPc(COOH)$_3$-CONH-MIL-101(Al) **(12-temp) (Figure 3. 27, p 72)** not absorbing in the Q-band area due to decomposed MPc molecules were also confirmed. PXRD results also displayed that the presence of MPc molecules in high concentration had a definite effect on the crystallinity of the MOF's structure **(Figure 3. 29, p 75)**. ASAP results agreed with PXRD results showing that the presence of each MPc had a direct effect on the surface area of the MOF depending on the concentration MPc **(Figure 3. 28, p 73)**. Solid state electrochemistry also confirmed the presence of each MPc-containing MOF that were prepared through solution phase infiltration **(Section 3.5.2, p 86)**. A visual confirmation is also shown in **(Figure 3. 31, p 78)** which displays the colour of each MPc-containing MOF in comparison to pure NH_2-MIL-101(Al).

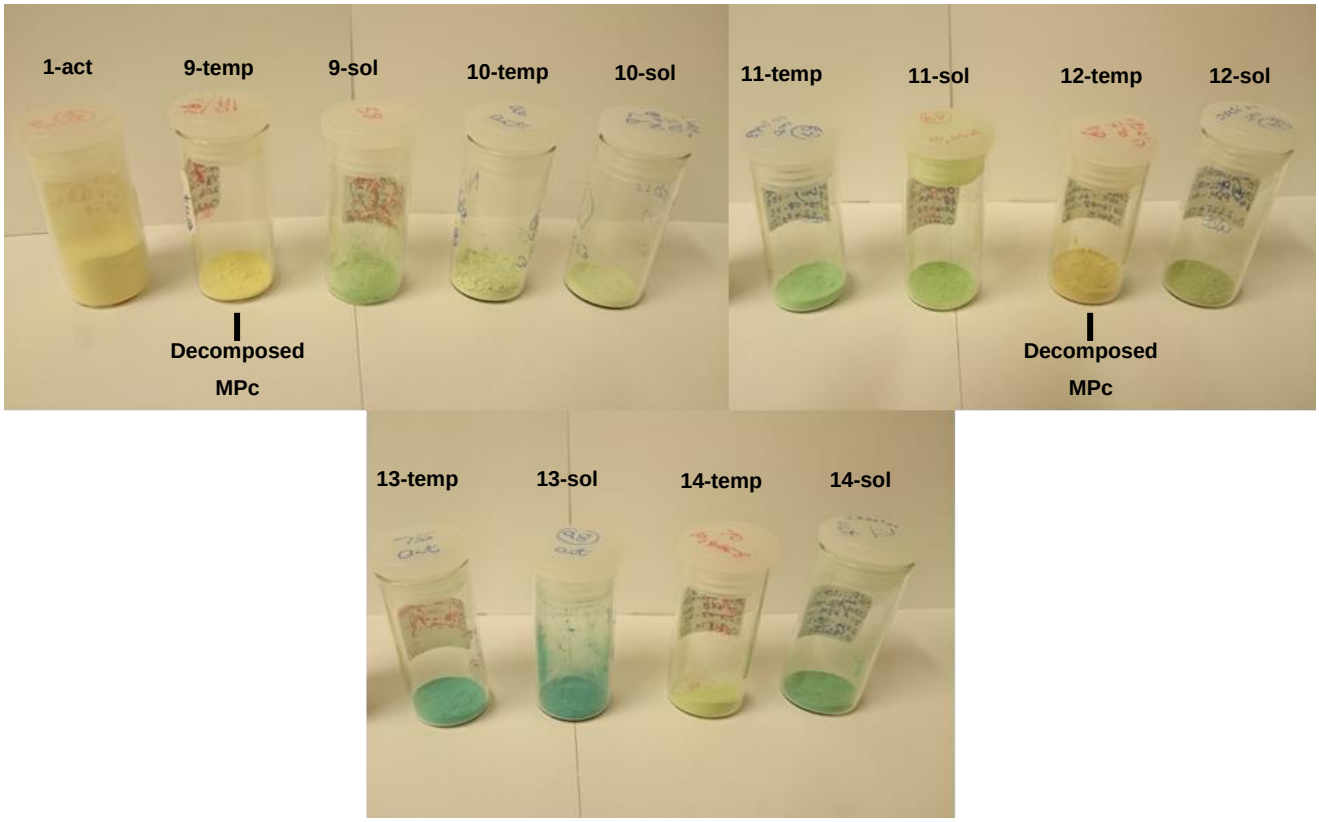

Figure 3. 31: Visual appearance of all MPc-containing MOFs showing the difference in color intensities between templating and solution phase infiltration.

3.4.4 Photocatalytic Testing of $CoPc(COOH)_3$-CONH-MIL-101(Al)

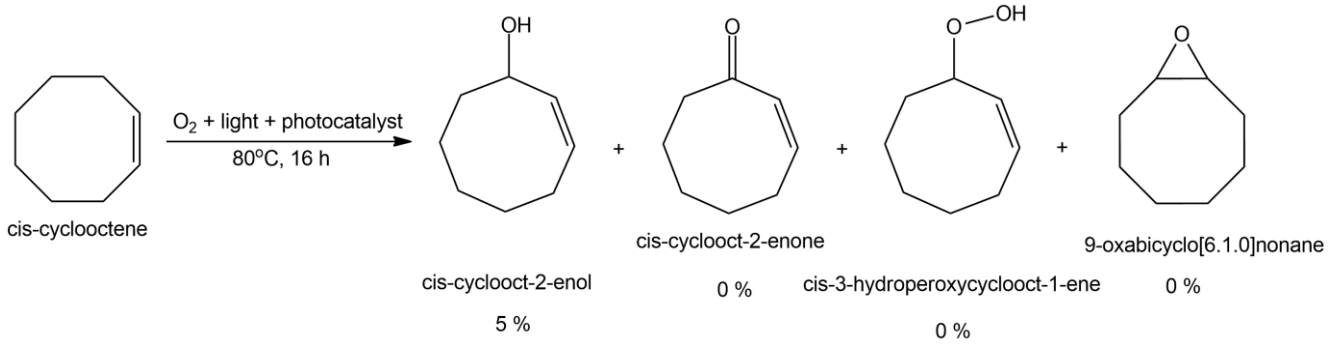

Scheme 3. 6: Photocatalysed oxidation of cis-cyclooctene using $CoPc(COOH)_3$-CONH-MIL-101(Al) **(13-sol)** as the catalyst.

By combining the MPc's strong light harvesting ability and NH_2-MIL-101(Al) as a porous support, the product may be a heterogeneous, green, photo-oxidation catalyst. For this study the best candidate for photo-oxidative capability, $CoPc(COOH)_3$-CONH-MIL-101(Al) **(13-sol)**, was investigated for the possible oxidation of cis-cyclooctene **(Scheme 3. 6, p 78)**. During the oxidation of cis-cyclooctene, four possible products can be obtained: an alcohol, ketone, peroxide or epoxide. After cis-cyclooctene was added to a glass reactor with freshly activated $CoPc(COOH)_3$-CONH-MIL-101(Al), medical air was bubbled through the mixture under vigorous stirring at 80°C for 16 hours, while the reaction was

irradiated with a mercury-halide lamp†. Since no solvent was added, the reaction mixture was cooled, the catalyst filtered off and the mixture analysed with ^{1}H NMR. Due to a low CoPc loading in the MOF, a conversion of only 5% from cis-cyclooctene selectively towards the alcohol cis-cyclooct-2-enol was achieved as shown by ^{1}H NMR **(Figure 3. 32, p 79)** (protons H_c could not be accurately integrated due to overlapping the peak of H_2O). Control reactions without the light source gave no conversion. A reaction with ZnPc(COOH)$_3$-CONH-MIL-101(Al) as catalyst also did not yield any product (See Appendix A-3 and A-4). The cobalt metal of the phthalocyanine was thus critical in the production of cis-cyclooct-2-enol. A similar study by Li and co-workers using Co-Ni-MOF-74 for the oxidation of cyclohexene[10] found that the particular MOF was exclusively selective towards cis-cyclohex-2-enol and cis-cyclohex-2-enone, as was found in this study for cis-cyclooct-2-enol.

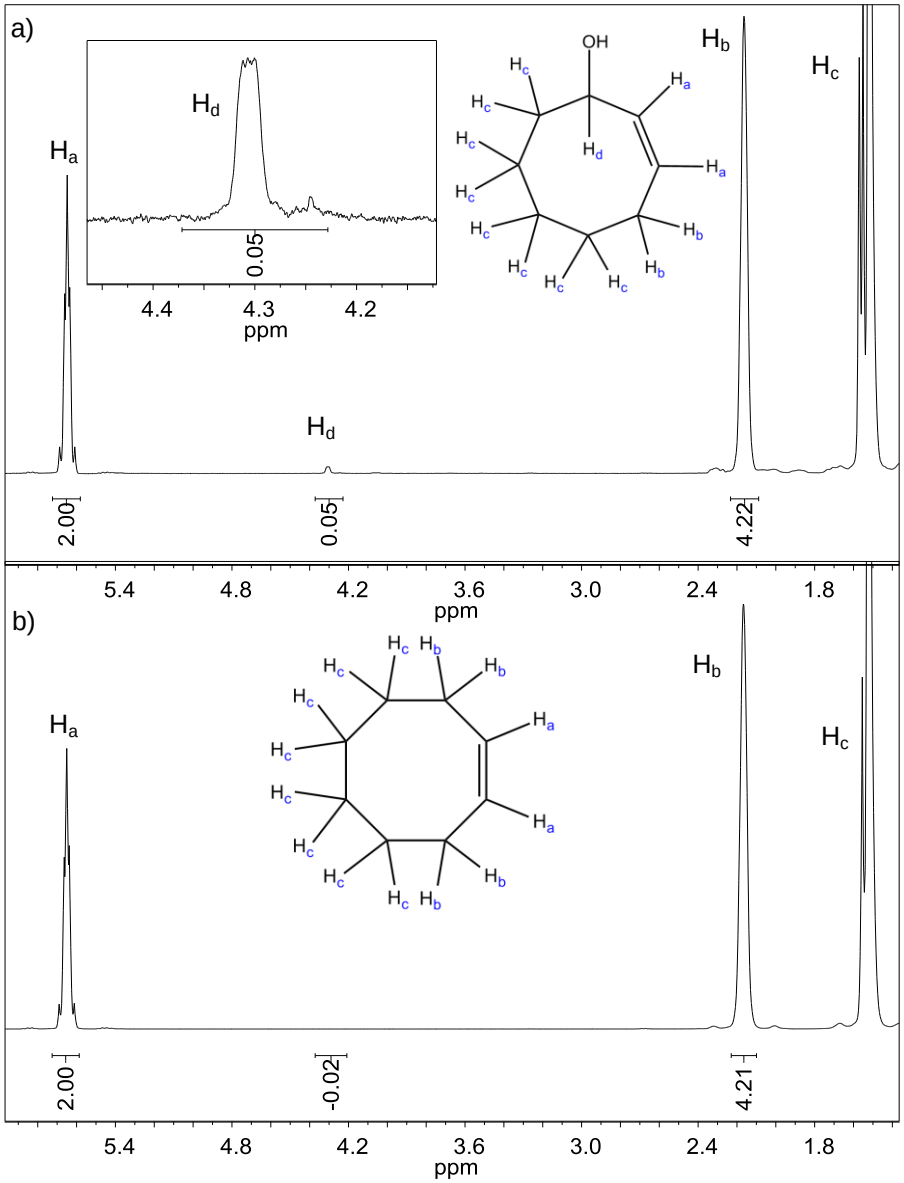

Figure 3. 32: ^{1}H NMR of a) cis-cyclooctene and b) the possible product mixture of cis-cyclooctene and cis-cyclooct-2-enol.

† This lamp produces a spectrum close to that of sunlight.

3.5 Electrochemistry

Two different cyclic voltammetry methods were used: liquid state for all MPcs and solid state for all MPc-loaded MOF products.

3.5.1 Liquid State Electrochemistry of Tetra-*tert*-butyl- and Tetracarboxy-functionalised Phthalocyanines

Unless otherwise stated all MPc^tBu_4 and all cyclic voltammograms were obtained at an MPc concentration of 0.25 mM in CH_2Cl_2, while the concentration for all $MPc(COOH)_4$ analyses were 0.5 mM in DMSO under Argon.

The cyclic voltammogram of $2HPc^tBu_4$ **(2) (Figure 3. 33, a, p 82)**, has the typical redox couples of a metal-free phthalocyanine: two oxidation processes **(Figure 3. 33, i & ii, p 82)** in the positive region of the solvent window with E°′ = 87 mV and 918 mV respectively; two of the four possible reduction processes normally associated with MPcs are observed in the negative region of the solvent window at E°′ = -1299 mV and -1687 mV respectively **(Figure 3. 33, iii & iv, p 82)**. The two oxidation processes **(i and ii)** for $2HPc^tBu_4$ and $ZnPc^tBu_4$ fall in the same formal reduction potential **(Figure 3. 33, a & b, p 82)**, but are shifted more negatively for $NiPc^tBu_4$: E°′ = -143 mV and 377 mV respectively **(Figure 3. 33c, p 82)**. For the reduction waves **(iii and iv)**, a negative shift was observed for both $ZnPc^tBu_4$ and $NiPc^tBu_4$ at E°′ = -1465 mV and -1853 mV respectively in comparison to those of $2HPc^tBu_4$. The central metal of the MPc thus have an effect on the formal reduction potentials of the specific MPc. In this study the effect is the largest for nickel. Since Ni and Zn are regarded as redox inactive metals, these four redox processes belong entirely to the Pc-ring in all three products: wave IV = $[MPc]^{2-}/[MPc]^{-\bullet}$, wave III = $[MPc]^{-\bullet}/[MPc]$, wave I = $[MPc]/[MPc]^{+\bullet}$ and wave II = $[MPc]^{-\bullet}/[MPc]^{2+}$. Waves I and II were overall found to be chemically semi-reversible due to low i_{pc}/i_{pa} values, but for waves III and IV i_{pc}/i_{pa} remained close to unity. This chemical semi-reversibility is not due to outside physical or chemical processes, but low solubility instead. Even though these three products are fairly soluble in CH_2Cl_2, aggregation can still occur at the concentrations used during the CV analyses (0.25 mM). During aggregation, the formed $[MPc]^{2-}$, $[MPc]^{-\bullet}$ and $[MPc]^{2+}$ species inside the inner stacked MPc layers are too insoluble to allow reversible redox processes. For $2HPc^tBu_4$ **(Figure 3. 33, a, p 82)**, wave I and II are regarded as electrochemically quasi reversible (90 mV < ΔE_p < 150 mV) as well as for wave I of $ZnPc^tBu_4$ **(Figure 3. 33, a & b, p 82)** and $NiPc^tBu_4$ **(Figure 3. 33, c, p 82)**. All other processes can be regarded as electrochemically reversible (ΔE_p < 90 mV).

The cyclic voltammograms of $ZnPc(COOH)_4$ **(a)** and $FeClPc(COOH)_4$ **(b) (Figure 3. 34, a & b, p 83)**, show only three processes in the solvent window of DMSO. Only $ZnPc(COOH)_4$ **(a)** displayed the Pc-ring oxidation step at 463 mV **(Figure 3. 34, ai, p 83)**. For $FeClPc(COOH)_4$ **(b)** the redox process marked $Fe^{2+/3+}$, is related to the central Fe^{2+} metal of the MPc. In the negative region of the solvent window two reduction processes **(iii and iv)** could be detected for both $ZnPc(COOH)_4$ and $FeClPc(COOH)_4$ at similar E°′ values **(see Table 3. 3, p 84)**. The low solubility of $ZnPc(COOH)_4$ resulted in electrochemical quasi-reversibility to irreversibility as well as chemical semi-reversibility for all three processes. $FeClPc(COOH)_4$ **(b)** has electrochemical reversible Pc-ring and metal redox processes with $\Delta E_p < 90$ mV. Chemical reversibility was also found for every wave except for the last Pc ring reduction **(Figure 3. 34, biv, p 83)** which is semi-reversible with an average i_{pc}/i_{pa} of 0.65. It is suspected that not only did the axial chloride of the Fe-Cl metal centre make the MPc more soluble; it could also have had a stabilisation effect during the redox states.

$CoPc(COOH)_4$ **(Figure 3. 34, c, p 83)** has two oxidation processes (E°′ = 74 mV (i) and 710 mV (ii)), two reduction processes (E°′ = -1627 mV (iii) and E_p = -2325 mV (iv)), as well as two metal-centered redox processes for $Co^{1+/2+}$ and $Co^{2+/3+}$ at E°′ = -738 mV and -289 mV respectively. For this specific case, ferrocene was used as an internal reference material in order to observe the cobalt redox process. The Ferrocene couple overshadows the first ring oxidation process of the Pc ring, therefore the analyte scans are included to observe the first Pc ring redox process **(Figure 3. 34, c2, p 83)**. Only wave **iii** ($[MPc]^{-\bullet}/[MPc]$) and the metal centered process, $Co^{2+/3+}$, were electrochemically reversible, whereas all other waves were quasi-reversible. All processes were chemically semi-reversible for $CoPc(COOH)_4$. $NiPc(COOH)_4$ **(8) (Figure 3. 34, d, p 83)** shows three redox processes in the negative section of the solvent window and no processes in the positive part. Wave **i** is electrochemically and chemically reversible, but waves **iii** and **iv** are only electrochemically reversible and chemically semi-reversible. This showed that the aggregation present, only affected the reduction waves and not the first oxidation wave.

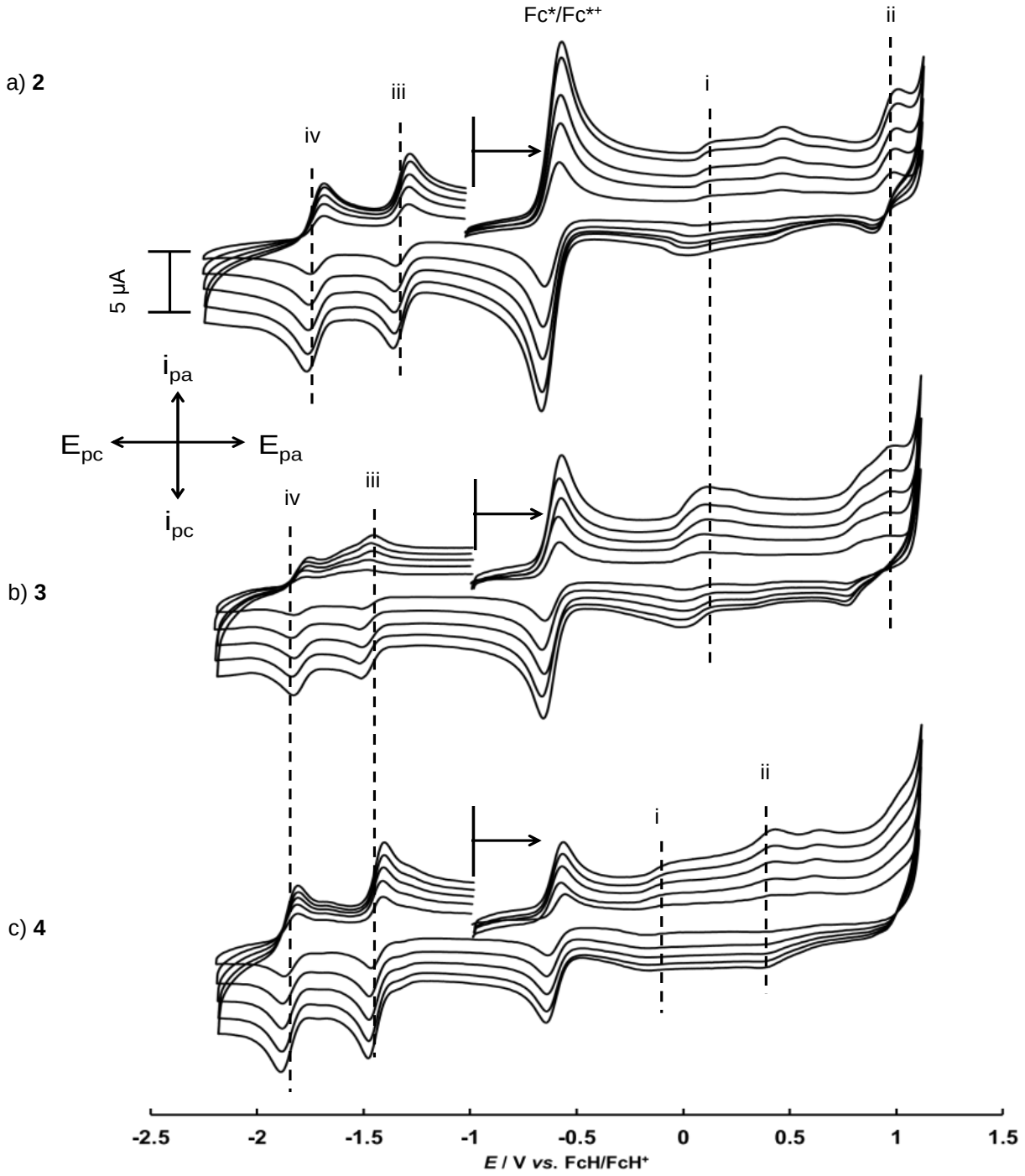

Figure 3. 33: Cyclic voltammograms (CVs) of 0.25 mM a) 2HPc^{t}Bu$_4$ **(2)**, b) ZnPc^{t}Bu$_4$ **(3)** and c) NiPc^{t}Bu$_4$ **(4)** at scan speeds 100, 200, 300, 400 and 500 mV s^{-1} with ~ 0.25 M [NBu$_4$][PF$_6$] as supporting electrolyte in CH_2Cl_2 under Argon. Fc* = Decamethylferrocene; FcH = Ferrocene.

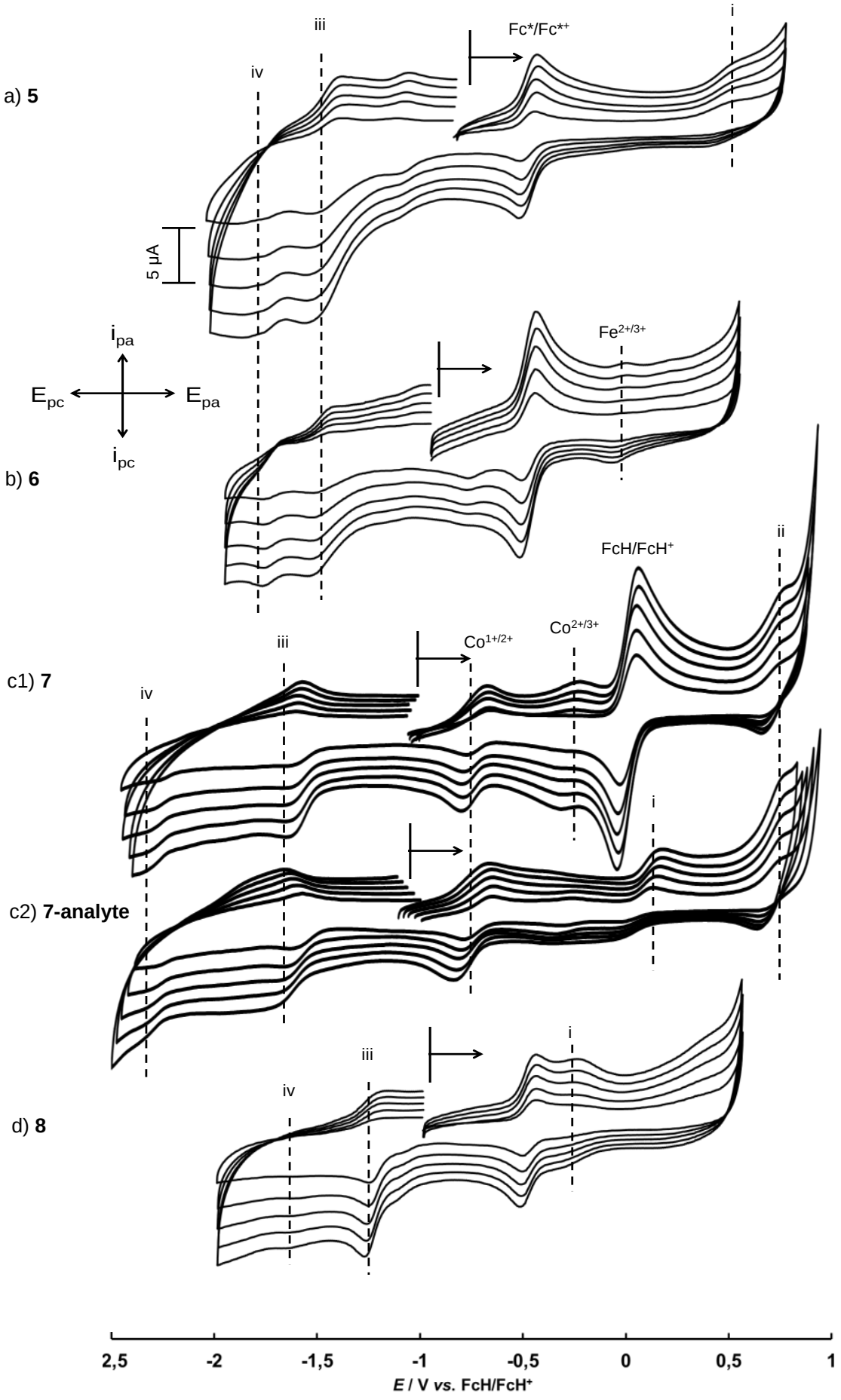

Figure 3. 34: Cyclic voltammograms (CVs) of 0.5 mM a) $ZnPc(COOH)_4$ **(5)**, b) $FeClPc(COOH)_4$ **(6)**, c) $CoPc(COOH)_4$ **(7)** and d) $NiPc(COOH)_4$ **(8)** at scan speeds 100, 200, 300, 400 and 500 mV s^{-1} with ~ 0.25 M $[NBu_4][PF_6]$ as supporting electrolyte in DMSO under Argon. Fc* = Decamethylferrocene; FcH = Ferrocene.

Table 3. 3: CV data of 2HPc^{t}Bu$_4$ **(2)**, ZnPc^{t}Bu$_4$ **(3)**, NiPc^{t}Bu$_4$ **(4)**, ZnPc(COOH)$_4$ **(5)**, FeClPc(COOH)$_4$ **(6)**, CoPc(COOH)$_4$ **(7)** and NiPc(COOH)$_4$ **(8)** at scan speeds 100, 200, 300, 400 and 500 mV s^{-1}. Compounds **2**, **3** and **4** were analysed in 0.25 mM while **5**, **6**, **7** and **8** was analysed in 0.5 mM with ~0.25 M [NBu_4][PF_6] as supporting electrolyte under Argon.

Product	*v*/ mV s^{-1}	Wave I					Wave II				
		E_{pa} (mV)	ΔE_p (mV)	E°′ (mV)	i_{pa} (μA)	i_{pc}/i_{pa}	E_{pa} (mV)	ΔE_p (mV)	E°′ (mV)	i_{pa} (μA)	i_{pc}/i_{pa}
2HPc^{t}Bu$_4$ **(2)**	100	145	77	106	0,74	0,16	964	78	924	2,14	0,38
	200	145	94	98	1,03	0,48	972	94	924	2,96	0,41
	300	145	122	83	1,19	0,51	964	94	916	3,91	0,42
	400	145	133	78	1,31	0,56	968	102	917	4,94	0,48
	500	145	148	71	1,44	0,62	964	102	913	5,15	0,56
ZnPc^{t}Bu$_4$ **(3)**	100	76	64	44	0,72	0,66	846	70	811	0,7	0,65
	200	90	78	51	0,96	0,67	862	78	822	0,98	0,56
	300	98	102	47	1,42	0,50	846	70	811	1,20	0,5
	400	103	107	49	1,56	0,49	865	89	820	1,32	0,49
	500	104	108	50	1,95	0,49	862	86,6	819	1,90	0,36
NiPc^{t}Bu$_4$ **(4)**	100	-105	79	-144	0,36	0,67	414	69	379	0,29	0,83
	200	-94	107	-147	0,48	0,50	414	68	380	0,43	0,89
	300	-105	86	-148	0,48	0,60	414	71	378	0,91	0,89
	400	-89	110	-144	0,67	0,43	414	77	375	1,08	0,84
	500	-73	118	-132	0,53	0,68	414	79	374	1,32	0,82
ZnPc(COOH)$_4$ **(5)**	100	508	91	462	0,48	0,35	-	-	-	-	-
	200	513	92	467	0,72	0,25	-	-	-	-	-
	300	521	118	462	0,84	0,23	-	-	-	-	-
	400	523	106	470	0,94	0,26	-	-	-	-	-
	500	520	131	455	0,99	0,24	-	-	-	-	-
FeClPc(COOH)$_4$ **(6)**	100	-	-	-	-	-	-	-	-	-	-
	200	-	-	-	-	-	-	-	-	-	-
	300	-	-	-	-	-	-	-	-	-	-
	400	-	-	-	-	-	-	-	-	-	-
	500	-	-	-	-	-	-	-	-	-	-
CoPc(COOH)$_4$ **(7)**	100	76	158	-3	1,26	0,29	767	63	735	0,83	0,50
	200	129	165	46	1,51	0,50	752	71	716	1,24	0,33
	300	168	180	78	1,96	0,31	759	74	722	1,66	0,38
	400	215	196	117	1,96	0,54	753	112	697	1,66	0,45
	500	232	205	129	2,41	0,44	736	118	676	1,74	0,48
NiPc(COOH)$_4$ **(8)**	100	-236	69	-270	0,23	0,80	-	-	--	-	-
	200	-235	70	-269	0,30	0,90	-	-	-	-	-
	300	-233	72	-269	0,32	0,90	-	-	-	-	-
	400	-232	73	-268	0,38	0,96	-	-	-	-	-
	500	-229	76	-267	0,45	0,97	-	-	-	-	-

		FeClPc(COOH)$_4$ **(6)** $M^{2+/3+}$				
		E_{pa} (mV)	ΔE_p (mV)	E°′ (mV)	i_{pa} (μA)	i_{pc}/i_{pa}
	100	-56	63	-87	0,21	1,00
	200	-55	65	-87	0,25	0,92
	300	-56	63	-87	0,39	0,95
	400	-58	63	-89	0,41	0,95
	500	-56	70	-91	0,43	0,95

Table 3. 4 continued:

Product	*v*/ mV s^{-1}	Wave III					Wave IV				
		E_{pc} (mV)	ΔE_p (mV)	$E^{\circ\prime}$ (mV)	i_{pc} (μA)	i_{pa}/i_{pc}	E_{pc} (mV)	ΔE_p (mV)	$E^{\circ\prime}$ (mV)	i_{pc} (μA)	i_{pa}/i_{pc}
$2HPc^tBu_4$ **(2)**	100	-1264	65	-1301	2,48	0,88	-1714	69	-1679	2,84	1
	200	-1262	68	-1296	3,94	0,86	-1721	74	-1684	3,79	0,97
	300	-1262	72	-1298	4,64	0,89	-1732	86	-1689	4,94	0,94
	400	-1262	74	-1299	5,80	0,82	-1734	86	-1691	6,18	0,93
	500	-1264	78	-1303	6,63	0,86	-1737	88	-1693	7,01	0,94
$ZnPc^tBu_4$ **(3)**	100	-1516	63	-1485	1,08	0,22	-1817	64	-1785	0,60	0,8
	200	-1518	64	-1485	1,20	0,42	-1820	67	-1786	0,96	0,87
	300	-1518	64	-1485	2,17	0,21	-1823	70	-1788	1,4	0,68
	400	-1516	63	-1485	2,65	0,22	-1830	78	-1790	1,68	0,87
	500	-1524	63	-1493	2,89	0,19	-1831	80	-1791	2,14	0,87
$NiPc^tBu_4$ **(4)**	100	-1476	66	-1443	2,14	0,90	-1872	64	-1840	1,68	0,86
	200	-1478	68	-1444	3,37	0,75	-1877	68	-1843	2,41	0,90
	300	-1479	71	-1444	4,93	0,68	-1888	79	-1849	3,01	0,96
	400	-1483	72	-1446	5,53	0,67	-1886	71	-1851	3,61	1,00
	500	-1484	75	-1446	5,29	0,89	-1889	72	-1853	4,33	0,94
$ZnPc(COOH)_4$ **(5)**	100	-1501	109	-1446	1,92	0,50	-1861	194	-1764	0,96	-
	200	-1513	122	-1452	3,13	0,38	-1862	197	-1764	1,08	-
	300	-1549	158	-1470	3,49	0,38	-1861	194	-1764	1,20	-
	400	-1554	162	-1473	4,45	0,31	-1862	197	-1764	1,32	-
	500	-1554	162	-1473	4,81	0,30	-1861	194	-1764	1,44	-
$FeClPc(COOH)_4$ **(6)**	100	-1561	81	-1521	0,82	0,38	-1810	84	-1768	0,43	0,95
	200	-1567	82	-1526	1,34	0,37	-1813	89	-1768	0,52	0,96
	300	-1563	82	-1522	1,65	0,31	-1810	84	-1768	0,66	0,94
	400	-1570	85	-1527	2,02	0,34	-1814	89	-1770	0,78	0,95
	500	-1576	96	-1528	2,06	0,35	-1818	92	-1772	0,87	0,95
$CoPc(COOH)_4$ **(7)**	100	-1651	68	-1617	1,32	0,16	-2259	-	-	0,83	-
	200	-1653	69	-1618	2,28	0,18	-2299	-	-	1,20	-
	300	-1648	64	-1616	2,48	0,20	-2314	-	-	1,24	-
	400	-1671	64	-1640	2,98	0,25	-2354	-	-	1,45	-
	500	-1686	77	-1647	3,52	0,24	-2401	-	-	1,57	-
$NiPc(COOH)_4$ **(8)**	100	-1269	66	-1236	0,83	0,45	-1627	63	-1596	0,02	-
	200	-1276	79	-1237	2,13	0,28	-1629	66	-1596	0,11	-
	300	-1276	73	-1240	2,57	0,26	-1627	62	-1596	0,23	-
	400	-1278	84	-1236	3,10	0,27	-1629	62	-1598	0,30	-
	500	-1279	94	-1232	3,63	0,25	-1627	67	-1594	0,38	-
		$CoPc(COOH)_4$ **(7)** $M^{1+/2+}$					$CoPc(COOH)_4$ **(7)** $M^{2+/3+}$				
		E_{pa} (mV)	ΔE_p (mV)	$E^{\circ\prime}$ (mV)	i_{pa} (μA)	i_{pc}/i_{pa}	E_{pa} (mV)	ΔE_p (mV)	$E^{\circ\prime}$ (mV)	i_{pa} (μA)	i_{pc}/i_{pa}
	100	-758	102	-707	1,66	0,50	-223	63	-255	0,08	0,50
	200	-789	102	-738	1,86	0,47	-263	79	-302	0,33	0,63
	300	-766	104	-714	2,07	0,44	-239	80	-279	0,83	0,50
	400	-813	102	-762	2,61	0,41	-263	85	-305	0,91	0,77
	500	-830	118	-771	2,98	0,42	-263	86	-305	1,37	0,61

3.5.2 Solid State Electrochemistry of NH_2-MIL-101(Al)-derivatives with Encapsulated Metallophthalocyanines

The following cyclic voltammograms were performed to investigate the active redox couples of the MOF-encapsulated MPcs. Typically about 0.5 mg of the MOF powder was applied via grafting to the working electrode (glassy carbon) and sealed with a double layer of Nafion® solution. After drying, cyclic voltammograms were taken at 100, 300 and 500 mV s^{-1} in a fully degassed solution of CH_2Cl_2 with ~ 0.25 M $[NBu_4][PF_6]$ as supporting electrolyte.

The cyclic voltammograms of $ZnPc^tBu_4$@NH_2-MIL-101(Al) **(9)** and $NiPc^tBu_4$@NH_2-MIL-101(Al) **(10) (Figure 3. 35, p 87)** both display one electrochemically irreversible process **(i)** (ΔE_p > 300 mV) in the positive region of the solvent window. These processes correlate well with the first Pc ring oxidation processes found earlier for $ZnPc^tBu_4$ and $NiPc^tBu_4$ during liquid state cyclic voltammetry **(Figure 3. 33, p 82)**. Due to the long redox couples the specific anodic and cathodic currents could not be accurately determined. This first redox process **(i)** of the encapsulated MPcs was observed for $ZnPc(COOH)_3$-CONH-MIL-101(Al) **(11)**, $CoPc(COOH)_3$-CONH-MIL-101(Al) **(13)** and $NiPc(COOH)_3$-CONH-MIL-101(Al) **(14)** at similar E°′ values of = 320 mV, 255 mV and 284 mV respectively **(Figure 3. 35, ci, ei and fi, p 87)**, but completely electrochemically and chemically irreversible. For $FeClPc(COOH)_3$-CONH-MIL-101(Al) **(12) (Figure 3. 35, d, p 87)**, the first oxidation process of the MPc ring is not observed, but an oxidation process correlating with the second MPc-ring oxidation is seen at ~E_{pa} = 875 mV **(ii)** and is completely electrochemically and chemically irreversible, due to no anodic peaks detected. A second oxidation process was also detected for $ZnPc(COOH)_3$-CONH-MIL-101(Al) **(ii)** and $NiPc(COOH)_3$-CONH-MIL-101(Al) at E°′ = 1159 mV and 1147 mV respectively as well as a third process for $NiPc(COOH)_3$-CONH-MIL-101(Al) **(iii)** at E°′ = 1383 mV, all electrochemically and chemically irreversible.

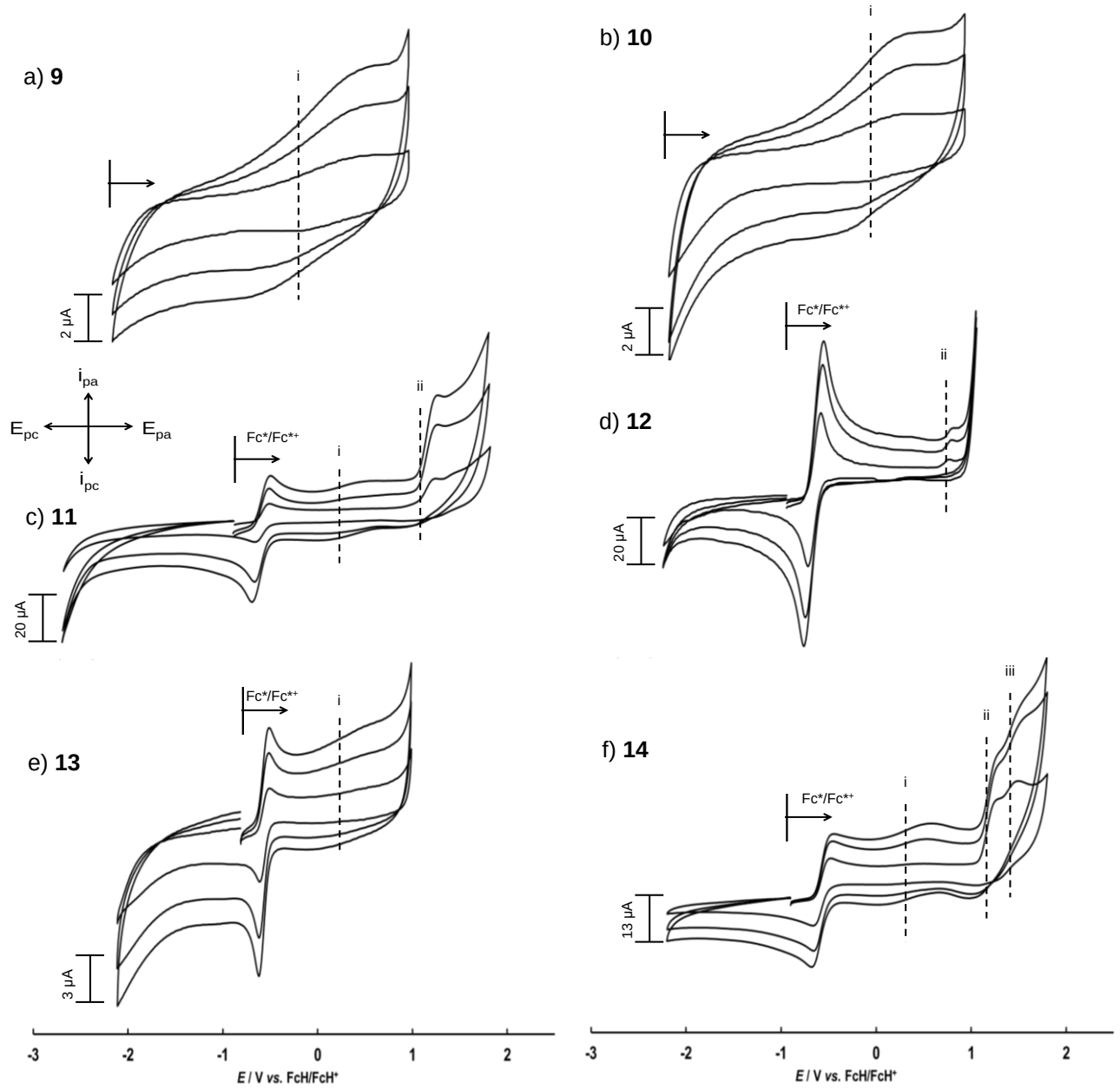

Figure 3. 35: Cyclic voltammograms (CVs) of a) $ZnPc^tBu_4@NH_2$-MIL-101(Al) **(9)**, b) $NiPc^tBu_4@NH_2$-MIL-101(Al) **(10)**, c) $ZnPc(COOH)_3$-CONH-MIL-101(Al) **(11)**, d) $FeClPc(COOH)_3$-CONH-MIL-101(Al) **(12)**, e) $CoPc(COOH)_3$-CONH-MIL-101(Al) **(13)** and f) $NiPc(COOH)_3$-CONH-MIL-101(Al) **(14)** at scan speeds 100, 300 and 500 mV s^{-1} with ~ 0.25 M $[NBu_4][PF_6]$ as supporting electrolyte in CH_2Cl_2 under Argon. For **9** and **10** the CVs are displayed without the internal reference, Fc*.

Table 3. 4: Electrochemical data of $ZnPc^tBu_4@NH_2$-MIL-101(Al) **(9)**, $NiPc^tBu_4@NH_2$-MIL-101(Al) **(10)**, $ZnPc(COOH)_3$-CONH-MIL-101(Al) **(11)**, $FeClPc(COOH)_3$-CONH-MIL-101(Al) **(12)**, $CoPc(COOH)_3$-CONH-MIL-101(Al) **(13)** and $NiPc(COOH)_3$-CONH-MIL-101(Al) **(14)** at scan speeds 100, 300 and 500 mV s^{-1} with ~ 0.25 M $[NBu_4][PF_6]$ as supporting electrolyte in CH_2Cl_2 under Argon.

Product	v/ mV s^{-1}	Wave I					Wave II				
		E_{pa} (mV)	ΔE_p (mV)	$E°'$ (mV)	i_{pa} (μA)	i_{pc}/i_{pa}	E_{pa} (mV)	ΔE_p (mV)	$E°'$ (mV)	i_{pa} (μA)	i_{pc}/i_{pa}
$ZnPc^tBu_4@NH_2$-MIL-101(Al) **(9)**	100	658	724	296	-	-	-	-	-	-	-
	300	658	1003	156	-	-	-	-	-	-	-
	500	632	1298	-17	-	-	-	-	-	-	-
$NiPc^tBu_4@NH_2$-MIL-101(Al) **(10)**	100	353	313	196	-	-	-	-	-	-	-
	300	423	493	176	-	-	-	-	-	-	-
	500	423	564	141	-	-	-	-	-	-	-
$ZnPc(COOH)_3$-CONH-MIL-101(Al) **(11)**	100	-	-	-	-	-	1240	197	1141	6.9	-
	300	564	489	320	1.8	0.51	1293	251	1168	22.9	-
	500	564	489	320	2.3	0.40	1293	251	1168	27.5	-
$FeClPc(COOH)_3$-CONH-MIL-101(Al) **(12)**	100	-	-	-	-	-	849	-	-	2.47	-
	300	-	-	-	-	-	880	-	-	3.95	-
	500	-	-	-	-	-	896	-	-	4.95	-
$CoPc(COOH)_3$-CONH-MIL-101(Al) **(13)**	100	495	479	255	0.02	0.50	-	-	-	-	-
	300	495	479	255	0.31	0.67	-	-	-	-	-
	500	495	542	223	0.62	0.67	-	-	-	-	-
$NiPc(COOH)_3$-CONH-MIL-101(Al) **(14)**	100	453	413	245	0.82	0.10	1260	187	1166	17.73	0.05
	300	541	463	309	2.06	0.60	1279	256	1151	19.44	0.04
	500	541	482	299	2.88	0.86	1279	311	1124	21.44	0.04

		Wave III				
		E_{pa} (mV)	ΔE_p (mV)	$E°'$ (mV)	i_{pa} (μA)	i_{pc}/i_{pa}
$NiPc(COOH)_3$-CONH-MIL-101(Al) **(14)**	100	1476	187	1383	22.26	0.07
	300	1555	-	-	34.63	-
	500	1555	-	-	35.46	-

3.6 References

[1] M. Hartmann and M. Fischer. *Micropor. Mesopor. Mat.* 2012, **164**, 38-43.

[2] E. Stavitski, M. Goesten, J. Juan-Alcañiz, A. Martinez-Joaristi, P. Serra-Crespo, A.V. Petukhov, J. Gascon and F. Kapteijn, *Angew. Chem. Int. Ed.* 2011, **50**, 9624-9628.

[3] T. Ahnfeldt, D. Gunzelmann, T. Loiseau, D. Hirsemann, J. Senker, G. Férey, and N. Stock, *Inorg. Chem.* 2009, **48**, 3057-3064.

[4] I.S. Hosu, Q. Wang, A. Vasilescu, S.F. Peteu, V. Raditoiu, S. Railian, V. Zaitsev, K. Turcheniuk, Q. Wang, M. Li, R. Boukherrouba and S. Szunerits, *RSC Adv*. 2015, **5**,1474-1487.

[5] X. Song, Y. She, H. Ji, and Y. Zhang, *Org. Process Res. Dev.* 2005, **9**, 2228-2232.

[6] A. Dhakshinamoorthy and H. Garcia, *Chem. Soc. Rev*. 2012, **41**, 5262-5284.

[7] P. Chowdhury, C. Bikkina and S. Gumma, *J. Phys. Chem. C*, 2009, **113**, 6616-6621.

[8] P.L. Llewellyn, S. Bourrelly, C. Serre, A. Vimont, M. Daturi, L. Hamon, G. De Weireld, J. Chang, D. Hong, Y.K. Hwang, S.H. Jhung and G. Férey, *Langmuir*, 2008, **24**, 7245-7250.

[9] A. Noguera-Díaz, N. Bimbo, L.T. Holyfield, I.Y. Ahmet, V.P. Ting and T.J. Mays, *Colloids and Surfaces A: Physicochem. Eng. Aspects*, 2016, **496**, 77-85.

[10] D. Sun, F. Sun, X. Deng, and Z. Li, *Inorg. Chem.* 2015, **54**, 8639-8643.

4 Experimental

4.1 Introduction

This chapter describes the instrumentation and chemicals used as well as the chemical procedures and reaction conditions employed. Spectra such as FTIR, TGA, ^{1}H-NMR, UV-Vis and Maldi-TOF mentioned in this chapter, can be found in the Appendix (p A-1 to A-11).

4.2 Materials and Techniques

4.2.1 Chemicals

Solid and liquid reagents as well as solvents were purchased directly from Merck or Aldrich and used without further purification unless otherwise stated. Water used was doubly distilled. A positive atmosphere of either nitrogen or argon was used for inert reactions. Kieselgel 60 (Merck) was used for all column chromatography.

4.2.2 Instrumentation

Fourier transform infrared spectroscopy was performed on a Bruker Tensor 27 IR spectrometer with OPUS v1.1 software.

Nuclear Magnetic Resonance spectroscopy was performed on a Bruker Avance II 600 and a Bruker Avance III HD 400. The samples were either dissolved in $CDCl_3$, or $(CD_3)_2SO$ and their ^{1}H spectra reported relative to $Si(CH_3)_4$ (TMS) at 0 ppm. All spectra were analysed with MestReNova v5.3.0-4469 software.

Surface area and porosity measurements were performed on a Micromeritics Surface Area and Porosity Analyzer (ASAP 2020). Data refinement was done with Microactive v1.01 software.

Thermogravimetric analyses were performed under nitrogen atmosphere on a Mettler Toledo TGA/SDTA851 with software: STAR SW v8.10.

Liquid UV-Vis spectroscopy was performed on a Shimadzu CPS 240A @ 15°C.

DRS-UV-Vis spectroscopy was performed on a PerkinElmer Lambda 35 @ 25°C.

Mass spectrometry was perfomed by means of a Matrix Assisted Laser Desorption Ionization Time-Of-Flight (TOF) Bruker Microflex LRF20 in either positive of negative mode with the minimum laser power (337 nm) required to observe signals. All supporting mass spectroscopy data are given in Appendix A-8 to A-11.

The visual analysis of melting points and phase transition temperatures were done with an Olymus BX-51 polarising microscope equiped with a Linkham TMS 92 controller and a Linkham THM 600 hot stage.

Low and wide angle PXRD analyses were performed at iThemba Labs on a Bruker AXS D8 Advance. A Cu-Kα radiation tube with LynxEye detectors were used for all experiments. The 2θ range was between 0.5° and 50° with an increment of 2θ = 0.0103°. An air scattering slit was used to obtain low angle diffraction peaks.

4.3 Electrochemistry

4.3.1 Liquid State Electrochemistry

A glassy carbon electrode with a 3 mm diameter, was employed by polishing the surface first with 1 micron and then ¼ micron diamond paste on a Bueler microcloth and washing the electrode with methanol, acetone, water and DCM before use. The three-electrode cell setup included a platinum wire as reference electrode and a platinum auxiliary electrode to complete the circuit. A ~0.25 M solution of $[NBu_4][PF_6]$ was used as supporting electrolyte. Unless otherwise stated, all MPc^tBu_4 experiments were performed with an MPc concentration of 0.25 mM in CH_2Cl_2 while all $MPc(COOH)_4$ experiments were performed with an MPc concentration of 0.5 mM in DMSO under Argon purged for 2-3 minutes. Decamethyl ferrocene was used as internal reference (0.1 mM) and referenced back to Fc/Fc^+ (0 V) except for $CoPc(COOH)_4$ where only Fc was used as internal reference.

4.3.2 Solid State Electrochemistry

The electrode preparation and cell setup was identical to that of the liquid state electrochemistry. The analyte was fixated as a solid onto the electrode surface via grafting and sealed with Nafion® twice. Measurements were taken in a ~0.25 M solution of $[NBu_4][PF_6]$ in anhydrous DCM, with decamethyl

ferrocene (~0.1 mM) as the internal reference and referenced back to Fc/Fc^+ (0 V). Prior to each experiment, the solution was purged with Argon for 2-3 minutes.

4.4 Synthesis of NH_2-MIL-101(Al) (1)

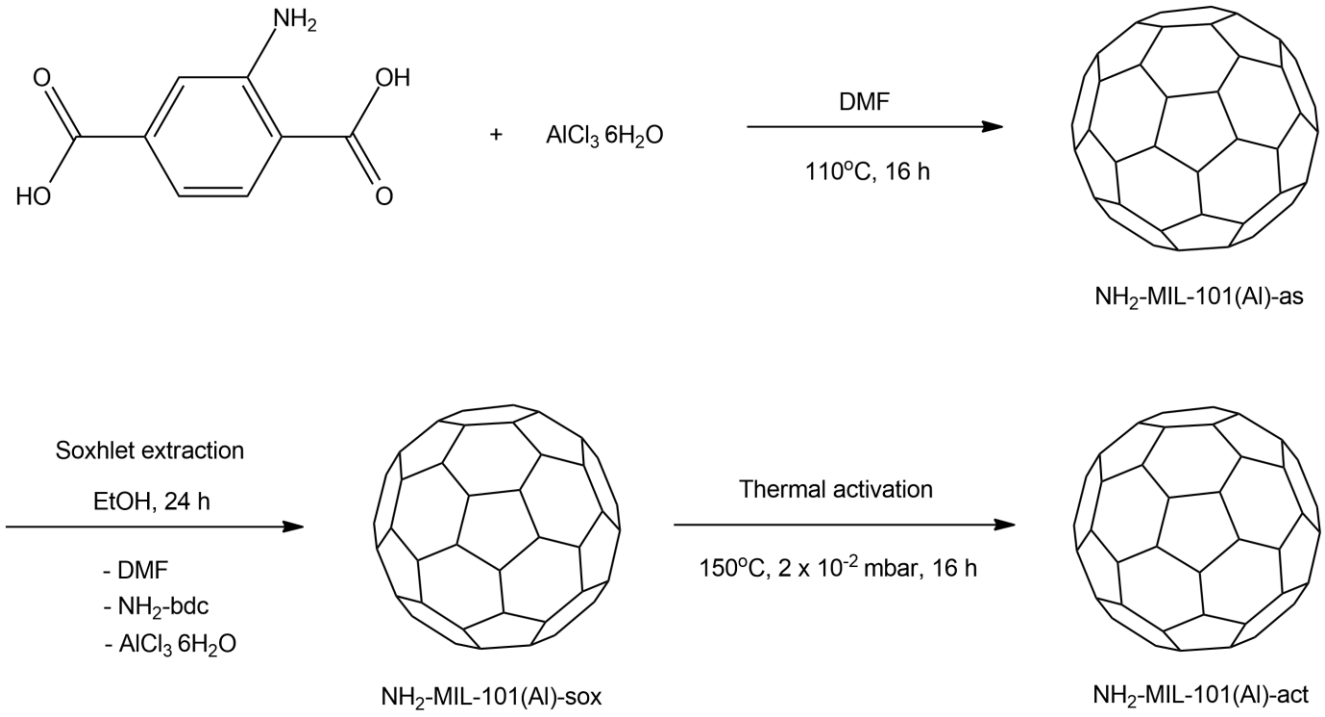

2-Aminoterephthalic acid (0.270 g, 1.49 mmol) was dissolved in hot, anhydrous DMF (60 cm^3, ~100°C). The DMF was allowed to reach 115°C when aluminium chloride hexahydrate (0.726 g, 3.00 mmol) was added in 7 portions with 15 minutes delay. The reaction mixture was stirred at 115°C for 16 hours before it was cooled down and filtered under vacuum. The crude product was washed with wet DMF (20 cm^3) and ethanol (20 cm^3). After drying in air (25°C, 3 h), the product was soxhlet extracted in ethanol for 24 hours. The product was dried in air (90°C, 24 h) and the final activation step was performed under vacuum in three temperature stages: 1) 50°C, 1 hour, 2) 100°C, 1 hour, 3) 150°C, 16 hours. The product was obtained as a light-yellow, amorphous powder (0.326 g, 31.0%). ν_{max}/cm^{-1} 3440 & 3357 (N-H), 1571 & 1496 (C-O asym.), 1434 & 1388 (C-O sym.). PXRD Figure 3.5, p 44.

4.5 Synthesis of 2(3),9(10),16(17),23(24)-Tetra-*tert*-butylphthalocyanine (2)

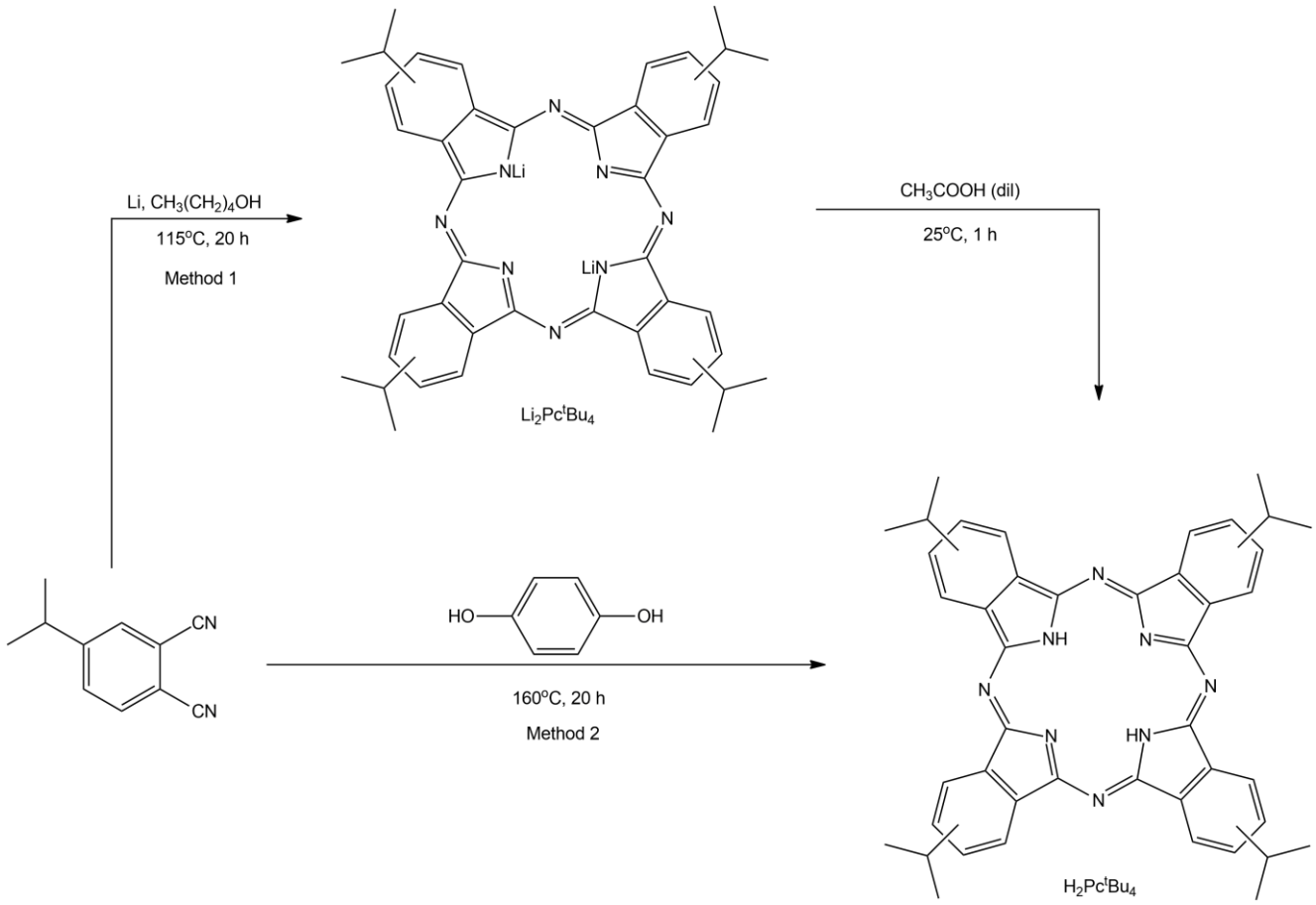

4.5.1 Method 1

Pentanol (1 cm^3) was added to 4-*tert*-butylphthalonitrile (0.051 g, 0.28 mmol) under an argon atmosphere at 115°C. Clean lithium metal (30 mg, 4.34 mmol) was added in three small portions and the mixture refluxed for 20 hours. The reaction was cooled to room temperature; acetic acid (20 cm^3, 5%) was added and stirred at room temperature for 1 hour. Water (50 cm^3) and DCM (30 cm^3) was added and the solution transferred to a separating funnel where the product was further extracted with DCM (2 x 10 cm^3). The organic phases were combined and the solvent evaporated under vacuum. The crude product was eluted through a short silica column with n-hexane:diethyl ether = 3:1. The product was recrystallised by dissolution it in hot n-hexane and slow precipitation by adding cold methanol until the solution turned murky. The product solution was capped and cooled overnight before it was filtered and washed with cold methanol (2 cm^3). After evacuating the product overnight at 50°C, it was collected as blue-black crystals (0.009 g, 17.6%). δ_H(600 MHz, $CDCl_3$)/ppm

9.39-9.32 (4H, m, Ar-H), 9.26-9.21 (4H, m, Ar-H), 8.21 (4H, m, Ar-H), 1.77 (36H, sd, $C(C\text{-}H_3)_3$), -0.86- -1.01 (2H, q, N-H). ν_{max}/cm^{-1} 2900 ($C(C\text{-}H_3)_3$). MS (M^+) Calcd. for $C_{48}H_{50}N_8$ m/z = 738.4. Found m/z = 738.4. Rf = 0.79 (hexane:ether = 3:1). m.p. > 250°C.

4.5.2 Method 2

4-*tert*-butylphthalonitrile (0.051 g, 0.28 mmol) together with hydroquinone (0.038 g, 0.34 mmol) was sealed under argon in a glass reactor. The reaction mixture was kept at 160°C for 20 hours before it was cooled to room temperature. After adding dichloromethane (DCM) (30 cm^3) and water (H_2O) (50 cm^3) to the crude reaction, the mixture was transferred to a separating funnel and quantitatively extracted with DCM (4 x 10 cm^3). The crude product was eluted through a short silica column with solvents n-hexane:diethyl ether = 3:1. The product was recrystallised by dissolution in hot n-hexane and slow precipitation by adding cold methanol until the solution turned murky. The product solution was capped and cooled overnight before it was filtered and washed with cold methanol (5 cm^3). After evacuating the product overnight at 50°C, it was collected as blue-black crystals (0.015 g, 29.3%). δ_H(600 MHz, $CDCl_3$)/ppm 9.3-9.28 (4H, m, Ar-H), 9.22-9.18 (4H, m, Ar-H), 8.20 (4H, m, Ar-H), 1.77 (36H, sd, $C(C\text{-}H_3)_3$), -0.97- -1.12 (2H, q, N-H). ν_{max}/cm^{-1} 2900 ($C(C\text{-}H_3)_3$). MS (M^+) Calcd. for $C_{48}H_{50}N_8$ m/z = 738.4. Found m/z = 738.4. Rf = 0.79 (hexane:ether = 3:1). m.p.. > 250°C.

4.6 Complexation of 2(3),9(10),16(17),23(24)-Tetra-*tert*-butyl-phthalocyanines with Zn^{2+} and Ni^{2+}

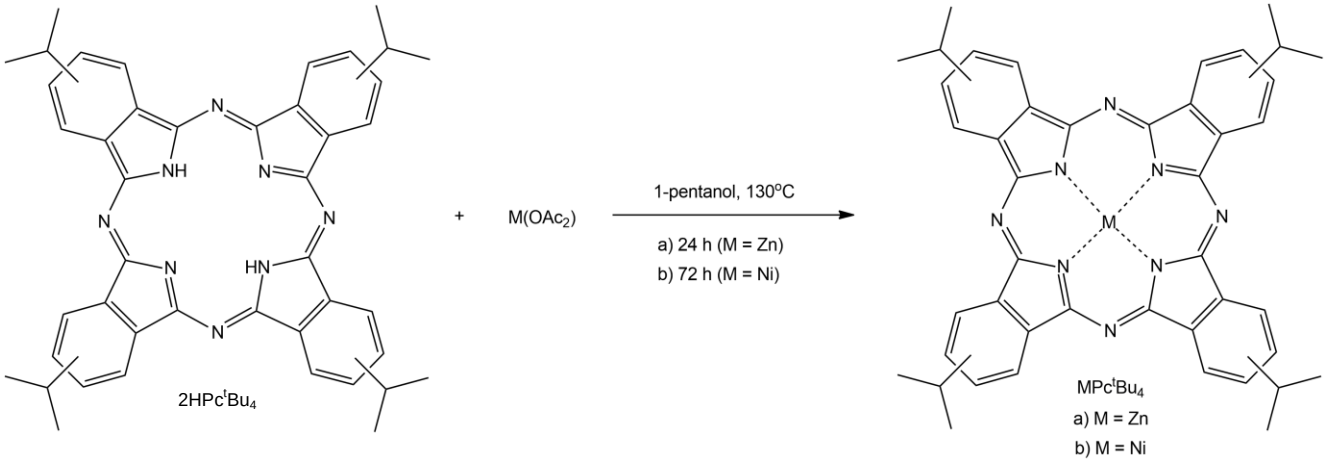

4.6.1 2(3),9(10),16(17),23(24)-Tetra-*tert*-butylphthalocyanatozinc (3)

Zinc(II)acetate dihydrate (0.078g, 0.36 mmol) and 2(3),9(10),16(17),23(24)-tetra-tert-butyl-phthalocyanine (0.051 g, 0.07 mmol) was mixed together in pentanol (4 cm^3) and reacted for 16 hours at 130°C. After cooling down to room temperature, methanol (2 cm^3) was added, the precipitate filtered and washed with cold methanol (10 cm^3). The crude product was recrystallised with THF/methanol, filtered, washed with clean methanol (1 cm^3) and dried under vacuum (70°C, 16 hours) to obtain the metallated phthalocyanine as blue-black flaky crystals (0.057 g, 104%). δ_H(600 MHz, $CDCl_3$)/ppm 8.98-8.73 (8H, m, Ar-H), 8.00 (4H, m, Ar-H), 1.71 (32H, sd, $C(C\text{-}H_3)_3$). ν_{max}/cm^{-1} 2900 ($C(C\text{-}H_3)_3$). MS (M^+) Calcd. for $C_{48}H_{48}N_8Zn$ m/z = 800.3. Found m/z = 800.5. Rf = 0.35 (hexane:ethyl acetate = 4:1). m.p. > 250°C.

4.6.2 2(3),9(10),16(17),23(24)-Tetra-*tert*-butylphthalocyanatonickel (4)

The same procedure was followed as for **4.6.1**, with nickel(II)acetate hexahydrate (0.085 g, 0.34 mmol) (instead of zinc(II)acetate dihydrate) mixed with 2(3),9(10),16(17),23(24)-tetra-tert-butylphthalocyanine (0.050 g, 0.07 mmol). After workup, the product was obtained as blue crystals (0.058 g, 107%). δ_H(600 MHz, $CDCl_3$)/ppm 9.23-9.05 (8H, m, Ar-H), 8.11 (4H, m, Ar-H), 1.75 (23H, sd, $C(C\text{-}H_3)_3$). ν_{max}/cm^{-1} 2900 ($C(C\text{-}H_3)_3$). MS (M^+) Calcd. for $C_{48}H_{48}N_8Ni$ m/z = 794.3. Found m/z = 794.3. Rf = 0.76 (hexane:ethyl acetate = 4:1). m.p. > 250°C.

4.6.3 Synthesis of Metalated 2(3),9(10),16(17),23(24)-Tetracarboxy-phthalocyanines

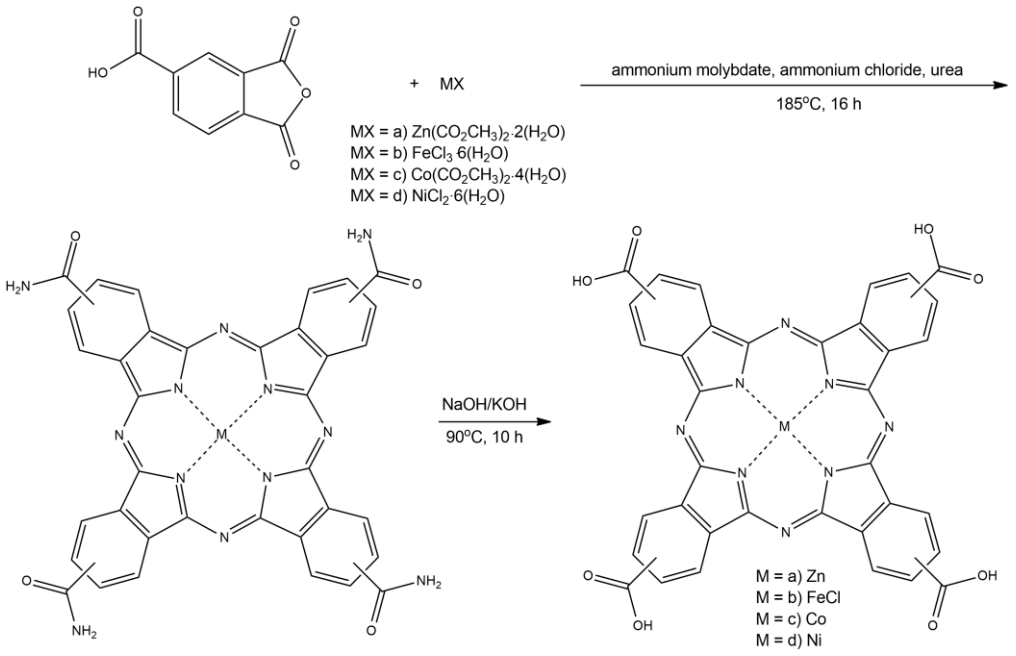

A general procedure was followed for the synthesis of the four tetracarboxylmetallophthalocyanines. A mixture of the particular metal salt, trimellitic anhydride (2.50 g, 11.89 mmol), ammonium chloride (0.50 g, 9.37 mmol), ammonium molybdate (0.25 g, 1.27 mmol) and urea (5.00 g, 83.42 mmol) was ground to a fine powder with a mortar and pestle, transferred to a glass tube, capped and allowed to react at 185°C for 16 hours. After cooling to room temperature, the solidified crude product was washed with methanol (100 cm^3), filtered under vacuum and dried at room temperature. The crude product was dissolved and hydrolysed in aqueous KOH (5 g, 45 cm^3 H_2O) in the absence of light for 5 hours at 90°C. The final product was cooled, filtered and washed with water (250 cm^3) before drying it at 70°C for 16 hours.

4.6.3.1 2(3),9(10),16(17),23(24)-Tetracarboxyphthalocyanatozinc (5)

Metal salt: zinc(II)acetate dihydrate (1.43 g, 6.49 mmol).
Product: dark crystals (0.100 g, 4.6 %). ν_{max}/cm^{-1} 3600-2300 (O-H), 1705 (C=O). MS (M^+) Calcd. for $C_{36}H_{16}N_8O_8Zn$ m/z = 752.0. Found m/z = 752.4. m.p. > 250°C.

4.6.3.2 2(3),9(10),16(17),23(24)-Tetracarboxyphthalocyanatoiron(III)chloride (6)

Metal salt: iron(III)chloride hexahydrate (1.760 g, 6.51 mmol).
Product: dark crystals (0.468 g, 20.1 %). ν_{max}/cm^{-1} 3600-2300 (O-H), 1705 (C=O). MS (M^+) Calcd. for $C_{36}H_{16}N_8O_8FeCl$ m/z = 779.0. Found m/z = 783.3. m.p. > 250°C.

4.6.3.3 2(3),9(10),16(17),23(24)-Tetracarboxyphthalocyanatocobalt (7)

Metal salt: cobalt(II)acetate tetrahydrate (0.810 g, 3.25 mmol).
Product: dark crystals (0.255 g, 21.8 %). ν_{max}/cm^{-1} 3600-2300 (O-H), 1705 (C=O). MS (M^+) Calcd. for $C_{36}H_{16}N_8O_8Co$ m/z = 747.0. Found m/z = 745.2. m.p. > 250°C.

4.6.3.4 2(3),9(10),16(17),23(24)-Tetracarboxyphthalocyanatonickel (8)

Metal salt: nickel(II)chloride hexahydrate (0.772 g, 3.25 mmol).
Product: dark crystals (0.615 g, 52.4 %). ν_{max}/cm^{-1} 3600-2300 (O-H), 1705 (C=O). MS (M^+) Calcd. for $C_{36}H_{16}N_8O_8Ni$ m/z = 746.0. Found m/z = 743.2. m.p. > 250°C.

4.7 Post-synthetic Modification of NH_2-MIL-101(Al)

Two methods were employed to encapsulate the MPc's in NH_2-MIL-101(Al): templating **(4.7.1, p 99)** and solution phase infiltration **(4.7.2, p 101)**. A general procedure was followed for each method unless otherwise stated. TGA's of all interim stages of PSM on products **9-14** are given in Appendix A-5 to A-6.

Templating reaction

2-Aminoterephthalic acid (0.27 g, 1.51 mmol) and the particular MPc (between 7.5 μmol and 13 μmol) were dissolved in hot, anhydrous DMF (60 cm^3, ~100°C). After heating the solution to 115°C, aluminiumchloride hexahydrate (0.723 g, 2.99 mmol) was added in 7 portions with a 15 min delay in a glass reactor. The reaction was kept at 115°C for 16 hours before it was cooled to room temperature and filtered under vacuum.

Workup

The crude product was washed with DMF (20 cm^3) followed by ethanol (20 cm^3). After drying in air (25°C, 3 h), the product was soxhlet extracted in ethanol for 24 hours. After drying the product (70°C, 16 h), it was stirred in DMF (20 cm^3) for 1 minute, filtered under vacuum and rinsed with ethanol (40 cm^3). After repeating this process twice more, the final product was dried at 70°C overnight and activated in vacuo (150°C, 5 $x10^{-2}$ mbar) overnight to obtain the MPc-containing MOF.

Infiltration

For solution phase infiltration, NH_2-MIL-101(Al)-act (0.25 g, 0.36 mmol) was re-activated (150°C, 5 $x10^{-2}$ mbar) for 5 hours and cooled down to room temperature before the particular dissolved MPc (sonicated in anhydrous DMF (10 cm^3, 30 min)) was added in vacuo. The pressure of the vessel was equalized and the phthalocyanine allowed to intrude into the MOF structure for 16 hours at room temperature.

Reaction

The mixture was heated to 100°C for 24 hours, cooled to room temperature and filtered under vacuum.

Workup

The crude product was washed with DMF (40 cm^3) followed by ethanol (80 cm^3). After drying the product in air, it was washed while stirring in DMF (20 cm^3) for 1 minute, filtered under vacuum and rinsed with ethanol (40 cm^3). This process was repeated twice more before the product was finally dried at 70 °C overnight and activated in vacuo (150°C, 5 $x10^{-2}$ mbar) overnight to obtain the MPc-containing MOF.

4.7.1 Method 1: Templating

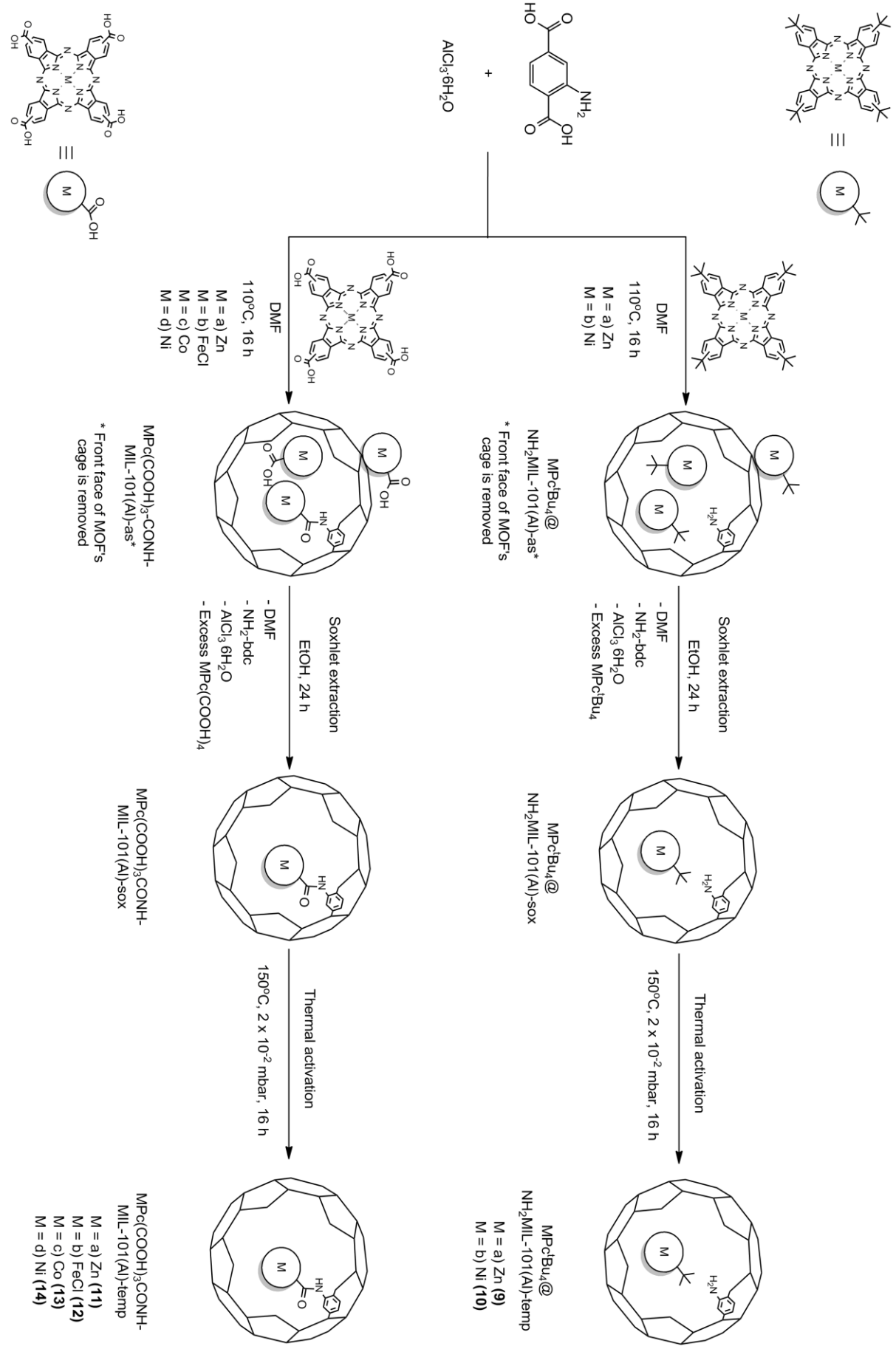

4.7.1.1 $ZnPc^tBu_4@NH_2$-MIL-101(Al)-temp (9-temp)

MPc: $ZnPc^tBu_4$ (10.4 mg 0.013 mmol).

Product: Yellow powder (0.282 g). ν_{max}/cm^{-1} 3458 & 3360 (N-H), 1575 & 1500 (C-O asym.), 1440 & 1388 (C-O sym.). PXRD Figure 3.24, a, p 68.

4.7.1.2 $NiPc^tBu_4@NH_2$-MIL-101(Al)-temp (10-temp)

MPc: $NiPc^tBu_4$ (10.3 mg 0.013 mmol).

Product: Light green powder (0.353 g). ν_{max}/cm^{-1} 3458 & 3360 (N-H), 1640 (C=O), 1575 & 1500 (C-O asym.), 1440 & 1388 (C-O sym.). PXRD Figure 3.24, c, p 68.

4.7.1.3 $ZnPc(COOH)_3$-CONH-MIL-101(Al)-temp (11-temp)

MPc: $ZnPc(COOH)_4$ (6.3 mg, 8.36 μmol).

Product: Green powder (0.324 g). ν_{max}/cm^{-1} 3440 & 3357 (N-H), 1571 & 1496 (C-O asym.), 1434 & 1394 (C-O sym.). PXRD Figure 3.29, a, p 75.

4.7.1.4 $FeClPc(COOH)_3$-CONH-MIL-101(Al)-temp (12-temp)

MPc: $FeClPc(COOH)_4$ (6.3 mg, 8.08 μmol).

Product: Brown powder (0.341 g). ν_{max}/cm^{-1} 3440 & 3357 (N-H), 1645 (C=O), 1571 & 1496 (C-O asym.), 1434 & 1394 (C-O sym.). PXRD Figure 3.29, c, p 75.

4.7.1.5 $CoPc(COOH)_3$-CONH-MIL-101(Al)-temp (13-temp)

MPc: $CoPc(COOH)_4$ (6.2 mg, 7.84 μmol).

Product: Blue-green powder (0.324 g). ν_{max}/cm^{-1} 3440 & 3357 (N-H), 1643 (C=O), 1571 & 1496 (C-O asym.), 1434 & 1394 (C-O sym.). PXRD Figure 3.29, e, p 75.

4.7.1.6 $NiPc(COOH)_3$-CONH-MIL-101(Al)-temp (14-temp)

MPc: $NiPc(COOH)_4$ (6.4 mg, 8.56 μmol).

Product: Light green powder (0.324 g). ν_{max}/cm^{-1} 3440 & 3357 (N-H), 1571 & 1496 (C-O asym.), 1434 & 1394 (C-O sym.). PXRD Figure 3.29, g, p 75.

4.7.2 Method 2: Solution Phase Infiltration

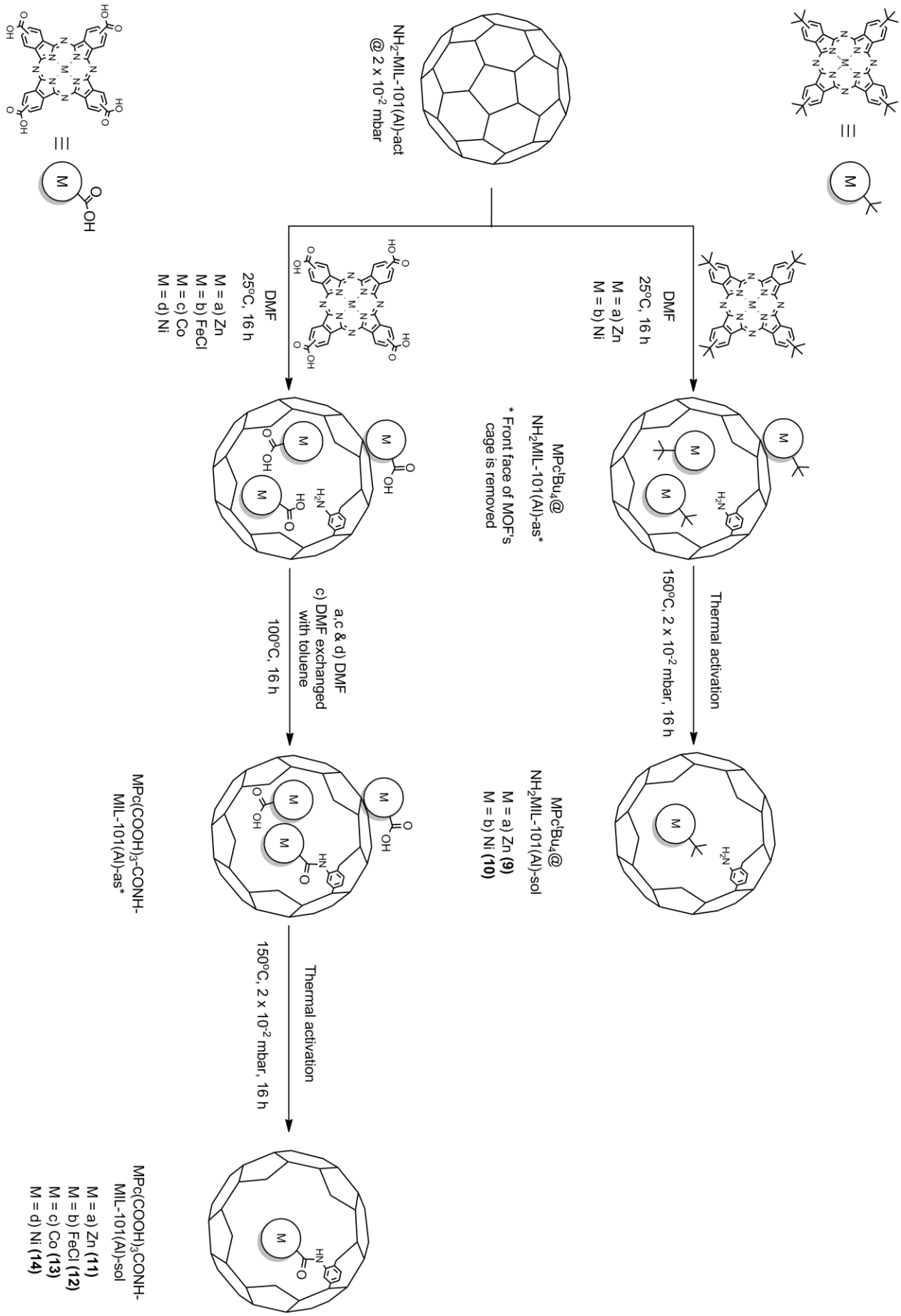

4.7.2.1 $ZnPc^tBu_4@NH_2$-MIL-101(Al)-sol (9-sol)

MPc: $ZnPc^tBu_4$ (10.3 mg 0.013 mmol).

Product: Green powder (0.188 g). ν_{max}/cm^{-1} 3458 & 3360 (N-H), 1575 & 1500 (C-O asym.), 1440 & 1388 (C-O sym.). PXRD Figure 3.24, b, p 68.

4.7.2.2 $NiPc^tBu_4@NH_2$-MIL-101(Al)-sol (10-sol)

MPc: $NiPc^tBu_4$ (10.3 mg 0.013 mmol).

Product: Light green powder (0.200 g). ν_{max}/cm^{-1} 3458 & 3360 (N-H), 1640 (C=O), 1575 & 1500 (C-O asym.), 1440 & 1388 (C-O sym.). PXRD Figure 3.24, d, p 68.

4.7.2.3 $ZnPc(COOH)_3$-CONH-MIL-101(Al)-sol (11-sol)

MPc: $ZnPc(COOH)_4$ (6.3 mg, 8.36 μmol).

Product: Green powder (0.272 g). ν_{max}/cm^{-1} 3440 & 3357 (N-H), 1571 & 1496 (C-O asym.), 1434 & 1394 (C-O sym.). PXRD Figure 3.29, b, p 75.

4.7.2.4 $FeClPc(COOH)_3$-CONH-MIL-101(Al)-sol (12-sol)

In a deviation from the general procedure, the DMF used as solvent during infiltration was then exchanged with anhydrous toluene for the amidation reaction. After infiltration for 16 hours at room temperature, the mixture was filtered under vacuum and washed with DMF (40 cm^3), followed by ethanol (80 cm^3) and dried for 5 hours at 70°C. After cooling to room temperature, anhydrous toluene (10 cm^3) was added and the process continued by reacting at 100°C for 24 hours.

MPc: $FeClPc(COOH)_4$ (6.3 mg, 8.08 μmol).

Product: Dark green powder (0.243 g). ν_{max}/cm^{-1} 3440 & 3357 (N-H), 1571 & 1496 (C-O asym.), 1434 & 1394 (C-O sym.). PXRD Figure 3.29, d, p 75.

4.7.2.5 $CoPc(COOH)_3$-CONH-MIL-101(Al)-sol (13-sol)

MPc: $CoPc(COOH)_4$ (6.3 mg, 8.39 μmol).

Product: Blue-green powder (0.272 g). ν_{max}/cm^{-1} 3440 & 3357 (N-H), 1571 & 1496 (C-O asym.), 1434 & 1394 (C-O sym.). PXRD Figure 3.29, f, p 75.

4.7.2.6 NiPc(COOH)$_3$-CONH-MIL-101(Al)-sol (14-sol)

MPc: NiPc(COOH)$_4$ (6.2 mg, 8.39 μmol).

Product: Dark green powder (0.222 g). ν_{max}/cm^{-1} 3440 & 3357 (N-H), 1645 (C=O), 1571 & 1496 (C-O asym.), 1434 & 1394 (C-O sym.). PXRD Figure 3.29, h, p 75.

4.8 Photocatalytic Oxidation of Cis-Cyclooctene

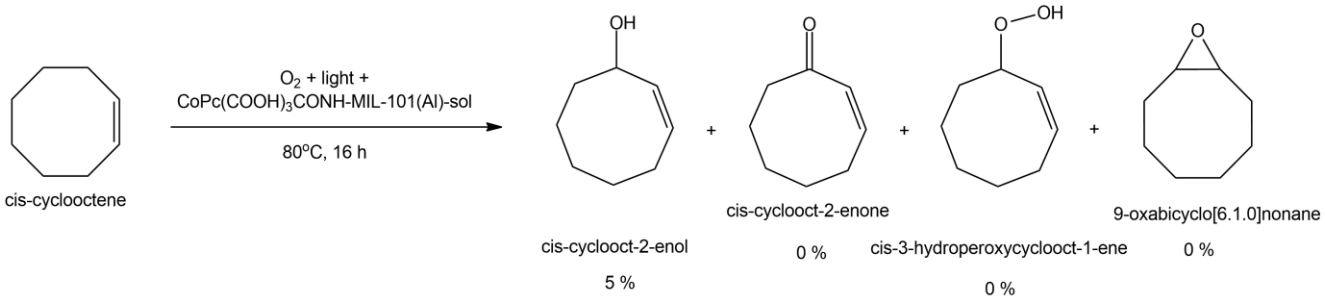

Cis-cyclooctene (10 cm^3, 0.19 mmol) was added to CoPc(COOH)$_3$-CONH-MIL-101(Al) (25 mg) in a glass reactor. The reaction mixture was irradiated with a 400 W mercury-halide lamp* at 80°C for 16 hours under constant bubbling of medical air. After cooling to room temperature the reaction mixture was filtered to obtain a mixture of cis-cyclooctene and cis-cycloocten-2-enol (9.9 cm^3, 5 %). δ_H(300 MHz, $CDCl_3$)/ppm 5.65 (2H, m, HC=CH), 4.31 (1H, sm, C-H), 2.16 (2H, sm, C-H_2), ~1.55 (8H, overlapping H_2O, C-H_2).

* The spectrum of this lamp closely resembles that of sunlight.

5 Conclusions and Future Perspectives

5.1 Conclusions

NH_2-MIL-101(Al) **(1)** was successfully synthesised during an adapted benchtop synthesis, optimised for the best possible yield (31.0%). The as-synthesised MOF was purified during a two-step method, first by soxhlet extraction of the unreacted NH_2-bdc molecules and DMF with ethanol and then by thermal activation under high vacuum. This process for NH_2-MIL-101(Al) is superior compared to previous activation methods, resulting in a BET surface area (3192 ± 57 m^2g^{-1}) which is 93 m^2g^{-1} larger than the current literature value (3099 m^2g^{-1}).

2(3),9(10),16(17),23(24)-Tetra-*tert*-butylphthalocyanine ($2HPc^tBu_4$ **2**) was successfully synthesised with two methods (lithium method and hydroquinone method). The hydroquinone method gave a 60% higher yield, since the lithium method made use of pentanol, a high-boiling solvent, while the reagents were in a melt, without any solvent, during the hydroquinone method. This improved the workup procedure and decreased product loss. $2HPc^tBu_4$ was metallated with Zn(II)acetate and Ni(II)acetate respectively, giving macrocycles with a higher tendency for aggregation than the metal-free $2HPc^tBu_4$. Metallation of $2HPc^tBu_4$ with the chloride salts of Zn and Ni was less successful. UV-Vis spectroscopy confirmed the successful metallation of $2HPc^tBu_4$ by giving distinct, single Q-band maxima for both $NiPc^tBu_4$ **(4)** (667 nm) and $ZnPc^tBu_4$ **(3)** (671 nm), compared to the double Q-band of $2HPc^tBu_4$. No aggregation was found for both metallated Pcs at concentrations below 19 μM.

$ZnPc(COOH)_4$ **(4)**, $FeClPc(COOH)_4$ **(5)**, $CoPc(COOH)_4$ **(6)** and $NiPc(COOH)_4$ **(7)** were synthesised using a two-step reaction method: cyclotetramerization of the specific metal and trimellitic anhydride with ammonium chloride and ammonium molybdate in molten urea, followed by the hydrolysis of the tetra-analido intermediates. Since these intermediates were prone to decomposition in basic conditions, limiting the reaction time for hydrolysis was crucial. $ZnPc(COOH)_4$ was successfully hydrolysed, while for $CoPc(COOH)_4$ 50% and for $NiPc(COOH)_4$ 25% of the analido groups were hydrolysed to carboxyl groups after the five hour time limit, as confirmed by MALDI-TOF MS. For concentrations

below 180 μM, only $NiPc(COOH)_4$ started to aggregate between 5 and 10 μM, whereas $ZnPc(COOH)_4$, $FeClPc(COOH)_4$ and $CoPc(COOH)_4$ showed little to no aggregation.

To incorporate the above MPcs inside the pores of NH_2-MIL-101(Al), two methods were compared: templating and solution phase infiltration. All MPc-containing products were characterised successfully with FTIR, TGA, DRS-UV-Vis, ASAP and PXRD.

FTIR results showed that NH_2-MIL-101(Al) still formed during the templating method, in spite of the presence of the MPcs in solution.

TGA results of the MPc-impregnated MOFs could not confirm the exact mass loss of the encapsulated MPcs, since its decomposition overlaps with the decomposition of the MOF. All these products showed a slightly lower thermal stability (up to 354°C) due to the presence of the MPc inside the MOF.

DRS-UV-Vis easily confirmed the presence of each MPc incorporated inside the MOF by the strong Q-band absorption of the MPc. It also showed that a higher loading of each particular MPc was achieved during solution phase infiltration, which gave stronger Q-bands than the MOF-encapsulated MPcs after the templating method. $ZnPc^tBu_4$ and $FeClPc(COOH)_4$ decomposed during templating, as seen from the yellow colour of the products, as well as the absence of their Q-band absorptions. Their decomposition occurred after thermal degradation of the solvent (DMF) at high temperature (~100°C). $FeClPc(COOH)_4$ (in DMF) also decomposed during solution phase infiltration, but when DMF was exchanged with toluene after infiltration, decomposition was minimal.

Surface area and porosity analyses showed that the highest N_2 uptake for each MOF-containing MPc was achieved after templating (N_2 uptake = between 2010 and 393 cm^3g^{-1}), with only $NiPc(COOH)_3$-CONH-MIL-101(Al) **(14-sol)** (N_2 uptake = 110 cm^3g^{-1}) as the exception. This is an indication that low amounts of MPc were encapsulated by NH_2-MIL-101(Al) during templating. When solution phase infiltration was used, a sharp decrease in N_2 uptake (between 244 and 89 cm^3g^{-1}) was found with a strong hysteresis, which suggests a high loading of the particular MPc.

PXRD analyses correlated strongly with ASAP results, showing that the products with high BET surface areas (low MPc load) portrayed well-defined, crystalline spectra in comparison to products with low BET surface areas (high MPc load) giving poor PXRD patterns.

Hydrogen storage trials of $CoPc(COOH)_3$-CONH-MIL-101(Al) **(13-sol)** and $NiPc(COOH)_3$-CONH MIL-101(Al) **(14-sol)** gave relatively low excess uptake values (0.47 wt% @ 16 bar and 1.5 wt% @ 128 bar respectively) showing that the presence of the MPc molecules in NH_2-MIL-101(Al) did not contribute to a higher H_2-uptake.

During a photo-catalytic trial, $CoPc(COOH)_3$-CONH-MIL-101(Al) **(13-sol)** was able to generate singlet oxygen to oxidise cis-cyclooctene to cis-cyclooct-2-enol. In spite of a low loading of $CoPc(COOH)_4$ in the MOF, it still achieved a conversion of 5% towards the alcohol.

Liquid state cyclic voltammetry (CV) of $2HPc^tBu_4$, $ZnPc^tBu_4$ and $NiPc^tBu_4$ showed the four expected Pc-ring-based couples in the solvent window of CH_2Cl_2. Due to low solubility some of these couples were electrochemically and chemically semi-reversible. The ring-based redox couples for $NiPc^tBu_4$ were found at lower formal reduction potentials than those of $2HPc^tBu_4$ and $ZnPc^tBu_4$, possibly due to the influence of the Ni^{2+} metal centre.

$ZnPc(COOH)_4$, $FeClPc(COOH)_4$, $CoPc(COOH)_4$ and $NiPc(COOH)_4$ are less soluble than the tertiary butyl substituted MPcs. Their cyclic voltammetry was thus performed in DMSO and at least three ring-based redox couples were detected for all four compounds. Only for $CoPc(COOH)_4$ a fourth ring-based process could be observed in the DMSO solvent window. In addition, $FeClPc(COOH)_4$ and $CoPc(COOH)_4$ both displayed metal-centred redox processes: $FeClPc(COOH)_4$ gave an $Fe^{2+/3+}$ couple at $E^{\circ\prime}$ = -88 mV vs. ferrocene, while $CoPc(COOH)_4$ showed couples for $Co^{1+/2+}$ and $Co^{2+/3+}$ at $E^{\circ\prime}$ = -738 mV and -289 mV vs. ferrocene respectively. The redox couples of all tetracarboxylated MPcs were electrochemically reversible or quasi-reversible (63 mV $\leq \Delta E_p \leq$ 118 mV vs. ferrocene for all couples).

Solid state, cyclic voltammetry of all the MPc@NH_2-MIL-101(Al) products displayed at least one MPc ring-based couple (near 200 mV vs. ferrocene). $ZnPc(COOH)_3$-CONH-MIL-101(Al) gave an additional redox processes at $E^{\circ\prime}$ = 1158 mV vs. ferrocene and $NiPc(COOH)_3$-CONH-MIL-101(Al) two additional processes ($E^{\circ\prime}$ = 1146 mV and 1383 mV vs. ferrocene) in the solvent window of DMSO. These processes were mostly electrochemically and chemically irreversible, but in spite of that, it showed that the MOF matrix could influence the flow of electrons during oxidation of the encapsulated MPcs.

5.2 Future Perspectives

The combination of MPcs and NH_2-MIL-101(Al) displays a promising research field which needs to be investigated and expanded further than the scope of this study. Different variations of NH_2-MIL-101(M) where M = Fe(III), V(III) and Cr(III) need to be impregnated with MPcs. This will give better insight into other heterogeneous catalytic applications such the Knoevenagel condensation of benzaldehyde and ethylcyanoacetate being catalysed by MPc@NH_2-MIL-101. Solar harvesting is an important applications for MPcs (M = Zn(II), In(III) and Mn(III)) which can be investigated with

high loadings of MPc@NH_2-MIL-101. The combination of different metal centres of NH_2-MIL-101 will also give better insight into the hydrogen storage capabilities of these materials. The loading of MPcs in the MOF's pores needs to be increased to achieve higher catalytic activity. A possibility would be to use unfunctionalised, MIL-101 as support material. Due to the lack of amine groups in the MOF's framework, there will be no interference when MPc molecules are intruded into the MOF. An alternative approach would be to combine small MPcs with large cage MOFs, such as MOF-74 or IRMOF-20, which can be possible future supports with a higher loading of MPc. Different functional groups on the peripheral as well as the non-peripheral position of the MPc ring need to be investigated, since it is known that functional groups with longer chain-lengths can improve solubility of the MPc. Together with improved solubility, aggregation also needs to be minimized. Non-peripheral as well as the axial attachment of ligands with alkyl chains and functional groups such as hydroxyls and hydroxides or leaving groups such as halides will help to alleviate aggregation of MPc molecules. Multi-functional heterogeneous catalysts can be developed when these functionalised MPcs are infiltrated and immobilised in a MOF matrix with large pores, such as IRMOF-16 and MOF-74.

Appendix

FTIR

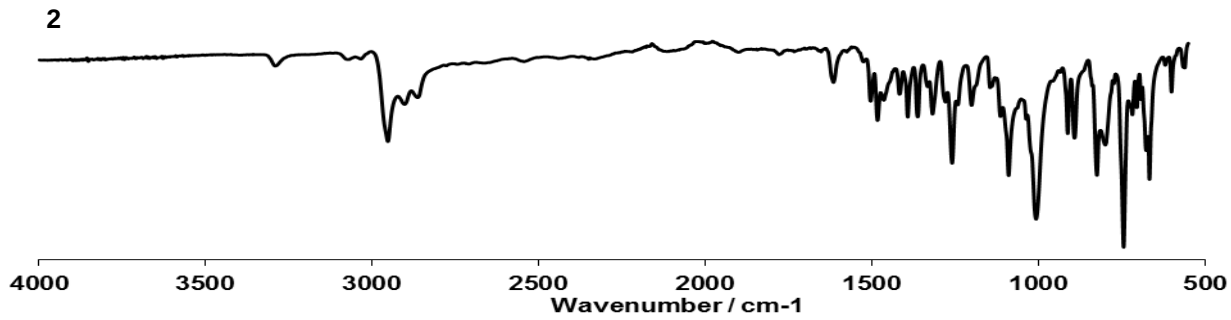

Figure 1: FTIR spectrum of 2HPc^{t}Bu$_4$ **(2)** synthesised through the hydroquinone method.

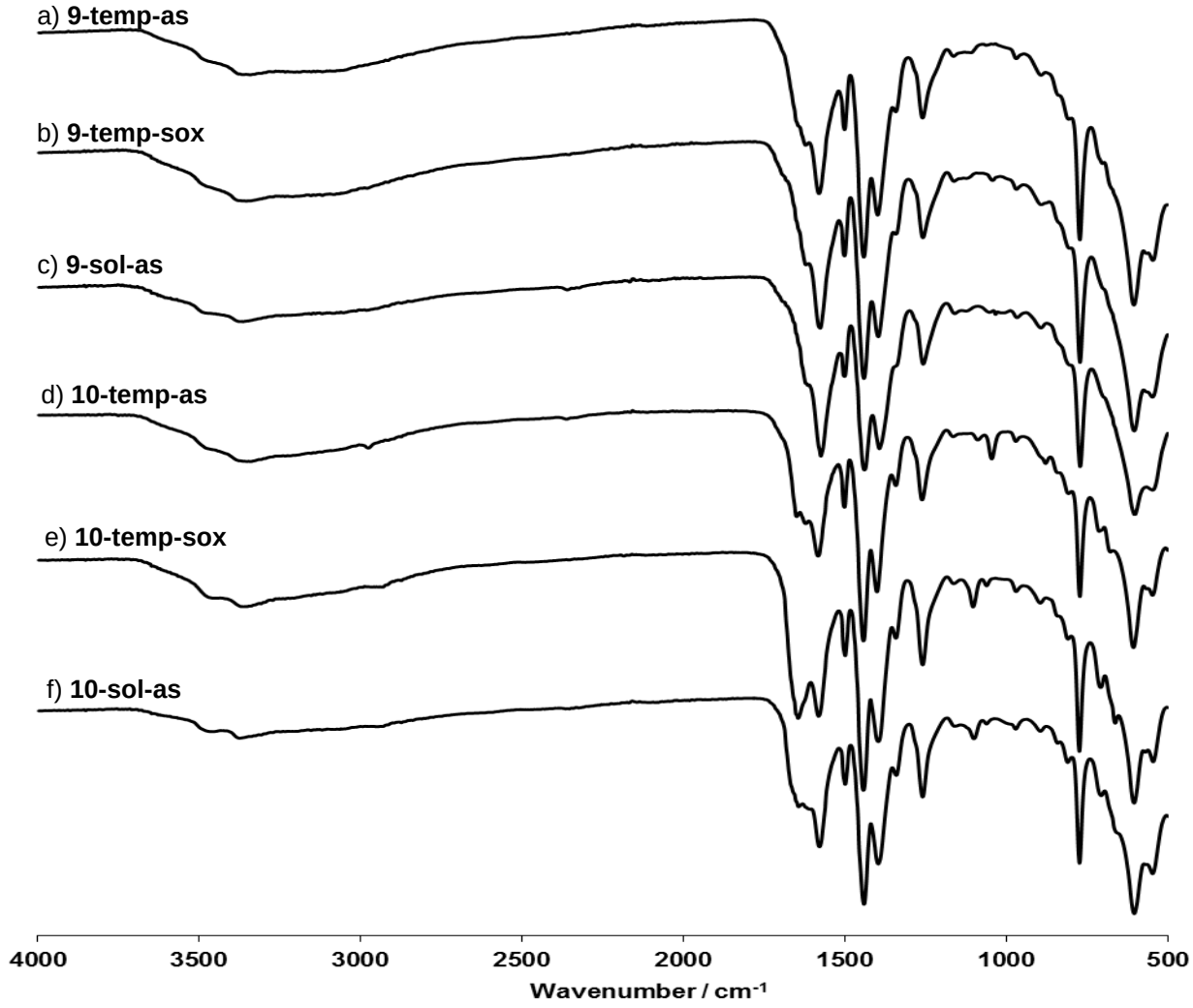

Figure 2: FTIR spectra of a) ZnPc^{t}Bu$_4$@NH$_2$-MIL-101(Al) **(9-temp-as)**, b) ZnPc^{t}Bu$_4$@NH$_2$-MIL-101(Al) **(9-temp-sox)**, c) ZnPc^{t}Bu$_4$@NH$_2$-MIL-101(Al) **(9-sol-as)**, d) ZnPc^{t}Bu$_4$@NH$_2$-MIL-101(Al) **(9-temp-as)**, e) NiPc^{t}Bu$_4$@NH$_2$-MIL-101(Al) **(10-temp-as)**, e) NiPc^{t}Bu$_4$@NH$_2$-MIL-101(Al) **(10-temp-sox)** and f) NiPc^{t}Bu$_4$@NH$_2$-MIL-101(Al) **(10-sol-as)**. **Temp** = templating method, **sol** = solution phase infiltration, **as** = as-synthesised and **sox** = soxhlet extracted.

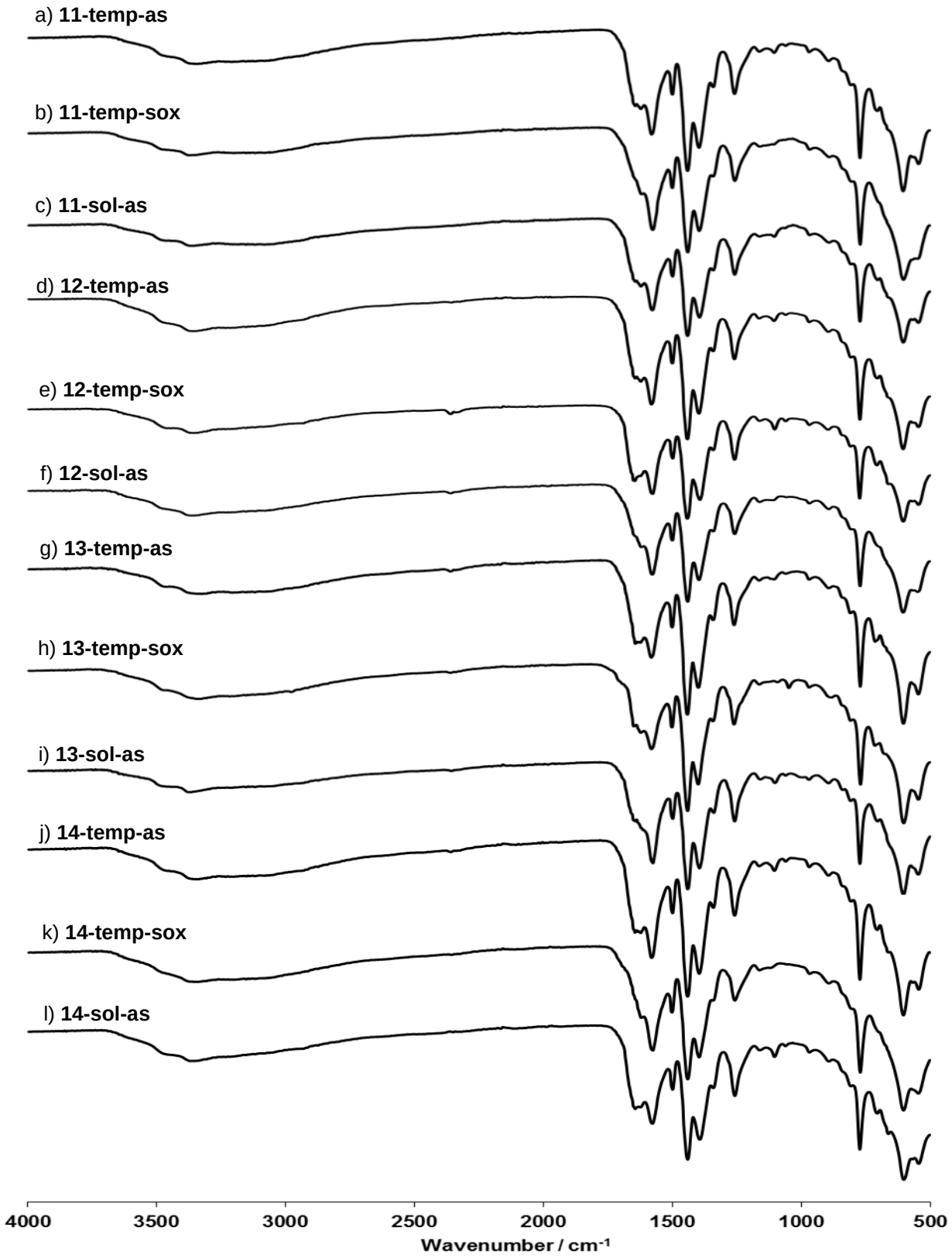

Figure 3: FTIR spectra of a) ZnPc(COOH)$_3$-CONH-MIL-101(Al) **(11-temp-as)**, b) ZnPc(COOH)$_3$-CONH-MIL-101(Al) **(11-temp-sox)**, c) ZnPc(COOH)$_3$-CONH-MIL-101(Al) **(11-sol-as)**, d) FeClPc(COOH)$_3$-CONH-MIL-101(Al) **(12-temp-as)**, e) FeClPc(COOH)$_3$-CONH-MIL-101(Al) **(12-temp-sox)**, f) FeClPc(COOH)$_3$-CONH-MIL-101(Al) **(12-sol-as)**, g) CoPc(COOH)$_3$-CONH-MIL-101(Al) **(13-temp-as)**, h) CoPc(COOH)$_3$-CONH-MIL-101(Al) **(13-temp-sox)**, i) CoPc(COOH)$_3$-CONH-MIL-101(Al) **(13-sol-as)**, j) NiPc(COOH)$_3$-CONH-MIL-101(Al) **(14-temp-as)**, k) NiPc(COOH)$_3$-CONH-MIL-101(Al) **(14-temp-sox)** and l) NiPc(COOH)$_3$-CONH-MIL-101(Al) **(14-sol-as)**. **Temp** = templating method, **sol** = solution phase infiltration, **as** = as-synthesised and **sox** = soxhlet extracted.

^{1}H-NMR

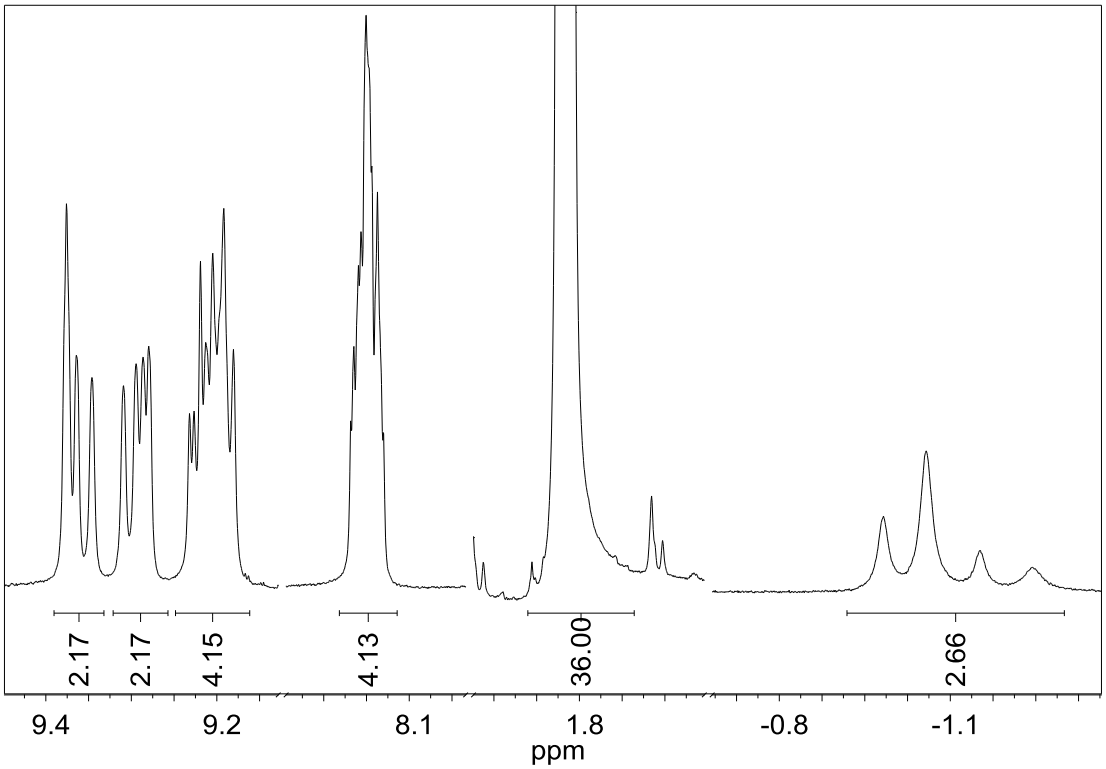

Figure 4: ^{1}H NMR spectrum of 2HPc^{t}Bu$_4$ **(2)** synthesised via the hydroquinone method.

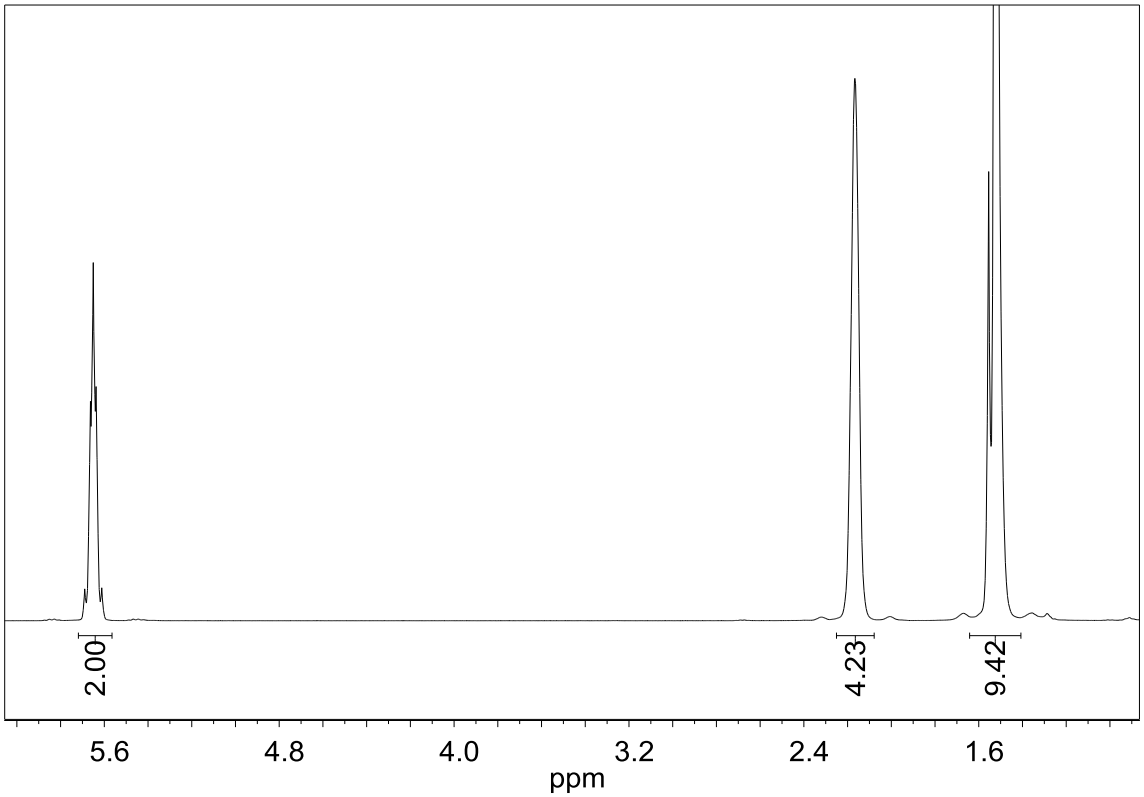

Figure 5: ^{1}H NMR control test for the photooxidation of cis-cyclooctene in the absence of light.

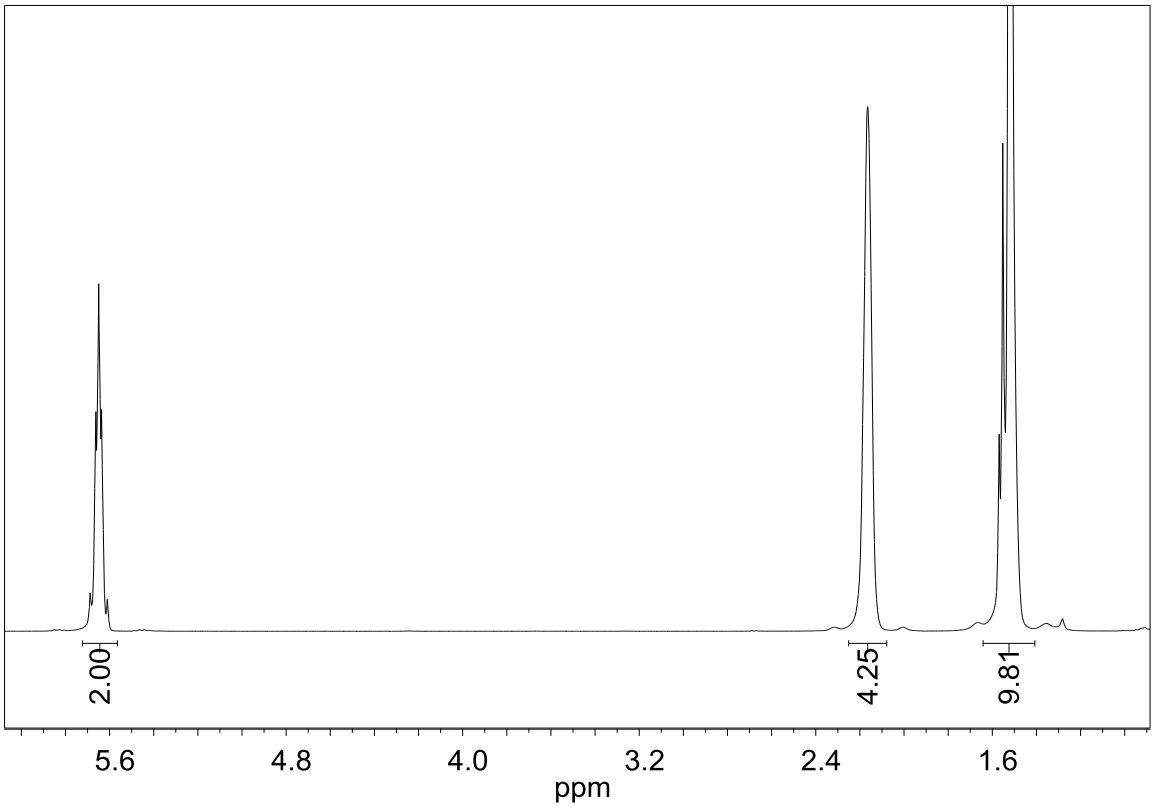

Figure 6: ^{1}H NMR control test for the photocatalysed oxidation of cis-cyclooctene using ZnPc(COOH)$_3$-CONH-MIL-101(Al) **(11-temp-sox)** as catalyst.

TGA

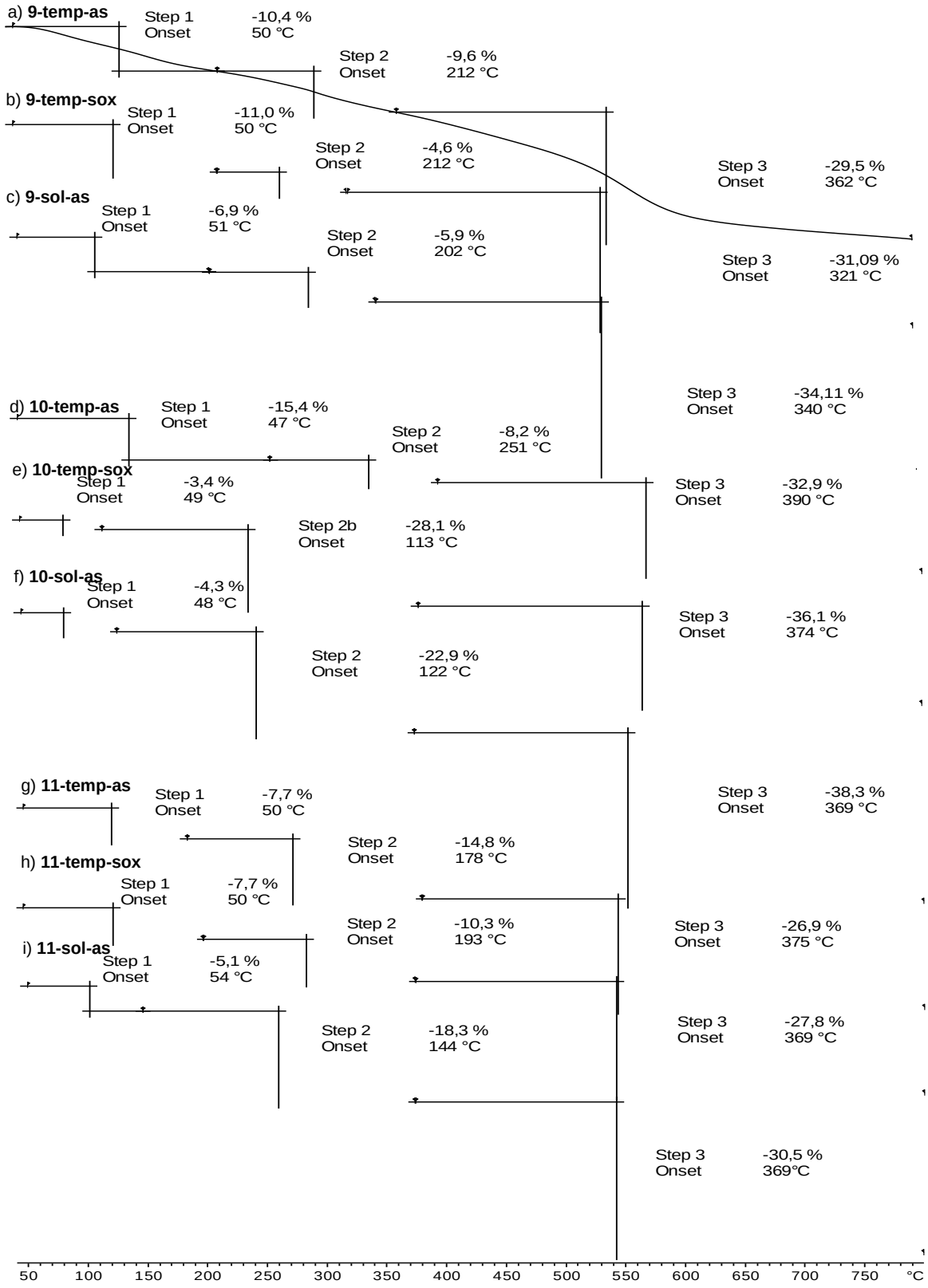

Figure 7: TGA thermograms of a) ZnPc^{t}Bu$_4$@NH$_2$-MIL-101(Al) **(9-temp-as)**, b) ZnPc^{t}Bu$_4$@NH$_2$-MIL-101(Al) **(9-temp-sox)**, c) ZnPc^{t}Bu$_4$@NH$_2$-MIL-101(Al) **(9-sol-as)**, d) ZnPc^{t}Bu$_4$@NH$_2$-MIL-101(Al) **(9-temp-as)**, e) NiPc^{t}Bu$_4$@NH$_2$-MIL-101(Al) **(10-temp-as)**, e) NiPc^{t}Bu$_4$@NH$_2$-MIL-101(Al) **(10-temp-sox)**, f) NiPc^{t}Bu$_4$@NH$_2$-MIL-101(Al) **(10-sol-as)**, g) ZnPc(COOH)$_3$-CONH-MIL-101(Al) **(11-temp-as)**, h) ZnPc(COOH)$_3$-CONH-MIL-101(Al) **(11-temp-sox)** and i) ZnPc(COOH)$_3$-CONH-MIL-101(Al) **(11-sol-as)**. **Temp** = templating method, **sol** = solution phase infiltration, **as** = as-synthesised and **sox** = soxhlet extracted.

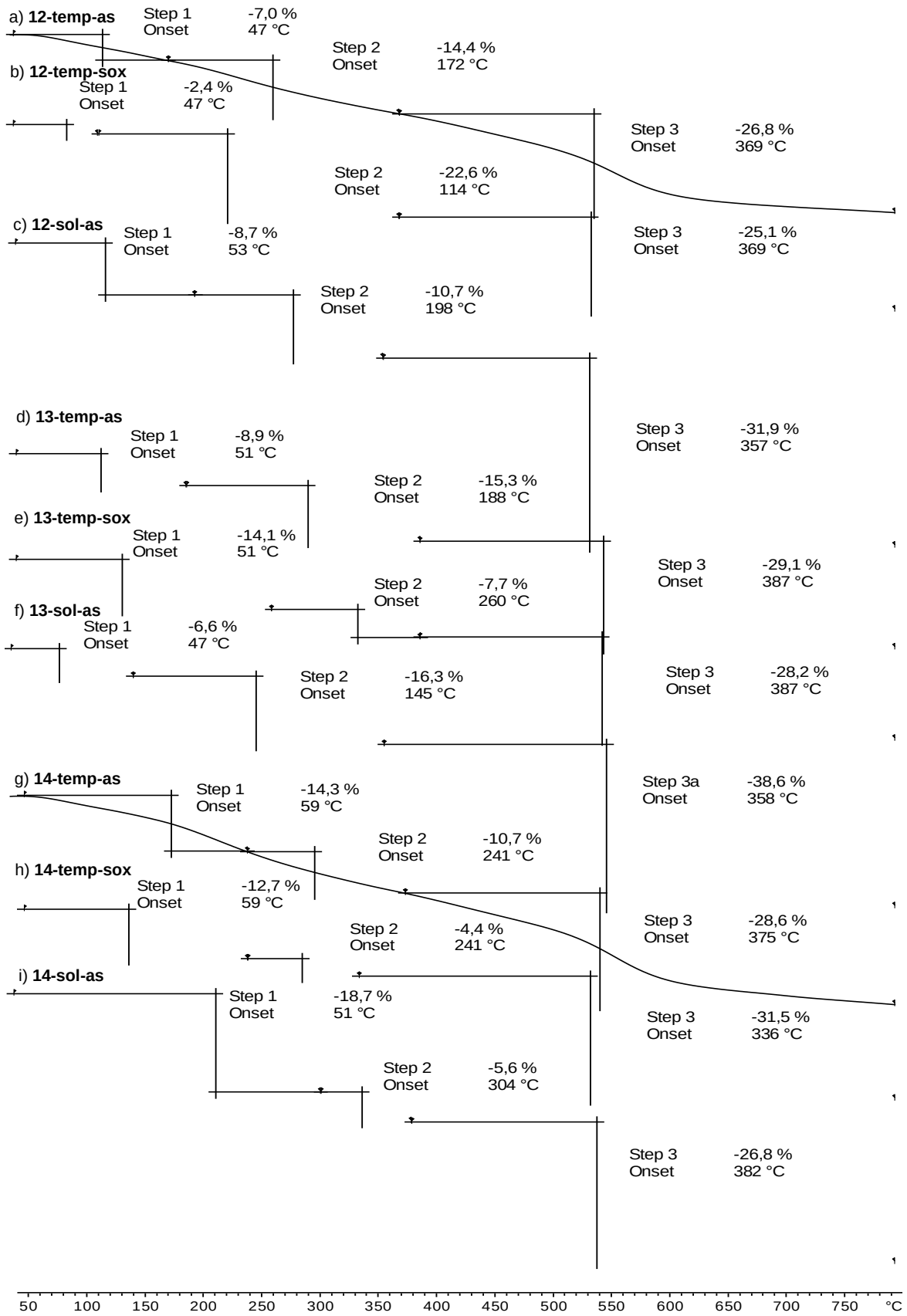

Figure 8: TGA thermograms of a) FeClPc(COOH)$_3$-CONH-MIL-101(Al) **(12-temp-as)**, b) FeClPc(COOH)$_3$-CONH-MIL-101(Al) **(12-temp-sox)**, c) FeClPc(COOH)$_3$-CONH-MIL-101(Al) **(12-sol-as)**, d) CoPc(COOH)$_3$-CONH-MIL-101(Al) **(13-temp-as)**, e) CoPc(COOH)$_3$-CONH-MIL-101(Al) **(13-temp-sox)**, f) CoPc(COOH)$_3$-CONH-MIL-101(Al) **(13-sol-as)**, g) NiPc(COOH)$_3$-CONH-MIL-101(Al) **(14-temp-as)**, h) NiPc(COOH)$_3$-CONH-MIL-101(Al) **(14-temp-sox)** and i) NiPc(COOH)$_3$-CONH-MIL-101(Al) **(14-sol-as)**. **Temp** = templating method, **sol** = solution phase infiltration, **as** = as-synthesised and **sox** = soxhlet extracted.

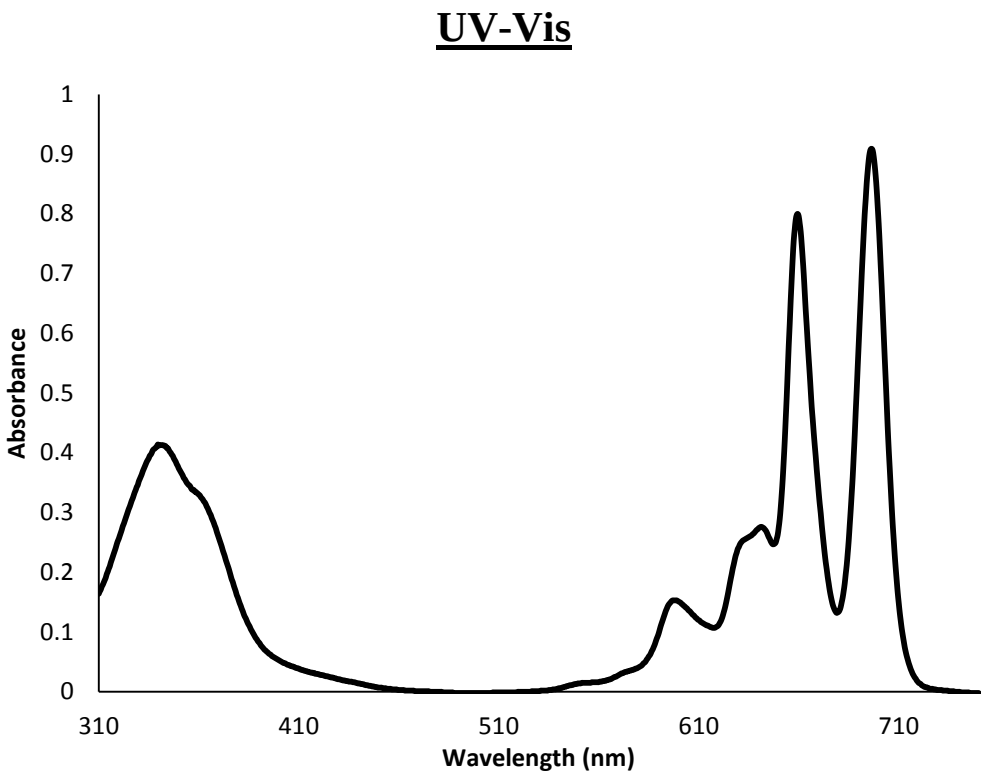

Figure 9: UV-Vis spectrum of 2HPc^{t}Bu$_4$ **(2)** synthesised through the hydroquinone method.

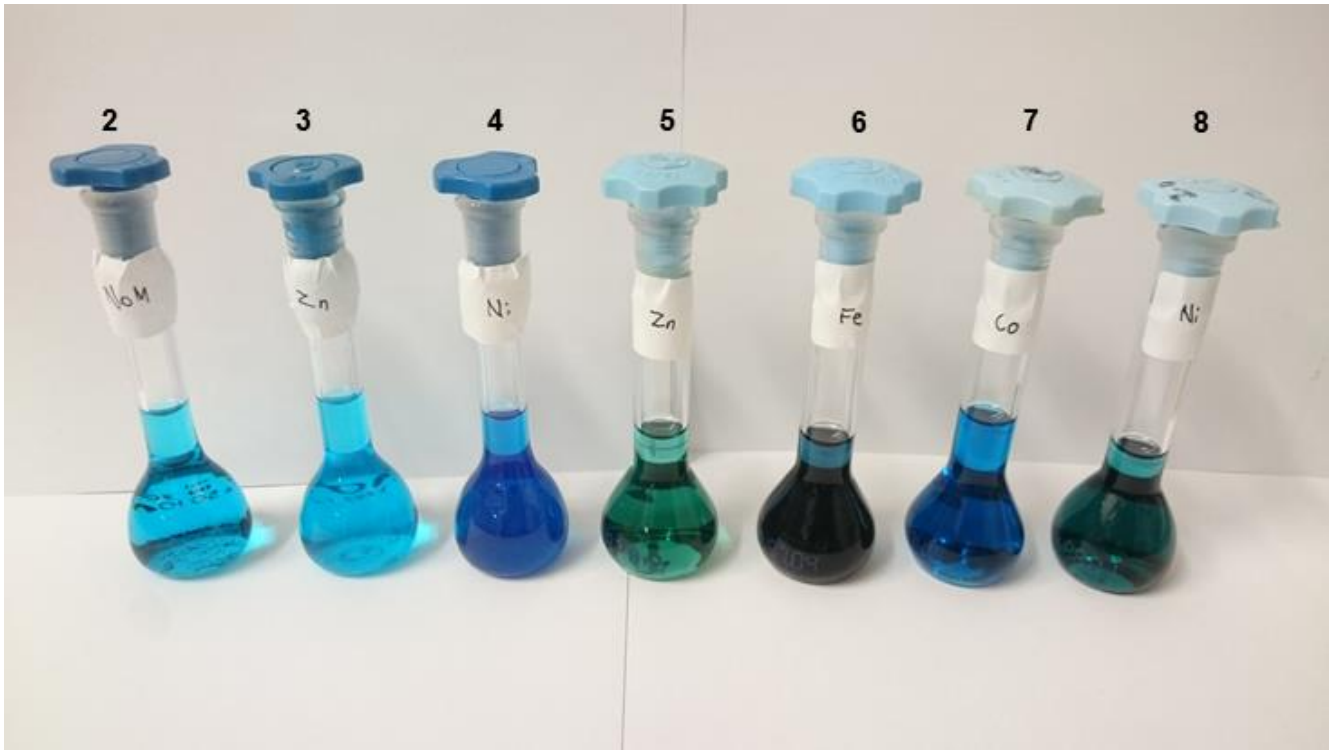

Figure 10: Equimolar solutions of 2HPc^{t}Bu$_4$ **(2)**, ZnPc^{t}Bu$_4$ **(3)**, NiPc^{t}Bu$_4$ **(4)** ZnPc(COOH)$_4$ **(5)**, FeClPc(COOH)$_4$ **(6)**, CoPc(COOH)$_4$ **(7)** and NiPc(COOH)$_4$ **(8)**.

Maldi-TOF

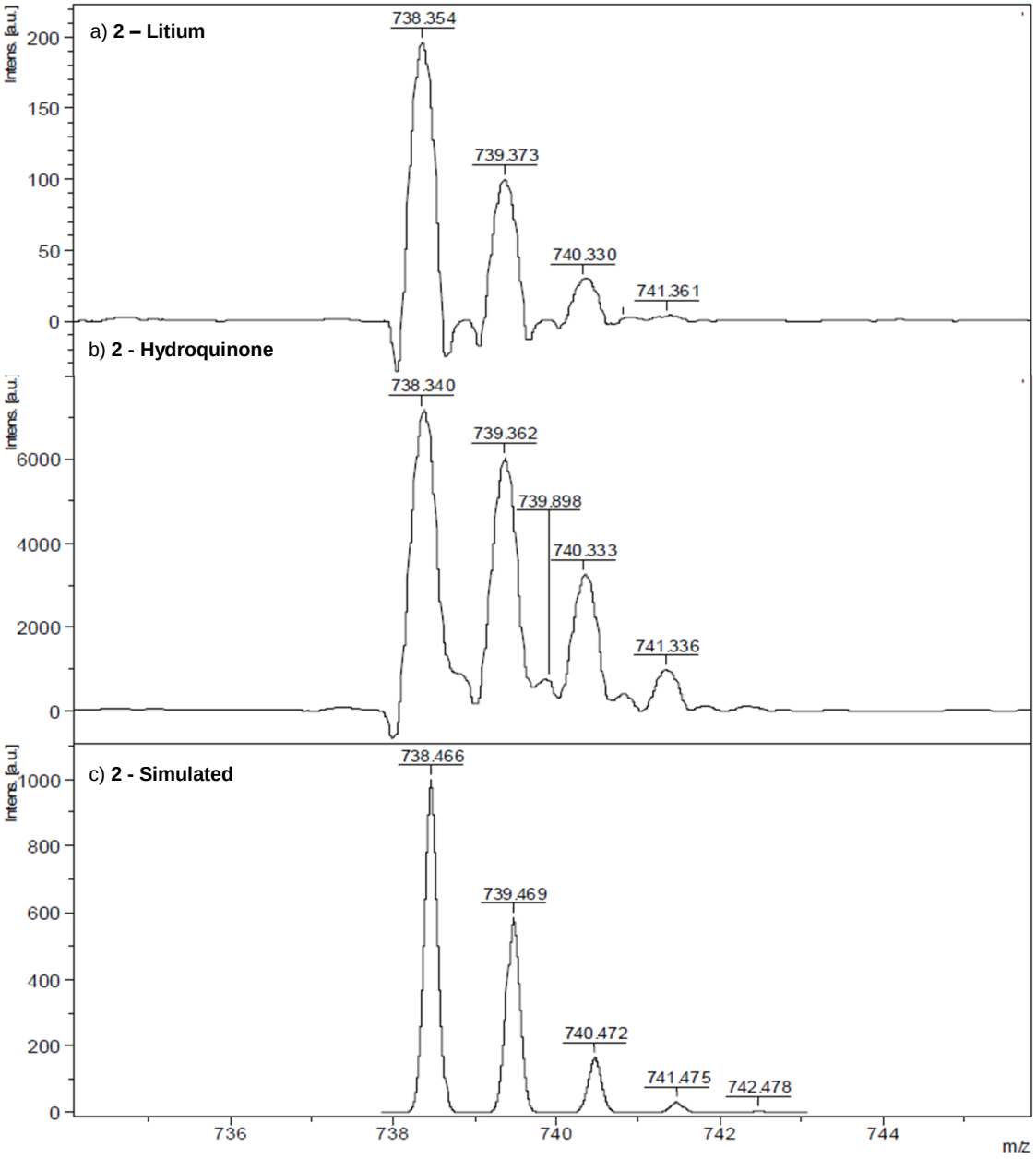

Figure 11: Maldi-TOF spectra of a) 2HPc^{t}Bu$_4$ **(2)** synthesised through the lithium method, b) 2HPc^{t}Bu$_4$ **(2)** synthesised through the hydroquinone method and c) simulation of **2**.

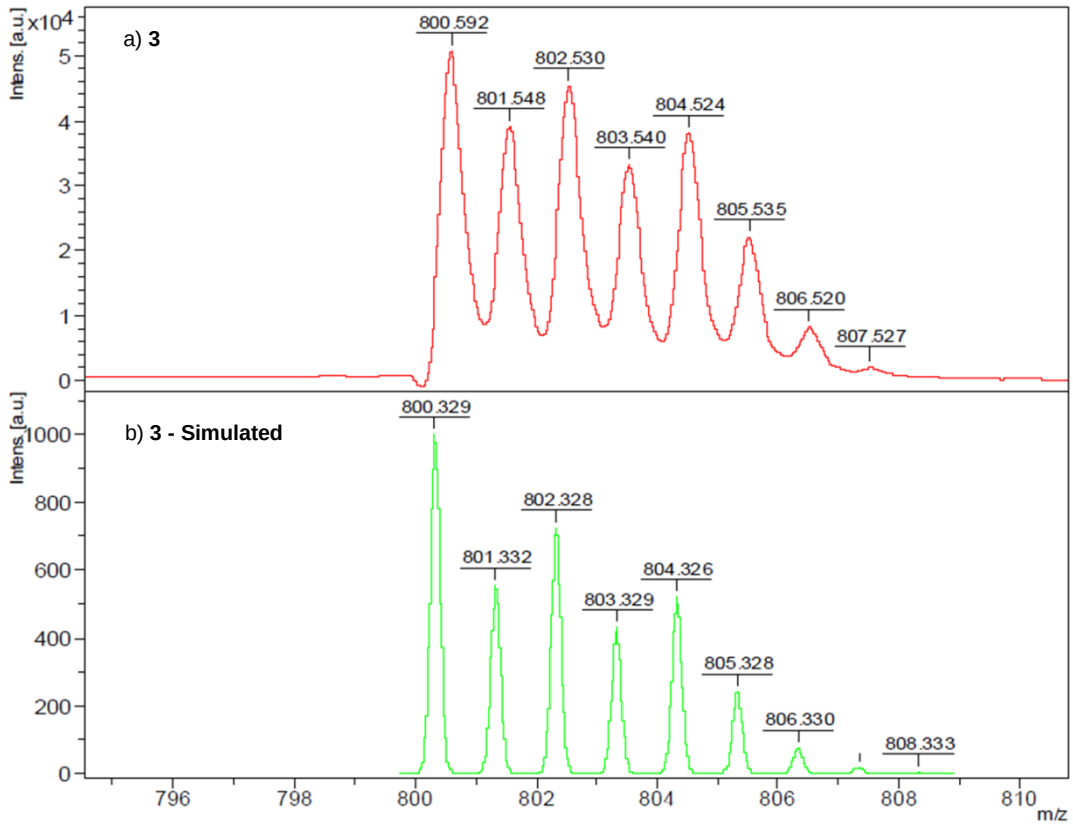

Figure 12: Maldi-TOF spectra of a) ZnPc^{t}Bu$_4$ **(3)** and b) simulation of **3**.

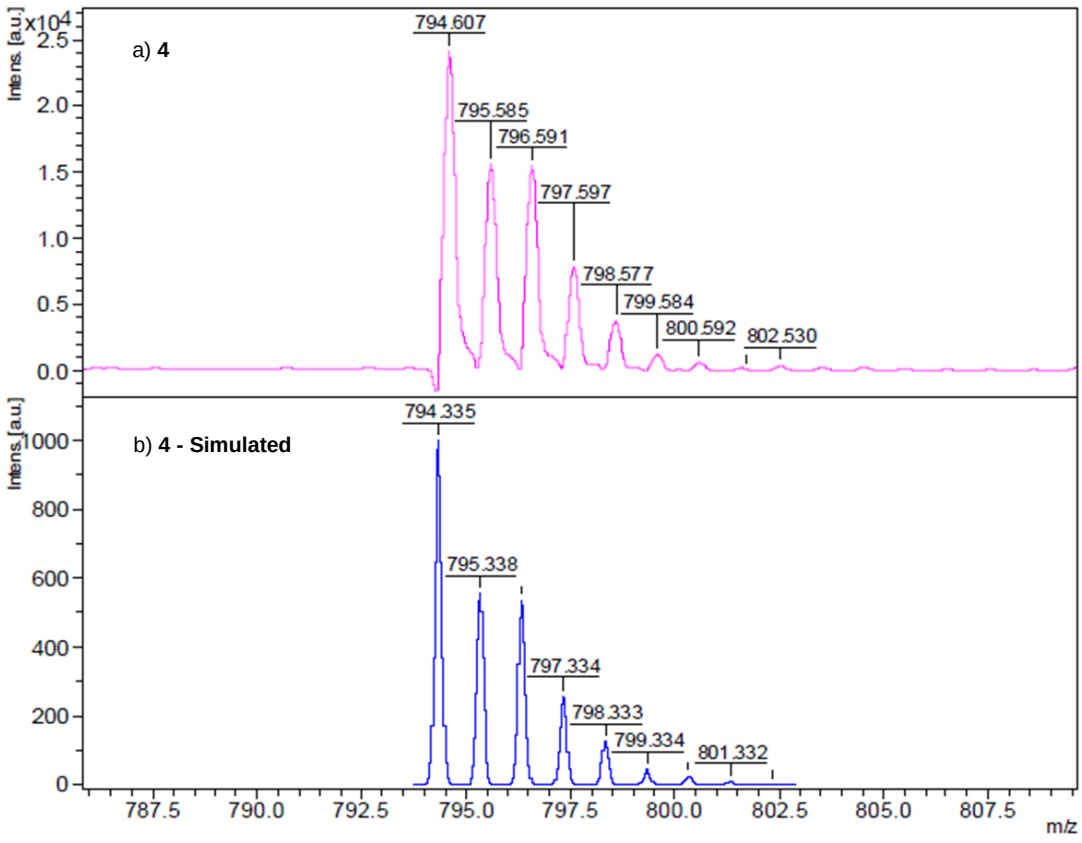

Figure 13: Maldi-TOF spectra of a) NiPc^{t}Bu$_4$ **(4)** and b) simulation of **4**.

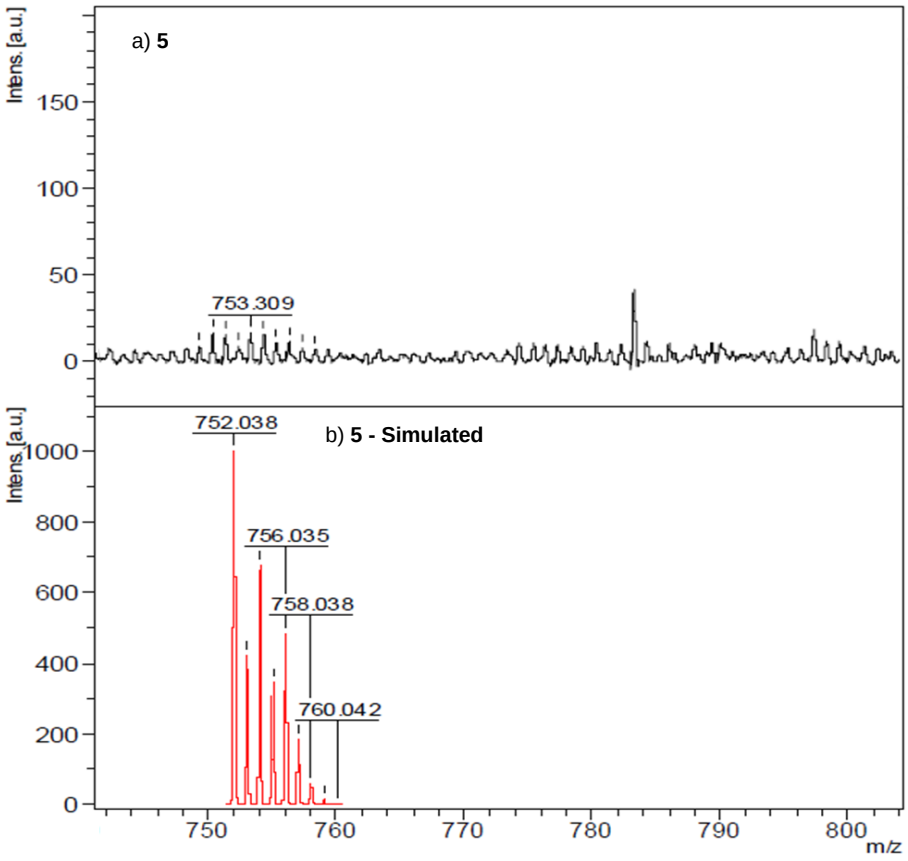

Figure 14: Maldi-TOF spectra of a) $ZnPc(COOH)_4$ **(5)** and b) simulation of **5**.

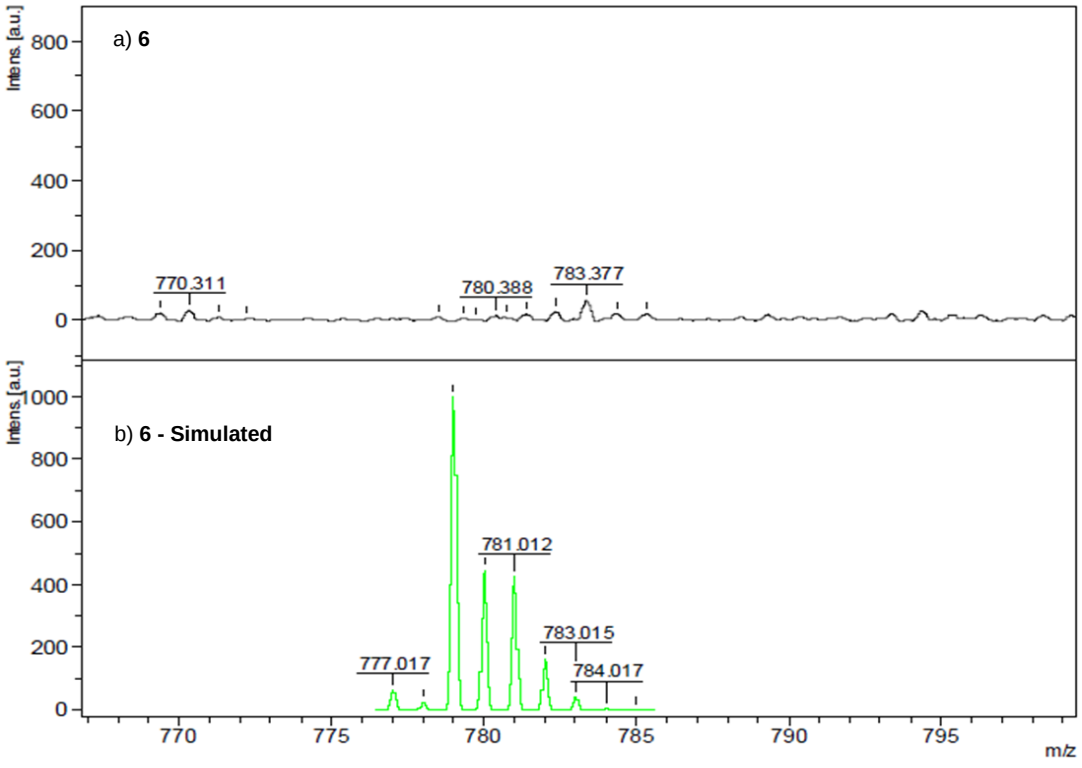

Figure 15: Maldi-TOF spectra of a) $FeClPc(COOH)_4$ **(6)** and b) simulation of **6**.

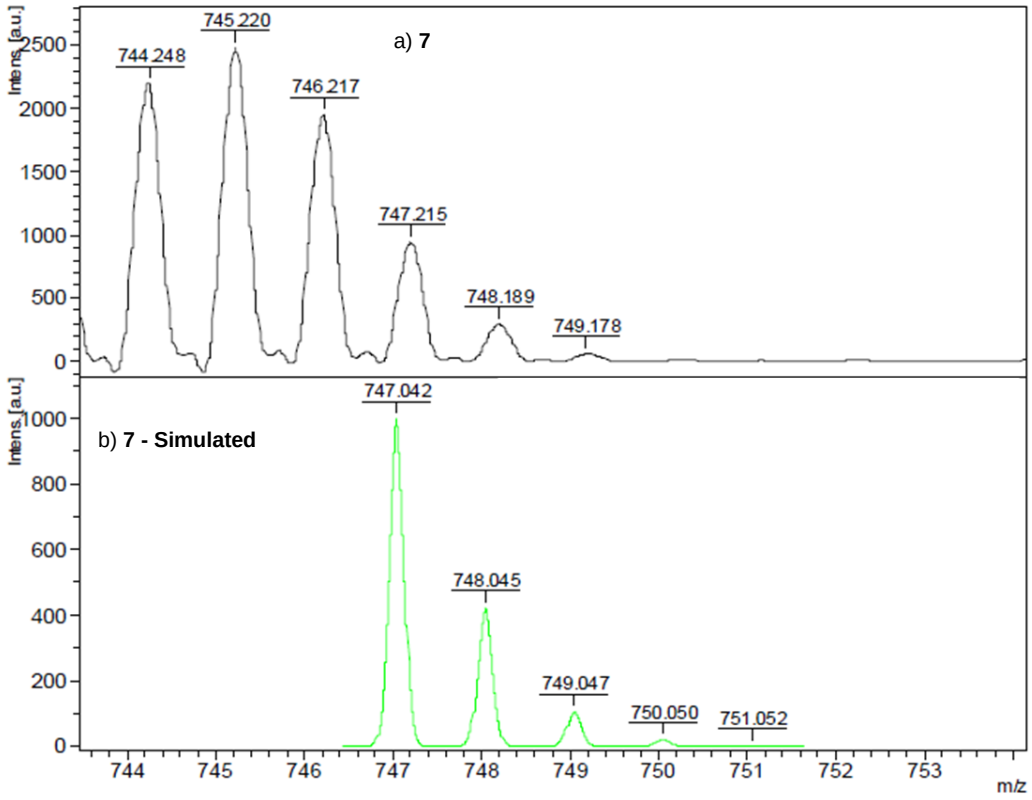

Figure 16: Maldi-TOF spectra of a) $CoPc(COOH)_4$ **(7)** and b) simulation of **7**.

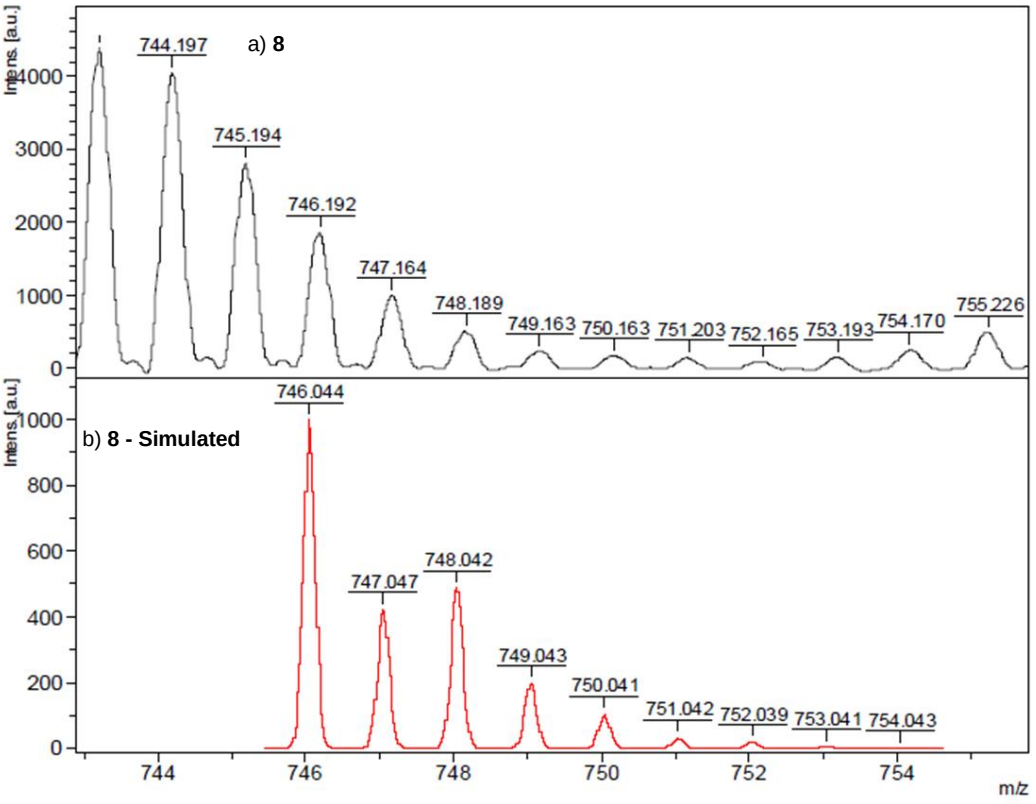

Figure 17: Maldi-TOF spectra of a) $NiPc(COOH)_4$ **(8)** and b) simulation of **8**.